AN ABSTRACT OF THE THESIS OF

Jerome Martin Dummer Jr. for the degree of Master of Ocean Engineering

in Ocean Engineering presented on December 14, 1979

Title: WAVE INTERACTION WITH PILE SUPPORTED HARBOR FACILITIES

Redacted for privacy

Abstract approved: ______________________
Dr. Charles K. Sollitt

A major fraction of all overwater harbor facilities are constructed upon relatively open pile frameworks. The supporting pile structure provides vessel access to the facility for loading and mooring while allowing circulation in the underlying marine environment. The utility of the structure is enhanced measurably if locally occurring waves are attenuated rather than reflected, so that commercial and recreational vessel activities can proceed unimpeded. The design of a pile structure can include considerations for wave attenuation if a satisfactory predictive method is available to quantify the wave-pile interaction phenomena. A theory which accounts for directionally sensitive inertial and viscous damping has been developed for a two-dimensional structure interacting with monochromatic waves. An equivalent work linearizing procedure yields a potential flow problem satisfied by an eigen-series solution. Linear wave theory is applied outside the pile structure and a sea wall of arbitrary

reflecting capacity may be specified at any distance from the leeward side of the structure. General solutions are matched at the sea-structure interface by requiring continuity of horizontal mass flux and pressure. The amplitude and phase of waves in the pile structure, the reflected wave and transmitted wave modes are solved from algebraic equations resulting from orthogonalization of the interfacial boundary conditions. Comparison with experimental results are made. Optimization of design techniques with regard to wave-structure interaction with pile configurations are described. Enhancement of pile structure behavior with common surplus materials is discussed.

Wave Interaction with Pile Supported Harbor Facilities

by

Jerome Martin Dummer Jr.

A THESIS

submitted to

Oregon State University

in partial fulfillment of
the requirements for the
degree of

Master of Ocean Engineering

June 1980

APPROVED:

Redacted for privacy

Professor of Civil Engineering

in charge of major

Redacted for privacy

Head of Department of Civil Engineering

Redacted for privacy

Dean of Graduate School

Date thesis is presented December 14, 1979

Typed by Clover Redfern for Jerome Martin Dummer Jr.

ACKNOWLEDGMENTS

This work is a result of research sponsored by the Oregon State University Sea Grant College Program, supported by NOAA Office of Sea Grant, U.S. Department of Commerce, under Grant Numbers 04-7-158-44085 and 04-8-M01-144. The U.S. Government is authorized to produce and distribute reprints for governmental purposes notwithstanding any copyright notation that may appear hereon. The writer wishes to gratefully acknowledge the participation and support of the Oregon State University Sea Grant College Program.

The writer also acknowledges with gratitude the patience, encouragement, and logistic support of Ms. Judith A. Dummer, the stimulation, supervision and conception of this research provided by Dr. Chalres K. Sollitt, and the assistance in reviewing the final draft provided by Dr. D.S. Burch, Dr. R.T. Hudspeth, Dr. P.D. Komar, Dr. W.H. Quinn, and Dr. L.J. Weber. The help and cooperation of all the above mentioned persons is greatly appreciated.

TABLE OF CONTENTS

Chapter		Page

LIST OF FIGURES

Figure		Page
7.4.	Reflection and transmission coefficients for varying values of f_x. $f_z = 1.5$.	210
7.5.	Reflection and transmission coefficients for varying values of f_x. $f_z = 2.0$.	211
7.6.	Reflection and transmission coefficients for varying values of f_z. $f_x = 0.01$.	212
7.7.	Reflection and transmission coefficients for varying values of f_z. $f_x = 1.0$.	213
7.8.	Reflection and transmission coefficients for varying values of f_z. $f_x = 2.0$.	214
7.9.	Reflection and transmission coefficients for varying values of f_z. $f_x = 3.0$.	215
7.10.	Reflection and transmission coefficients for varying values of f_z. $f_x = 4.0$.	216
7.11.	Reflection and transmission coefficients for varying values of C_{mx}, S_x. $C_{mz} = 0.0$, $S_z = 1.0$.	221
7.12.	Reflection and transmission coefficients for varying values of C_{mx}, S_x. $C_{mz} = 0.5$, $S_z = 1.024$.	222
7.13.	Reflection and transmission coefficients for varying values of C_{mx}, S_x. $C_{mz} = 1.0$, $S_z = 1.05$.	223
7.14.	Reflection and transmission coefficients for varying values of C_{mx}, S_x. $C_{mz} = 2.0$, $S_z = 1.1$.	224
7.15.	Reflection and transmission coefficients for varying values of C_{mx}, S_x. $C_{mz} = 4.0$, $S_x = 1.19$.	225
7.16.	Reflection and transmission coefficients for varying values of C_{mx}, S_x. $C_{mz} = 0.0$, $S_z = 1.0$.	228
7.17.	Reflection and transmission coefficients for varying values of C_{mx}, S_x. $C_{mz} = 0.5$, $S_z = 1.2$.	229

Figure		Page

WAVE INTERACTION WITH PILE SUPPORTED HARBOR FACILITIES

I. INTRODUCTION

1.1. The Problem Statement

A small amplitude, harmonic, monochromatic, two dimensional wave is normally incident upon a permeable structure composed of multiple rows and columns of structural members.[1/] The structural configuration is not restricted except that it must:

(1) Be a regularly repeated matrix over some distance interval in the direction perpendicular to the direction of wave advance, i.e., in the lateral, or, y-direction (see Fig. 1.2);

(2) Extend from the bottom to some point at or above the still water level;

(3) Be confined by vertical, parallel, lateral boundaries or extend indefinitely laterally.

At the boundary between Regions I and II ($x = -b$, see Fig. 1.1) a portion of the incident wave energy is reflected from the structure, a portion is dissipated, and a portion is transmitted into the structure. Energy dissipation within and at the boundaries of the structure is due

---

[1/] Although circular cylindrical piles are generally depicted within this paper as the structural members (see Fig. 1.2), it is important to note that the theory is applicable for any structural elements for which viscous and inertial loss coefficients may be quantified.

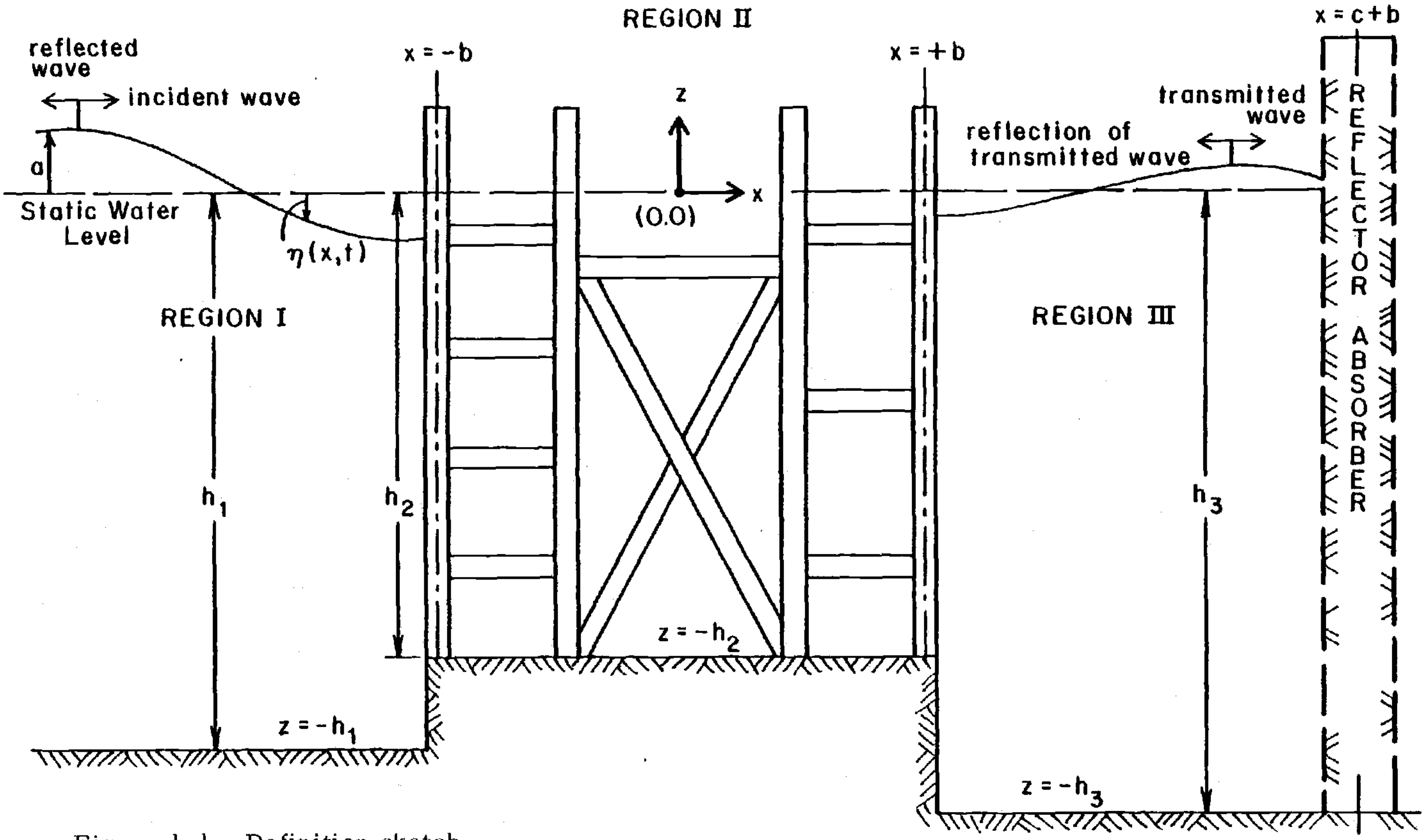

Figure 1.1. Definition sketch.

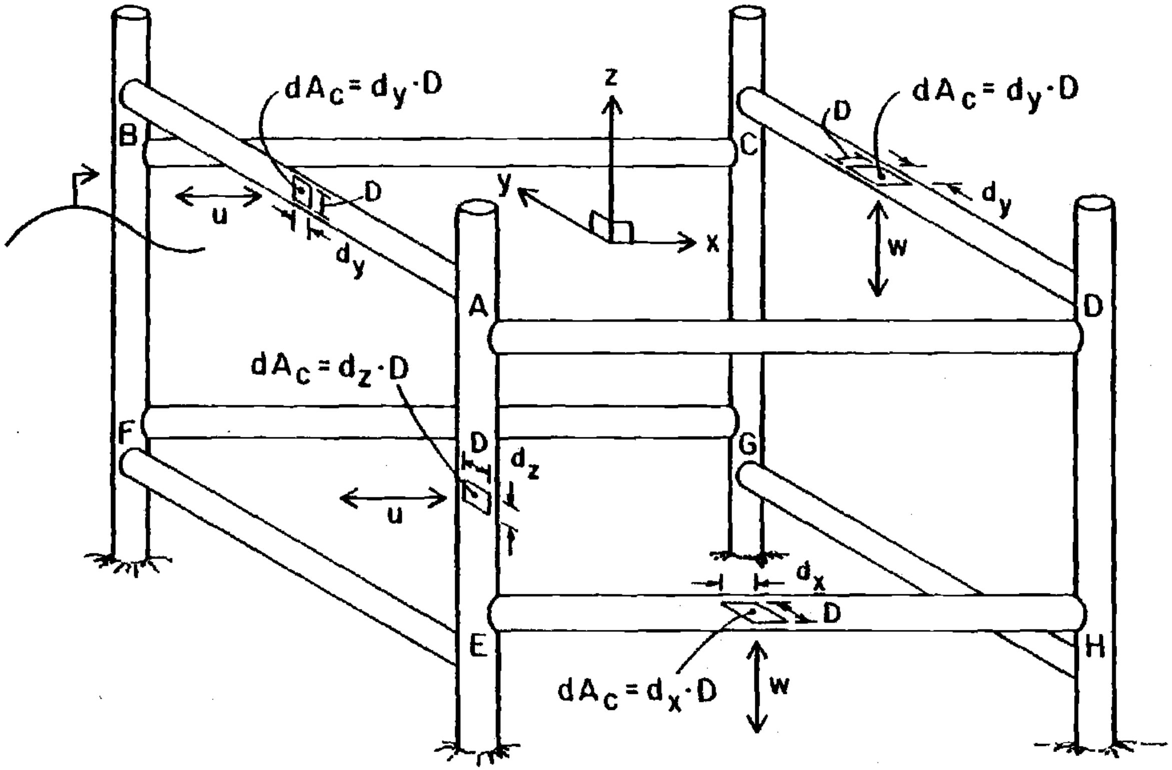

Figure 1.2. Definition sketch for a pile matrix.

to both viscous interaction of the fluid particles with the structural members and inertial effects. Each time the portion of the wave transmitted into the structure at $x = -b$ interacts with a structural member, some portion of its energy is further reflected, dissipated and transmitted. Thus, multiple reflected and transmitted wave forms are present within the structure simultaneously, the net result being a damped partial standing wave in Region II.

A wave-structure interaction similar to that at $x = -b$ also occurs at the boundary between Regions II and III, $x = b$, so that a portion of the wave is transmitted into Region III. At $x = c + b$ (see Fig. 1.1) the wave encounters an object of known reflection characteristics. The reflection coefficient of this object is a historically, empirically, or analytically known constant, C_{RA}, such that $0 \leq C_{RA} \leq 1$, depending on whether the object represents a complete energy dissipator such as a beach, an intermediate reflector such as another porous structure, or a complete reflector such as a seawall. Henceforth this object will be termed a 'reflector-absorber'. Any portion of the transmitted wave in Region III that is reflected by the reflector-absorber propagates back towards Region I in reverse of the above sequence.

Assuming that the:

(1) bottom is impermeable;

(2) structure is rigid;

(3) incident wave is defined by linear wave theory;

(4) wave frequency is constant in all regions;

(5) incident wave frequency, σ, and wave height, H_i, are known;

(6) fluid is incompressible;

(7) time dependency of all waveforms is simple harmonic of the form $\exp[-i\sigma t]$,

this research provides an analytical solution for the velocity potentials in Regions I, II and III and the reflection and transmission coefficients for the structure. The reflection C_r, and transmission, C_T, coefficients are defined as the amplitude (or wave height) of the first modal waveform propagating in the negative x-direction on the seaward side of the structure and in the positive x-direction on the leeward side respectively, rendered dimensionless by division by the incident wave amplitude (or wave height). However, local maximum wave amplitudes which include the superposition of evanescent modes as well as the propagating mode in the vicinity of the structure are also evaluated as part of the total solution.

Such a solution will inevitably be valuable for the optimization of new pile matrix facilities for ports and harbors. That is, structures may be designed to maximize wave energy dissipation, and minimize wave reflection and transmission, thereby reducing local wave energy. Furthermore, existing structures may be analyzed to determine the feasibility of modification in order to further reduce reflected, transmitted, and partial standing waves adjacent to the structures.

In addition, the theory is easily adapted for the analysis of wave dissipators such as scrap automobile tire matrices. These relatively inexpensive dissipators are at present effective only for limited incident wave regimes. This solution may be employed to predict their performance under any given design wave regime without resorting to costly or time consuming model studies.

Finally, the solution yields a description of the instantaneous local pressure and flow fields within and adjacent to the structure. This information may be utilized for the calculation of local, instantaneous forces on any structural member. Thus, the ocean engineer is provided with a design aid which provides both wave forces and an optimization of wave-structure interaction.

1.2. Method of Solution

Modified Navier-Stokes equations of motion are developed in the x and z-directions. The damping terms are derived from the steady flow form drag relationship and from the inertial losses due to water particle accelerations about the structural members, i.e., the losses are attributed to Morison (1950) type force dissipation. The drag terms are linearized with respect to velocity using a Lorentz (1926) equivalent work scheme. A velocity potential is defined for use in the linearized equations of motion and this leads to a modified Laplace equation. Employing the standard linear wave theory dynamic and kinematic free surface boundary condition and the impermeable bottom boundary condition, the solution for the modified Laplace equation yields the velocity potential as an infinite eigen-series. The velocity potential equation is applied in Regions I, II and III to yield velocity potential expressions for the reflected wave in Region I, the transmitted and reflected wave potentials in Region III and, the two damped partial standing wave potentials within the structure. Using these velocity potentials and the boundary conditions of horizontal mass flux continuity and pressure continuity at the leeward and seaward interfaces, a system of $4 \times N$ simultaneous equations is generated (where N is the integer number at which the infinite eigen-series is truncated). Since the solution for the modified Laplace equation was found using a separation of variables technique and since the depth dependent term satisfies the necessary criteria for a well posed Sturm-Liouville problem, it is appropriate to employ the principle of orthogonality to eliminate the depth dependence from the $4 \times N$ system of simultaneous equations. The $4 \times N$ unknown amplitude coefficients are then rendered dimensionless by division by the incident wave amplitude and their solution is obtained through the use of a high speed digital computer matrix solution routine.

It is worthy of note that the total solution of the problem is an iterative one. This is a consequence of the linearization scheme in which a dimensionless damping coefficient is found as a function of velocity. This velocity, however, is unknown unless the problem is solved. Therefore, the damping coefficients are assumed for the x and z-directions, the first solution is achieved and the damping coefficients are recalculated from the calculated velocities. This process is repeated until the beginning and ending damping coefficients in each direction match to an acceptable degree of accuracy. Generally, convergence is rapid and large blocks of computation time are not required.

1.3. Review of Previous Research

A great deal of research has been conducted on the subject of the interaction of ocean waves with permeable structures. Both analytical and empirical studies have been conducted numerous times for structures composed of piles, rubble, and other permeable materials. This review primarily concerns itself with the analytical studies, although, a few of the purely empirical projects are discussed herein. To avoid unnecessary duplication of work, the reader is also advised to consult Sollitt and Cross (1972) for a review of the research conducted by Goda and Ippen (1963), Kamel (1969), and Ijima Eguchi, and Kobayashi (1971). For the most part, the following review is conducted in chronological order. No bias or partiality is projected or implied.

1.3.1. Todd (1948), "Model Experiments on Different Designs of Breakwaters"

Todd (1948) has compiled the results of an extensive number of World War II experimental studies conducted on wave transmission through porous breakwaters. Wiegel (1964) presents Todd's tabulated results.

1.3.2. Costello (1952), "Damping of Water Waves by Vertical Circular Cylinders"

Costello (1952) addresses the subject of wave transmission through a dense matrix of vertical piles. Laboratory tests were conducted for five different matrix configurations which extended fully across the width of the wave tank. Piles were modeled using 3/8 inch circular wooden dowels. The model tests range of Reynold's numbers (based on the maximum water particle velocity and the pile diameter) was $400 \leq \mathbb{R} \leq 7000$. Consequently, the author concluded that scale effects may be pertinent to the extension of the study results to prototype applications.

Costello's research indicated that the transmission coefficient was relatively insensitive to changes in the dimensionless water depth, h/L, over the test range $0.2 < h/L < 0.71$. However, the transmission coefficient was found to be a monotonically decreasing function of the incident wave steepness, H_i/L, over the test range $0.01 < H_i/L < 0.12$, i.e., steeper waves yielded lower relative transmissions.

Also, decreasing the lateral spacing between piles was found to have a greater effect on reducing the wave transmission than decreasing the in-line spacing. In fact, doubling the in-line length of the structure by doubling the number of piles (while maintaining constant uniform pile to pile spacing in each direction) yielded only an average 18 percent reduction in wave transmission for a wave steepness of 0.1. Finally, Costello found the maximum wave reduction for all configurations tested to be a 58 percent reduction. This was produced by the densest structure at a wave steepness of 0.08. It is not possible to calculate what the ratio of the in-line structural length to the wavelength is for that particular case, but it is known to be in excess of 52 percent.

Costello made no attempt to determine the magnitude of wave reflections for any of his tests.

1.3.3. Wiegel (1964), Oceanographical Engineering and Nagai (1966), "Researches on Steel-Pipe Breakwater"

Wiegel (1964) established an analytical expression for the transmission coefficient for a single row of closely spaced piles. His analysis relies on the assumption that the ratio of transmitted wave power to the incident wave power is equal to the ratio of the gap width, S, between the piles, to the gap width plus the pile diameter, S + D. Then, using linear wave theory, Wiegel obtains

$$\frac{H_T}{H_i} = \sqrt{\frac{P_I}{P_I}} = \sqrt{\frac{S}{S+D}}$$

Wiegel's experiments indicated that the measured transmitted wave height generally exceeded the predicted height by about 25 percent. However, Nagai (1966) applied the above formula for model studies of the steel pipe breakwater in the Port of Osaka and found the measured values exceeded the predicted values by only 6 to 11 percent when no over-topping occurred.

Nagai's experiments also included a model in which vertical steel plates extending some vertical distance, z', below the still water surface were welded across the gaps between the steel piles. Thus, the upper z' depth of the breakwater appeared as a solid barrier while the lower portion behaved as a closely spaced pile breakwater. Nagai multiplied the above transmission formula by Wiegel (1964) times that developed by Weigel (1960) for the transmission of water waves past a rigid thin barrier to yield the modified Wiegel-Nagai transmission coefficient as

$$\frac{H_T}{H_i} = \sqrt{\frac{S}{S+D}} \times \sqrt{\frac{\dfrac{4\pi(z+h)/L + \sinh(4\pi(z+h)/L)}{\sinh(4\pi h/L)}}{1 + \dfrac{4\pi h/L}{\sinh(4\pi h/L)}}}$$

Nagai found that this transmission coefficient agreed quite well with his model studies when no overtopping occurred.

Neither Nagai nor Wiegel examined wave reflections from the structures nor did they analyze more than one row of vertical piles.

1.3.4. Hayashi, Hattori, Kano, Shirai (1966), "Hydraulic Research on the Closely Spaced Pile Breakwater"

Hayashi et al. (1966) developed analytical expressions for both the transmission, C_T, and reflection, C_r, coefficients for a single row of closely spaced piles. The analysis employed a long wave assumption, from which he concluded that the velocity profile over the water depth must be approximately uniform. Then, using the continuity equation for an incompressible fluid and the velocity relationship for a jet between the piles from the Bernoulli equation, Hayashi obtained

$$C_T = 4(h/H_i)\xi[-\xi+\sqrt{\epsilon^2+H_i/2h}]$$

where

$$\xi = C\left(\frac{S}{S+D}\right) \Big/ \sqrt{1-\left(\frac{S}{S+D}\right)^2}$$

C = discharge coefficient = $C_v \times C_c$

C_v = velocity coefficient = function of the Reynolds number

C_c = coefficient of contraction for the jet between the piles

S = gap width between the piles

D = pile diameter

H_i = incident wave height

h = water depth

and

$$C_r = 1 - C_T$$

Agreement between Hayashi's experimental results and theoretical predictions for the reflection and transmission coefficient were not particularly good. The correlation between the theoretical and actual transmission coefficient might be termed acceptable for engineering design purposes. The predicted reflection coefficient appears to underestimate the measured coefficient by an average difference of between 0.15 and 0.2. However, it is noteworthy that Hayashi conducted his experiments at a dimensionless water depth of $h/L = 0.09$ which does not fit the definition for the assumed long waves given by Ippen (1966) or the <u>Shore Protection Manual</u> (1975).

Hayashi uses discharge coefficient, C, of 0.9 and 1.0 for his theoretical predictions. No explanation is given as to how these values were chosen. Also, the discharge coefficient is a function of the velocity coefficient which is a function of the Reynolds number.

Since the Reynolds number is dependent on the velocity and velocity is time dependent for oscillatory flow, it appears as though the use of a constant discharge coefficient ignores the time dependency of the problem.

Hayashi did not examine the problem of multiple rows of piles.

1.3.5. Lean (1967), "A Simplified Theory of Permeable Wave Absorbers"

Lean (1967) used the small amplitude long wave assumption to develop a theory for wave reflection from permeable wave absorbers. Lean's theory does not concern itself with wave transmission since the rear face of the absorber is assumed to be a solid barrier. The long wave assumption produces a one dimensional analytical solution that yields exponential wave decay within the structure.

Wave dissipation is accounted for by a Lorentz type linearization of the drag formula, allowing a linearized differential momentum equation to be coupled with the one dimensional continuity equation to describe the problem. Solutions for the free surface displacement and the horizontal water particle velocity are then obtained. Assuming that no energy is lost at the seaward interface of the structure, and setting the friction terms to zero outside the absorber, Lean quantifies the unknown amplitude coefficients by requiring continuity of both the water surface and the horizontal velocity at the interface.

Thus, a solution for the reflection coefficient is obtained.

Lean's research also examined the theoretical effects of linear and parabolic impermeable slopes beneath the absorber. No experiments were conducted to calibrate the theory. No method of quantifying the loss coefficient for the permeable material is given.

1.3.6. Hayashi, Hattori, and Shirai (1968), "Closely Spaced Pile Breakwater as a Protection Structure Against Beach Erosion"

Hayashi et al. (1968) extend their previous work, Hayashi et al. (1966), by considering the two dimensional case without the long wave assumption. However, the solution is only quasi-two dimensional since the depth dependence is eliminated by averaging over the water depth to establish the mean horizontal water particle velocities for the incident, reflected and transmitted waves. Again, using the continuity equation over the water depth and the equation of the discharge velocity from a jet to solve for the transmitted velocity, Hayashi solves for the transmission, C_T, and reflection, C_r, coefficients as

$$C_T = \frac{4h}{H_i}\,\xi\,\frac{a^2kh}{\alpha\tanh(kh)}\left[-\xi+\sqrt{\xi^2+\frac{H_i\alpha\tanh(kh)}{2ha^2kh}}\,\right]$$

where

$$a = 4\int_0^{\pi/2}\sqrt{\sin 2\pi\zeta}\cdot\sin 2\pi\zeta\, d\zeta = 1.1139$$

α = kinetic energy correction factor

$$= \left(\frac{kh}{\sinh(kh)}\right)^2 \left(1 + \frac{\sinh^2(kh)}{3}\right)$$

All other terms are as previously defined and

$$C_r = 1 - C_T$$

Hayashi's experimental data for both the reflection and the transmission coefficients agree quite well with those predicted by the theory. The theory is only applicable for one row of piles and, again, Hayashi does not express a method for evaluating the discharge coefficient, C.

1.3.7. Terrett, Osorio, and Lean (1968), "Model Studies of a Perforated Breakwater"

The development by Terrett et al. (1968) is essentially identical to that of Lean (1967). A long wave assumption and a Lorentz linearization of the drag are again employed to solve the continuity and momentum system of linear partial differential equations. The development differs from that of Lean (1967) in that the interfacial boundary conditions require horizontal mass flux continuity and a momentum balance which incorporates the inertial effects of the water particles accelerating past the absorber.

A method of quantifying the drag coefficient, the linearized friction factor, and the virtual mass coefficient for the structure studied is given, although, the mass coefficient is found by fitting the theory to the model study data. The solution for the reflection coefficient is given for obliquely incident as well as normally incident waves by

$$C_r^2 = N/M$$

where

$$N = [\cos k_2 \ell - C_m k_2 \sin k_2 \ell]^2 + [\frac{f}{C_2} - \frac{k_1}{k_2 \cos \theta}]^2 \sin^2 k_2 \ell$$

$$M = [\cos k_2 \ell - C_m k_2 \sin k_2 \ell]^2 + [\frac{f}{C_2} + \frac{k_1}{k_2 \cos \theta}]^2 \sin^2 k_2 \ell$$

ℓ = length from the front face of the breakwater to the reflecting barrier at the rear

k_1 = wave number outside the breakwater = $2\pi/L_1$

k_2 = wave number inside the breakwater = $2\pi/L_2$

C_m = virtual mass coefficient

θ = angle between the normal to the wave crest and the normal to the face of the breakwater

$$\frac{f}{C_2} = (\frac{8}{3\pi}) C_D (\frac{A}{h_2}) 2 \sin k_2 \ell / M$$

A = incident wave amplitude

C_D = drag coefficient

Comparison between the theoretical values and the experimental values indicated that the theory worked well for predicting the minimum reflection coefficient for the structure and the associated wave period. However, the theory generally over-predicted the reflection for higher, longer waves.

1.3.8. Kondo (1970), "An Analytical Approach to Wave Transmission Through Permeable Structures"

Kondo (1970) uses a long wave assumption and linearized equations of motion similar to those employed by Lean (1967) and Terrett et al. (1968) to develop an analytical solution for flow in homogeneous, vertical faced, permeable breakwaters. Kondo's analysis differs from the others in that it recognizes the phase differences between the incident, reflected, and transmitted waves. In addition, Kondo employs the use of three interfacial boundary conditions--to obtain a solution which requires exponential wave decay within the structure. Also, equations for the reflection and transmission coefficients, mean rate of energy flux, and mean rate of energy dissipation for the structure are derived.

Kondo's Fig. 5, comparing the experimental and theoretical transmission coefficients for vertical rock filled breakwater models, was erroneous in the referenced publication. Kondo has provided an errata sheet which indicates that the theory consistently overpredicts the actual transmission coefficient. The theoretical reflection coefficient was not compared to experimental values.

Coefficients relating losses to the permeable media properties are described, although the methods of quantifying such coefficients are not always explicit.

1.3.9. Sawaragi and Iwata (1970), "Effect of Structural Shape on Wave Run-Up and Wave Damping"

Sawaragi et al. (1970) have developed a theory for the reflection and transmission of water waves normally incident upon one or two rows of vertical piles. Linear wave theory and the assumption that $kh < 1$ (where k is the wave number, $2\pi/L$, and h is the water depth) are employed. Phase differences between the incident, reflected and transmitted waves are included in the theory but are set equal to zero to facilitate the final solution. Energy losses are accounted for by a non-linearized drag relationship and substituted into the Bernoulli equation written across the pile interface. The flow velocity at the interface is obtained from the Bernoulli relationship. Continuity of horizontal mass flux is then used to relate the interfacial velocity with the transmitted wave water particle velocity. The reflection and transmission coefficients are then calculable.

The theoretical predictions for the reflection and transmission coefficients are in good agreement with the experimental values for both the single and double row cases, although, the drag coefficient is obtained by fitting the theory to the data. It should be noted, however, that the solutions are not particularly sensitive to changes in the drag coefficient and that a drag coefficient of from unity to the fitted value of 2.6 appear to give acceptable results. Finally, the experiments were conducted for only one wave case while the gap distance between the piles was varied. Consequently, generalizations about the validity of the theory over the range of small amplitude gravity waves may not be justified.

1.3.10. Hattori (1972), "Transmission of Water Waves Through Perforated Wall"

Hattori analyzed shallow water small amplitude waves normally incident upon a perforated wall breakwater. Linear wave theory is used to define the velocity potential expressions for the incident, reflected and transmitted waves. Zero phase change is assumed. The continuity equation is used to relate the depth averaged horizontal water particle velocity on the seaward and leeward sides of the breakwater to the horizontal jet velocity through the perforations. The Bernoulli equation is written for a control volume extending from the seaward side of the breakwater to the interface and solved to obtain an expression for the interfacial jet velocity. The depth averaged incident and reflected velocities and velocity potentials are used in the

Bernoulli equation so that it becomes necessary to apply kinetic energy and velocity potential correction factors respectively. The expression thus obtained for the interfacial jet velocity is then time averaged over one-half a wave period. The equation for the mean flux of momentum during a half wave cycle through a control volume extending from the interface into the leeward side of the breakwater is then evaluated using the expression for the time averaged interfacial jet velocity and the continuity equation. Finally, employing the assumption that the incident, reflected, and transmitted wave numbers and angular frequencies are equal, the reflection and transmission coefficients are derived from the momentum equation and the continuity equation.

Using his experimental data to quantify the discharge coefficient for a jet, Hattori's theory correlates well with experimental reflection and transmission coefficients. No alternative method of establishing this coefficient is stated.

1.3.11. Sollitt and Cross (1972), "Wave Reflection and Transmission at Permeable Breakwaters"

Sollitt et al. (1972) have analyzed the problem of small amplitude water waves normally incident upon a vertical sided, homogeneous, crib style breakwater, conventional layered trapezoidal rubble mount breakwater, and a multiple row vertical pile matrix. Two dimensional solutions for the velocity potential, pressure field, and the reflection and transmission coefficients are obtained.

The solution technique is similar to the one described for this paper in Section 1.2 although Sollitt employs the use of the total instantaneous velocity vector, q, in prescribing the equation of motion rather than its vectorial component parts, u and w. In the rubble mound breakwater cases, damping is introduced to the Navier-Stokes equations of motion through the use of an inertial loss term and by the laminar and turbulent damping terms specified by Ward (1964) and Dinoy (1971) for the pressure drop through large-grain permeable media under steady, non-convective flow conditions. For the conventional breakwater case, Sollitt incorporates a term for energy loss due to breaking waves on the sloped seaward face. A Lorentz type linearization scheme is employed and the analysis proceeds as described in Section 1.2 of this paper.

For the vertical pile matrix case, the solution technique is similar to that described in Section 1.2. However, the drag force on the vertical piles is proportional to the square of the horizontal water particle velocity, u, but Sollitt (1972) performs the linearization in terms of q, the total instantaneous velocity vector. This allows the 'leakage' of horizontal damping stress to the vertical components.

Agreement between the theoretical and experimental transmission coefficients for the crib style breakwater over the ranges of

$0.25 \leq kh \leq 3.5$ and $0.008 < H_i/L < 0.05$ is acceptable for the smaller of the two breakwater widths tested. However, the theory unacceptably over predicts the transmission coefficient over a wide range of low steepness waves in the larger width case. Also the theory unacceptably underestimates the reflection coefficient for low steepness waves and tends toward over-estimation at higher steepnesses for both breakwater widths.

Good agreement between the theoretical and measured transmission coefficients is found for the conventional breakwater. However the loss coefficient for breaking waves is determined by fitting the theory to the data. The reflection coefficient exhibits the same sort of behavior previously described, i.e., under-prediction at low wave steepnesses and a trend toward over-prediction at higher steepnesses.

The transmission coefficients for the model pile matrices are in good agreement with those predicted by the theory. No data was available for a comparison with the predicted reflection coefficient.

With the exception of the breaking wave loss coefficient, steady flow tests or other measures for quantifying the loss coefficients for use in the theory are described.

1.3.12. Kondo and Toma (1972), "Reflection and Transmission for a Porous Structure

Kondo (1972) conducts a series of experiments on an idealized porous breakwater composed of horizontal and vertical circular cylinders to determine the effects of variations in longitudinal (in-line) structural width. Waves are normally incident on the structure and the water depth, wave period, and wave height are varied.

The transmission coefficient is found to decrease in an exponential manner for increasing non-dimensional structural width, B/L, and increase for low amplitude, long period waves. The reflection coefficient exhibits a peaking effect within the approximate range of $0.2 \leq B/L \leq 0.25$ and then decreases to a nearly uniform value.

Kondo compares the experimental transmission coefficient with the theoretical values developed by Kondo (1970) and finds reasonable agreement but it appears to be poorly correlated with experimental values from other investigators at the larger values of B/L. Kondo modifies the reflection coefficient development from his previous paper to include the wave reflected from the rear of the structure as well as that from the front. The modified values compare more favorably with his experimental values than the 1970 theory, but still appear to be lacking a high degree of accuracy. However, the reflection coefficients from the modified theory agree quite well with Kamel's (1969) experimental values.

A method of quantifying loss coefficients for the model structure is described in the paper.

1.3.13. McCorquodale (1972), "Wave Energy Dissipation in Rockfill"

McCorquodale has analyzed wave motion in embankments of coarse granular media using a finite element approach. The analysis is conducted for an impervious core structure. Energy loss terms incorporate laminar and turbulent losses as well as an inertial term to account for the unsteady nature of the flow. However, the inertial term is assumed to be small compared to the other terms in order to facilitate a simplifying transform.

Six nodal conditions are developed along the boundaries of the structure and a finite element numerical analysis is employed to obtain a solution for the free surface displacement within the structure. The theoretical wave height within the structure compares well with preliminary experimental values.

A method of determining loss coefficients for theoretical applications is not clarified.

1.3.14. Sawaragi and Iwata (1973), "On Wave Deformation Due to Permeable Structures"

Sawaragi et al. (1973) analyze multiple row vertical pile structures and perforated vertical wall breakwaters with and without a reflecting quay wall. The small amplitude, shallow water wave assumption is used for both developments.

The vertical pile analysis is identical to that developed by Sawaragi and Iwata (1970) except that multiple (infinite if desired) numbers of internal reflected waves are included. Also, the number of rows of piles in the structure is allowed to exceed two by iteratively stepping up the number of rows in the structure. The solution requires the assumption that the phase differences between the incident, reflected, and transmitted waves be zero. In addition, the successive reflection and transmission coefficients are required to be constant for a given pile row as the multiple reflections encounter and re-encounter that row. This assumption would appear to violate Costello's (1952) conclusion that wave transmission increases as the wave steepness decreases unless the wave steepness of the multiple reflections remain constant. But wave steepness must decrease each time the wave encounters a row of piles due to reflection, attenuation and partial transmission unless the wavelength decreases at an appropriate rate to accommodate the decrease in wave height.

The theoretical reflection coefficient agrees well with experimental values for four or less rows of piles. The theoretical transmission coefficient, on the other hand, correlates acceptably with measured values for only one or two rows of piles and thereafter consistently under predicts the experimental data.

A method of determining the damping coefficient for the theory is not specified.

The expressions for the reflection coefficient for the system of a perforated wall breakwater with a reflecting quay wall are obtained from the general equations derived for the pile matrix breakwater with the exception that the local transmission and reflection coefficients at the quay wall are zero and unity, respectively. Again, the local transmission and reflection coefficients at the perforated wall are assumed to be constant for all of the multiple wave reflections.

The theoretical reflection coefficient for this case generally agrees acceptably with experimental values for a range of dimensionless longitudinal structural widths, x/L, deep water wave steepnesses, H_o/L_o, dimensionless perforation diameters, D/H_o, and dimensionless perforated wall widths, B/D. Again, a method of quantifying the damping coefficient is not specified.

The solution for the isolated perforated wall is obtained in a manner which appears similar to that employed by Hattori (1972). A jet velocity is established using the laws of conservation of mass and energy. Losses are attributed to sudden expansion and contraction of the flow and friction. Linear wave theory is employed on both the seaward and leeward sides of the wall. The solution for the reflection and transmission coefficients is obtained in terms of discharge, expansion, contraction and frictional coefficients.

The theoretical reflection and transmission coefficients for the isolated wall compare favorably with the experimental data obtained by Sawaragi and with that of another investigator. The theory does not appear to be highly sensitive to changes in the discharge coefficient. The author indicates that this coefficient must be evaluated experimentally but was not explicit regarding the method used in determining the other loss coefficients.

It is interesting to note that Sawaragi theoretically and empirically found that reflections were minimized in the pile and quay wall breakwater cases when the distance between the pile rows and between the perforated and quay walls were odd integer multiples of the wavelength divided by four. The reflections reached a maximum when that distance was an even integer multiple of $L/4$. This indicates that resonant interaction of the structure and wave regime are crucial to its performance as a wave attenuator.

1.3.15. Kondo and Toma (1974), "Breaking Wave Transformation by Porous Breakwaters"

Kondo et al. (1974) conducted a model investigation of breaking or near breaking waves normally incident upon porous structures. Two of the models are cylindrical pipe matrices of rectangular and trapezoidal cross section while a third is a conventional homogeneous granular media breakwater model of trapezoidal cross section.

The results indicate that the transmission coefficient of all three structures decreases with increasing dimensionless wave height, H_i/h, until the absolute maximum dimensionless wave height was reached and breaking occurred. Since wave instability did not always occur at the same H_i/h value it was possible to have both a breaking wave and a non-breaking wave at the same value of H_i/h even though all other factors were equal. Under these conditions, it was found that the transmission coefficient was essentially the same for both the breaking and the non-breaking wave. However, the wave heights inside the cylinder matrix structures appeared to be lower if breaking occurred right at the structure as opposed to prior breaking or non-breaking conditions.

The non-breaking wave reflection coefficient for both the trapezoidal models tended towards a maximum at an approximate value of $H_i/h \approx 0.6$. Scatter in the data made any trends (with regard to H_i/h) in the reflection coefficient of the rectangular cylinder matrix indiscernable. The reflection coefficient for the rectangular structure appeared to be highly sensitive to changes in its dimensionless longitudinal width, B/L, achieving a minimum value at $B/L = 0.45$ and a maximum at $B/L = 0.2$.

The analytical theory developed by Kondo (1970, 1972) to predict the reflection and transmission for porous structures is applied to both the rectangular and the trapezoidal cylindrical matrix structures.

However the latter application required the analysis be conducted using an equivalent rectangular structure such that the average longitudinal thicknesses below the still water level of the trapezoidal and equivalent rectangular structure were equal. Kondo indicates that the theoretical transmission coefficient generally over estimates the actual value for both types of structure. The theoretical reflection coefficient for the rectangular matrix splits the scatter in the data and consequently is judged acceptable. In the equivalent rectangular case the reflection theory and experimental data have opposing slopes and thus do not correlate well.

1.3.16. Madsen (1974), "Wave Transmission Through Porous Structures"

Madsen achieves an explicit analytical solution for small amplitude long waves normally incident on a porous structure of rectangular cross section. The solution is similar to the long wave solution developed by Sollitt and Cross (1972).

The theory is developed by applying linear wave theory with the long wave assumption on the seaward and leeward sides of the structure. Continuity of the water surface elevation and mass flux continuity are employed to obtain the interfacial boundary conditions. A narrow longitudinal structural width, a linearly varying free surface profile and a horizontal velocity which is uniform over the depth and varies linearly over the longitudinal structural width are assumed within the confines of the structure. The continuity equation and conservation of momentum across the structure are used to develop the internal flow description and relate it to the external linear wave theory conditions. Horizontal forces applied to the control volume for use in the momentum equation are attributed to the hydrostatic pressure differential due to the linearly varying free surface condition, and also to frictional and inertial resistance forces within the structure. The added mass coefficient of the inertial term is assumed to be zero for the closely packed structure being considered. A solution for the average horizontal velocity within the structure is obtained and related to the external velocities using the boundary conditions. Simplified expressions for the reflection and transmission coefficient are then developed.

The theory is compared to experimental values obtained by Sollitt and Cross (1972) and is found to acceptably predict wave transmission but not reflection.

A recommended procedure for establishing the frictional loss coefficients for rubble mound structures is given in detail.

1.3.17. Grune and Kohlhase (1974), "Wave Transmission Through Vertical Slotted Walls"

Grune et al. have conducted an experimental investigation of waves normally and obliquely incident on a single row of closely spaced piles. The investigators have varied the standard motif for these experiments by varying the angle of wave attack. Also, H-beam piles and several piles of varied rectangular cross section are used rather than the standard cylindrical piles. Variables for the tests in addition to the angle of wave attack and pile cross section are the wave steepness, H_i/L, the ratio of the lateral pile thickness to the lateral center to center pile spacing, W, and the ratio of the longitudinal pile thickness to the lateral pile width, t/b. Wave transmission was the quantity of interest and therefore reflections were ignored.

Wave transmission was found to decrease with increasing wave steepness but it is interesting to note that the decrease in the transmission coefficient over the range $0.025 \leq H_i/L \leq 0.08$ was only about 0.1 for all angles of wave attack. The transmission decreased significantly for increasing values of W but decreased only moderately with increasing t/b values. Finally, the transmission was found to decrease significantly as the angle the wave crest line formed with the pile row increased from 0° (normal incidence) to 90° for the ranges $0.4 \leq W \leq 0.68$, $0.025 \leq H_i/L \leq 0.067$.

Hartmann's (1969) equation for the transmission coefficient

$$C_T = \sqrt{1-W^2}$$

was found to fit the data for normally incident waves well. The investigators modified this equation to fit the data for obliquely incident waves such that

$$C_T = .5\sqrt{1-W^2}\,(1+\cos^a\beta)$$

where

a = shape coefficient for the pile cross section (a = 1.0 for H-beams of t/b = 2.0; a = 0.5 for rectangular cross sections of t/b = 1.5

β = angle formed between the wave crest line and the pile row.

1.3.18. Ijima, Chou, Yumura (1974), "Wave Scattering by Permeable and Impermeable Breakwater of Arbitrary Shape"

Ijima obtains an elegant three dimensional solution for the wave scattering problem for permeable structures of arbitrary shape. Only two regions are considered in the development of the theory, Region I being outside the structure and Region II inside the structure. A spatial velocity potential is defined for each region and is required to satisfy Laplaces equation in three dimensions. The spatial potential in Region I is written in terms of a known incident functional of the horizontal directions, x and y, an unknown propagating functional of the horizontal directions; and an infinite series of functionals of the horizontal directions representing the evanescent modes. The depth dependent functions are hyperbolic cosines and trigonometric cosines for the propagating and evanescent modes respectively. Similarly, the velocity potential inside the structure is expressed in terms of an infinite series of functionals in the horizontal directions and complex hyperbolic functions of depth representing the damped partial standing wave within the structure. All three of the unknown functionals are required to satisfy Helmholtz's equations, thereby yielding Hankel and Bessel function solutions. These are rewritten by means of Green's identity formula expressing the spatial functionals in terms of the surface integral of the product of the functional (evaluated on the surface of the structure) times the appropriate Hankel or Bessel function.

Having derived unquantified relations for the three unknown functionals, the velocity potential expressions are substituted into the interfacial boundary conditions of continuity of mass and pressure and the resulting equations are orthogonalized over the depth interval. The functional expressions are then substituted into these equations and their solution is obtained numerically. This yields the solution for the velocity potential expressions and the problem is solved.

The theoretical predictions for wave heights around the structure agree well with experimental values.

A method of quantifying the Darcian fluid resistance coefficient for the theoretical losses is not stated.

1.3.19. Nasser and McCorquodale (1975), "Wave Motion in Rockfill"

Nasser et al. (1975) have presented a one dimensional numerical model for non-linear waves normally incident upon a vertical face rockfill structure with an impermeable central core. The model provides a quantitative description of the flow, the external free surface and the internal phreatic surface. A non-Darcian frictional resistance term is incorporated to account for losses. The loss coefficients are determined by permeameter tests on the porous media. Assumptions that the incident waves are long, and thus the free surface is reasonably flat, and that the pressure distribution inside and outside the structure is approximately hydrostatic are employed in the development.

A system of non-linear differential equations comprised of the momentum equation, the continuity equation, and the total differential for the velocity and the surface displacement are written for the internal and external regions. The characteristic directional transformations are derived using the conventional method of characteristics and the equations of motion along the characteristics are written. The equations of motion are then modified in terms of a finite difference numerical solution scheme.

A non-linear waveform composed of two unequal half sinusoids was used as the incident wave. The amplitude of the upper half sinusoid was higher and the half wavelength was shorter than the respective counterparts of the lower half in order to simulate the crest and trough portions of a non-linear wave. The internal boundary condition requires the normal velocity at the impermeable core be zero. The internal and external free surfaces were required to match at the interface only when water was flowing into the structure since a head differential may exist across the interface when water leaves the rockfill. Under this latter condition the internal interfacial phreatic surface was allowed to drop at the maximum pore velocity under a unit piezometric gradient.

The theoretical computation of the phreatic surface within the structure agreed well with that measured experimentally. The computed reflection coefficient also was in acceptable agreement with the measured data.

The investigators have indicated that the model may be modified easily for permeable breakwaters and was being adapted at the publication time to treat sloping embankments.

1.3.20. Massel (1976), "Interaction of Water Waves with Cylinder Barrier"

Massel (1976) analyzes the complicated three dimensional problem of small amplitude wave interaction with a single row of closely spaced cylinders at an arbitrary angle of wave incidence. The solution yields a description of the flow field in the immediate vicinity of the row of piles, the induced wave forces on the piles, and the reflection and transmission coefficients for the structure. Waves are assumed to be relatively long with regard to the pile diameter and the fluid is assumed to be an ideal inviscid fluid. Massel indicates that applications of the theory should be restricted to conditions in which the drag force is considered negligible in comparison with the inertial force and that the theory only satisfies the boundary conditions on the cylinders. It is therefore approximately correct only in the immediate vicinity of the pile row.

The solution is obtained by defining a velocity potential as the sum of incident and scattered potentials. Then

> Using a Bessel coordinate transformation for each cylinder arrangement and applying the boundary conditions on all cylinders, the unknown scattering coefficients are obtained by means of a matrix inversion procedure which requires . . . . the services of high speed computers (Massel, 1976).

The boundary condition referred to by the investigator requires that the normal velocity at each cylinder surface be zero.

The transmission coefficient is found by relating the average energy flux between the piles to the average energy flux of the incident wave. The reflection coefficient is found from

$$C_r = \sqrt{1 - C_T^2}$$

since energy dissipation is neglected by the author throughout the analysis.

Correlation between the predicted transmission and reflection coefficients and the measured values is not good although the reflection coefficient might be judged acceptable for relatively large and relatively small spacings between piles.

1.3.21. Nagai (1976), "Perforated Vertical Wall Breakwater"

Nagai (1976) has conducted an experimental investigation of the wave attenuation characteristics of a box type wave absorber. The wave absorber consists of a perforated box mounted to a rigid impermeable vertical sea wall. The investigator recommends that the draft of the absorber be considerably less than the water depth to decrease the standing wave phenomenon on the seaward side of the absorber. The top, bottom and seaward faces of the box are perforated to admit and dissipate incident wave energy. The porosities of these three faces and the longitudinal width of the absorber were varied in the experiments as well as the incident wave period and wave height.

The results indicate that the box type wave absorber is an effective method of reducing reflected wave energy from impermeable seawalls. Minimum reflection coefficients of approximately 0.1 were found for some of the test configurations when the ratio of the longitudinal width of the box to the incident wavelength was between 0.13 and 0.18. The reflection coefficient was also shown to be generally less than that of the standard perforated vertical wall breakwater over a significant range of the above mentioned ratio.

A theory predicting the reflection coefficient is discussed qualitatively but is not presented in detail. The theory appears to correlate well with experimental values.

1.3.22. Numata (1976), "Laboratory Formulation for Transmission and Reflection at Permeable Breakwaters of Artificial Blocks"

Numata (1976) has conducted model studies of wave reflection and transmission for crib style and trapezoidal breakwaters composed of artificial blocks and has developed empirical relationships to predict the reflection and transmission coefficients for the structures. In addition, using the experimental data obtained by Le Mehaute (1958), Tominaga and Sakamoto (1970), and Sollitt and Cross (1972), he has fitted an empirical expression yielding the reflection and transmission coefficients for crib style breakwaters made up of rubble.

The empirical reflection and transmission coefficient expressions for all three types of breakwaters examined generally compare favorably with the measured data with the restrictions that the dimensionless water depth, h/L, be less than 0.25, and that no wave overtopping occurs at the breakwaters.

1.3.23. Ijima, Tanaka, and Okuzono (1976), "Permeable Seawall with Reservoir and the Use of Warock"

Ijima et al. (1976) analytically and experimentally investigate several configurations of porous structures in conjunction with reflecting quay walls. Two analytical techniques are employed. First, the one dimensional, small amplitude, long wave equations of momentum and mass continuity are written (see Lean, 1967) for the regions seaward and leeward of a porous, vertical faced structure. The leeward region is defined as the reservoir contained between the rear face of the porous structure and the reflecting quay wall. The momentum equation is modified within the structure to incorporate linearized drag and inertial losses. Using the interfacial boundary conditions of continuity of horizontal velocity and free surface displacement, the internal equations are coupled with those of the seaward and leeward regions.

The reflection coefficients obtained from the above theory generally correlated well with experimental values when the longitudinal width of the porous structure was equal to the water depth. Less satisfactory comparisons were achieved when the longitudinal width was one-half the water depth, $B/h = 0.5$. Acceptable agreement for this condition was obtained only at large values of the dimensionless ratio, X/h, defined by the distance from the front of the porous structure to the reflecting wall, X, divided by the water depth. In all cases the theoretical and experimental reflection coefficients were found to be minima at $X/L \approx 0.18$ which is in agreement with Nagai (1976). The discrepancy between this finding and that of Sawaragi and Iwata (1973) is explained as being due to the fact that the energy dissipation for very thin walled porous structures is entirely due to jet type dissipation and therefore the maximum occurs at the nodal points of the standing wave. However, for the larger longitudal widths employed by Nagai (1976) and Ijima et al. (1976), the accelerations induced by the reservoir phase lag become significant.

The second method of analysis employed was that developed by Ijima et al. (1974) using Green's identity theorem. This method is further detailed by Ijima, Chou, and Yoshida (1976). The method is applicable for structures of arbitrary shape but in this case it is applied to porous structures of rectangular, trapezoidal and inverted trapezoidal cross section. Also, the angle the reflecting wall forms with the vertical direction is allowed to assume values of +30°, 0° and -30°.

Reflection coefficients predicted by this method are not presented graphically with the experimental values so a comparison is difficult to make, however, it appears as though the trends of the predicted and measured reflection coefficients are similar. The investigators judged the rectangular and trapezoidal cross sectional structures in conjunction with a reflecting wall at +30° (sloping up and away in the direction of wave advance) to be the least reflective.

The method of quantifying loss coefficients for the theoretical predictions was not described.

1.3.24. Kondo, Toma, and Yano (1976), "Laboratory Study on Pervious Core Breakwaters"

Kondo et al. (1976) have conducted an experimental evaluation of permeable cores for use in porous breakwaters. The models employed were of rectangular and trapezoidal cross section and were composed of either a matrix of vertical and horizontal circular cylinders or rubble. Reflection and transmission coefficients were measured for a variety of tests which included structures with and without cores and the core section alone. The effects of varying the wave period, the longitudinal core width, the core location (front face of structure, center, rear face) and the dimensionless incident wave height, H_i/h were also investigated. In addition, the effect of substituting a perforated vertical wall for the core section was examined.

The results indicate that a reduction in transmitted wave height and, to some degree, in the reflected wave height may be achieved for structures with a core located at the leeward face of the structure. Also, thin perforated walls provide approximately the same function as the permeable cores albeit to a somewhat lesser degree.

Kondo presents a synoptic description of the analytical theory for the prediction of reflection and transmission coefficients developed by Kondo, Toma, and Kasaï (1976, in Japanese). The theory assumes small amplitude, long waves are normally incident upon a rectangular breakwater composed of vertical sections of varying permeabilities. Waves are assumed to reflect and transmit one time only at each vertical section, i.e., multiple reflections at an individual vertical section are not considered. The theory is similar to that developed by Sawargi and Iwata (1970, 1973) in that the reflected wave is the sum of the waves reflected from each face while the transmitted wave is that wave which is successively transmitted past each vertical section. However the internal reflection and transmission coefficients at each successive face are allowed to vary in Kondo's theory.

Frictional losses within the structure are accounted for using a linearized Dupuit Forcheimer's law thereby yielding exponential damping as a function of a damping factor. The damping factor is allowed to vary in each vertical section. A technique for establishing the damping factor is not described.

The theoretical predictions for the transmission coefficients of a number of cases are generally in good agreement with the experimental values. The theoretical reflection coefficients, however, correlate reasonably well with experimental values only for the cases in which perforated vertical walls were being examined.

The predicted reflection and transmission coefficients are obtained through the use of an iterative computer algorithm.

1.3.25. Madsen and White (1976), "Wave Transmission Through Trapezoidal Breakwaters"

Madsen et al. (1976) develop an explicit analytical theory for the prediction of reflection and transmission coefficients of a multi-layered rubble mound, trapezoidal breakwater subjected to small amplitude, normally incident, relatively long waves. Loss coefficients are determined through the use of known empirical equations. The solution is relatively uncomplicated so that evaluation by a computer is not a necessity. The solution assumes that incident waves do not break on the seaward face of the structure and that the armor layer on that face is composed of natural stones.

The analysis first accounts for the external frictional energy dissipation due to wave run-up on the seaward face of the structure. Madsen and White (1976a) present a model which is considered appropriate when the slope and the roughness characteristic of the seaward face of the structure are known. Having established the external surface losses, the internal wave dissipation is accounted for by the theory developed by Madson and White (1974). However, that theory is only applicable for vertical faced rectangular structures. Consequently, it is necessary to define an equivalent breakwater of rectangular cross section. Based on steady flow considerations, the equivalent rectangular breakwater is defined as that homogeneous rectangular structure which yields the same volumetric discharge as the layered trapezoidal breakwater for a given flow condition.

The internal resistance losses are assumed to be strictly of a turbulent nature so that only one loss coefficient for the Dupuit-Forcheimer resistance formula need be determined. Empirically determined values of the loss coefficient are established as a function of the porosity. Thus, multiple loss coefficients occur for the multiple layer trapezoidal breakwater and only one for the homogeneous equivalent rectangular breakwater. Therefore, in order to apply the definition of the equivalent breakwater to evaluate its dimensions it is necessary to sum the losses over the different layers in the trapezoidal breakwater. Discharge rates are then established for both the trapezoidal and equivalent breakwaters as functions of the head losses across them and equated (as per the definition of the equivalent breakwater) to solve for the equivalent breakwater's longitudinal width. The reflection and transmission coefficients for the equivalent rectangular structure are then found using the theory of Madsen and White (1974) and are combined with the prescribed external losses to yield the reflection and transmission coefficients for the multi-layered, rubble mound, trapezoidal breakwater.

Comparison between the theoretical transmission coefficient and the experimental values obtained by Sollitt and Cross (1972) for conventional rubble mound breakwaters shows good agreement over the entire range of $0.002 < H_i/L < 0.03$. The theoretical reflection coefficient, however, increases with increasing wave steepness while the experimental reflection coefficient exhibits opposite behavior. Thus, correlation is acceptable over only a limited range of wave steepness.

1.3.26. Nagai and Kakuno (1976), "Slit-Type Breakwater; Box-Type Absorber"

Nagai et al. (1976) conducted an experimental study of box-type wave absorbers (see Nagai, 1976) and perforated vertical wall breakwaters in conjunction with a reflecting wall. The box-type wave absorber is shown to be generally more effective in reducing the partial standing wave on the seaward side of the structure and thus more effective in attenuating the incident wave energy. The ratio of the longitudinal width of the structure to the incident wave length is shown to be a critical factor with regard to the amount of wave reflection from the absorber. Minimum reflection was generally found to occur for values of the ratio between 0.15 and 0.18.

The theory described by Nagai (1976) is presented in detail for the analysis of the box-type absorber. The theory assumes shallow water, small amplitude waves are normally incident upon the structure. The theory also includes a phase shift at the seaward wall of the structure. A solution is obtained by assuming a value for the phase shift and the transmission coefficient of the seaward wall, so that the composite wave form external to the structure may be written as the sum of the incident wave, the wave reflected from the porous seaward wall and the wave reflected from the back wall.

Using the averaged measured values of the porous seaward wall's transmission coefficient from the model studies, the predicted reflection coefficient correlates well with the experimental data.

1.3.27. Berkhoff and van der Weide (1976), "Wave Forces on a Row of Cylindrical Piles of Large Diameter"

Berkoff solves a three dimensional scattered wave problem for a matrix of large inertially dominated piles. Linear wave theory is considered applicable and Laplace's equation in three dimensions becomes the governing differential equation. The solution for the velocity potential is also required to satisfy Helmholz' equation, the dynamic and kinematic free surface and the impermeable bottom boundary conditions from linear wave theory. In addition, the normal velocity on the surface of the piles is required to be zero.

A solution is obtained by "assuming that the scattered wave field may be considered as a result of a series of singular sources located along the circumference of the pile" (Berkhoff et al., 1978). The scattered wave functional is then evaluated as the surface integral of the product of the source distribution function and the source potential function.

It should be noted that this solution technique is valid for large, inertially dominated piles and is not, therefore, appropriate for applications in which viscous forces are large.

1.4. Scope

The preceding literature review is by no means exhaustive. It is, however, indicative of contemporary investigations of wave attenuation at porous matrix structures. Common deficiencies exhibited by most of the investigations are the failure to quantify loss coefficients and a general lack of accuracy for both wave reflection and transmission over a wide range of incident wave characteristics. The study described herein complements previous work by addressing the two dimensional problem with anisotropic damping. Further extensions are achieved through the inclusion of the reflector-absorber and variable water depths in the three regions of interest.

In addition, this research seeks a solution for which the anisotropic energy loss coefficients may be evaluated satisfactorily using coefficients disclosed in the technical literature, or, which may be determined by steady state laboratory tests. These coefficients and the methods of determining them are described in detail in Chapters V and VIII.

The theoretical solution incorporating these extensions is evaluated by comparison with experiments in Chapter VIII. Both pile matrix models and a scrap automobile tire matrix model are examined theoretically and experimentally.

II. THE BOUNDARY VALUE PROBLEM

2.1. Equations of Motion

Assuming an incompressible fluid and that gravity is the only significant body force, a modification of the two dimensional Navier-Stokes equations of motion is applicable. That is

$$\frac{Du}{Dt} = -\frac{1}{\rho}\frac{\partial(P+\gamma z)}{\partial x} + \text{Damping} \tag{2.1.1}$$

and

$$\frac{Dw}{Dt} = -\frac{1}{\rho}\frac{\partial(P+\gamma z)}{\partial z} + \text{Damping} \tag{2.1.2}$$

where

u = seepage velocity in the x direction at a point

w = seepage velocity in the z direction at a point

ρ = density of the fluid

P = instantaneous dynamic pressure at a point

γ = specific weight of the fluid

ν = kinematic viscosity of the fluid

$\vec{\nabla}$ = gradient operator = $\vec{i}\,\partial(\ )/\partial x + \vec{j}\,\partial(\ )/\partial y + \vec{k}\,\partial(\ )/\partial z$

D/Dt = total derivative with respect to time

It is convenient for the derivation of the damping forces to employ the seepage velocities (u and w) as defined for porous media, i.e., a local, spatially and temporally averaged flow velocity in which the time span and length scale over which the velocity is averaged is small compared to the wave period (T) and wavelength (L). Thus, the use of the seepage velocity eliminates perturbations of the velocity due to structural irregularities (spatial) and transient eddy fluctuations (temporal).

The respective velocity components, u and w, are assumed to be the products of unknown spatial functions of both the horizontal and vertical directions and the simple harmonic temporal function $\exp[-i\sigma t]$, i.e.,

$$u = U(x, z)\exp[-i\sigma t]$$

and

$$w = W(x, z)\exp[-i\sigma t]$$

where

$i = \sqrt{-1}$

σ = incident angular wave frequency = 2π/wave period

$U(x, z), W(x, z)$ = unknown spatial functions

Now, expanding the total derivatives of Eqs. (2.1.1 and 2.1.2), respectively, in terms of the independent variables x, z, and t yields

$$\frac{Du}{Dt} = \frac{\partial u}{\partial x}\frac{dx}{dt} + \frac{\partial u}{\partial z}\frac{dz}{dt} + \frac{\partial u}{\partial t}$$

$$= u\frac{\partial u}{\partial x} + w\frac{\partial u}{\partial z} + \frac{\partial u}{\partial t} \tag{2.1.3}$$

and

$$\frac{Dw}{Dt} = \frac{\partial w}{\partial x}\frac{dx}{dt} + \frac{\partial w}{\partial z}\frac{dz}{dt} + \frac{\partial w}{\partial t}$$

$$= u\frac{\partial w}{\partial x} + w\frac{\partial w}{\partial z} + \frac{\partial w}{\partial t} \tag{2.1.4}$$

Small amplitude wave velocity components and their spatial derivatives are both small. Consequently their products are so small that

$$u\frac{\partial u}{\partial x}, \quad w\frac{\partial u}{\partial z} \ll \frac{\partial u}{\partial t}$$

and

$$u\frac{\partial w}{\partial x}, \quad w\frac{\partial w}{\partial z} \ll \frac{\partial w}{\partial t}$$

Employing the above relationships, Eqs. (2.1.3 and 2.1.4) are re-written such that

$$\frac{Du}{Dt} = \cancelto{0}{u\frac{\partial u}{\partial x}} + \cancelto{0}{w\frac{\partial u}{\partial z}} + \frac{\partial u}{\partial t}$$

or

$$\frac{Du}{Dt} \approx \frac{\partial u}{\partial t}$$

and

$$\frac{Dw}{Dt} = \overset{0}{u\frac{\partial w}{\partial x} + w\frac{\partial w}{\partial z}} + \frac{\partial w}{\partial t}$$

or

$$\frac{Dw}{Dt} \simeq \frac{\partial w}{\partial t}$$

Substituting the above small amplitude approximations for the respective total derivatives into Eqs. (2.1.1 and 2.1.2) yields

$$\frac{\partial u}{\partial t} = -\frac{1}{\rho}\frac{\partial(P+\gamma z)}{\partial x} + \text{Damping} \tag{2.1.5}$$

and

$$\frac{\partial w}{\partial t} = -\frac{1}{\rho}\frac{\partial(P+\gamma z)}{\partial z} + \text{Damping} \tag{2.1.6}$$

2.2. Derivation of Damping Forces

Attenuation of the wave motion within the matrix structure (Region II) is due to the viscous interaction of the fluid particles with the structural members and the inertial effects produced by the local accelerations of the fluid particles about the structural members.

The viscous interaction of the fluid with the structure is described by a drag force resulting from skin friction and form drag. Research has shown the skin friction effects to be negligible with respect to form drag for relatively smooth objects with appreciable dimension normal to the flow. This investigation will therefore neglect skin friction effects. However, this does not constitute a limiting approximation since these effects may be easily introduced into the theory by increasing the drag coefficient to account for marine fouling and the resultant additional losses (see the Shore Protection Manual, 1975, pg. 7-103). It should be noted at this time that losses related to the transverse, or 'lift', force may also be accounted for by increasing the drag coefficient by an appropriate amount (see Section 5.4). Therefore using the steady flow drag relationship, viscous damping in the horizontal and vertical directions, respectively, are given by

$$dF_{Dx} = -\rho C_{Dx} \frac{u}{2} |u| dA_c \tag{2.2.1}$$

and

$$dF_{Dz} = -\rho C_{Dz} \frac{w}{2} |w| dA_c \tag{2.2.2}$$

where

$C_{D(x,z)}$ = drag coefficient for the respective direction. The drag coefficient is a function of the Reynolds number and hence a function of the local instantaneous velocity.

dA_c = differential element of area projected onto a plane normal to the flow direction

The inertial damping effects account for the change in the kinetic energy of the flow field due to the ± accelerations of the water particles about the structural members (Gibson and Wang, 1977). The resulting pressure distribution may be integrated over the surface of the member to yield an inertial force which is proportional to the undisturbed local acceleration (Robertson, 1965), i.e.,

$$dF_{Ix} = -\rho C_{mx} \frac{\partial u}{\partial t} dV \tag{2.2.3}$$

and

$$dF_{Iz} = -\rho C_{mz} \frac{\partial w}{\partial t} dV \tag{2.2.4}$$

where

$C_{m(x,z)}$ = virtual or 'added' mass coefficient for the respective direction

dV = differential element of structural member volume about which the fluid accelerates

2.3. Adaptation of the Damping Force Equations to the Equations of Motion

The viscous and inertial force equations presented in the previous section describe the forces exerted on the structure by the fluid and, by Newton's third law, by the structure on the fluid. Hence these forces account for the 'Damping' portion of Eqs. (2.1.5 and 2.1.6). However, some modification of the damping force equations is necessary to adapt them for use in the equations of motion. Specifically, the damping force equations must first be converted to a force per unit mass. This is accomplished by dividing the damping force by the product of the fluid mass density and a differential element of fluid volume. The second modification entails the adaptation of the quantities

dA_c and dV in Eqs. (2.2.1, 2.2.2 and 2.2.3, 2.2.4), respectively, for the general structure being considered. The final modification required is the linearization of the viscous damping equation with respect to the velocity in order to facilitate an analytical solution.

Before proceeding with these modifications, it will be helpful to establish the following definitions corresponding to Fig. 1.2.

V_T = total volume of structure, e.g., volume of rectangular prism ABCDEFGH

V_{Sx} = volume of structural members whose longitudinal axis is in the x direction, e.g., members AD and BC

V_{Sy} = volume of structural members whose longitudinal axis is in the y direction, e.g., members AB and DC

V_{Sz} = volume of structural members whose longitudinal axis is in the z direction, e.g., members AE, BF, CG, and DH

Should diagonal members be present within the structure, it is recommended that they be resolved into equivalent orthogonal members such that the longitudinal centerlines of the equivalent members intersect at the mid-point of the original member. The cross sectional dimensions of the equivalent members should be chosen to preserve the projections of the cross sectional areas of the original member onto the planes normal to the flow direction. The equivalent members then contribute to the appropriate volume, V_{Sx}, V_{Sy}, or V_{Sz}.

$$V_f = \text{volume of fluid within the structure}$$

$$= V_T - (V_{Sx}+V_{Sy}+V_{Sz})$$

$$\epsilon = V_f/V_T = \text{porosity of the structure} \tag{2.3.1}$$

$$\epsilon_x = V_{Sx}/V_T = \text{ratio of solid volumes in the x direction to the total volume} \tag{2.3.2}$$

$$\epsilon_y = V_{Sy}/V_T = \text{ratio of solid volumes in the y direction to the total volume} \tag{2.3.3}$$

$$\epsilon_z = V_{Sz}/V_T = \text{ratio of solid volumes in the z direction to the total volume} \tag{2.3.4}$$

It is again noteworthy that although Fig. 1.2 and the following presentation are for a matrix of circular cylindrical piles, only minor adjustments are required for alternative matrix structures provided that a means of quantifying the drag and inertial coefficients is available.

2.3.1. Adaptation of the Viscous Damping Equations for the Equations of Motion

Figure 1.2 depicts a simple circular pile matrix with horizontal and vertical members. Since skin friction is being neglected only the vertical and y-directed members interact with the horizontal component of fluid velocity, u. Similarly, only the x-directed and y-directed members interact with the vertical velocity component, w.

Thus, the viscous damping for either particular direction may be represented as the sum of the damping contributions of those members whose longitudinal axis is normal to the flow direction.

2.3.1a. Vertical Piles Contribution to Horizontal Viscous Damping. Using Eq. (2.2.1), the horizontal differential drag force exerted upon a differential element of a vertical pile is given by

$$dF_{Dx} = C_{Dx}\rho \frac{u}{2} |u| dA_c$$

where

$dA_c = dz \cdot D$ (see Fig. 1.2)

D = pile diameter

Converting the above differential force to a differential force per unit mass by dividing by the quantity ρdV_f and reversing the sign yields the equal and opposite viscous damping force per unit mass exerted on the fluid by the pile element as

$$\frac{dF_f}{d(\text{fluid mass})} = -\frac{dF_D}{\rho dV_f} = \frac{-C_D \frac{u}{2} |u| D dz}{dV_f}$$

where

dV_f = differential volume of fluid upon which the reactive damping stress is applied.

The above equation yields the force per unit mass of fluid in the vicinity of the differential pile element being considered. Noting that this equation is non-linear in u, it is necessary to define a linear equivalent such that

$$\frac{dF_f}{d(\text{mass of fluid})} = -\frac{dF_D}{\rho dV_f} = \frac{-C_D u|u| D dz}{2dV_f} = -f_{xz}\sigma u \qquad (2.3.5)$$

where

f_{xz} = dimensionless damping coefficient where the x subscript indicates flow direction and the z subscript indicates the direction of the pile's longitudinal axis

Strict equality between the non-linear and linear equations above is not possible, however, employing Lorentz' condition of equivalent work (Lorentz, 1926) to evaluate the damping coefficient, f_{xz}, will require that both the non-linear and linear equations dissipate the same amount of energy during one wave period over the entire structure. Thus the linearized equation establishes a structurally and temporally averaged resistance to flow due to the presence of the vertically oriented piles. That is, instead of encountering localized flow resistance in the immediate vicinity of the vertical structural member, the 'linearized' fluid particles encounter a uniformly distributed, temporally averaged, directionally sensitive unsteady flow resistance at every point within the structure. The dimensionless damping coefficient f_{xz} is evaluated in Chapter V using Lorentz' condition of equivalent work.

2.3.1b. y-Directed Piles Contribution to Horizontal Viscous Damping. The contribution of the y-directed piles horizontal viscous damping is developed similar to the vertical piles. That is, the drag relationship given by Eq. (2.2.1) is employed such that

$$dF_D = C_D \rho \frac{u}{2} |u| dA_c$$

where

$$dA_c = dy \cdot \text{Diameter} = dy \cdot D$$

The force per unit mass of fluid exerted on the fluid by the pile is therefore

$$\frac{dF_f}{d(\text{mass of fluid})} = -\frac{dF_D}{\rho dV_f} = \frac{-C_D u |u| D dy}{2dV_f}$$

Linearizing the above equation in u as was done for the vertical piles yields

$$\frac{dF_f}{d(\text{mass of fluid})} = -\frac{dF_D}{\rho dV_f} = \frac{-C_D u |u| D dy}{2dV_f} = -f_{xy} \sigma u \qquad (2.3.6)$$

where

f_{xy} = dimensionless damping coefficient for x-directed flow against y-directed piles

The dimensionless damping coefficient f_{xy} is evaluated in Chapter V using Lorentz' condition of equivalent work.

2.3.1c. Total Viscous Damping Equation for the Horizontal Equation of Motion. Viscous fluid damping within the structure due to the interaction of the horizontal fluid velocity component with the structural members is the sum of the vertical and y-directed piles contributions. Therefore, the viscous fluid damping force per unit mass of fluid in Region II is given by the sum of the linearized portions of Eqs. (2.3.5 and 2.3.6), i.e.,

$$\begin{aligned}\frac{dF_{f\ total}}{d(\text{mass of fluid})} &= (-f_{xz}\sigma u) + (-f_{xy}\sigma u) \\ &= -\sigma u(f_{xz}+f_{xy}) \\ &= -f_x\sigma u \qquad (2.3.7)\end{aligned}$$

where

$f_x = f_{xz} + f_{xy}$ = total dimensionless damping coefficient for the x-direction.

2.3.1d. y-Directed Piles Contribution to Viscous Damping in the Vertical Direction. Using the drag force relationship given by Eq. (2.2.2) for a differential element of a pile whose longitudinal axis runs in the y-direction yields the differential vertical viscous drag force on the pile element as

$$dF_D = C_D \rho \frac{w}{2} |w| dA_c$$

where

$$dA_c = dy \cdot \text{Diameter} = dy \cdot D$$

Dividing the above equation by ρdV_f and reversing the sign yields the viscous damping force per unit mass exerted by the piles on the water particles, i.e.,

$$\frac{dF_f}{d(\text{mass of fluid})} = -\frac{dF_D}{\rho dV_f} = \frac{-C_D D w|w| dy}{2dV_f}$$

Linearizing the above equation in w as was done for u in Sections 2.3.1a and 2.3.1b yields

$$\frac{dF_f}{d(\text{mass of fluid})} = -\frac{dF_D}{\rho dV_f} = \frac{-C_D D w|w| dy}{2dV_f} \cong -f_{zy}\sigma w \qquad (2.3.8)$$

where

f_{zy} = dimensionless damping coefficient for vertical flow past y-directed piles

The dimensionless damping coefficient, f_{zy}, is evaluated in Chapter V using Lorentz' condition of equivalent work.

<u>2.3.1e. x-Directed Piles Contribution to Viscous Damping in the Vertical Direction</u>. Again, using Eq. (2.2.2) applied to a differential element of a pile whose longitudinal axis runs in the x-direction yields the vertical differential viscous drag force on the element as

$$\frac{dF_f}{d(\text{mass of fluid})} = -\frac{dF_D}{\rho dV_f} = \frac{-C_D Dw|w|dx}{2dV_f}$$

Linearizing the above equation in w yields

$$\frac{dF_f}{d(\text{mass of fluid})} = -\frac{dF_D}{\rho dV_f} = \frac{-C_D Dw|w|dx}{2dV_f} \equiv -f_{zx}\sigma w \qquad (2.3.9)$$

where

f_{zx} = dimensionless damping coefficient for vertical flow past x-directed piles

The dimensionless damping coefficient, f_{zx}, is evaluated in Chapter V using Lorentz' condition of equivalent work.

2.3.1f. Total Viscous Damping Equation for the Vertical Equation of Motion. Vertical viscous fluid damping within the structure is the sum of the components of vertical viscous damping contributed by the y and x-directed piles. Thus the vertical viscous fluid damping force per unit mass of fluid in Region II is given by the sum of the linear portions of Eqs. (2.3.8 and 2.3.9), i.e.,

$$\begin{aligned} \frac{dF_{f\,\text{total}}}{d(\text{mass of fluid})} &= (-f_{zy}\sigma w) + (-f_{zx}\sigma w) \\ &= -\sigma w(f_{zy}+f_{zx}) \\ &= -f_z\sigma w \qquad (2.3.10) \end{aligned}$$

where

$f_z = f_{zy} + f_{zx}$ = total dimensionless damping coefficient for the vertical direction

2.3.2. Adaptation of the Inertial Damping Force Equations for the Equations of Motion

The differential inertial damping force for the horizontal direction is given by Eq. (2.2.3). Again, only the vertical and y-directed members contribute to the horizontal damping force. Dividing Eq. (2.2.3) by ρdV_f yields the horizontal inertial damping force per mass of fluid as

$$\frac{dF_{Ix}}{d(\text{mass of fluid})} = -C_{mx} \frac{\partial u}{\partial t} \frac{dV}{dV_f}$$

The ratio dV/dV_f represents the ratio of the small solid element of structural volume about which the local fluid accelerates to the local volume of fluid being accelerated. On a macroscopic scale, this ratio is approximated by the ratio

$$\frac{V_{Sz}+V_{Sy}}{V_f} \approx \frac{dV}{dV_f}$$

when only the vertical and y-directed piles are considered. Multiplying the above equation by the quantity $[(1/V_T)/(1/V_T)]$ and referring to the definitions of Section 2.3 yields

$$\frac{\epsilon_y + \epsilon_z}{\epsilon} \simeq \frac{dV}{dV_f}$$

This approximation is true only in a structurally averaged sense, i.e., it tends to spread the local inertial stresses uniformly over the structure. However, spatial averaging is congruous with the Lorentz' linearization technique employed for the viscous stresses in the preceding section, and, thus it is appropriate to approximate the horizontal differential inertial damping force per unit mass of fluid as

$$\frac{dF_{Ix}}{d(\text{mass of fluid})} = -C_{mx} \frac{\partial u}{\partial t} \left[\frac{\epsilon_y + \epsilon_z}{\epsilon}\right] \tag{2.3.11}$$

By similar reasoning, the approximate vertical differential inertial damping force per unit mass of fluid is

$$\frac{dF_{Iz}}{d(\text{mass of fluid})} = -C_{mz} \frac{\partial w}{\partial t} \left[\frac{\epsilon_y + \epsilon_x}{\epsilon}\right] \tag{2.3.12}$$

2.4. Linearized Equations of Motion

The modified Navier-Stokes equations of motion for the x and z-directions may now be re-written using the damping forces per unit mass given by Eqs. (2.3.7, 2.3.11) and Eqs. (2.3.10, 2.3.12) in Eq. (2.1.5) and Eq. (2.1.6) respectively, i.e.,

$$\frac{\partial u}{\partial t} = -\frac{1}{\rho}\frac{\partial(P+\gamma z)}{\partial x} - f_x \sigma u - C_{mx}\frac{\partial u}{\partial t}\left[\frac{\epsilon_y+\epsilon_z}{\epsilon}\right]$$

and

$$\frac{\partial w}{\partial t} = -\frac{1}{\rho}\frac{\partial(P+\gamma z)}{\partial z} - f_z \sigma w - C_{mz}\frac{\partial w}{\partial t}\left[\frac{\epsilon_y+\epsilon_x}{\epsilon}\right]$$

Rearranging yields

$$S_x \frac{\partial u}{\partial t} = -\frac{1}{\rho}\frac{\partial(P+\gamma z)}{\partial x} - f_x \sigma u \tag{2.4.1}$$

and

$$S_z \frac{\partial w}{\partial t} = -\frac{1}{\rho}\frac{\partial(P+\gamma z)}{\partial z} - f_z \sigma w \tag{2.4.2}$$

where

S_x = inertial coefficient for the x-direction = $\{1+C_{mx}[\frac{\epsilon_y+\epsilon_z}{\epsilon}]\}$ (2.4.3)

S_z = inertial coefficient for the z-direction = $\{1+C_{mz}[\frac{\epsilon_y+\epsilon_x}{\epsilon}]\}$ (2.4.4)

2.5. A Velocity Potential

The linearized equations of motion have been derived as

$$S_x \frac{\partial u}{\partial t} = -\frac{1}{\rho}\frac{\partial(P+\gamma z)}{\partial x} - f_x \sigma u \tag{2.4.1}$$

in the x-direction, and

$$S_z \frac{\partial w}{\partial t} = -\frac{1}{\rho}\frac{\partial(P+\gamma z)}{\partial z} - f_z \sigma w \tag{2.4.2}$$

in the z-direction. Employing the assumption of simple harmonic time dependency, the horizontal and vertical velocity components may be expressed as

$$u = U(x, z)e^{-i\sigma t}$$

and

$$w = W(x, z)e^{-i\sigma t}$$

where

$U(x, z), W(x, z)$ = unknown spatial functions

Taking the partial derivative of the above velocity expressions with respect to time, substituting the results into Eqs. (2.4.1 and 2.4.2) and collecting velocity terms yields

$$S_x(-i\sigma u) + f_x \sigma u = -\frac{1}{\rho}\frac{\partial(P+\gamma z)}{\partial x}$$

in the x-direction. Or

$$A_x u = -\frac{1}{\rho}\frac{\partial(P+\gamma z)}{\partial x} \qquad (2.5.1)$$

where

$$A_x = f_x \sigma - i\sigma S_x$$

And

$$A_z w = -\frac{1}{\rho}\frac{\partial(P+\gamma z)}{\partial z} \qquad (2.5.2)$$

where

$$A_z = f_z \sigma - i\sigma S_z$$

in the z-direction. Since the velocities u and w of Eqs. (2.5.1 and 2.5.2) are the vector components of the total instantaneous velocity and A_x and A_z are scalar constants it is appropriate to add Eqs. (2.5.1 and 2.5.2) vectorially, i.e.,

$$\vec{i}\, A_x u + \vec{k}\, A_z w = -\frac{1}{\rho}\left[\vec{i}\frac{\partial}{\partial x} + \vec{k}\frac{\partial}{\partial z}\right][P+\gamma z]$$

where

$\vec{i}$ = unit vector in the x-direction

$\vec{k}$ = unit vector in the z-direction

Noting that $\left[\vec{i}\frac{\partial}{\partial x} + \vec{k}\frac{\partial}{\partial z}\right]$ is the two dimensional gradient operator, $\vec{\nabla}$, that the quantity $[P+\gamma z]$ is a scalar quantity, and that the curl of the vectorial gradient of any scalar is identically equal to zero, the curl of both sides of the above equation is taken such that

$$\vec{\nabla} \times [\vec{i}\, A_x u + \vec{k}\, A_z w] = -\frac{1}{\rho}\{\vec{\nabla} \times \vec{\nabla}\, [P+\gamma z]\} = 0$$

Since the right hand side of the above equation is identically equal to zero the left hand side must also equal zero. Using the identity that the curl of the vectorial gradient of any scalar is zero again, the left hand side is re-written in terms of the vectorial gradient of the two dimensional scalar, ϕ, i.e.,

$$\vec{\nabla} \times [\vec{i}\, A_x u + \vec{k}\, A_z w] = \vec{\nabla} \times \vec{\nabla}\, (\phi) = 0$$

where

ϕ = scalar velocity potential function

Thus

$$i\, A_x u + k\, A_z w = \nabla \phi = i \frac{\partial \phi}{\partial x} + k \frac{\partial \phi}{\partial z}$$

Equating vector components yields

$$A_x u = \frac{\partial \phi}{\partial x} \qquad (2.5.3)$$

or

$$u = \frac{1}{A_x} \frac{\partial \phi}{\partial x} \qquad (2.5.4)$$

and similarly

$$A_z w = \frac{\partial \phi}{\partial z} \qquad (2.5.5)$$

and

$$w = \frac{i}{A_z} \frac{\partial \phi}{\partial z} \qquad (2.5.6)$$

Equations (2.5.3 and 2.5.5) define a velocity potential function, ϕ, for homogeneous, anisotropic damping. ϕ is, more precisely, a combined acceleration and velocity potential because of the behavior of A_x and A_z, e.g., Eqs. (2.4.1), (2.5.1) and (2.5.3). In simple harmonic motions, however, the velocities and accelerations are directly proportional, hence, ϕ shall be referred to as a velocity potential throughout this study.

2.6. The Bernoulli Equation and the Linearized Boundary Conditions

Substitution of Eq. (2.5.3) into Eq. (2.5.1) reduces the equation to horizontal gradients, i.e.,

$$A_x u = \frac{\partial \phi}{\partial x} = -\frac{1}{\rho}\frac{\partial (P+\gamma z)}{\partial x}$$

Since the fluid density is assumed to be constant and $\gamma/\rho = g$, where g is the gravitational acceleration, simplification of the above equation yields

$$\frac{\partial(\phi + P/\rho + gz)}{\partial x} = 0$$

Similarly, substituting Eq. (2.5.5) into Eq. (2.5.2), and performing some algebraic manipulations yields

$$\frac{\partial(\phi + P/\rho + gz)}{\partial z} = 0$$

The previous two equations indicate that the quantity $(\phi + P/\rho + gz)$ is a constant in space. If this quantity is not a constant, it can only be a function of time. Thus the above two equations yield the Bernoulli equation as

$$\phi + \frac{P}{\rho} + gz = F(t) \tag{2.6.1}$$

The vertical displacement of the free surface from the still water surface is defined as $\eta(x,t)$ in Figure 1.1. Consequently, a water particle at the free surface has the vertical coordinate $z = \eta$. Substituting this value of z and the fact that the pressure at the free surface is atmospheric, or zero gage pressure, into Eq. (2.6.1) yields

$$\phi + g\eta = F(t)$$

at $z = \eta$. Or,

$$\eta(x,t) = \frac{1}{g}\left[F(t)-\phi\right] \tag{2.6.2}$$

at $z = \eta$. Taking the partial derivative of Eq. (2.6.2) with respect to time yields

$$\frac{\partial \eta}{\partial t} = \frac{1}{g}\frac{\partial\left[F(t)-\phi\right]}{\partial t} \tag{2.6.3}$$

Assuming a fluid particle at the free surface remains at the free surface during the wave cycle requires that the water surface rises and falls at a rate equal to the vertical velocity, w. Thus

$$\frac{D\eta}{Dt} = w = \frac{\partial \eta}{\partial t} + \frac{\partial \eta}{\partial x}\frac{dx}{dt}$$

at $z = \eta$. For small amplitude waves the second order term $(\partial\eta/\partial x \times dx/dt)$ is negligible, therefore

$$\frac{D\eta}{Dt} = \frac{\partial\eta}{\partial t} = w = \frac{1}{A_z}\frac{\partial\phi}{\partial z} = \frac{1}{g}\frac{\partial(F(t)-\phi)}{\partial t} \tag{2.6.4}$$

at $z = \eta$. The velocity components, u and w, and hence the velocity potential, ϕ, are assumed to be simple harmonic functions of time. Consequently, the velocity potential may be expressed as

$$\phi = \Phi(x, z)e^{-i\sigma t}$$

where

$\Phi(x, z)$ = an unknown spatial function

Substitution of the partial derivative of the above expression with respect to time into Eq. (2.6.4) yields

$$\frac{\partial\phi}{\partial z} = \frac{A_z}{g}\left[i\sigma\phi + \frac{\partial F(t)}{\partial t}\right]$$

at $z = \eta$. Or,

$$0 = g\frac{\partial\phi}{\partial z} - A_z\left[i\sigma\phi + \frac{\partial F(t)}{\partial t}\right] \tag{2.6.5}$$

at $z = \eta$. Equation (2.6.5) constitutes the combined kinematic and dynamic free surface boundary condition.

Assuming the bottom to be non-deformable, impermeable, and horizontal requires the vertical velocity component to vanish at the bottom, i.e.,

$$w = 0 = \frac{1}{A_z} \frac{\partial \phi}{\partial z} \tag{2.6.6}$$

at $z = -h$. Equation (2.6.6) is termed the bottom boundary condition.

Finally conservation of mass for an incompressible fluid must be satisfied such that

$$\frac{\partial u}{\partial x} + \frac{\partial w}{\partial z} = 0$$

Substituting Eqs. (2.5.4 and 2.5.6) into the above expression yields the governing differential equation for the problem as a variation of the Laplace equation, i.e.,

$$\frac{1}{A_x} \frac{\partial^2 \phi}{\partial x^2} + \frac{1}{A_z} \frac{\partial^2 \phi}{\partial z^2} = 0 \tag{2.6.7}$$

2.7. Summary of the Boundary Value Problem

Equation (2.6.7) is a second-order linear, homogeneous partial differential equation which is very similar in form to Laplace's equation $(\nabla^2 \phi = 0)$. The boundary value problem for the structure being considered is specified by Eqs. (2.6.7, 2.6.5 and 2.6.6) and is repeated here in summary;

Differential equation:

$$\frac{1}{A_x} \frac{\partial^2 \phi}{\partial x^2} + \frac{1}{A_z} \frac{\partial^2 \phi}{\partial z^2} = 0 \tag{2.6.7}$$

Free surface boundary condition:

$$g \frac{\partial \phi}{\partial z} - A_z \left[\frac{\partial F(t)}{\partial t} + i\sigma\phi \right] = 0 \quad \text{at} \quad z = \eta \tag{2.6.5}$$

Bottom boundary condition:

$$\frac{1}{A_z} \frac{\partial \phi}{\partial z} = 0 \quad \text{at} \quad z = -h \tag{2.6.6}$$

2.8. Solution of the Boundary Value Problem

The differential equation, Eq. (2.6.7), is linear, second order, and homogeneous. The boundary conditions (Eqs. 2.6.5 and 2.6.6) are linear, first order, and also homogeneous. Finally, the flow boundaries of the system are coincident with the directions of the chosen coordinate system. These facts indicate that a solution to the boundary value problem is available through the use of the separation of variables technique (Robertson, 1965).

The separation of variables technique requires that

$$\phi = X(x) \cdot Z(z) \cdot T(t) \tag{2.8.1}$$

where

$X(x)$ = an unknown function of x only

$Z(z)$ = an unknown function of z only

$T(t)$ = simple harmonic function of time = $e^{-i\sigma t}$

Substituting Eq. (2.8.1) into Eq. (2.6.7) and performing the indicated partial differentiations yields

$$\frac{1}{A_x} X''Ze^{-i\sigma t} + \frac{1}{A_z} XZ''e^{-i\sigma t} = 0$$

where

X'' = the second partial differentiation of X with respect to x

Z'' = the second partial differentiation of Z with respect to z

Or, after simplifying,

$$-\frac{A_z}{A_x}\frac{X''}{X} = \frac{Z''}{Z}$$

Since the left hand side of the above equation is a function of x only and the right hand side is a function of z only, both sides must be equal to a constant, k_{mn}^2, in order for the equality to be preserved over the entire domain of x and z, i.e.,

$$-\frac{A_x}{A_z}\frac{X''}{X} = \frac{Z''}{Z} = k_{mn}^2 \qquad (2.8.2)$$

where

k_{mn}^2 = a non-zero constant. The subscript n is used in anticipation of designating the infinite number of modal values of k corresponding to the eigen-series solution. The leading subscript, m, is used to designate the region number since k will vary in accordance with the water depths, h_m (see Fig. 1.1).

For the special case in which k_{mn} is equal to zero the above equation is simplified and re-written as

$$X_0'' = Z_0'' = 0 \tag{2.8.3}$$

Rearranging and separating Eq. (2.8.2) yields the two ordinary differential equations

$$X'' + \frac{A_x}{A_z} k_{mn}^2 X = 0$$

and

$$Z'' - k_{mn}^2 Z = 0$$

The general solutions of the above two ordinary differential equations are, respectively,

$$X(x) = De^{i\sqrt{A_x/A_z}k_{mn}x} + Ee^{-i\sqrt{A_x/A_z}k_{mn}x} \tag{2.8.4}$$

$$Z(z) = Fe^{k_{mn}z} + Ge^{-k_{mn}z} \tag{2.8.5}$$

where

D, E, F, G = constants which may be complex. Note that the constant F used here is not related to the Bernoulli constant F(t) of Eq. (2.6.1).

Substitution of Eqs. (2.8.4 and 2.8.5) into Eq. (2.8.1) and employing the assumption of simple harmonic time dependency yields the velocity potential expression when k_{mn}^2 does not equal zero as

$$\phi_k = [De^{i\sqrt{A_x/A_z}k_{mn}x} + Ee^{-i\sqrt{A_x/A_z}k_{mn}x}][Fe^{k_{mn}z} + Ge^{-k_{mn}z}]e^{-i\sigma t} \tag{2.8.6}$$

Separating Eq. (2.8.3) and integrating twice yields

$$X(x)_0 = Mx + Q$$

$$Z(z)_0 = Rz + S$$

where

M, Q, R, S = constants. Note that S is not related to the inertial coefficients S_x and S_z.

0 = subscript indicating the special case when $k_{mn} = 0$

Substitution of the above two equations into Eq. (2.8.1) and again employing the assumption of simple harmonic time dependency yields the velocity potential expression when k_{mn} equals zero as

$$\phi_0 = [Mx+Q][Rz+S]e^{-i\sigma t} \tag{2.8.7}$$

Since the differential equation, Eq. (2.6.7), is linear, superposition of all of the independent solutions yields the total, or complete, solution. Thus, the total velocity potential solution is obtained by adding Eqs. (2.8.6 and 2.8.7) such that

$$\phi = \phi_k + \phi_0$$

or

$$\phi = \left\{[De^{i\sqrt{A_x/A_z}k_{mn}x} + Ee^{-i\sqrt{A_x/A_z}k_{mn}x}][Fe^{k_{mn}z} + Ge^{-k_{mn}z}] + [Mx+Q][Rz+S]\right\} e^{-i\sigma t}$$

Now substituting the above expression for the velocity potential into the bottom boundary condition, Eq. (2.6.6), performing the indicated differentiation, and evaluating at $z = -h_m$ yields

$$0 = \frac{e^{-i\sigma t}}{A_x}\left\{[k_{mn}(De^{i\sqrt{A_x/A_z}k_{mn}x} + Ee^{-i\sqrt{A_x/A_z}k_{mn}x})(Fe^{-k_{mn}h_m} - Ge^{k_{mn}h_m})] + [R(Mx+Q)]\right\}$$

where the subscript m of h_m denotes the region number as it does for k_{mn}. Since $e^{-i\sigma t}$ is not always zero, and since it is not possible for the polynomial (second) bracketed term in the above equation to be always of equal magnitude and opposite sign as that of the (first) bracketed product of exponentials, it is apparent that both of the bracketed terms must be equal to zero, i.e.,

$$0 = k_{mn}(De^{i\sqrt{A_x/A_z}k_{mn}x} + Ee^{-i\sqrt{A_x/A_z}k_{mn}x})(Fe^{-k_{mn}h_m} - Ge^{k_{mn}h_m})$$

and

$$0 = R(Mx+Q) \tag{2.8.8}$$

For the former of the above two equations, k_{mn} has been restricted to non-zero values, while D and E may not both be equal to zero or the velocity potential ϕ_k is always zero. It is essential that ϕ_k be non-zero in order to obtain a viable solution with respect to observed wave phenomena. Hence

$$0 = Fe^{-k_{mn}h_m} - Ge^{k_{mn}h_m}$$

or

$$F = Ge^{2k_{mn}h_m}$$

Substitution of the above expression for F into Eq. (2.2.5), and factoring out the term $2Ge^{k_{mn}h_m}$ yields

$$Z(z) = 2Ge^{k_{mn}h_m}\left[\frac{e^{k_{mn}(h_m+z)} + e^{-k_{mn}(h_m+z)}}{2}\right]$$

or

$$Z(z) = 2Ge^{k_{mn}h_m}\,\mathrm{ch}.\,k_{mn}(h_m+z) \tag{2.8.9}$$

where

$\mathrm{ch}.\,k_{mn}(h_m+z)$ = hyperbolic cosine of the complex argument $[k_{mn}(h_m+z)]$

Combining Eqs. (2.8.1, 2.8.4 and 2.8.9) and the assumption of a simple harmonic time dependency allows the velocity potential for non-zero values of k_{mn} to be expressed as

$$\Phi_k = [De^{i\sqrt{A_x/A_z}k_{mn}x} + Ee^{-i\sqrt{A_x/A_z}k_{mn}x}][ch.\,k_{mn}(h_m+z)]e^{-i\sigma t} \tag{2.8.10}$$

where the constants D and E have been used to absorb the constant factor $2Ge^{k_{mn}h_m}$. Now, returning to Eq. (2.8.8), it is apparent that either R equals zero or that both M and Q are zero. If this latter possibility is true then Φ_0 is always zero. Although it is not known whether or not Φ_0 is physically relevant to the solution, it will be retained for the present by assuming that R is zero. Hence the velocity potential expression when k_{mn} is zero becomes

$$\Phi_0 = S(Mx+Q)e^{-i\sigma t}$$

The total velocity potential expression is re-written by adding the above equation and Eq. (2.8.10) to yield

$$\Phi = \left\{[De^{i\sqrt{A_x/A_z}k_{mn}x} + Ee^{-i\sqrt{A_x/A_z}k_{mn}x}][ch.\,k_{mn}(h_m+z)] + [S(Mx+Q)]\right\} e^{-i\sigma t} \tag{2.8.11}$$

2.9. Evaluation of the Bernoulli Function, F(t)

It is necessary to impose the combined kinematic and dynamic free surface boundary condition, Eq. (2.6.5), on Eq. (2.8.11) in order to further evaluate the velocity potential expression. However, examination of Eq. (2.6.5) reveals that it will be advantageous to first establish the unknown Bernoulli function, $F(t)$.

Equation (2.6.2) specifies the displacement of the free surface, η, as

$$\eta(x,t) = \frac{1}{g}\left[F(t) - \phi\right] \tag{2.6.2}$$

Both η and ϕ are, by assumption, required to be simple harmonic functions of time. Noting that the integral of any linear simple harmonic function of time over a full wave period, T, must be zero, the integral with respect to time of Eq. (2.6.2) is taken over a wave period such that

$$\int_t^{t+T} \cancelto{0}{\eta(x,t)}\,dt = \frac{1}{g}\int_t^{t+T} F(t)\,dt - \int_t^{t+T} \cancelto{0}{\phi(x,z,t)}\,dt$$

Thus

$$0 = \int_t^{t+T} F(t)\,dt$$

Two possibilities exist, either $F(t)$ is also a simple harmonic function or else it is zero. Assuming the former to be true, $F(t)$ may be expressed as

$$F(t) = d e^{-i\sigma t} \tag{2.9.1}$$

where d = a constant.

2.10. The Dispersion Equation

Substituting Eqs. (2.8.11 and 2.9.1) into the kinematic and dynamic free surface boundary condition, Eq. (2.6.5), performing the indicated differentiations, and employing the small amplitude approximation

$$z = \eta \Rightarrow z \approx 0$$

to evaluate the resulting expression yields

$$0 = gk_{mn}\,\text{sh.}\,k_{mn}h_m\left[De^{i\sqrt{A_x/A_z}\,k_{mn}x} + Ee^{-i\sqrt{A_x/A_z}\,k_{mn}x}\right]e^{-i\sigma t}$$
$$- i\sigma A_z e^{-i\sigma t}\left\{-d + (\text{ch.}\,k_{mn}h_m)\left[De^{i\sqrt{A_x/A_z}\,k_{mn}x} + Ee^{-i\sqrt{A_x/A_z}\,k_{mn}x}\right] + S(Mx+Q)\right\}$$

where

$\text{sh.}\,k_{mn}h_m$ = hyperbolic sine of the complex argument $k_{mn}h_m$

or, rearranging and cancelling $e^{-i\sigma t}$

$$gk_{mn}(\text{sh.}\,k_{mn}h_m)[X(x)] = i\sigma A_z\{(\text{ch.}\,k_{mn}h_m)[X(x)] + S(Mx+Q) - d\}$$

where $X(x)$ is defined by Eq. (2.8.4) as

$$X(x) = De^{i\sqrt{A_x/A_z}\,k_{mn}x} + Ee^{-i\sqrt{A_x/A_z}\,k_{mn}x}$$

Now dividing both sides of the above equation by $X(x)$ and rearranging yields

$$gk_{mn}(\mathrm{sh.}\, k_{mn}h_m) - i\sigma A_z(\mathrm{ch.}\, k_{mn}h_m) = \frac{S(Mx+Q)-d}{X(x)} \tag{2.10.1}$$

The left hand side (L.H.S.) of the above equation is a constant. The right hand side (R.H.S.) is a first order polynomial function of x divided by a complex exponential function of x. It is not possible for this quotient to be a constant over the x domains of any of the three regions unless the numerator of the R.H.S. is zero or the denominator is infinite. The latter possibility is eliminated by choosing the root of (A_x/A_z) (see Appendix A) so that waves decay exponentially when acted upon by the damping terms described in Section (2.2). Consequently

$$S(Mx+Q) - d = 0$$

Two distinct possibilities exist for the above equation, i.e., first either

$$S = d = 0$$

in which case

$$\Phi_0 = F(t) = 0$$

or, secondly

$$M = 0$$

and

$$SQ - d = 0$$

The former possibility requires that ϕ_0 and $F(t)$ both be identically equal to zero since R, S, and d are all zero. The latter possibility requires that ϕ_0 be strictly constant in space, since R and M are both zero, and that ϕ_0 and $F(t)$ be equal, i.e.,

$$\phi_0 = SQe^{-i\sigma t} = F(t) = de^{-i\sigma t}$$

Now, considering Eqs. (2.6.1, 2.6.2 and 2.6.5) it is apparent that the velocity potential term, ϕ, (containing ϕ_0) is always of opposite sign as that of $F(t)$ and therefore ϕ_0 and $F(t)$ must cancel. Furthermore, examination of Eqs. (2.5.4, 2.5.6, 2.6.6 and 2.6.7) reveal that the ϕ_0 term does not contribute to the velocity components or to the boundary value problem since its spatial derivatives are zero. Thus it may be concluded that the result is the same regardless which of these possibilities is actually correct. That is, ϕ_0 and $F(t)$ either cancel or do not contribute. Consequently, both ϕ_0 and $F(t)$ will be excluded from the remainder of this investigation as though both of these quantities were identically equal to zero.

Employing this conclusion allows Eq. (2.10.1) to be re-written as

$$i\sigma A_z(\mathrm{ch}.\,k_{mn}h_m) = gk_{mn}(\mathrm{sh}.\,k_{mn}h_m)$$

or

$$i\sigma A_z = gk_{mn}\,\mathrm{th}.\,k_{mn}h_m$$

where

$$\mathrm{th}.\,k_{mn}h_m = \text{hyperbolic tangent of } k_{mn}h_m = \frac{\mathrm{sh}.\,k_{mn}h_m}{\mathrm{ch}.\,k_{mn}h_m}$$

Remembering that

$$A_z = f_z\sigma - iS_z\sigma$$

the above equation becomes

$$\sigma^2(S_z+if_z) = gk_{mn}\,\mathrm{th}.\,k_{mn}h_m \qquad (2.10.2)$$

The left hand side of the above equation is a complex constant when the vertical damping coefficient, f_z, does not equal zero. The water depth, h_m, and the gravitational acceleration, g, on the right hand side are both real values. Hence, it is apparent that k_{mn} must be complex.

Rewriting the hyperbolic tangent in terms of the hyperbolic sine and cosine, multiplying both sides of the above equation by the water depth, h_m, and rearranging yields

$$\frac{h_m \sigma^2 (S_z + if_z)}{g} = k_{mn} h_m \frac{sh.\, k_{mn} h_m}{ch.\, k_{mn} h_m}$$

Now, substituting the series expansions for the hyperbolic sine and cosine of a complex argument (Abramowitz and Stegun, 1970) into the above equation yields

$$\frac{h_m \sigma^2 (S_z + if_z)}{g} = \lambda \left[\frac{\lambda + \frac{\lambda^3}{3!} + \frac{\lambda^5}{5!} + \ldots}{1 + \frac{\lambda^2}{2!} + \frac{\lambda^4}{4!} + \ldots} \right]$$

where

λ = complex value $k_{mn} h_m$

Multiplying both sides of the above equation by the denominator of the R.H.S. yields

$$\frac{h_m \sigma^2}{g} (S_z + if_z)\left(1 + \frac{\lambda^2}{2!} + \frac{\lambda^4}{4!} + \ldots\right) = \lambda^2 + \frac{\lambda^4}{3!} + \frac{\lambda^6}{5!} + \ldots$$

Subtracting the R.H.S. from both sides of the above equation yields a complex polynomial function of λ as

$$0 = -(\Gamma + i\omega) + \frac{\lambda^2}{2}[2 - (\Gamma + i\omega)] + \frac{\lambda^4}{4!}[4 - (\Gamma + i\omega)] + \frac{\lambda^6}{6!}[6 - (\Gamma + i\omega)] \ldots \qquad (2.10.3)$$

where

$$\Gamma = \frac{h_m \sigma^2}{g} S_z$$

$$\omega = \frac{h_m \sigma^2}{g} f_z$$

The

> 'Fundamental Theorem of Algebra' requires that every polynomial equation of the form
>
> $$c_0\lambda^n + c_1\lambda^{n-1} + c_2\lambda^{n-2} + c_3\lambda^{n-3} \ldots + c_{n-1}\lambda + c_n = 0$$
>
> in which the coefficients $c_0 \ldots c_n$ are any complex numbers, whose degree n is greater than or equal to one, and whose leading coefficient c_0 is not zero, possesses precisely n roots in the complex number system, provided that each multiple root of multiplicity m is counted as m roots (Thomas, 1968).

Since Eq. (2.10.3) is a complex polynomial of infinite degree, it must have an infinite number of roots, λ_n. Furthermore solution of the complex dispersion equation, Eq. (2.10.2), using a Newton-Raphson technique (see Chapter VI) demonstrates that there are an infinite number of unique roots, λ_n,[2/] and thus an infinite number of complex values $k_{mn}h_m$. Since h_m is a real constant, it is apparent

[2/] It is possible to prove this mathematically, as well, by expanding the λ^n terms of Eq. (2.10.3) using DeMoivre's theorem and then equating the real and imaginary parts of the resulting equation to zero. This yields two equations which are trigonometric series with variable modulating amplitudes such that an infinite number of λ_n values may be shown to satisfy the equations.

then that there must be an infinite number of unique complex values k_{mn} which satisfy Eq. (2.10.2).

Equation (2.10.2) represents the complex dispersion equation within the porous structure. It also represents the characteristic equation for obtaining the infinite number of eigenvalues, k_{mn}, for the solutions of the separated ordinary differential equations given by Eqs. (2.8.4 and 2.8.5). Corresponding to each eigenvalue, k_{mn}, there is an eigenfunction, ϕ_n. Since the problem being considered is linear, the total solution, ϕ, is the linear superposition of all the individual ϕ_n solutions, i.e.,

$$\phi = \sum_{n=1}^{\infty} \phi_n \tag{2.10.4}$$

where, having concluded that ϕ_0 does not contribute to the solution, ϕ_n is obtained from Eq. (2.8.11) as

$$\phi_n = [De^{i\sqrt{A_x/A_z}k_{mn}x} + Ee^{-i\sqrt{A_x/A_z}k_{mn}x}][ch.k_{mn}(h_m+z)]e^{-i\sigma t} \tag{2.10.5}$$

2.11. The Unknown Amplitude Coefficients

Considering $F(t)$ be to zero, the free surface displacement is obtained from Eq. (2.6.2) as

$$\eta = -\phi/g \tag{2.11.1}$$

at $z = \eta$. Substituting Eq. (2.10.5) for ϕ into Eq. (2.11.1) and employing the small amplitude surface approximation

$$z = \eta \Rightarrow z \approx 0$$

yields

$$\eta = -\frac{ch.\, k_{mn} h_m}{g} [De^{-i(\sigma t - \sqrt{A_x/A_z}\, k_{mn} x)} + Ee^{-i(\sigma t + \sqrt{A_x/A_z}\, k_{mn} x)}] \tag{2.11.2}$$

at $z = 0$. The two exponential terms within the brackets represent two wave forms oriented in opposite directions such that

$$\eta = \eta_+ + \eta_-$$

where η_+ is a waveform oriented in the positive x-direction and η_- is a waveform oriented in the negative x-direction. Since the time and x-dependence of waves oriented in the positive x-direction must be of opposite signs

$$\eta_+ = -\frac{ch.\, k_{mn} h_m}{g} [De^{-i(\sigma t - \sqrt{A_x/A_z}\, k_{mn} x)}]$$

and similarly, since the x and t-dependence of waves oriented in the negative x-direction must be of the same sign

$$\eta_- = -\frac{ch.k_{mn}h_m}{g}[Ee^{-i(\sigma t+\sqrt{A_x/A_z}k_{mn}x)}]$$

The amplitudes of the waveforms expressed by the exponentially damped, periodic waveforms above are defined as the maximum values of the free surface displacement realized when the complex exponential functions attain their maximum values of unity. Consequently

$$a_+ = -\frac{Dch.k_{mn}h_m}{g}$$

where

a_+ = amplitude of the waveform oriented in the positive x-direction

or

$$D = -\frac{a_+g}{ch.k_{mn}h_m} \tag{2.11.3}$$

and

$$a_- = -\frac{E\ ch.k_{mn}h_m}{g}$$

where

a_- = amplitude of the waveform oriented in the negative x-direction

or

$$E = -\frac{a_-g}{ch.k_{mn}h_m} \tag{2.11.4}$$

Substitution of the expressions for D and E above into Eq. (2.10.5) yields the single mode velocity potential as

$$\phi_n = -g[a_{+n} e^{i\sqrt{A_x/A_z}\,k_{mn} x} + a_{-n} e^{-i\sqrt{A_x/A_z}\,k_{mn} x}][\frac{\mathrm{ch.}\,k_{mn}(h_m+z)}{\mathrm{ch.}\,k_{mn} h_m}]e^{-i\sigma t} \tag{2.11.5}$$

In similar fashion, the free surface displacement of each individual modal waveform is found from Eq. (2.10.1) using Eqs. (2.10.2 and 2.10.3) as

$$\eta_n = a_{+n} e^{-i(\sigma t - \sqrt{A_x/A_z}\,k_{mn} x)} + a_{-n} e^{-i(\sigma t + \sqrt{A_x/A_z}\,k_{mn} x)} \tag{2.11.6}$$

at $z = 0$. Thus, the total water surface profile is given by

$$\eta = \sum_{n=1}^{\infty} \eta_n \tag{2.11.7}$$

Assuming that the appropriate sign of the complex square root of $[A_x/A_z]$ is chosen (see Section 3.2.1 and Appendix A), Eqs. (2.11.6 and 2.11.7) describe a series of sinusoidal waveforms within the structure which decay exponentially in space. The decay rate is a function of the quantity $[A_x/A_z]$. Since this quantity is a function of the angular frequency, and the inertial and damping coefficients for both directions, it is readily perceived that energy dissipation within the structure is also a function of these parameters as might have been intuitively suspected.

III. THE FLOW FIELD SOLUTION

3.1. The Velocity Potentials Outside the Structure

The expression for the velocity potential modes specified by Eq. (2.11.5) is applicable only where damping is described by the viscous and inertial terms developed in Chapter I. Since no damping occurs in Regions I and III (see Fig. 1.1), some modifications of Eq. (2.11.5) are necessary in order to establish the form of the velocity potential expressions in these regions.

Remembering that

$$A_x = f_x\sigma - i\sigma S_x$$

$$A_z = f_z\sigma - i\sigma S_z$$

and noting that in clean water without damping

$$f_x = f_z = 0$$

and

$$S_x = S_z = 1.0$$

It follows that

$$A_x = A_z = -i\sigma$$

in Regions I and III. Now, substituting the above relations for A_x

and A_z into Eq. (2.11.5), the modal velocity potentials outside the structure have the general form

$$\phi_n = -g[a_{+n}e^{ik_{mn}x} + a_{-n}e^{-ik_{mn}x}][\frac{ch.k_{mn}(h_m+z)}{ch.k_{mn}h_m}]e^{-i\sigma t} \text{ [3/]} \qquad (3.1.1)$$

The dispersion equation in the outer regions is found from Eq. (2.10.2) by again employing the values $f_z = 0$, $S_z = 1.0$, i.e.,

$$\sigma^2 = gk_{mn}\, th.k_{mn}h_m \qquad (3.1.2)$$

in Regions I and III. The eigenvalues, k_{mn}, which satisfy the above equation are found using the Newton-Raphson technique described in Chapter VI. There is one real value of k_{mn} which satisfies Eq. (3.1.2). This value corresponds to the propagating, or first $(n = 1)$, wave mode. Also, there are an infinite number of pure imaginary k_{mn}'s which satisfy Eq. (3.1.2) and correspond to the evanescent wave modes $(2 \leq n \leq \infty)$ generated at the seaward and leeward structural interfaces. The evanescent modes represent local standing waves with spatially decaying amplitudes and are

---

[3/] It should be noted that the use of the symbols a_{+n} and a_{-n} in Eqs. (2.11.5 and 3.1.1) does not imply that the amplitudes of a particular wave mode will in general be equal in all three regions. These symbols are used to indicate a modal amplitude coefficient in the general sense and will be redefined in a more explicit manner in the next section.

included to satisfy irregularities in the vicinity of the interfacial boundaries (Sollitt and Cross, 1972).

The multiple eigenvalues, k_{mn}, which satisfy Eq. (3.1.2), require eigen-series solutions for the Region I and III velocity potentials in direct analogy with Eq. (2.10.4), i.e.,

$$\Phi_{1,3} = \sum_{n=1}^{\infty} \Phi_n \tag{3.1.3}$$

where Φ_n is given by Eq. (3.1.1) for Regions I and III.

3.2. Application of the Velocity Potential Equations

The general forms of the modal velocity potential equations for Region II and Regions I and III have been derived as Eq. (2.11.5) and Eq. (3.1.1) respectively. It will now be helpful to adapt them to the problem being considered. This is accomplished by referencing the spatial phases to the appropriate interfacial planes and by redefining the amplitude coefficients in Regions I and III in terms of the incident, reflected and transmitted wave amplitudes.

3.2.1. Region II

Beginning with Eq. (2.11.5), it is apparent that propagating waves entering the structure from the seaward side as well as the evanescent modes generated at the interface $(x = -b)$ have maximum amplitudes at the interface since damping within the structure causes wave amplitudes to decay as the waveform moves into the structure. Consequently, the spatial phase for waveforms associated with the seaward interface, i. e., the 'a_{+n}' term of Eq. (2.11.5), is referenced to $x = -b$. In a similar fashion, propagating waves reflected from the leeward face, and/or re-entering the leeward face after being reflected by the reflector-absorber, as well as the evanescent modes generated at the interface, have maximum amplitudes at the leeward interface $(x = +b)$. Hence the spatial phase for the 'a_{-n}'[4/] term of Eq. (2.11.5) is referenced to $x = b$. Re-writing Eq. (2.11.5) using the spatial phases delineated above yields the modal velocity potential for Region II as

$$\phi_{2n} = -g[a_{+n} e^{i\sqrt{A_x/A_z}k_{2n}(x+b)} + a_{-n} e^{-i\sqrt{A_x/A_z}k_{2n}(x-b)}]$$

$$\times \left[\frac{ch.k_{2n}(h_2+z)}{ch.k_{2n}h_2} \right] e^{-i\sigma t} \tag{3.2.1}$$

where

k_{2n} = the nth mode eigenvalue satisfying Eq. (2.10.2)

h_2 = the water depth in Region II

4/ It should be noted again that the minus subscript of a_{-n} does not indicate negative summation modes. Rather, it denotes that this term is the unknown amplitude coefficient for wave modes within the structure that are oriented in the negative direction.

From Eq. (2.10.4), the total velocity potential solution in Region II is

$$\phi_2 = \sum_{n=1}^{\infty} - g[a_{+n} e^{i\sqrt{A_x/A_z}k_{2n}(x+b)} + a_{-n} e^{-i\sqrt{A_x/A_z}k_{2n}(x-b)}]$$

$$\times [\frac{ch.\, k_{2n}(h_2+z)}{ch.\, k_{2n}h_2}]e^{-i\sigma t} \quad (3.2.2)$$

The complex square root, $\sqrt{A_x/A_z}$, in the exponentials of Eq. (3.2.1) has two roots. In addition, this research has found that if the complex eigenvalue

$$k_{2n} = a + ib$$

where

$$a, b = \text{strictly real numbers}$$

is a solution of Eq. (2.5.2) then

$$-k_{2n} = -a - ib$$

is also a solution, i.e., k_{2n} has a positive and negative solution. Since wave amplification within the structure is physically irrelevant, the roots of $\sqrt{A_x/A_z}$ and k_{2n} must be chosen so that the product

$$\pm i\sqrt{A_x/A_z}k_{2n}(x\pm b)$$

insures wave decay for both exponential terms of Eq. (3.2.1). A method of complying with this requirement is described in Appendix A.

Having obtained an expression for the total velocity potential in Region II, it is now possible to specify the instantaneous pressure within the region. Solving Eq. (2.6.1) for the pressure term, P, where $F(t)$ has been shown to be zero, and substituting Eq. (3.2.2) for the velocity potential yields

$$P_2 = -\rho[\dot{\phi}_2 + gz] \tag{3.2.3}$$

where

P_2 = the total pressure term in Region II

ϕ_{2n} = modal velocity potential in Region II expressed by Eq. (3.2.1)

3.2.2. Region I

In Region I, the total velocity potential is the linear superposition of the incident wave velocity potential and the eigen-series representing the reflected wave potentials, i.e.,

$$\phi_1 = \phi_i + \sum_{n=1}^{\infty} \phi_{rn}$$

where

ϕ_i = the incident wave velocity potential

ϕ_{rn} = nth mode of the reflected wave velocity potential

In accordance with the definition sketch, Fig. 1.1, the incident wave propagates in the positive x-direction and is therefore represented by the 'a_{+n}' term of Eq. (3.1.1). However, only the propagating mode is present $(n = 1)$ and the amplitude, a_i, is a known quantity. Hence the a_{+n} amplitude coefficient of Eq. (3.1.1) is replaced by a_i. The spatial phase of the incident wave is referenced to the seaward interface at $x = -b$ so that

$$\phi_i = -g a_i e^{ik_{11}(x+b)} \left[\frac{\text{ch.} k_{11}(h_1+z)}{\text{ch.} k_{11} h_1} \right] e^{-i\sigma t} \qquad (3.2.5)$$

where

k_{11} = the real eigenvalue satisfying Eq. (3.1.2) in Region I

h_1 = the water depth in Region I

The reflected waveform in Region I is the linear superposition of the propagating waveform reflected from the seaward interface when the incident wave encounters it, the propagating waveforms which are reflected in Regions II and III and transmitted back across the seaward interface, and finally, the evanescent modes $(n \geq 2)$ generated at the interface. Consequently, the reflected wave velocity potential is an infinite eigen-series where the modal components are represented by the 'a_{-n}' term of Eq. (3.1.1). Referencing the spatial phase to $x = -b$ and renaming the amplitude coefficient a_{-n} as a_{rn}, the reflected wave modal velocity potential is found from

Eq. (3.1.1) as

$$\phi_{rn} = -ga_{rn}e^{-ik_{1n}(x+b)}\left[\frac{ch.\,k_{1n}(h_1+z)}{ch.\,k_{1n}h_1}\right]e^{-i\sigma t} \tag{3.2.6}$$

where

k_{1n} = n^{th} modal eigenvalue satisfying Eq. (3.1.2) in Region I

Combining Eqs. (3.2.4, 3.2.5 and 3.2.6) yields the total velocity potential in Region I as

$$\phi_1 = -ge^{-i\sigma t}\left\{ a_i e^{ik_{11}(x+b)}\left[\frac{ch.\,k_{11}(h_1+z)}{ch.\,k_{11}h_1}\right] + \sum_{n=1}^{\infty} a_{rn}e^{-ik_{1n}(x+b)}\left[\frac{ch.\,k_{1n}(h_1+z)}{ch.\,k_{1n}h_1}\right]\right\} \tag{3.2.7}$$

The total instantaneous pressure equation in Region I is found in a manner similar to that in Region II, so that

$$P_1 = -\rho(\dot{\phi}_1+gz) \tag{3.2.8}$$

where

ϕ_1 is given by Eq. (3.2.7)

P_1 = the total pressure term in Region I

3.2.3. Region III

The total velocity potential in Region III is the linear superposition of the eigen-series solutions representing the transmitted waves and the waves reflected from the reflector-absorber, i.e.,

$$\phi_3 = \sum_{n=1}^{\infty} (\phi_{Tn}+\phi_{RAn}) \tag{3.2.9}$$

where

ϕ_{Tn} = the n^{th} mode of the transmitted wave velocity potential

ϕ_{RAn} = the n^{th} mode of the velocity potential due to the reflection of the transmitted waveforms at the reflector-absorber

The transmitted waveform in Region III is the linear superposition of the propagating waveforms transmitted from Region II through the leeward interface, the waveforms reflected from the reflector-absorber and re-reflected at the leeward interface, and finally, the evanescent modes $(n \geq 2)$ generated at the interface. Hence the transmitted wave velocity potential is an infinite eigen-series where the modal components are represented by the 'a_{+n}' term of Eq. (3.1.1). Referencing the spatial phase to the interface at $x = b$ and renaming the amplitude coefficient a_{+n} as a_{Tn}, the modal velocity potential of the transmitted wave is obtained from Eq. (3.1.1) as

$$\phi_{Tn} = -ga_{Tn} e^{ik_{3n}(x-b)} \left[\frac{ch.\, k_{3n}(h_3+z)}{ch.\, k_{3n} h_3} \right] e^{-i\sigma t} \tag{3.2.10}$$

where

k_{3n} = the n^{th} eigenvalue satisfying Eq. (3.1.2) in Region III

h_3 = water depth in Region III

The total transmitted wave potential is therefore

$$\phi_T = \sum_{n=1}^{\infty} \phi_{Tn}$$

and the total transmitted waveform, η_T, is found by substituting the above two equations into Eq. (2.6.2) and evaluating at $z = 0$, such that

$$\eta_T = \sum_{n=1}^{\infty} a_{Tn} e^{ik_{3n}(x-b)} e^{-i\sigma t} \tag{3.2.11}$$

The velocity potential of the wave reflected from the reflector absorber is established by propagating the transmitted waveform in Region III over the distance between the structure and the reflector-absorber, c, (see Fig. 1.1), so that Eq. (3.2.11) is evaluated at $x = c+b$ as

$$\eta_T\Big|_{x=c+b} = \sum_{n=1}^{\infty} a_{Tn} e^{i[k_{3n}(c+b-b)]} e^{-i\sigma t}$$

$$= \sum_{n=1}^{\infty} a_{Tn} e^{i(k_{3n}c)} e^{-i\sigma t}$$

This wave is reflected from the reflector-absorber by an amount C_{RA} (the historically, empirically, or analytically established reflection coefficient for the reflector-absorber) and propagates in the negative x direction back toward the structure. Thus the signs of the x-dependent exponential and the time dependent exponential must be the same while the spatial phase is referenced to $x = b+c$, i.e.,

$$\eta_{RA} = C_{RA}\eta_T\Big|_{x=c+b} e^{-i[k_{3n}(x-(b+c))]}$$

$$= \sum_{n=1}^{\infty} C_{RA} a_{Tn} e^{ik_{3n}c} e^{-i[k_{3n}(x-(b+c))+\sigma t]}$$

$$= \sum_{n=1}^{\infty} C_{RA} a_{Tn} e^{-i[k_{3n}(x-(b+2c))+\sigma t]} \tag{3.2.12}$$

The total reflected velocity potential ϕ_{RA} is found from Eq. (3.1.12) by multiplying by $-g$ and including the depth dependent term

$$\frac{ch.\, k_{3n}(h_3+z)}{ch.\, k_{3n}h_3}$$

such that

$$\phi_{RA} = \sum_{n=1}^{\infty} - gC_{RA}a_{Tn}e^{-ik_{3n}[x-(b+2c)]}\left[\frac{ch.\, k_{3n}(h_3+z)}{ch.\, k_{3n}h_3}\right]e^{-i\sigma t} \qquad (3.2.13)$$

The total velocity potential expression in Region III is obtained from Eqs. (3.2.9, 3.2.10 and 3.2.13) as

$$\phi_3 = \sum_{n=1}^{\infty} - ga_{Tn}[e^{ik_{3n}(x-b)} + C_{RA}e^{-ik_{3n}[x-(b+2c)]}]\left[\frac{ch.\, k_{3n}(h_3+z)}{ch.\, k_{3n}h_3}\right]e^{-i\sigma t} \qquad (3.2.14)$$

The total instantaneous pressure equation for Region III is derived in the same fashion as those of Regions I and II, i.e.,

$$P_3 = -\rho(\phi_3 + gz) \qquad (3.2.15)$$

where

ϕ_3 is given by Eq. (3.2.14)

P_3 = total pressure in Region III

3.3. The Interfacial Boundary Conditions

The velocity potential and dynamic pressure equations have been derived for Regions I, II and III as Eqs. (3.2.2, 3.2.3, 3.2.7, 3.2.8, 3.2.14 and 3.2.15) using the unknown amplitude coefficients a_{+n},

a_{-n}, a_{rn}, a_{Tn}. Truncating the infinite eigen-series in each of the above equations as n goes to some finite value N necessitates the quantification of N values for each of the four unknown amplitude coefficients. Consequently $4 \times N$ boundary conditions are required. Since the solutions in adjacent regions must be continuous at the interfacial boundaries, it is apparent that the appropriate boundary conditions are continuity of pressure and horizontal mass flux at the interfacial planes defined at $x = -b$ and $x = b$. Furthermore, since the fluid is assumed to be incompressible, the requirement of horizontal mass flux continuity at the interfacial planes reduces to continuity of the local horizontal volumetric flow rates. Application of the imposed continuities at N points along each interfacial plane yields sufficient boundary conditions to evaluate the $4 \times N$ unknown amplitude coefficients.

3.3.1. Flow Continuity

Referring to the idealized planar interfaces shown in Fig. 3.1, the interfacial boundary conditions requiring continuity of the horizontal volumetric flow rates at the seaward and leeward interfaces, respectively, may be expressed as

$$u_1 A_1 = u_2 A_2 \qquad \text{for} \qquad -h_2 \leq z \leq 0$$

$$u_1 = 0 \qquad \text{for} \qquad -h_1 \leq z < -h_2$$

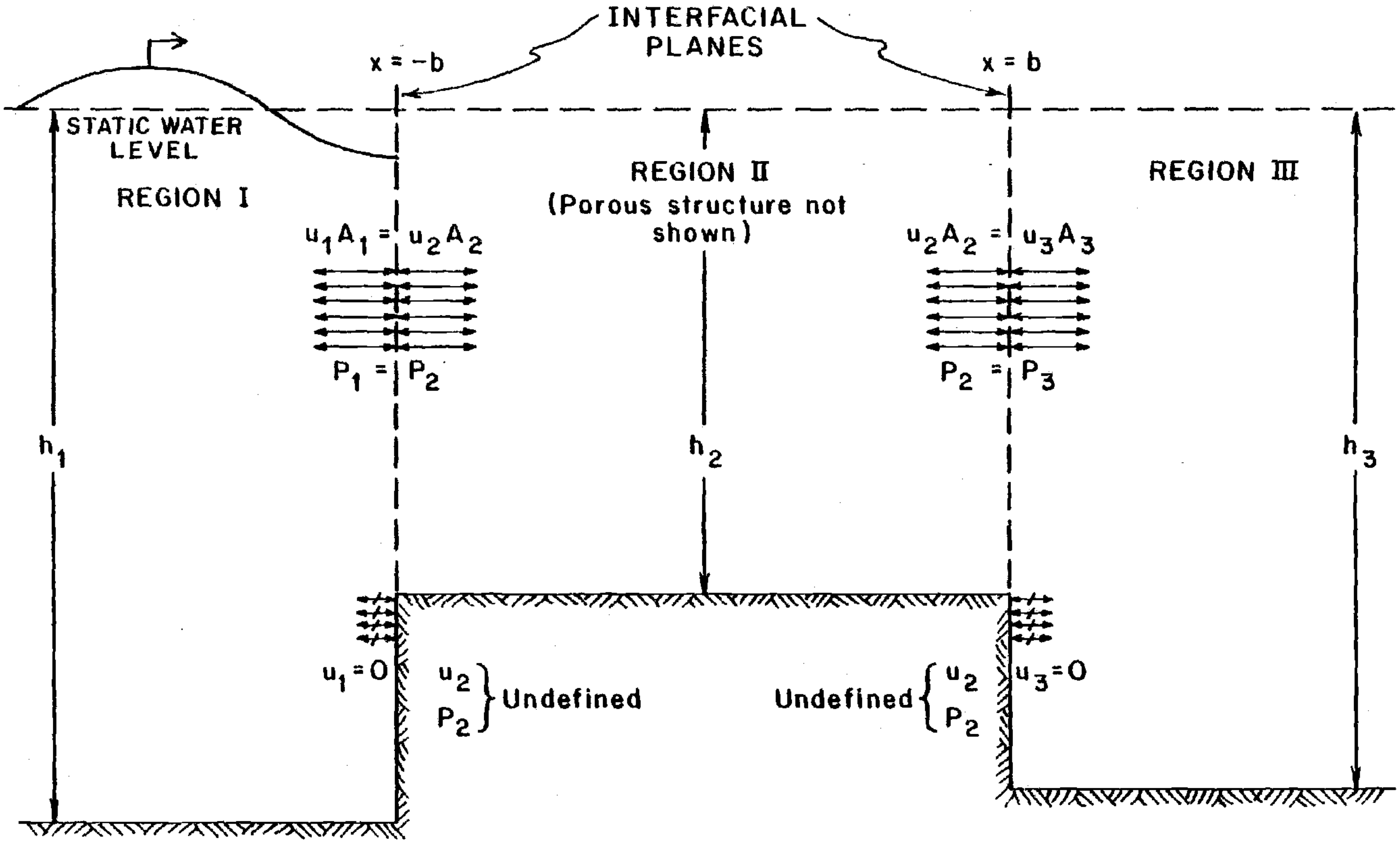

Figure 3. 1. Interfacial boundary conditions and idealized bottom discontinuities.

at $x = -b$, and

$$u_3 A_3 = u_2 A_2 \quad \text{for} \quad -h_2 \leq z \leq 0$$
$$u_3 = 0 \quad \text{for} \quad -h_3 \leq z < -h_2$$

at $x = b$. Or, rearranging

$$u_1 = u_2(A_2/A_1) \quad \text{for} \quad -h_2 \leq z \leq 0$$
$$u_1 = 0 \quad \text{for} \quad -h_1 \leq z < -h_2 \tag{3.3.1}$$

at $x = -b$, and similarly

$$u_3 = u_2(A_2/A_3) \quad \text{for} \quad -h_2 \leq z \leq 0$$
$$u_3 = 0 \quad \text{for} \quad -h_3 \leq z < -h_2 \tag{3.3.2}$$

at $x = b$, where A_1, A_2, A_3 are the cross sectional flow areas along stream tubes in the subscripted regions. Since the horizontal velocity components are functions of the depth, it is important that the vertical dimension of the cross sectional areas be small in order to avoid large variations of the velocity over the area. Thus the cross sectional areas in Region I and III are the products of some small vertical increment, Δz, and some lateral distance Y. The cross sectional areas in Region II are the cross sectional areas in Region I and III less the convergence effects produced by the structural members, ΔA_{solid}, i.e.,

$$A_1, A_3 = Y * \Delta z$$

$$A_2 = (Y * \Delta z) - \Delta A_{solid}$$

Dividing the latter equation by the former yields the area ratios of Eqs. (3.3.1 and 3.3.2) as

$$(A_2/A_1), (A_2/A_3) = 1 - (\Delta A_{solid}/Y * \Delta z) \qquad (3.3.3)$$

Considering the fact that horizontal, diagonal, and vertical structural members may be present at the interface it is apparent that the quantity

$$\Delta A_{solid}/Y * \Delta z$$

may vary considerably in the vertical and lateral directions over the interfaces. To be mathematically rigorous, a numerical algorithm would be required to evaluate this quantity at discrete locations along the interfaces. This cumbersome problem is mitigated by approximating the above quantity as the ratio of the total cross sectional area of the interfacial structural members to the total interfacial area over some lateral distance Y. However, it is felt that a better approximation is achieved using the ratio of the volume of structural members to the total volume since, to personify, the fluid particles 'feel' (in a pressure sense) their environment for some distance about themselves. It is recommended that this approximating ratio be that of the total volume of all structural members to the total volume of the entire structure for a dense homogeneous structure, or that of the volume of the interfacial structural members to an interfacial volume (the longitudinal dimension being the average pile diameter) for more random structures. Thus

$$\frac{\Delta A_{solid}}{Y^* \Delta z} \simeq \frac{V_{solid}}{V_{total}}$$

or, referring to the definitions described in Section 2.3

$$\frac{\Delta A_{solid}}{Y^* \Delta z} \approx \frac{V_{solid}}{V_{total}} = 1 - \epsilon \qquad (3.3.4)$$

where

ϵ = either the total porosity defined in Eq. (2.3.1) or the local porosity at the interface described in the above narrative for random structures

The above approximation constitutes an averaging of the localized flow characteristics and is therefore consistent with the formulation of the linear damping losses for the equations of motion.

Combining Eqs. (3.3.3 and 3.3.4) with the boundary conditions given by Eqs. (3.3.1 and 3.3.2) yields

$$u_1 = \begin{cases} u_2 \epsilon & \text{for} \quad -h_2 \leq z \leq 0 \\ 0 & \text{for} \quad -h_1 \leq z < -h_2 \end{cases}$$

at $x = -b$, and

$$u_3 = \begin{cases} u_2 \epsilon & \text{for} \quad -h_2 \leq z \leq 0 \\ 0 & \text{for} \quad -h_3 \leq z < -h_2 \end{cases}$$

at $x = b$. Now remembering that

$$u = \frac{1}{A_x} \frac{\partial \phi}{\partial x}$$

$$A_x = f_x \sigma - i\sigma S_x$$

and that

$$f_x = 0, \quad S_x = 1.0$$

in Regions I and III, the above boundary conditions may be re-written respectively as

$$-\frac{1}{i\sigma} \frac{\partial \phi_1}{\partial x} = \begin{cases} \dfrac{\epsilon}{A_x} \dfrac{\partial \phi_2}{\partial x} & \text{for} \quad -h_2 \leq z \leq 0 \\ 0 & \text{for} \quad -h_1 \leq z < -h_2 \end{cases} \tag{3.3.5}$$

at $x = -b$ and

$$-\frac{1}{i\sigma}\frac{\partial\phi_3}{\partial x} = \begin{cases} \dfrac{\epsilon}{A_x}\dfrac{\partial\phi_2}{\partial x} & \text{for} \quad -h_2 \le z \le 0 \\ 0 & \text{for} \quad -h_3 \le z \le -h_2 \end{cases} \tag{3.3.6}$$

at $x = b$. Substituting the velocity potential expressions given by Eqs. (3.2.7 and 3.2.2) into Eq. (3.3.5) and performing the indicated differentiations yields

$$\frac{ge^{-i\sigma t}}{\sigma}\left\{a_i k_{11} e^{ik_{11}(x+b)}\left[\frac{\text{ch.}\,k_{11}(h_1+z)}{\text{ch.}\,k_{11}h_1}\right] - \sum_{n=1}^{\infty} a_{rn} k_{1n} e^{-ik_{1n}(x+b)}\left[\frac{\text{ch.}\,k_{1n}(h_1+z)}{\text{ch.}\,k_{1n}h_1}\right]\right\}$$

$$= \begin{cases} -\dfrac{\epsilon}{A_x} ge^{-i\sigma t}\, i\sqrt{A_x/A_z}\displaystyle\sum_{n=1}^{\infty} k_{2n} \\ \times\left[a_{+n} e^{i\sqrt{A_x/A_z}k_{2n}(x+b)} - a_{-n} e^{-i\sqrt{A_x/A_z}k_{2n}(x-b)}\right]\left[\dfrac{\text{ch.}\,k_{2n}(h_2+z)}{\text{ch.}\,k_{2n}h_2}\right] \\ \qquad\qquad \text{for} \quad -h_2 \le z \le 0 \\ 0 \qquad\qquad \text{for} \quad -h_1 \le z < -h_2 \end{cases}$$

at $x = -b$. Now, evaluating the above equation at $x = -b$, cancelling common terms and rearranging yields the horizontal mass flux boundary condition for the interfacial plane at $x = -b$ as

$$a_i k_{11}\left[\frac{ch.\, k_{11}(h_1+z)}{ch.\, k_{11}h_1}\right] - \sum_{n=1}^{\infty} a_{rn} k_{1n}\left[\frac{ch.\, k_{1n}(h_1+z)}{ch.\, k_{1n}h_1}\right]$$

$$= \begin{cases} \beta \sum_{n=1}^{\infty} k_{2n}\left[a_{+n} - a_{-n} e^{i2bk_{2n}\sqrt{A_x/A_z}}\right]\left[\frac{ch.\, k_{2n}(h_2+z)}{ch.\, k_{2n}h_2}\right] & \text{for } -h_2 \leq z \leq 0 \\ 0 & \text{for } -h_1 \leq z < -h_2 \end{cases} \tag{3.3.7}$$

where

$$\beta = \frac{-i\sigma\epsilon\sqrt{A_x/A_z}}{A_x}$$

Similarly, substituting the velocity potential expressions given by Eqs. (3.2.14 and 3.2.2) into Eq. (3.3.6), performing the indicated differentiations, evaluating at $x = b$, and simplifying, yield the horizontal mass flux boundary condition for the interface at $x = b$ as

$$\sum_{n=1}^{\infty} a_{Tn} k_{3n}\left[\frac{ch.\, k_{3n}(h_3+z)}{ch.\, k_{3n}h_3}\right]\left[1 - C_{RA} e^{i2ck_{3n}}\right] \tag{3.3.8}$$

$$= \begin{cases} \zeta \sum_{n=1}^{\infty} k_{2n}\left[\frac{ch.\, k_{2n}(h_2+z)}{ch.\, k_{2n}h_2}\right]\left[a_{+n} e^{i2bk_{2n}\sqrt{A_x/A_z}} - a_{-n}\right] & \text{for } -h_2 \leq z \leq 0 \\ 0 & \text{for } -h_3 \leq z < -h_2 \end{cases}$$

where

$$\zeta^{5/} = \frac{-i\sigma\epsilon\sqrt{A_x/A_z}}{A_x}$$

3.3.2. Pressure Continuity

Referring to Fig. 3.1, the interfacial boundary conditions requiring continuity of pressure at the seaward and leeward interfaces, respectively, are

$$P_1 = P_2 \quad \text{for} \quad -h_2 \leq z \leq 0$$

at $x = -b$, and

$$P_3 = P_2 \quad \text{for} \quad -h_2 \leq z \leq 0$$

at $x = b$.

Substitution of Eqs. (3.2.8 and 3.2.3) into the former boundary condition and Eqs. (3.2.15 and 3.2.8) into the latter yield

$$-\rho(\phi_1+gz) = -\rho(\phi_2+gz) \quad \text{for} \quad -h_2 \leq z \leq 0 \qquad (3.3.9)$$

at $x = -b$, and

5/ The constants ζ and β are equal unless the porosity term, ϵ, is the local interfacial porosity. In that case, these constants will vary in direct proportion to the ratio of the seaward interfacial porosity to that of the leeward interface.

$$-\rho(\varphi_3+gz) = -\rho(\varphi_2+gz) \qquad \text{for} \quad -h_2 \leq z \leq 0 \tag{3.3.10}$$

at $x = b$.

Substituting the velocity potential expressions given by Eqs. (3.2.8 and 3.2.2) into Eq. (3.2.9), evaluating the resulting equation at $x = -b$, and simplifying, yields the continuity of pressure interfacial boundary condition for the interfacial plane at $x = -b$ as

$$a_i\left[\frac{\text{ch.}\,k_{11}(h_1+z)}{\text{ch.}\,k_{11}h_1}\right] + \sum_{n=1}^{\infty} a_{rn}\left[\frac{\text{ch.}\,k_{1n}(h_1+z)}{\text{ch.}\,k_{1n}h_1}\right]$$

$$= \sum_{n=1}^{\infty} \left[a_{+n}+a_{-n}e^{i2bk_{2n}\sqrt{A_x/A_z}}\right]\left[\frac{\text{ch.}\,k_{2n}(h_2+z)}{\text{ch.}\,k_{2n}h_2}\right] \quad \text{for} \quad -h_2 \leq z \leq 0 \tag{3.3.11}$$

Similarly, substitution of the velocity potential expressions given by Eqs. (3.2.14 and 3.2.2) into Eq. (3.2.10), evaluating at $x = b$, and simplifying, yields the continuity of pressure interfacial boundary condition for the interfacial plane at $x = b$ as

$$\sum_{n=1}^{\infty} a_{Tn}\left[1+C_{RA}e^{i2ck_{3n}}\right]\left[\frac{\text{ch.}\,k_{3n}(h_3+z)}{\text{ch.}\,k_{3n}h_3}\right]$$

$$= \sum_{n=1}^{\infty} \left[a_{+n}e^{i2bk_{2n}\sqrt{A_x/A_z}} + a_{-n}\right]\left[\frac{\text{ch.}\,k_{2n}(h_2+z)}{\text{ch.}\,k_{2n}h_2}\right] \quad \text{for} \quad -h_2 \leq z \leq 0 \tag{3.3.12}$$

Equations (3.3.7, 3.3.8, 3.3.11 and 3.3.12) describe a system of four simultaneous equations which specify continuity of mass flux and pressure over the vertical domains of each interface. If each of the infinite summations are truncated at some value N and each equation is applied at N discrete z coordinates on the interface, 4N equations are generated to solve for 4N unknown amplitude coefficients, i.e., N values of each a_{rn}, a_{Tn}, a_{+n}, and a_{-n}. Although the solution for such a system is not particularly arduous in a computational sense, a somewhat simplified and more satisfactory system of 4N equations is obtained by applying the principle of orthogonality over the depth domain, as discussed in the next chapter.

IV. ORTHOGONALIZATION

4.1. The Principle of Orthogonality

The differential equation and the boundary conditions written for the z-variable of the separable velocity potential satisfy the requirements for a second order Sturm-Liouville boundary value problem with a unit weight function (see Wylie, 1975, p. 360). The solutions, $Z_n(z)$, must therefore form an orthogonal system with respect to a unit weight function over the depth interval. It follows, then, that the z-dependent terms of the velocity potential expressions and of the simultaneous system of equations given by Eqs. (3.3.7, 3.3.8, 3.3.11 and 3.3.12) also form an orthogonal system with respect to the unit weight function over the depth interval.

The general property of any orthogonal set of functions, $F_n(\tau)$, is that

$$\int_a^b \psi(\tau)F_m(\tau)F_n(\tau)d\tau = 0$$

where

$\psi(\tau)$ = weight function = unity for the present problem

$F_n(\tau)$ = any function, n, of the orthogonal set of functions

$F_m(\tau)$ = a particular function, m, of the orthogonal set of functions

$a \leq \tau \leq b$ = interval of orthogonality; the boundary conditions at

$\tau = a$ and $\tau = b$ are homogeneous

when $n \neq m$, is applied to the present problem such that

$$\int_{-h}^{0} Z_n(z) Z_m(z) dz = 0 \tag{4.1.1}$$

Employing this property, the depth dependence of the system of simultaneous equations given by Eqs. (3.3.7, 3.3.8, 3.3.11 and 3.3.12) is eliminated and a series of algebraic equations is created.

4.2. Orthogonalization

The horizontal mass flux boundary condition Eqs. (3.3.7 and 3.3.8) are orthogonalized over the outer region depth intervals in order to retain the behavior of the solid portions of the idealized interfaces, i.e., over the intervals $-h_1 \leq z \leq 0$, and $-h_3 \leq z \leq 0$, respectively, as shown in Fig. 3.1.

Beginning with Eq. (3.3.7), both sides of the equation are multiplied by the z-dependent portion of ϕ_1, $\mathrm{ch.}k_{1m}(h_1+z)$, and the integral over the Region I depth interval is taken to yield

$$\frac{a_i k_{11}}{ch.\,k_{11}h_1}\int_{-h_2}^{0} ch.\,k_{11}(h_1+z)ch.\,k_{1m}(h_1+z)dz$$

$$-\sum_{n=1}^{\infty}\frac{a_{rn}k_{1n}}{ch.\,k_{1n}h_1}\int_{-h_2}^{0} ch.\,k_{1n}(h_1+z)ch.\,k_{1m}(h_1+z)dz$$

$$=\beta\sum_{n=1}^{\infty}k_{2n}\frac{[a_{+n}-a_{-n}e^{i2bk_{2n}\sqrt{A_x/A_z}}]}{ch.\,k_{2n}h_2}\int_{-h_2}^{0} ch.\,k_{2n}(h_2+z)ch.\,k_{1m}(h_1+z)dz$$

and

$$\frac{a_i k_{11}}{ch.\,k_{11}h_1}\int_{-h_1}^{-h_2} ch.\,k_{11}(h_1+z)ch.\,k_{1m}(h_1+z)dz$$

$$-\sum_{n=1}^{\infty}\frac{a_{rn}k_{1n}}{ch.\,k_{1n}h_1}\int_{-h_1}^{-h_2} ch.\,k_{1n}(h_1+z)ch.\,k_{1m}(h_1+z)dz=\int_{-h_1}^{-h_2}0dz$$

Adding the above two equations yields

$$\frac{a_i k_{11}}{ch.\,k_{11}h_1}\int_{-h_1}^{0} ch.\,k_{11}(h_1+z)ch.\,k_{1m}(h_1+z)dz$$

$$-\sum_{n=1}^{\infty}\frac{a_{rn}k_{1n}}{ch.\,k_{1n}h_1}\int_{-h_1}^{0} ch.\,k_{1n}(h_1+z)ch.\,k_{1m}(h_1+z)dz\quad=$$

$$= \beta \sum_{n=1}^{\infty} k_{2n} \frac{[a_{+n} - a_{-n} e^{i2bk_{2n}\sqrt{A_x/A_z}}]}{ch.\, k_{2n} h_2} \int_{-h_2}^{0} ch.\, k_{2n}(h_2+z) ch.\, k_{1m}(h_1+z) dz$$

The orthogonality principle described by Eq. (4.1.1) can be applied to both of the integrals on the left hand side (L.H.S.) of the above equation. Consequently, only the $n = m$ terms survive. Equation (4.1.1) may not, in general, be applied to the integral on the right hand side (R.H.S.) since the depth dependent functions from different regions do not form an orthogonal set unless the eigenvalues, k_n, are equal. Thus the above equation is re-written as

$$\frac{a_i k_{11}}{ch.\, k_{11} h_1} \int_{-h_1}^{0} ch.^2 k_{11}(h_1+z) dz - \frac{a_{rn} k_{1m}}{ch.\, k_{1m} h_1} \int_{-h_1}^{0} ch.^2 k_{1m}(h_1+z) dz$$

$$= \beta \sum_{n=1}^{\infty} k_{2n} \frac{[a_{+n} - a_{-n} e^{i2bk_{2n}\sqrt{A_x/A_z}}]}{ch.\, k_{2n} h_2} \int_{-h_2}^{0} ch.\, k_{2n}(h_2+z) ch.\, k_{1m}(h_1+z) dz$$

The indicated integrations are performed in Appendix B and reduce to

$$\frac{\delta_{1m} a_i k_{11}}{ch.\, k_{11} h_1} \left[\frac{sh.\, 2k_{11}(h_1+z)}{4k_{11}} + \frac{(h_1+z)}{2} \right|_{-h_1}^{0}$$

$$- \frac{a_{rm} k_{1m}}{ch.\, k_{1m} h_1} \left[\frac{sh.\, 2k_{1m}(h_1+z)}{4k_{1m}} + \frac{(h_1+z)}{2} \right|_{-h_1}^{0}$$

$$= \beta \sum_{n=1}^{\infty} k_{2n} \frac{[a_{+n} - a_{-n} e^{i2bk_{2n}\sqrt{A_x/A_z}}]}{ch.\, k_{2n} h_2}$$

$$\times \left[\frac{k_{1m} ch.\, k_{2n}(h_2+z) sh.\, k_{1m}(h_1+z) - k_{2n} ch.\, k_{1m}(h_1+z) sh.\, k_{2n}(h_2+z)}{k_{1m}^2 - k_{2n}^2} \right|_{-h_2}^{0}$$

where

$$\delta_{1m} = \text{Kronecker delta} = \begin{Bmatrix} 0 & \text{when} & m \neq 1 \\ 1 & \text{when} & m = 1 \end{Bmatrix}$$

Evaluating the above equation at the indicated limits yields

$$\frac{\delta_{1m} a_i k_{11}}{ch.\, k_{11} h_1} \left[\frac{sh.\, 2k_{11} h_1}{4k_{11}} + \frac{h_1}{2} \right] - \frac{a_{rm} k_{1m}}{ch.\, k_{1m} h_1} \left[\frac{sh.\, 2k_{1m} h_1}{4k_{1m}} + \frac{h_1}{2} \right]$$

$$= \beta \sum_{n=1}^{\infty} k_{2n} \frac{[a_{+n} - a_{-n} e^{i2bk_{2n}\sqrt{A_x/A_z}}]}{ch.\, k_{2n} h_2}$$

$$\times \left[\frac{\left\{ k_{1m} ch.\, (k_{2n} h_2) sh.\, (k_{1m} h_1) - k_{2n} ch.\, (k_{1m} h_1) sh.\, (k_{2n} h_2) - k_{1m} sh.\, k_{1m}(h_1 - h_2) \right\}}{k_{1m}^2 - k_{2n}^2} \right]$$

Finally, each term in the above equation is rendered dimensionless and of the order of unity by division by the incident wave term

$$\frac{a_i k_{11}}{ch.\, k_{11}h_1}\left[\frac{sh.\, 2k_{11}h_1}{4k_{11}}+\frac{h_1}{2}\right] \tag{4.2.1}$$

After rearranging, the orthogonalized horizontal mass flux boundary condition at the seaward interface becomes

$$\begin{aligned}\delta_{1m} &= C_{rm}\,\frac{ch.\, k_{11}h_1}{ch.\, k_{1m}h_1}\left[\frac{sh.(2k_{1m}h_1)+2k_{1m}h_1}{sh.(2k_{11}h_1)+2k_{11}h_1}\right] \\ &+\beta'\sum_{n=1}^{N} k_{2n}\,\frac{[C_{+n}-C_{-n}e^{i2bk_{2n}\sqrt{A_x/A_z}}]}{ch.\, k_{2n}h_2} \\ &\times\left[\frac{\left\{\begin{array}{l}k_{1m}ch.(k_{2n}h_2)sh.(k_{1m}h_1) \\ -k_{2n}ch.(k_{1m}h_1)sh.(k_{2n}h_2)-k_{1m}sh.\, k_{1m}(h_1-h_2)\end{array}\right\}}{k_{1m}^2-k_{2n}^2}\right]\end{aligned} \tag{4.2.2}$$

where

$C_{rm} = \frac{a_{rm}}{a_i}$ = complex reflection coefficient corresponding to the m^{th} mode of the reflected waveforms in Region I. The reflection coefficient defined in Chapter I for the structure as a whole is the modulus of the first, i.e., propagating, mode, $|C_{r1}|$

$C_{+n} = \frac{a_{+n}}{a_i}$ = dimensionless amplitude coefficient corresponding to the n^{th} mode of the Region II waveforms referenced to the seaward interface

$C_{-n} = \frac{a_{-n}}{a_i}$ = dimensionless amplitude coefficient corresponding to the n^{th} mode of the Region II waveforms referenced to the leeward interface

$$\beta' = \frac{4\beta \text{ch.} k_{11}h_1}{\text{sh.}(2k_{11}h_1) + 2k_{11}h_1}$$

$$\beta = \frac{-i\sigma\epsilon\sqrt{A_x/A_z}}{A_x}$$

N = the value at which the infinite eigen-series is truncated. Values of N between five and ten have shown sufficient accuracy for the present study

It is noteworthy that Eq (4.2.2) may be solved N times since m is some particular value in the range $1 \leq m \leq N$. Thus, by using N different values of m, N different equations are obtained.

The orthogonalization process for the horizontal mass flux boundary condition at the leeward interface, Eq. (3.3.8) is accomplished in the same manner as that presented for the seaward interface. That is, both sides of Eq. (3.3.8) are multiplied by $\text{ch.} k_{3m}(h_3+z)$ and integrated over the Region III depth interval so that

$$\sum_{n=1}^{\infty} \frac{a_{Tn}k_{3n}}{ch.\,k_{3n}h_3}\,[1-C_{RA}e^{i2ck_{3n}}]\int_{-h_3}^{-h_2} ch.\,k_{3n}(h_3+z)ch.\,k_{3m}(h_3+z)dz$$

$$= \int_{-h_3}^{-h_2} 0\,dz$$

and

$$\sum_{n=1}^{\infty} \frac{a_{Tn}k_{3n}}{ch.\,k_{3n}h_3}\,[1-C_{ra}e^{i2ck_{3n}}]\int_{-h_2}^{0} ch.\,k_{3n}(h_3+z)ch.\,k_{3m}(h_3+z)dz$$

$$= \zeta\sum_{n=1}^{\infty} \frac{k_{2n}}{ch.\,k_{2n}h_2}\,[a_{+n}e^{i2bk_{2n}\sqrt{A_x/A_z}} - a_{-n}]$$

$$\times \int_{-h_2}^{0} ch.\,k_{2n}(h_2+z)ch.\,k_{3m}(h_3+z)dz$$

Adding the above two equations yields

$$\sum_{n=1}^{\infty} \frac{a_{Tn}k_{3n}}{ch.\,k_{3n}h_3}\,[1-C_{RA}e^{i2ck_{3n}}]\int_{-h_3}^{0} ch.\,k_{3n}(h_3+z)ch.\,k_{3m}(h_3+z)dz$$

$$= \zeta\sum_{n=1}^{\infty} \frac{k_{2n}}{ch.\,k_{2n}h_2}\,[a_{+n}e^{i2bk_{2n}\sqrt{A_x/A_z}} - a_{-n}]$$

$$\times \int_{-h_2}^{0} ch.\,k_{2n}(h_2+z)ch.\,k_{3m}(h_3+z)dz$$

The orthogonality property set forth by Eq. (4.1.1) is applicable for the integral on the L.H.S. of the above equation. Since the integral is zero unless $n = m$, the summation is dropped. The integrand on the R.H.S. is not the product of two orthogonal functions and therefore Eq. (4.1.1) is not applicable. Thus, the above equation is re-written as

$$\frac{a_{Tm} k_{3m}}{ch.k_{3m}h_3}\left[1 - C_{RA} e^{i2ck_{3m}}\right] \int_{-h_3}^{0} ch.^2 k_{3m}(h_3+z)dz$$

$$= \zeta \sum_{n=1}^{\infty} \frac{k_{2n}}{ch.k_{2n}h_2}\left[a_{+n} e^{i2bk_{2n}\sqrt{A_x/A_z}} - a_{-n}\right]$$

$$\times \int_{-h_2}^{0} ch.k_{2n}(h_2+z)ch.k_{3m}(h_3+z)dz$$

The indicated integrations are performed in Appendix B. After evaluating the integrals at the specified limits, dividing both sides of the resulting equation by Eq. (4.2.1), truncating the infinite eigen-series at some value, N, and rearranging, the orthogonalized horizontal mass flux boundary condition at the leeward interface is obtained as

$$0 = C_{Tm} \frac{ch.\, k_{11}h_1}{ch.\, k_{3m}h_3} [1 - C_{RA} e^{i2ck_{3m}}] \left[\frac{sh.(2k_{3m}h_3) + 2k_{3m}h_3}{sh.(2k_{11}h_1) + 2k_{11}h_1} \right]$$

$$- \zeta' \sum_{n=1}^{N} \frac{k_{2n}}{ch.\, k_{2n}h_2} [C_{+n} e^{i2bk_{2n}\sqrt{A_x/A_z}} - C_{-n}]$$

$$\times \left[\frac{\begin{Bmatrix} k_{3m} ch.(k_{2n}h_2) sh.(k_{3m}h_3) \\ - k_{2n} ch.(k_{3m}h_3) sh.(k_{2n}h_2) - k_{3m} sh.\, k_{3m}(h_3 - h_2) \end{Bmatrix}}{k_{3m}^2 - k_{2n}^2} \right] \quad (4.2.3)$$

where

$C_{Tm} = \frac{a_{Tm}}{a_i}$ = complex transmission coefficient corresponding to the m^{th} mode of the transmitted waveforms in Region III. The transmission coefficient defined in Chapter I for the structure as a whole is the modulus of the first, i.e., propagating, mode $|C_{T1}|$

$$\zeta' = \frac{4\zeta ch.\, k_{11}h_1}{sh.(2k_{11}h_1) + 2k_{11}h_1}$$

$$\zeta = \frac{-i\sigma\epsilon^{6/}\sqrt{A_x/A_z}}{A_x}$$

6/ Again, it is important to note that β and ζ, and hence β' and ζ', are not necessarily equal since the porosity term, ϵ, may be an interfacial porosity for non-homogeneous structures. In such a case, the relationship between β and ζ, and β' and ζ', is

Note that Eq. (4.2.3) may also be written N different times by allowing m to take on N different values.

The orthogonalization of the pressure continuity boundary condition equations, Eqs. (3.3.11 and 3.3.12), is accomplished in a manner similar to that described for the horizontal mass flux equations. However, examination of Fig. 3.1 reveals that the pressure matching condition is inappropriate below Region II over the range $-h_1 \leq z < -h_2$. Consequently, the orthogonalization process must be confined to the Region II depth interval and, therefore, is conducted with respect to the Region II depth dependent functions.

Proceeding as before, both sides of Eq. (3.3.11) are multiplied by $\mathrm{ch.}\, k_{2m}(h_2+z)$ and the integral over the Region II depth interval is taken to yield

$$\frac{a_i}{\mathrm{ch.}\, k_{11}h_1}\int_{-h_2}^{0}\mathrm{ch.}\, k_{11}(h_1+z)\,\mathrm{ch.}\, k_{2m}(h_2+z)dz$$

$$+\sum_{n=1}^{\infty}\frac{a_{rn}}{\mathrm{ch.}\, k_{1n}h_1}\int_{-h_2}^{0}\mathrm{ch.}\, k_{1n}(h_1+z)\,\mathrm{ch.}\, k_{2m}(h_2+z)dz$$

$$=\sum_{n=1}^{\infty}\frac{[a_{+n}+a_{-n}e^{i2bk_{2n}\sqrt{A_x/A_z}}]}{\mathrm{ch.}\, k_{2n}h_2}\int_{-h_2}^{0}\mathrm{ch.}\, k_{2n}(h_2+z)\,\mathrm{ch.}\, k_{2m}(h_2+z)dz$$

determined by the relationship of the local interfacial porosities at the seaward and leeward interfaces.

The orthogonality property given by Eq. (4.1.1) is applicable only for the integral on the R.H.S. of the above equation. Since this property requires the integral of the cross products $(n \neq m)$ to be zero, the summation is dropped on the R.H.S. and the integrand becomes the square of the 'm' term. As before, the eigenvalues, k_{mn}, will not be equal for adjacent regions and hence the depth dependent terms from adjacent regions do not form an orthogonal set. Consequently, Eq. (4.1.1) may not be applied on the R.H.S. of the above equation. Employing these facts, the above equation is re-written as

$$\frac{a_i}{ch.k_{11}h_1}\int_{-h_2}^{0} ch.k_{11}(h_1+z)ch.k_{2m}(h_2+z)dz$$

$$+\sum_{n=1}^{\infty}\frac{a_{rn}}{ch.k_{1n}h_1}\int_{-h_2}^{0} ch.k_{1n}(h_1+z)ch.k_{2m}(h_2+z)dz$$

$$=\frac{[a_{+m}+a_{-m}e^{i2bk_{2m}\sqrt{A_x/A_z}}]}{ch.k_{2m}h_2}\int_{-h_2}^{0} ch.^2k_{2m}(h_2+z)dz$$

The indicated integrations are performed in Appendix B. Evaluating the integrals at the specified limits yields

$$\frac{a_i}{ch.\,k_{11}h_1}\left[\frac{\left\{k_{2m}ch.\,(k_{11}h_1)sh.\,(k_{2m}h_1) - k_{11}ch.\,(k_{2m}h_2)sh.\,(k_{11}h_1)+k_{11}sh.\,k_{11}(h_1-h_2)\right\}}{k_{2m}^2-k_{11}^2}\right]$$

$$+\sum_{n=1}^{\infty}\frac{a_{rn}}{ch.\,k_{1n}h_1}\left[\frac{\left\{k_{2m}ch.\,(k_{1n}h_1)sh.\,(k_{2m}h_2) -k_{1n}ch.\,(k_{2m}h_2)sh.\,(k_{1n}h_1)+k_{1n}sh.\,k_{1n}(h_1-h_2)\right\}}{k_{2m}^2-k_{1n}^2}\right].$$

$$=\left[\frac{a_{+m}+a_{-m}e^{i2bk_{2m}\sqrt{A_x/A_z}}}{ch.\,k_{2m}h_2}\right]\left[\frac{sh.(2k_{2m}h_2)+2k_{2m}h_2}{4k_{2m}}\right]$$

Dividing both sides of the above equation by the incident wave term

$$\frac{a_i}{ch.\,k_{11}h_1}\left[\frac{\left\{k_{2m}ch.\,(k_{11}h_1)sh.\,(k_{2m}h_2) -k_{11}ch.\,(k_{2m}h_2)sh.\,(k_{11}h_1)+k_{11}sh.\,k_{11}(h_1-h_2)\right\}}{k_{2m}^2-k_{11}^2}\right] \tag{4.2.4}$$

truncating the infinite eigen-series at some value N and rearranging yields the orthogonalized pressure continuity boundary condition at the seaward interface as

$$1 = \frac{C_{+m} + C_{-m} e^{i2bk_{2m}\sqrt{A_x/A_z}}}{4k_{2m}\,\mathrm{ch.}\,k_{2m}h_2}$$

$$\times \left[\frac{(\mathrm{sh.}(2k_{2m}h_2) + 2k_{2m}h_2)(k_{2m}^2 - k_{11}^2)(\mathrm{ch.}\,k_{11}h_1)}{\left\{ k_{2m}\,\mathrm{ch.}\,(k_{11}h_1)\,\mathrm{sh.}\,(k_{2m}h_2) - k_{11}\,\mathrm{ch.}\,(k_{2m}h_2)\,\mathrm{sh.}\,(k_{11}h_1) + k_{11}\,\mathrm{sh.}\,k_{11}(h_1 - h_2) \right\}} \right]$$

$$- \sum_{n=1}^{N} C_{rn} \frac{(k_{2m}^2 - k_{11}^2)(\mathrm{ch.}\,k_{11}h_1)}{(k_{2m}^2 - k_{1n}^2)(\mathrm{ch.}\,k_{1n}h_1)}$$

$$\times \left[\frac{\left\{ k_{2m}\,\mathrm{ch.}\,(k_{1n}h_1)\,\mathrm{sh.}\,(k_{2m}h_2) - k_{1n}\,\mathrm{ch.}\,(k_{2m}h_2)\,\mathrm{sh.}\,(k_{1n}h_1) + k_{1n}\,\mathrm{sh.}\,k_{1n}(h_1 - h_2) \right\}}{\left\{ k_{2m}\,\mathrm{ch.}\,(k_{11}h_1)\,\mathrm{sh.}\,(k_{2m}h_2) - k_{11}\,\mathrm{ch.}\,(k_{2m}h_2)\,\mathrm{sh.}\,(k_{11}h_1) + k_{11}\,\mathrm{sh.}\,k_{11}(h_1 - h_2) \right\}} \right] \quad (4.2.5)$$

Again, Eq. (4.2.5) may be written and solved N times since m may assume any value within the range $1 \leq m \leq N$.

Following a similar procedure, Eq. (3.3.12) is orthogonalized by first multiplying both sides of the equation by $\mathrm{ch.}\,k_{2m}(h_2+z)$ and taking the integral over the Region II depth interval so that

$$\sum_{n=1}^{\infty} a_{Tn} \frac{[1+C_{RA} e^{i2ck_{3n}}]}{ch.\,k_{3n}h_3} \int_{-h_2}^{0} ch.\,k_{3n}(h_3+z)\,ch.\,k_{2m}(h_2+z)dz$$

$$= \sum_{n=1}^{\infty} \frac{[a_{+n} e^{i2bk_{2n}\sqrt{A_x/A_z}} + a_{-n}]}{ch.\,k_{2n}h_2} \int_{-h_2}^{0} ch.\,k_{2n}(h_2+z)\,ch.\,k_{2m}(h_2+z)dz$$

As before, the orthogonality property described by Eq. (4.1.1) is applicable for the integral on the R.H.S. but not the integral on the left. Hence the above equation is re-written as

$$\sum_{n=1}^{\infty} a_{Tn} \frac{[1+C_{RA} e^{i2ck_{3n}}]}{ch.\,k_{3n}h_3} \int_{-h_2}^{0} ch.\,k_{3n}(h_3+z)\,ch.\,k_{2m}(h_2+z)dz$$

$$= \frac{[a_{+m} e^{i2bk_{2m}\sqrt{A_x/A_z}} + a_{-m}]}{ch.\,k_{2m}h_2} \int_{-h_2}^{0} ch.^2 k_{2m}(h_2+z)dz$$

The indicated integrations are performed in Appendix B. After evaluating the integrals at the specified limits, dividing both sides of the resulting equation by Eq. (4.2.4), truncating the infinite series at some value N, and rearranging, the orthogonalized pressure continuity boundary condition at the leeward interface is obtained as

$$0 = \sum_{n=1}^{N} C_{Tn} \left[\frac{(1+C_{RA} e^{i2ck_{3n}})(ch.\, k_{11}h_1)(k_{2m}^2 - k_{11}^2)}{(ch.\, k_{3n}h_3)(k_{2m}^2 - k_{3n}^2)} \right]$$

$$\times \left[\frac{\left\{ \begin{array}{l} k_{2m} ch.\,(k_{3n}h_3) sh.\,(k_{2m}h_2) \\ -k_{3n} ch.\,(k_{2m}h_2) sh.\,(k_{3n}h_3) + k_{3n} sh.\, k_{3n}(h_3 - h_2) \end{array} \right\}}{\left\{ \begin{array}{l} k_{2m} ch.\,(k_{11}h_1) sh.\,(k_{2m}h_2) - k_{11} ch.\,(k_{2m}h_2) sh.\,(k_{11}h_1) \\ +k_{11} sh.\, k_{11}(h_1 - h_2) \end{array} \right\}} \right]$$

$$- \left[\frac{C_{+m} e^{i2bk_{2m}\sqrt{A_x/A_z}} + C_{-m}}{4k_{2m} ch.\, k_{2m}h_2} \right]$$

$$\times \left[\frac{(ch.\, k_{11}h_1)(k_{2m}^2 - k_{11}^2)(sh.(2k_{2m}h_2) + 2k_{2m}h_2)}{\left\{ \begin{array}{l} k_{2m} ch.\,(k_{11}h_1) sh.\,(k_{2m}h_2) - k_{11} ch.\,(k_{2m}h_2) sh.\,(k_{11}h_1) \\ +k_{11} sh.\, k_{11}(h_1 - h_2) \end{array} \right\}} \right] \quad (4.2.6)$$

Equation (4.2.6) may be written N times similar to Eqs. (4.2.2, 4.2.3 and 4.2.5). Thus, these four equations describe a system of $4N$ simultaneous equations which may be easily solved by a high speed digital computer to yield the $4N$ complex coefficients C_{rn}, C_{Tn}, C_{+n}, C_{-n}. The reflection and transmission coefficients defined for the structure in Chapter I are obtained as the modulus values of the first, or propagating, modes of the complex values C_{rn} and C_{Tn}, i.e.,

$$C_r = |C_{r1}|$$

and

$$C_T = |C_{T1}|$$

In addition, the ratio of the amplitude of the superposition of all the reflected wave components (propagating and evanescent) at the seaward interface to the incident wave amplitude is given by

$$\left| \sum_{n=1}^{N} C_{rn} \right|$$

while that for the superposition of all of the transmitted wave components at the leeward interface is given by

$$\left| \sum_{n=1}^{N} C_{Tn} \right|$$

V. LOSS COEFFICIENTS

5.1. Lorentz' Condition of Equivalent Work

Equations (2.3.5, 2.3.6, 2.3.8 and 2.3.9) define linearized viscous damping relationships in terms of the dimensionless damping coefficients f_{xz}, f_{xy}, f_{zy} and f_{zx} respectively. Strict equality between the linear and non-linear forms of the viscous damping relationships is not possible, and yet, the linearized form is required in order to facilitate an analytical solution. Hence, some error is introduced into the analytical solution. It is hypothesized that this error will be minimized if the dimensionless damping coefficients are quantified using a Lorentz equivalent work scheme.

The equivalent work condition, commonly attributed to H. A. Lorentz (1926), requires that fluid energy dissipation accounted for by the linear damping relationship over the entire structure during one wave period be exactly equal to that quantity dissipated by non-linear viscous damping. Energy is a quantity which pertains strictly to the real world, thus energy dissipation is attributed to the real portion of the complex velocities only. It is therefore appropriate to use the real velocities, u_R and w_R, to evaluate the dimensionless damping coefficients by means of Lorentz' condition of equivalent work.

5.1.1. Quantification of f_{xz}

The non-linear and linear viscous damping forces exerted by a differential element of a vertical pile on a differential mass of fluid are given by Eq. (2.3.5) as

$$\frac{dF_f}{dm_f} = \frac{-C_D u|u| D dz}{2dV_f} \equiv -f_{xz}\sigma u \qquad (2.3.5)$$

where

$\equiv$ represents equality in the equivalent work sense

Anticipating the Lorentz equivalent work scheme, Eq. (2.3.5) is re-written using the real portion of the complex velocity such that

$$\frac{-C_D u_R |u_R| D dz}{2dV_f} \equiv -f_{xz}\sigma u_R \qquad (5.1.1)$$

The steady flow drag coefficient is known to be a function of the Reynolds number, $\mathbb{R}$, for low values of the Reynolds number and to approximate a constant for higher values. Sollitt and Cross (1972) and Kondo (1972) have found the following drag coefficient relationship to be appropriate

$$C_D = \frac{A}{\mathbb{R}} + B$$ [7/]

[7/] The constants A and B and the general behavior of the drag coefficient are discussed in detail in the next section.

where

A, B = constants

$\mathbb{R}$ = Reynolds number = $|u_R| D/\nu$; $|w_R| D/\nu$

u_R, w_R = the real part of the local instantaneous water particle velocity

D = pile diameter or representative cross sectional dimension

ν = kinematic viscosity

Substituting this relationship for the drag coefficient, C_D, in Eq. (5.1.1) yields

$$-\frac{A\nu}{|u_R| D} \frac{u_R |u_R| D dz}{2dV_f} - \frac{B u_R |u_R| D dz}{2dV_f} \equiv -f_{xz} \sigma u_R$$

or

$$-\frac{A\nu u_R dz}{2dV_f} - \frac{B u_R |u_R| D dz}{2dV_f} = -f_{xz} \sigma u_R$$

Now multiplying both sides of the above equation by the water particle velocity, u_R, to obtain the power dissipated per fluid mass and then multiplying by the fluid density, ρ, yields the power dissipated per unit fluid volume as

$$-\frac{\rho A \nu u_R^2 dz}{2dV_f} - \frac{\rho B |u_R^3| D dz}{2dV_f} \equiv -\rho f_{xz} \sigma u_R^2$$

Integrating the above expression over a full wave period and over the volume of fluid within the structure yields the energy dissipated within the structure during one wave period. Employing Lorentz' condition of equivalent work requires that this energy dissipation be equivalent for the non-linear L.H.S. and the linear R.H.S. of the above equation, i.e.,

$$\int_{t_0}^{t_0+T} dt \int_0^{V_f} \left[- \frac{\rho A \nu u_R^2 dz}{2dV_f} - \frac{\rho B |u_R^3| Ddz}{2dV_f} \right] dV_f = \int_{t_0}^{t_0+T} dt \int_0^{V_f} -\rho f_{xz} \sigma u_R^2 dV_f \tag{5.1.2}$$

where

V_f = volume of fluid within the structure. For a structural configuration that repeats itself over some regular interval, Y, in the lateral, or y-direction, it is recommended that only that fluid that lies within the ranges, $0 \leq y \leq Y$, $-b \leq x \leq b$, $-h_2 \leq z \leq 0$ be considered. This recommendation is justified by the two dimensionality of the problem and by the reduction of computational requirements which will become apparent shortly.

The L.H.S. of the above equation represents the fluid energy dissipated by the local reciprocal drag force applied by a differential element of a vertical member on the local fluid element. Thus, the integral over the fluid volume is equivalent to the summation of the bracketed quantity at each vertical pile location over the depth interval $-h_2 \leq z \leq 0$, i.e., the summation of the depth integrals at each vertical pile location within the structure. The R.H.S. of the above equation represents the fluid energy dissipated by the linearized, spatially uniform drag force per unit fluid mass. The spatial uniformity implies that

$$V_f = \epsilon V_T$$

$$dV_f = \epsilon dV_T = \epsilon\, dxdydz$$

and that

$$\int_0^{V_f} dV_f = \int_0^{V_T} \epsilon\, dV_T = \epsilon \int_0^{Y} dy \int_{-b}^{b} dx \int_{-h_2}^{0} dz .$$

Employing all of the above conditions allows Eq. (5.1.2) to be re-written as

$$\int_{t_0}^{t_0+T} dt \int_{-h_2}^{0} \sum_{j=1}^{N_z} -\rho\left[\frac{A\nu u_R^2 + B|u_R^3|D}{2}\right]_j dz$$

$$= \epsilon \int_{t_0}^{t_0+T} dt \int_0^{Y} dy \int_{-b}^{b} dx \int_{-h_2}^{0} -\rho f_{xz} \sigma u_R^2 dz$$

where

N_z = number of vertical piles within the structural volume defined by the ranges $-b \leq x \leq b$, $0 \leq y \leq Y$, $-h_2 \leq z \leq 0$

Requiring that the damping coefficient f_{xz} be constant in space and time, it is evaluated from the above equation as

$$f_{xz} = \frac{\int_{t_0}^{t_0+T} dt \sum_{j=1}^{N_z} \int_{-h_2}^{0} [A\nu u_R^2 + B|u_R^3|D]_j dz}{2\epsilon\sigma Y \int_{t_0}^{t_0+T} dt \int_{-b}^{b} dx \int_{-h_2}^{0} u_R^2 dz} \tag{5.1.3}$$

where the integration with respect to y on the R.H.S. is equivalent to multiplication by Y for the two dimensional problem.

The temporal integrations in Eq. (5.1.3) are performed using the method and notation employed by Sollitt and Cross (1972) as follows:

Let the complex horizontal water particle velocity u be expressed as

$$u = (U_R + iU_I)e^{-i\sigma t}$$

where

U_R, U_I = real spatial functions

or

$$u = (U_R + iU_I)(\cos \sigma t - i \sin \sigma t)$$

Therefore

$$u_R = U_R \cos \sigma t + U_I \sin \sigma t \tag{5.1.4}$$

Employing the definition

$$\frac{U_I}{U_R} = \cot \theta_1 = \frac{\cos \theta_1}{\sin \theta_1}$$

Eq. (5.1.4) is re-written as

$$u_R = \frac{u_R}{\sin \theta_1} [\sin \theta_1 \cos \sigma t + \cos \theta_1 \sin \sigma t]$$

or

$$u_R = \frac{u_R}{\sin \theta_1} \sin(\sigma t + \theta_1)$$

Now, constructing the phase triangle

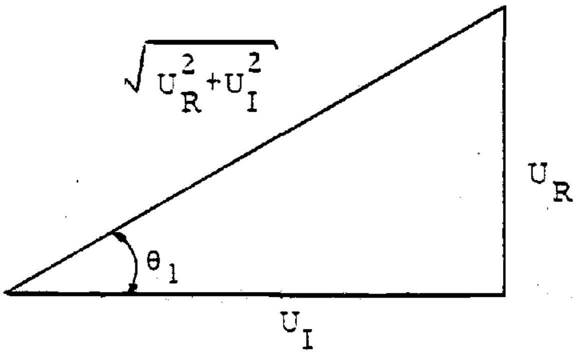

reveals that

$$\frac{U_R}{\sin \theta_1} = \frac{U_R}{U_R/\sqrt{U_R^2+U_I^2}} = \sqrt{U_R^2+U_I^2}$$

Consequently

$$u_R = \sqrt{U_R^2+U_I^2}\,\sin(\sigma t+\theta_1) \tag{5.1.5}$$

Now, employing the transformations

$$\theta = \sigma t + \theta_1$$

$$d\theta = \sigma dt$$

or

$$d\theta/\sigma = dt$$

and noting that when

$$\left\{\begin{array}{ll} t = t_0, & \theta = \sigma t_0 + \theta_1 \\ t = t_0 + T, & \theta = \sigma t_0 + 2\pi + \theta_1 \end{array}\right\}$$

Eq. (5.1.5). is re-written as

$$u_R = \sqrt{U_R^2+U_I^2}\,\sin\theta$$

and, by substitution, Eq. (5.1.3) becomes

$$f_{xz} = \frac{\sum_{j=1}^{N_x} A\nu \int_{-h_2}^{0} (U_R^2+U_I^2)_j dz \int_{\sigma t_0+\theta_1}^{\sigma t_0+2\pi+\theta_1} \sin^2\theta \frac{d\theta}{\sigma} + DB \int_{-h_2}^{0} (U_R^2+U_I^2)_j^{3/2} dz \int_{\sigma t_0+\theta_1}^{\sigma t_0+2\pi+\theta_1} |\sin^3\theta| \frac{d\theta}{\sigma}}{2Y\epsilon\sigma \int_{-b}^{b} dx \int_{-h_2}^{0} (U_R^2+U_I^2) \int_{\sigma t_0+\theta_1}^{\sigma t_0+2\pi+\theta_1} \sin^2\theta \frac{d\theta}{\sigma}} \tag{5.1.6}$$

Remembering that the temporal integration was necessitated by the requirement that the energy dissipated during a full wave period be equivalent for the non-linear and linearized damping equations allows one to specify the lower limit, i.e., the beginning of the wave period time interval, at any convenient time, t_0, as long as the upper limit is t_0 plus one wave period. In evaluating the integrals with respect to θ in Eq. (5.1.6) it is convenient to let

$$t_0 = -\frac{\theta_1}{\sigma}$$

Furthermore, to evaluate the integral of the absolute value of $\sin^3\theta$ it is necessary to separate the integral into two integrals with the appropriate limits and signs to insure positive values of the function, i.e.,

$$\int_0^{2\pi} |\sin^3\theta|\, d\theta = \int_0^{\pi} \sin^3\theta d\theta - \int_{\pi}^{2\pi} \sin^3\theta d\theta$$

Substitution of $t_0 = -\theta/\sigma$ into the integration limits of Eq. (5.1.6) and rearranging the integral of the absolute value of $\sin^3\theta$ as above yields

$$f_{xz} = \left[\frac{\frac{1}{\sigma}\sum_{j=1}^{N_z}\left\{ A\nu \int_{-h_2}^{0} (U_R^2+U_I^2)_j dz \int_0^{2\pi} \sin^2\theta d\theta + DB \int_{-h_2}^{0} (U_R^2+U_I^2)_j^{3/2} dz \left(\int_0^{\pi} \sin^3\theta d\theta - \int_{\pi}^{2\pi} \sin^3\theta d\theta \right) \right\}}{2Y\epsilon \int_{-b}^{b} dx \int_{-h_2}^{0} (U_R^2+U_I^2) dz \int_{\pi}^{2\pi} \sin^2\theta d\theta} \right]$$

Performing the integrations yields

$$f_{xz} = \frac{\sum_{j=1}^{N_z} \left\{ A\nu \frac{T}{2} \int_{-h_2}^{0} (U_R^2+U_I^2)_j dz + DB\left(\frac{4T}{3\pi}\right) \int_{-h_2}^{0} (U_R^2+U_I^2)_j^{3/2} dz \right\}}{2\pi Y\epsilon \int_{-b}^{b} dx \int_{-h_2}^{0} (U_R^2+U_I^2) dz} \qquad (5.1.7)$$

The depth integrals in the numerator of Eq. (5.1.7) are performed numerically at each vertical pile location. The spatial integrations in the denominator, however, may be performed analytically by again employing the method developed by Sollitt and Cross (1972) and by utilizing the following complex algebraic identities

$$(Q_1 \pm Q_2)^* = Q_1^* \pm Q_2^*$$

$$(Q_1 x Q_2)^* = Q_1^* x Q_2^*$$

$$(Q_1 / Q_2)^* = Q_1^* / Q_2^*$$

where

Q_1, Q_2 = complex functions

$*$ = denotes the complex conjugate of the complex function

Now, remembering that the horizontal velocity component may be expressed as

$$u = (U_R + iU_I) e^{-i\sigma t}$$

define

$$U = u / e^{-i\sigma t} = U_R + iU_I$$

so that

$$UU^* = (U_R + iU_I)(U_R - iU_I)$$

or

$$UU^* = U_R^2 + U_I^2$$

Substituting the above equation into the denominator of Eq. (5.1.7) yields the denominator as

$$2\pi Y \epsilon \int_{-b}^{b} dx \int_{-h_2}^{0} UU^{*} dz \tag{5.1.8}$$

where

$$U = u/e^{-i\sigma t} = \frac{1}{A_x} \frac{\partial}{\partial x}\left[\sum_{n=1}^{\infty} \phi_{2n}\right] \Big/ e^{-i\sigma t}$$

or

$$U = \frac{ig}{A_x} \sqrt{A_x / A_z} \sum_{n=1}^{\infty} k_{2n}[a_{+n} e^{ik_{2n}\sqrt{A_x/A_z}(x+b)} - a_{-n} e^{-ik_{2n}\sqrt{A_x/A_z}(x-b)}]$$

$$\times \left[\frac{ch.\, k_{2n}(h_2+z)}{ch.\, k_{2n}h_2}\right] \tag{5.1.9}$$

and (from the complex algebraic identities) where

$$U^{*} = \frac{-ig}{A_x^{*}} \sqrt{A_x^{*}/A_z^{*}} \sum_{m=1}^{\infty} k_{2m}^{*}[a_{+m}^{*} e^{-ik_{2m}^{*}\sqrt{A_x^{*}/A_z^{*}}(x+b)} - a_{-m}^{*} e^{ik_{2m}^{*}\sqrt{A_x^{*}/A_z^{*}}(x-b)}]$$

$$\times \left[\frac{ch.\, k_{2m}^{*}(h_2+z)}{ch.\, k_{2m}^{*}h_2}\right] \tag{5.1.10}$$

Combining Eqs. (5.1.8, 5.1.9 and 5.1.10) yields the denominator of Eq. (5.1.7) as

$$\frac{2\pi\gamma\epsilon g^2\sqrt{A_x A_x^*/A_z A_z^*}}{A_x A_x^*}$$

$$\times \sum_{m=1}^{\infty}\left[\sum_{n=1}^{\infty} k_{2n}k_{2m}^* \int_{-h_2}^{0} \frac{\text{ch.}\, k_{2n}(h_2+z)\,\text{ch.}\, k_{2m}^*(h_2+z)}{\text{ch.}\, k_{2n}h_2\,\text{ch.}\, k_{2m}^*h_2}\, dz\right.$$

$$\times \int_{-b}^{b}\left\{a_{+n}a_{+m}^* e^{i(x+b)[\sqrt{A_x/A_z}\,k_{2n} - \sqrt{A_x^*/A_z^*}\,k_{2m}^*]}\right.$$

$$- a_{+n}a_{-m}^* e^{i[k_{2n}\sqrt{A_x/A_z}(x+b) - k_{2m}^*\sqrt{A_x^*/A_z^*}(x-b)]}$$

$$- a_{-n}a_{+m}^* e^{-i[k_{2n}\sqrt{A_x/A_z}(x-b) + k_{2m}^*\sqrt{A_x^*/A_z^*}(x+b)]}$$

$$\left.\left. + a_{-n}a_{-m}^* e^{-i(x-b)[\sqrt{A_x/A_z}\,k_{2n} - \sqrt{A_x^*/A_z^*}\,k_{2m}^*]}\right\} dx\right]$$

The depth integral is performed in Appendix B. It is important to note that the property of orthogonality described by Eq. (4.1.1) is not applicable for this integral since the conjugate of the eigenvalue k_{2n} does not satisfy the Region II dispersion equation. Hence the double summation must be retained in order to include the cross products. The integrations with respect to x are straightforward so that after evaluating all of the integrals at the appropriate limits and truncating the infinite eigen-series at some value N, the denominator of Eq. (5.1.7) takes the form

$$\frac{-i2\pi Y\epsilon g^2\sqrt{A_xA_x^*/A_zA_z^*}}{A_xA_x^*}$$

$$\times\sum_{m=1}^{N}\sum_{n=1}^{N}\Bigg[\left[\frac{k_{2n}k_{2m}^*}{ch.\,k_{2n}h_2\;ch.\,k_{2m}^*h_2}\right]$$

$$\times\left[\frac{k_{2m}^*ch.\,(k_{2n}h_2)sh.\,(k_{2m}^*h_2)-k_{2n}ch.\,(k_{2m}^*h_2)sh.\,(k_{2n}h_2)}{k_{2m}^{*2}-k_{2n}^2}\right]$$

$$\times\Bigg\{\frac{a_{+n}a_{+m}^*\left[e^{i2b(k_{2n}\sqrt{A_x/A_z}-k_{2m}^*\sqrt{A_x^*/A_z^*})}-1\right]}{(k_{2n}\sqrt{A_x/A_z}-k_{2m}^*\sqrt{A_x^*/A_z^*})}$$

$$+\frac{a_{+n}a_{-m}^*\left[e^{-i2bk_{2m}^*\sqrt{A_x^*/A_z^*}}-e^{i2bk_{2n}\sqrt{A_x/A_z}}\right]}{(k_{2n}\sqrt{A_x/A_z}+k_{2m}^*\sqrt{A_x^*/A_z^*})}$$

$$+\frac{a_{-n}a_{+m}^*\left[e^{-i2bk_{2m}^*\sqrt{A_x^*/A_z^*}}-e^{i2bk_{2n}\sqrt{A_x/A_z}}\right]}{(k_{2n}\sqrt{A_x/A_z}+k_{2m}^*\sqrt{A_x^*/A_z^*})}$$

$$+\frac{a_{-n}a_{-m}^*\left[e^{i2b(k_{2n}\sqrt{A_x/A_z}-k_{2m}^*\sqrt{A_x^*/A_z^*})}-1\right]}{(k_{2n}\sqrt{A_x/A_z}-k_{2m}^*\sqrt{A_x^*/A_z^*})}\Bigg\}\Bigg]$$

(5.1.11)

5.1.2. Quantification of f_{xy}

Structural members whose longitudinal axes parallel the y-axis interact with both the horizontal and vertical velocity components. Equation (2.3.6) describes the horizontal non-linear and linear fluid damping forces applied per differential mass of fluid. Anticipating the use of Lorentz' condition of equivalent work, Eq. (2.3.6) is re-written using the real portion of the complex horizontal velocity component, i.e.,

$$\frac{-C_D u_R |u_R| Ddy}{2dV_f} \equiv -f_{xy}\sigma u_R$$

Proceeding in a manner identical to that detailed in Section 5.1.1, the dimensionless horizontal damping coefficient for y-directed piles is expressed as

$$f_{xy} = \frac{Y \sum_{j=1}^{N_y} \left[\frac{A\nu T}{2} (U_R^2 + U_I^2)_j + \frac{4}{3\pi} BDT(U_R^2 + U_I^2)_j^{3/2} \right]}{2\pi Y \epsilon \int_{-b}^{b} dx \int_{-h_2}^{0} (U_R^2 + U_I^2) dz} \tag{5.1.12}$$

where

N_y = number of y-directed structural members within the structural volume defined by the ranges $-b \leq x \leq b$, $0 \leq y \leq Y$, $-h_2 \leq z \leq 0$.

Equation (5.1.2) is similar to Eq. (5.1.7) with the exceptions that the summation is carried out at each y-directed pile within the structural volume and that the depth integral is replaced by an integral over the lateral width Y. For the two dimensional problem being considered, the lateral integration is equivalent to multiplication by Y. Noting that denominators of Eqs. (5.1.7 and 5.1.12) are identical, it is apparent that Eq. (5.1.11) also yields the denominator of Eq. (5.1.12). The numerator of Eq. (5.1.12) is evaluated numerically.

5.1.3. Quantification of f_{zy}

Equation (2.3.8) describes the vertical non-linear and linear fluid damping forces applied per differential mass of fluid. As before, this equation is re-written using the real portion of the vertical velocity component such that

$$\frac{-C_D D w_R |w_R| dy}{2 dV_f} \equiv -f_{zy} \sigma w_R$$

Again, following the procedure developed by Sollitt and Cross (1972) as outlined in Section 5.1.1 of this paper, the dimensionless vertical damping coefficient for y-directed piles is expressed as

$$f_{zy} = \frac{Y \sum_{j=1}^{N_y} \left[\frac{A\nu T}{2} (W_R^2 + W_I^2)_j + \frac{4}{3\pi} DBT (W_R^2 + W_I^2)_j^{3/2} \right]}{2\pi Y \epsilon \int_{-b}^{b} dx \int_{-h_2}^{0} (W_R^2 + W_I^2) dz} \tag{5.1.13}$$

where

W_R, W_I = real spatial functions of x and z obtained when the complex vertical velocity component, w, is expressed as

$$w = (W_R + iW_I) e^{-i\sigma t}$$

The denominator of Eq. (5.1.13) is evaluated in a manner similar to that of Eq. (5.1.7) when the definition

$$W \equiv w/e^{-i\sigma t} = W_R + iW_I$$

is employed such that

$$WW^* = (W_R^2 + W_I^2)$$

where

$*$ = denotes the complex conjugate

From the definition above

$$W = \frac{1}{A_z}\left[\frac{\partial}{\partial z}\left\{\sum_{n=1}^{\infty}\phi_{2n}\right\}\right] \Big/ e^{-i\sigma t}$$

or

$$W = \frac{g}{A_z}\sum_{n=1}^{\infty} k_{2n}\frac{sh.\,k_{2n}(h_2+z)}{ch.\,k_{2n}h_2}$$

$$\times\ [a_{+n}e^{ik_{2n}\sqrt{A_x/A_z}(x+b)} + a_{-n}e^{-ik_{2n}\sqrt{A_x/A_z}(x-b)}]$$

and from the complex algebraic identities of Section 5.1.1

$$W^* = \frac{g}{A_z^*}\sum_{m=1}^{\infty} k_{2m}^*\frac{sh.\,k_{2m}^*(h_2+z)}{ch.\,k_{2m}^*h_2}$$

$$\times\ [a_{+m}^* e^{-ik_{2m}^*\sqrt{A_x^*/A_z^*}(x+b)} + a_{-m}^* e^{ik_{2m}^*\sqrt{A_x^*/A_z^*}(x-b)}]$$

so that

$$WW^* = W_R^2 + W_I^2 = \frac{2\pi\epsilon Y g^2}{A_z A_z^*}\sum_{m=1}^{\infty}\left[\sum_{n=1}^{\infty} k_{2n}k_{2m}^*\frac{sh.\,k_{2n}(h_2+z)\,sh.\,k_{2m}^*(h_2+z)}{ch.\,k_{2n}h_2\ ch.\,k_{2m}^*h_2}\right.$$

$$\times\left\{a_{+n}a_{+m}^* e^{i(x+b)[k_{2n}\sqrt{A_x/A_z} - k_{2m}^*\sqrt{A_x^*/A_z^*}]}\right.$$

$$+\ a_{+n}a_{-m}^* e^{i[k_{2n}\sqrt{A_x/A_z}(x+b)+k_{2m}^*\sqrt{A_x^*/A_z^*}(x-b)]} \quad +$$

$$+ a_{-n} a^*_{+m} e^{-i[k_{2n}\sqrt{A_x/A_z}(x-b)+k^*_{2m}\sqrt{A^*_x/A^*_z}(x+b)]}$$

$$\left. + a_{-n} a^*_{-m} e^{-i(x-b)[k_{2n}\sqrt{A_x/A_z}-k^*_{2m}\sqrt{A^*_x/A^*_z}]} \right\}\Bigg]$$

Substituting the above equation into the denominator of Eq. (5.1.13), performing the indicated integrations,[8/] evaluating the results at the specified limits, and truncating the infinite eigen-series at some value N yields the denominator of Eq. (5.1.13) as

$$\frac{-i2\pi\epsilon Y g^2}{A_z A^*_z} \sum_{m=1}^{N} \sum_{n=1}^{N} \Bigg[\Big[\frac{k_{2n} k^*_{2m}}{\mathrm{ch.}(k_{2n}h_2)\,\mathrm{ch.}(k^*_{2m}h_2)}\Big]$$

$$\times \Big[\frac{k^*_{2m}\,\mathrm{sh.}(k_{2n}h_2)\,\mathrm{ch.}(k^*_{2m}h_2)-k_{2n}\,\mathrm{sh.}(k^*_{2m}h_2)\,\mathrm{ch.}(k_{2n}h_2)}{k^{*2}_{2m}-k^2_{2n}}\Big]$$

$$\times \left\{ \frac{a_{+n} a^*_{+m}[e^{i2b(k_{2n}\sqrt{A_x/A_z}-k^*_{2m}\sqrt{A^*_x/A^*_z})}-1]}{k_{2n}\sqrt{A_x/A_z}-k^*_{2m}\sqrt{A^*_x/A^*_z}} \right.$$

$$+ \frac{a_{+n} a^*_{-m}[e^{i2bk_{2n}\sqrt{A_x/A_z}}-e^{-i2bk^*_{2m}\sqrt{A^*_x/A^*_z}}]}{k_{2n}\sqrt{A_x/A_z}+k^*_{2m}\sqrt{A^*_x/A^*_z}} \quad +$$

8/ The depth dependent integration is performed in Appendix B. The x-dependent integrations are straight forward.

$$+\frac{a_{-n}a^{*}_{+m}\left[e^{i2bk_{2n}\sqrt{A_x/A_z}}-e^{-i2bk^{*}_{2m}\sqrt{A^{*}_x/A^{*}_z}}\right]}{k_{2n}\sqrt{A_x/A_z}+k^{*}_{2m}\sqrt{A^{*}_x/A^{*}_z}}$$

$$\left.\left.+\frac{a_{-n}a^{*}_{-m}\left[e^{i2b\left(k_{2n}\sqrt{A_x/A_z}-k^{*}_{2m}\sqrt{A^{*}_x/A^{*}_z}\right)}-1\right]}{k_{2n}\sqrt{A_x/A_z}-k^{*}_{2m}\sqrt{A^{*}_x/A^{*}_z}}\right\}\right] \tag{5.1.14}$$

The numerator of Eq. (5.1.13) is evaluated numerically at each y-directed pile location.

5.1.4. Quantification of f_{zx}

Equation (2.3.9) describes the non-linear and linear fluid damping forces per differential mass of fluid due to vertical flow past x-directed structural members. Rewriting this equation using the real portion of the vertical velocity component yields

$$\frac{-C_D D w_R |w_R| dx}{2dV_f} \equiv -f_{zx}\sigma w_R$$

Employing the procedure developed by Sollitt and Cross (1972) as described in Section 5.1.1 of this paper, the dimensionless vertical damping coefficient for x-directed piles is found to be

$$f_{zx} = \frac{\sum_{j=1}^{N_x}\left[\frac{A\nu T}{2}\int_{x_{0j}}^{x_{0j}+\ell_j}(W_R^2+W_I^2)_j dx + \frac{4}{3\pi} BDT\int_{x_{0j}}^{x_{0j}+\ell_j}(W_R^2+W_I^2)_j^{3/2} dx\right]}{2\pi Y\epsilon\int_{-b}^{b} dx\int_{-h_2}^{0}(W_R^2+W_I^2)dz} \tag{5.1.15}$$

where

N_x = number of x-directed structural members within the structural volume defined by the ranges $-b \le x \le b$, $0 \le y \le Y$, $-h_2 \le z \le 0$

x_{0j} = seaward most x-coordinate of the j^{th} x-directed structural member

ℓ_j = length of the j^{th} x-directed structural member

The spatial integral with respect to x in the numerator of Eq. (5.1.15) is performed numerically by summing discrete contributions along the length, ℓ_j, of each x-directed pile. Since the x-directed piles may not be continuous from $x = -b$ to $x = b$ (see Fig. 1.1) it is necessary to perform this integral over each pile length, i.e., over the range $x_{0j} \le x \le x_{0j}+\ell_j$. The sum of all of these contributions from the N_x different x-directed piles is then performed.

The denominator of Eq. (5.1.15) is identical to that of Eq. (5.1.13) and is therefore evaluated by Eq. (5.1.14).

5.2. The Drag Coefficient

The dimensionless viscous damping coefficients f_{xz}, f_{xy}, f_{zy}, and f_{zx} may be calculated from Eqs. (5.1.7, 5.1.12, 5.1.13 and 5.1.15) respectively if the flow field within the structure, the incident wave characteristics, the structural configuration and the drag coefficient are all known. The flow field within, and adjacent to, the structure is one of the primary objectives of this investigation and, hence, is unknown. However by initially assuming the values of the total horizontal and vertical dimensionless damping coefficients, f_x and f_z, and employing an iterative calculation of the flow field and the damping coefficients, a solution is achieved if the remainder of the above required knowns are available. Assuming that the incident wave characteristics and the structural configuration are both 'given' design criteria, only the drag coefficient remains to be determined.

The drag coefficient for steady flow about cylinders has been quantified as a function of the Reynolds number (see Schlicting, 1968, and Figs. 5.1 and 5.2) by extensive experimental research. However, the drag coefficient for unsteady, oscillatory flows has only recently, by comparison, been addressed. Consequently, knowledge regarding it is somewhat limited. Initial attempts to quantify C_D as a function of only the Reynolds number yielded widely scattered data. However, as early as 1956 Keulegan and Carpenter (1956) had

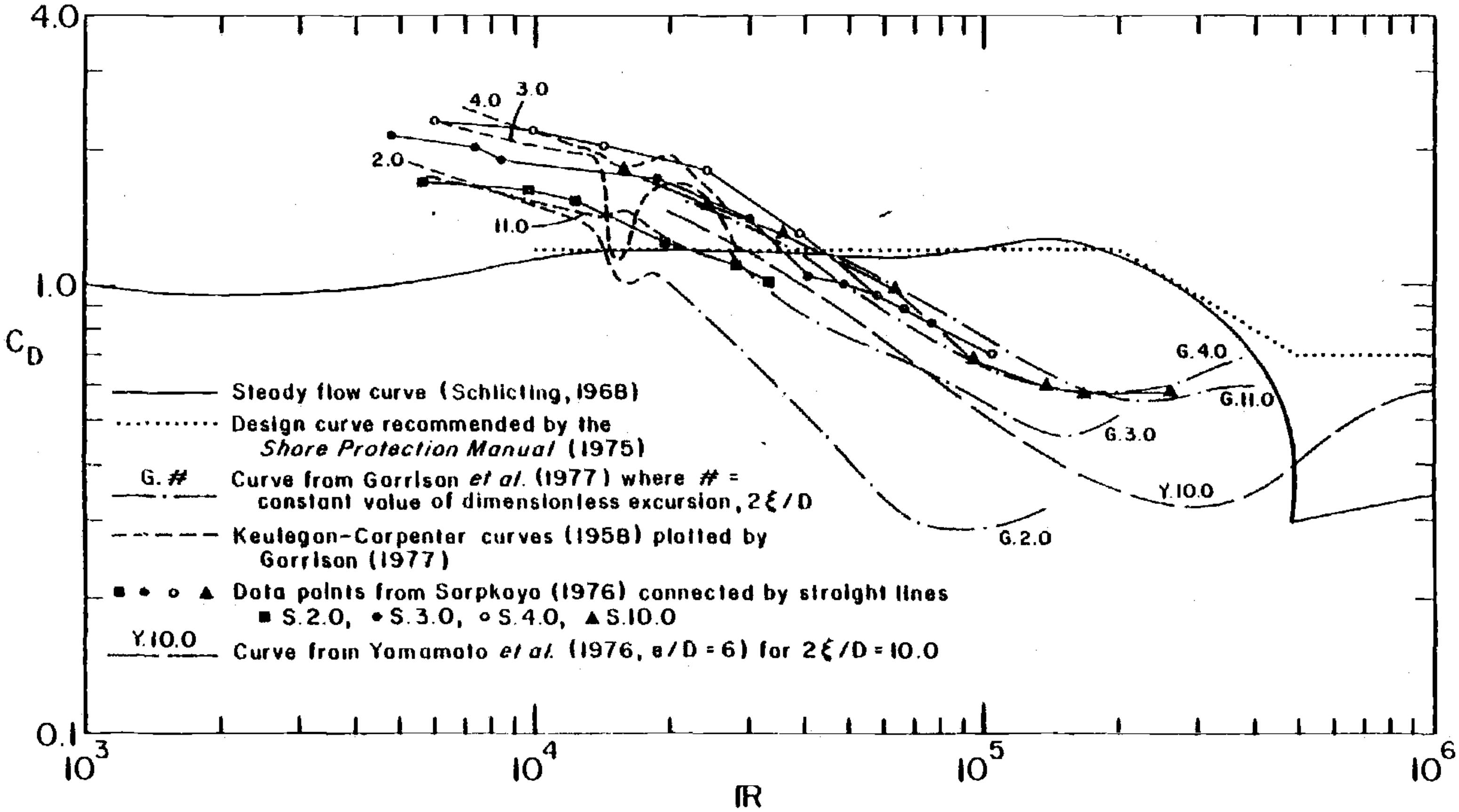

Figure 5.1. Drag coefficient versus the Reynolds number for constant values of the dimensionless water particle excursion, $2\xi/D$.

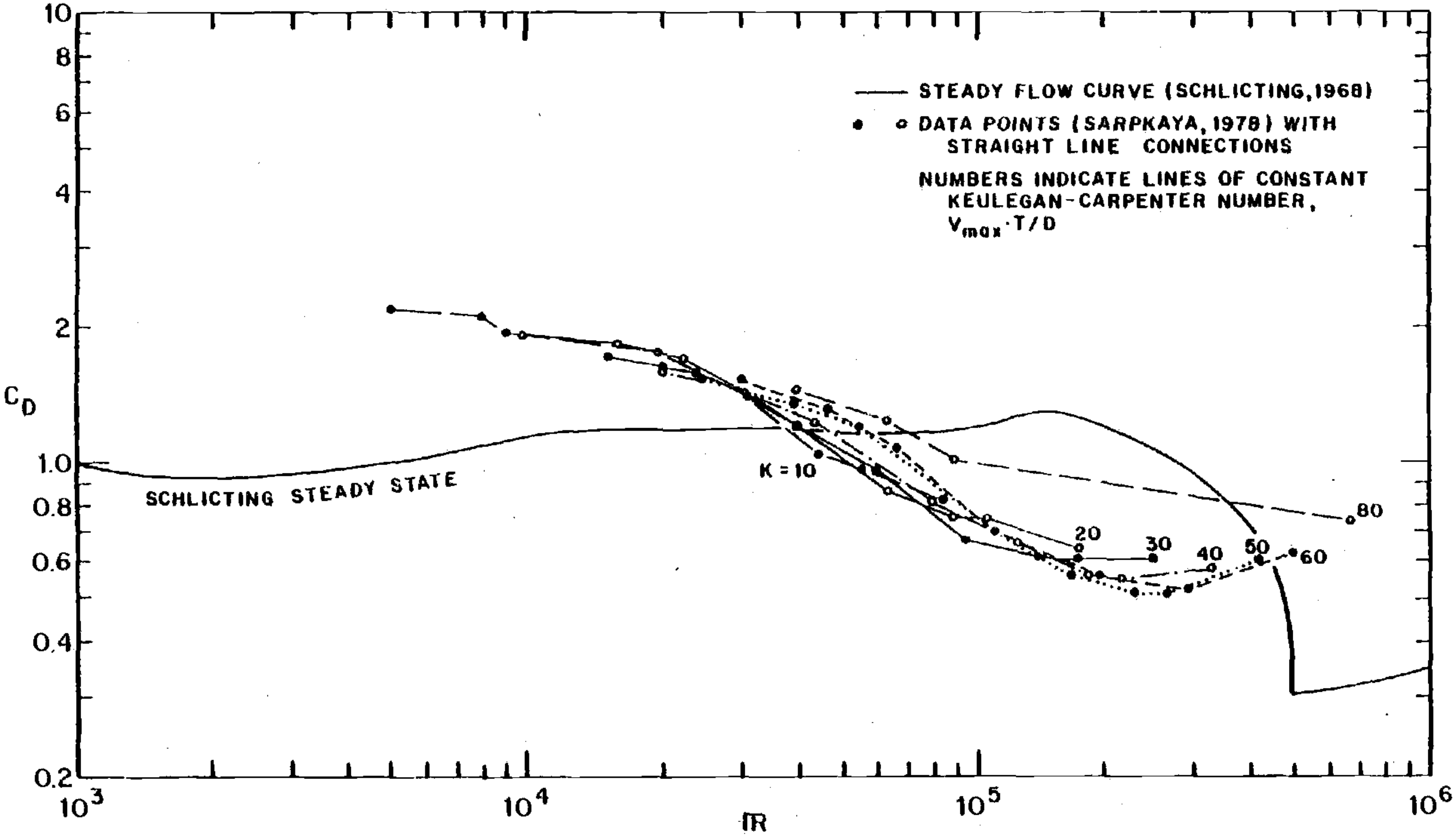

Figure 5. 2. Single cylinder oscillatory flow form drag coefficient versus the Reynolds number for constant values of the Keulegan-Carpenter parameter.

identified an additional parameter of import, i.e., the Keulegan-Carpenter, or period, parameter K

$$K = V_{max} T/D$$

where

V_{max} = maximum velocity

T = oscillation period

D = cylinder diameter

This parameter is essentially the same as the dimensionless water particle excursion parameter,

$$2\xi/D$$

where

ξ = amplitude of the water particle displacement

since, using linear wave theory, the parameters are related by the constant π, such that

$$2\xi/D = \left(\frac{1}{\pi}\right) V_{max} T/D$$

Recent investigations by Sarpkaya (1976), Yamamoto and Nath (1976), and Garrison, Field and May (1977) have indicated that the drag coefficients for simple harmonic flows tend to behave well as a function of the Reynolds number when isolated for constant values of the dimensionless water particle excursion parameter. The results of Keulegan and Carpenter (1956), as plotted by Garrison et al. (1977), and Garrison's own work correlate well. Although Sarpkaya's results (1976) were reported in terms of the Keulegan-Carpenter parameter (see Fig. 5.2) the data is quite easily plotted for constant values of the dimensionless water particle excursion as shown in Fig. 5.1 and as described above. Sarpkaya's results also tend to agree acceptably with those of Garrison et al. and Keulegan and Carpenter. Only the work of Yamamoto and Nath (1976) for the single case of $2\xi/D = 10$ does not agree favorably with the others. The reason for this discrepancy is not known, but, granting that it is a valid discrepancy does not alter the fact that three different investigations achieved reasonably similar results. Thus, for the purposes of this investigation it is concluded that the drag coefficient may adequately be described as a function of the Reynolds number for constant values of the dimensionless water particle excursion $2\xi/D$.

Figure 5.2 depicts Sarpkaya's results versus the Reynolds number for constant values of the Keulegan-Carpenter parameter. Comparison of Figs. 5.1 and 5.2 indicate that drag coefficient is more responsive to small changes in the dimensionless water particle excursion than small changes in the Keulegan-Carpenter parameter since the latter parameter is larger than the former by a constant factor of π. Hence the dimensionless water particle excursion has been chosen as the more appropriate parameter.

5.3. Proximity Effects--A Literature Review

The preceding discussion has addressed the general behavior of the drag coefficient for a single, isolated, smooth cylinder subjected to simple harmonic flow conditions. Coastal structures, however, are often constructed of a multitude of such members which, depending upon wave loading, active and passive structural loads, foundation requirements, and numerous other factors, may be in close proximity with one another. Under certain conditions this proximity is known to produce significant changes in the drag coefficient and thus it is important to try to identify those conditions. For this reason it will be helpful to conduct a review of previous technical literature regarding this subject. Unlike the literature review conducted in Chapter I, the format for the following review is based on the number of cylinders involved, i.e., those investigations involving only two cylinders are examined first, three cylinders next, etc. etc.

5.3.1. Zdravkovich (1977), "Review of Flow Interference Between Two Circular Cylinders in Various Arrangements"

Zdravkovich (1977) has compiled the results of 40 steady flow investigations of the effects of two cylinders in close proximity with one another. The review is divided into three sections, the first of which deals with cylinders in a 'tandem arrangement', i.e., two cylinders arranged so that a plane containing the centerlines of both cylinders is parallel to the flow direction. The drag coefficient of the downstream cylinder is shown to be less than that of a single isolated cylinder for center to center spacings between the cylinders as large as 50 cylinder diameters. It is probable that this reduction in drag at large spacings is due to the turbulent boundary layer about the downstream cylinder induced by the turbulent wake of the upstream cylinder. At smaller spacings the drag coefficient is further reduced by the shielding effect of the upstream cylinder. The drag coefficient of the upstream cylinder is also lower than that of a single isolated cylinder for spacings less than approximately four cylinder diameters. Thus the total drag force on a tandem arrangement of two cylinders is, in general, less than that of two isolated cylinders and, in some cases, may even be less than the total force on a single isolated cylinder. The drag coefficient of both cylinders is shown to be dependent on the Reynolds number.

The drag measurements as well as velocity profile and pressure distribution measurements confirmed a bistable nature of the flow pattern at some critical spacing of the cylinders. That is at some particular spacing, usually between three and four cylinder diameters, two different flow patterns about the cylinders may exist where all of the deterministic parameters such as blockage ratio, Reynolds number, etc. remain unchanged. This bistable phenomena may produce two significantly different drag forces on the cylinders. Although the exact cause is not specified, the bistable flow pattern appears to be directly related to the formation (or lack of) a vortex in the lee of the upstream cylinder.

The second two cylinder configuration reviewed by Zdravkovich is the side by side, or transverse, arrangement in which the plane containing the cylinder centerlines is normal to the flow direction. The drag coefficients of cylinders in the transverse arrangement generally appear to be greater than those of a single isolated cylinder. However, for cylinder spacings from 1.1 to 2 diameters the bistable flow pattern was again observed such that the drag coefficient varied both above and below that of the single isolated cylinder. Also, a significant increase in the lift forces acting on the cylinders was found in the bistable range. Cylinder spacings in excess of four diameters appeared to produce little or no proximity effects.

The final two cylinder configuration reviewed by Zdravkovich is the staggered configuration. This configuration is any arrangement which is not side by side or tandem. Plots are provided which detail the lift and drag coefficients and the general proximity effects. These plots are rather complex and a simple narrative here would, at best, be confusing. Therefore the reader is referred to Zdravkovich (1977) for detailed information. However in a strictly qualitative sense it can be seen that the drag coefficient of the downstream cylinder remains approximately constant for constant transverse spacing and variable in line spacings in excess of five cylinder diameters. On the other hand, increasing the transverse spacing generally increases the drag coefficient.

The results contained in the review by Zdravkovich are not particularly applicable to the present problem since they are restricted to steady flow with only two cylinders involved and are conducted at low blockage ratios. The present study deals with oscillatory flow through an infinite porous matrix so that the flow is not free to diverge around the structure as a whole. However, Zdravkovich's review is pertinent in the fact that it illustrates the complex nature of proximity effects and provides the fundamental insights which may be useful for an extension to oscillatory flow.

5.3.2. Dalton and Szabo (1977), "Drag on a Group of Cylinders"

Dalton and Szabo (1977) have conducted steady flow wind tunnel experiments for two and three cylinder arrangements alligned along a common axis at angles with the direction of flow of 0° (parallel to the flow), 30°, 60°, and 90° (normal to the flow). The experiments were conducted at Reynolds numbers of 2.78, 5.20, 6.75 and 7.82×10^4. Mach numbers were sufficiently low so that compressibility effects were negligible.

The results of the two cylinder case alligned parallel to the flow, i.e., the tandem arrangement, indicated that the drag coefficient of the upstream cylinder decreased as the center to center spacing increased from touching cylinders to approximately three diameters. Further increases in spacing caused the upstream cylinder drag to increase and asymptotically approach the single isolated cylinder drag coefficient at a center to center spacing of approximately five diameters. These results are very similar to those reviewed by Zdravkovich (1977). The initial decrease in the drag coefficient is accounted for by the inhibition of the formation of vortices in the lee of the upstream cylinder due to the close proximity of the downstream cylinder. No Reynolds number effect is apparent.

The drag coefficient for the downstream cylinder in the tandem arrangement was found to be negative for very small spacings and gradually increased to a value of zero at a center to center spacing of approximately three diameters for all Reynolds numbers tested. Further increase in the spacing produced similar increases in the drag coefficient until a leveling off trend occurred at a center to center spacing of about five diameters. At this spacing the drag coefficient is still considerably less than that of a single isolated cylinder. The bistable flow phenomena was not observed in either the upstream or downstream measured drag forces.

The drag coefficient for the upstream cylinder when the cylinders are aligned at an angle of 30° to the flow direction is very similar to that observed for the tandem arrangement. The drag on the downstream cylinder is significantly affected by this 'staggered' configuration. That is, all values of the drag coefficient are positive at the smallest spacings and, although still less than those of a single isolated cylinder, at larger spacings they are considerably larger than those of the tandem cylinder case.

A trend similar to the 30° alignment case is also found for the two cylinders aligned at an angle of 60° to the flow direction, i.e., the drag coefficient for the upstream cylinder is a function of the center to center spacing but is almost unmodified by alignment angle while the drag coefficient of the downstream cylinder is increased somewhat over the 30° case. Although the downstream cylinder drag coefficient is still less, it approaches the single isolated cylinder value rather closely for spacings larger than five diameters at the highest Reynolds number tested. It is concluded that the increase in the downstream drag coefficient with the increase in the angle of alignment to the flow is due to the decrease in the sheltering effect of the upstream cylinder. This statement appears to be substantiated by the further increase in the drag coefficients for the side by side arrangement. A slight reduction of the drag coefficient is observed at the smaller spacings but increases with increasing spacing are realized at a center to center spacing of approximately three diameters. Values of the single isolated cylinder drag coefficient are found at lateral spacings exceeding four diameters. The drag coefficient did not appear to exceed the single isolated cylinder value for any spacing tested as reported by Zdravkovich (1977) nor was the bistable flow pattern observed.

For three cylinders aligned parallel to the flow the reported drag coefficients for the upstream cylinder are very similar to those of the two cylinder case. The magnitudes of the negative drag coefficients of the downstream cylinder for very small center to center spacings are much greater than those of the two cylinders for the two higher Reynolds number cases.

Increased spacing causes rapidly increasing drag coefficients such that the downstream cylinder drag coefficient is zero for all Reynolds numbers tested at center to center spacings between the middle and downstream cylinder of approximately three diameters. Further increases in spacing causes the downstream cylinder drag coefficient to approach that of the middle cylinder at spacings of four to five diameters.

The middle cylinder drag coefficient is always positive and gradually increases with increased spacings although it remains well below the single isolated cylinder drag coefficient over the range of center to center spacings tested.

For three cylinders aligned at angles of 30° and 60° to the direction of the flow, the drag coefficient of the upstream cylinder is again similar to that of the upstream cylinder for the 0° case. The drag coefficients of the downstream and middle cylinder both increase significantly with increasing angles. The drag coefficients of the downstream cylinder are always positive and again increase rapidly with increased spacing such that they approach the middle cylinder values at center to center spacings of approximately four diameters. The middle cylinder drag coefficients increase gradually with increased spacing, once again approaching more closely the single cylinder values with increasing angles and larger spacings.

The drag coefficients of the two outside cylinders when three cylinders are aligned normal to the flow appear to approximate, or be slightly lower than, the single cylinder case over the experimental range of spacings from one to five diameters. The middle cylinder drag coefficient is smaller than the isolated cylinder case at small spacings but approaches those of the outside cylinders at spacings larger than five diameters.

Again, the findings of Dalton and Szabo's investigation appear to have little bearing on the present study since the experiments were conducted for steady flow at small blockage ratios. However, these results tend to support the fundamental hypothesis that sheltering and turbulence are responsible for significantly lower drag forces on downstream cylinders and that proximity effects extend for approximately four to five diameters in the lateral direction and considerably more than this in the downstream direction.

5.3.3. Ball and Cox (1978), "Hydrodynamic Drag Forces on Groups of Flat Plates"

Ball and Cox (1978) have conducted a steady flow hydraulic drag force investigation for various series of vertical flat plates. Results of these experiments are then compared with the results obtained for a five plate by ten plate rectangular matrix. The purpose of this comparison is to ascertain whether or not the results of testing the component parts individually may be combined to predict the effects on the total structure. All tests were carried out at a constant Reynolds number (based on the constant one inch plate width) of 3.9×10^3 and a constant Froude number of 0.1.

Lateral, or transverse, proximity effects were examined in two separate tests with two and five plates aligned normal to the flow. Both tests indicated some form of the bistable flow pattern so that two different drag forces were measured at constant, small, spacings. The higher drag force of the two was always greater than that of a single isolated plate. In all cases the drag force began to decrease toward the single isolated plate case as the center to center spacing between plates exceeded four plate widths, and very nearly approximated the single plate case at seven plate widths. Ball generalized that lateral interference will increase drag forces but that this effect is dampened, even for small spacings, due to the fact that for small blockages the flow is free to diverge around the structure.

In line, or longitudinal, proximity effects were studied in three separate tests. The first of which examined two plates aligned parallel to the flow at variable spacings. The results are qualitatively similar to those reviewed by Zdravkovich (1977) although the bistable flow pattern is not reported by Ball for this configuration. However, it is interesting to note that the drag on the downstream plate is still considerably below that of a single isolated plate at spacings in excess of 30 plate widths.

The second test examining longitudinal proximity effects consisted of a variable number of from two to ten plates spaced at a constant interval of five plate widths parallel to the flow. Ball's results indicate that the addition of plates downstream always decreases the drag on the existing plates and that all values were always less than the single plate drag force. It is also noteworthy that the minimum drag always occurs at the intermediate plate positions. Furthermore, the plot of the drag force versus the plate position reveals that there may be several relative maxima and minima, i.e., the drag force does not monotonically increase or decrease downstream.

The final longitudinal proximity experiment entailed five plates aligned parallel to the flow for variable spacing intervals from two to ten plate widths. Again all drag forces for the five plates were less than that of a single isolated plate. For small spacings the drag force on the second plate from the upstream end was negative. Also, increasing the spacing generally increased the drag force on all plates.

Combined longitudinal and lateral proximity effects were investigated in experiments with a 50 plate matrix: five plates aligned normal to the flow direction by ten plates aligned parallel to the flow. Constant longitudinal spacing intervals of five and ten plate widths were held while the lateral spacings were varied from two to eight plate widths. The drag forces on all plates were, again, less than that of a single isolated plate. Drag forces on all plates were also generally reduced by decreasing the lateral spacing. Although this is contrary to what might be intuitively expected, it is congruous with the hypothesis that for small lateral spacings and small blockages, flow diverges around and out of the middle of the plate matrix thereby decreasing the plate drag forces. Increasing the longitudinal spacing tended to increase the average drag force of the group as would be inferred from the longitudinal tests. However, a plate to plate comparison indicates this is only true for the group average since individual plates are significantly affected by vortices and flow diverging and converging in and out of the matrix. Hence it is concluded that combined lateral and longitudinal proximity effects may not, in general, be predicted from results of experiments on the component parts.

Repeating, this investigation was conducted for steady flow at low blockage ratios and thus is of limited use. However the above stated conclusion is important to note.

5.3.4. Hansen, Jacobsen and Lundgren (1979), "Hydrodynamic Forces on Composite Risers and Individual Cylinders"

Hansen et al. (1979) have conducted model experiments to determine the drag, lift, inertial, and total force coefficients for a composite riser system consisting of a central pipe surrounded by a circle of 12 evenly spaced smaller pipes. Hansen's results indicated

> That even with a distance greater than 3.5 diameters between the pipes in the outer ring and a relatively small central cylinder, a composite riser behaves largely as a closed body when exposed to currents or oscillating flow (Hansen et al., 1979).

Thus, it may be concluded that to a large degree flow tends to diverge around the composite riser and therefore the results are not wholly suited to the present investigation. However it is interesting to note that the reported oscillatory flow drag coefficients for the individual pipes of the surrounding circle were considerably higher than those of a single cylinder subjected to steady flow. This comparison may be somewhat misleading since the Reynolds number computation for the individual pipes of the outer ring was based on the pitch diameter[9/] of the composite system rather than the diameters of the outer pipes. This caused the Rynolds number to increase by at least an order of magnitude into the supercritical range of steady flow drag coefficients. Had the outer ring pipe diameters been used to compute the Reynolds number, the oscillatory flow drag coefficients and that of a single cylinder in steady flow would have correlated more closely. Sheltering effects appear to be negligible among the outer pipes but the drag on the central pipe appears to be somewhat reduced.

Other important features of Hansen's results were the magnitude of the lift and inertial coefficients. The lift, or transverse, force coefficients of the outer ring pipes were generally comparable to the magnitude of the drag coefficients and often exceeded them. In addition, inertial coefficient values in excess of four were also reported. However, the results published were for only one Keulegan-Carpenter number (K = 46) and three Reynolds numbers (3.5, 6.4, and 7.9 x 10^5 based on the pitch diameter) so that no generalizations are implied.

[9/] The pitch diameter is defined as the diameter of the encircling ring of pipes around the central pipe.

5.3.5. Sarpkaya (1979), "Hydrodynamic Forces on Various Multiple-Tube Riser Configurations"

Sarpkaya (1979) has conducted a literature review of flow interference between two or more adjacent members and carried out a model study of two circular composite riser configurations to determine drag and inertial coefficients for oscillatory flow conditions. Unfortunately, the results are presented for the composite riser as a whole rather than its component parts. The results of Sarpkaya's literature review have led to a conclusion similar to that of Ball and Cox (1978), i.e., that proximity effects may not be "generalized nor predicted on the basis of relatively idealized situations" (Sarpkaya, 1979).

5.3.6. Laird (1964), "Wave Forces on Piling" and Laird (1966), "Flexibility in Cylinder Groups Oscillated in Water"

Laird (1964, 1966) has conducted oscillatory flow experiments to determine drag coefficients on various vertical cylinder configurations. These configurations included a 24 cylinder rectangular matrix (8 x 3 cylinders), a 23 cylinder staggered rectangular matrix, and several five pile dolphin arrangements in which some or all of the cylinders were flexibly supported.

The results of the 24 cylinder matrix and 23 cylinder staggered matrix are reported as the average drag coefficients obtained by assuming that each cylinder of the matrix contributes the same drag force to the total drag force. The results published by Laird (1964) for these configurations are plotted in Fig. 5.3 for two different angles of incidence. It is apparent from this figure that the drag coefficient of the rectangular model is somewhat less than that of the staggered model for the normally incident case. This is undoubtedly due to the increase in the shielding effect for cylinders aligned parallel to the flow. This fact is substantiated by the decrease in the drag coefficient of the staggered model for an angle of incidence of 45°, i.e., the cylinders are more closely aligned with the flow direction in this case and hence drag is reduced. Furthermore the drag on the rectangular model is increased at the 45° angle of incidence since it begins to resemble the staggered configuration at this angle.

Comparison of Fig. 5.3 with Figs. 5.1 and 5.2 indicates that the trend of the average drag coefficients for the staggered pattern is slightly lower than those of a single isolated pile in oscillatory flow and that of the rectangular pattern is lower still. Thus, it appears that even for close lateral spacing the longitudinal shielding effect is dominant. However, the cylinder matrices tested by Laird occupied only a small portion of the tank width, allowing the flow to diverge around the models as well as through them. This fact, in addition to the sheltering effect, might be responsible for the decrease in the drag coefficient.

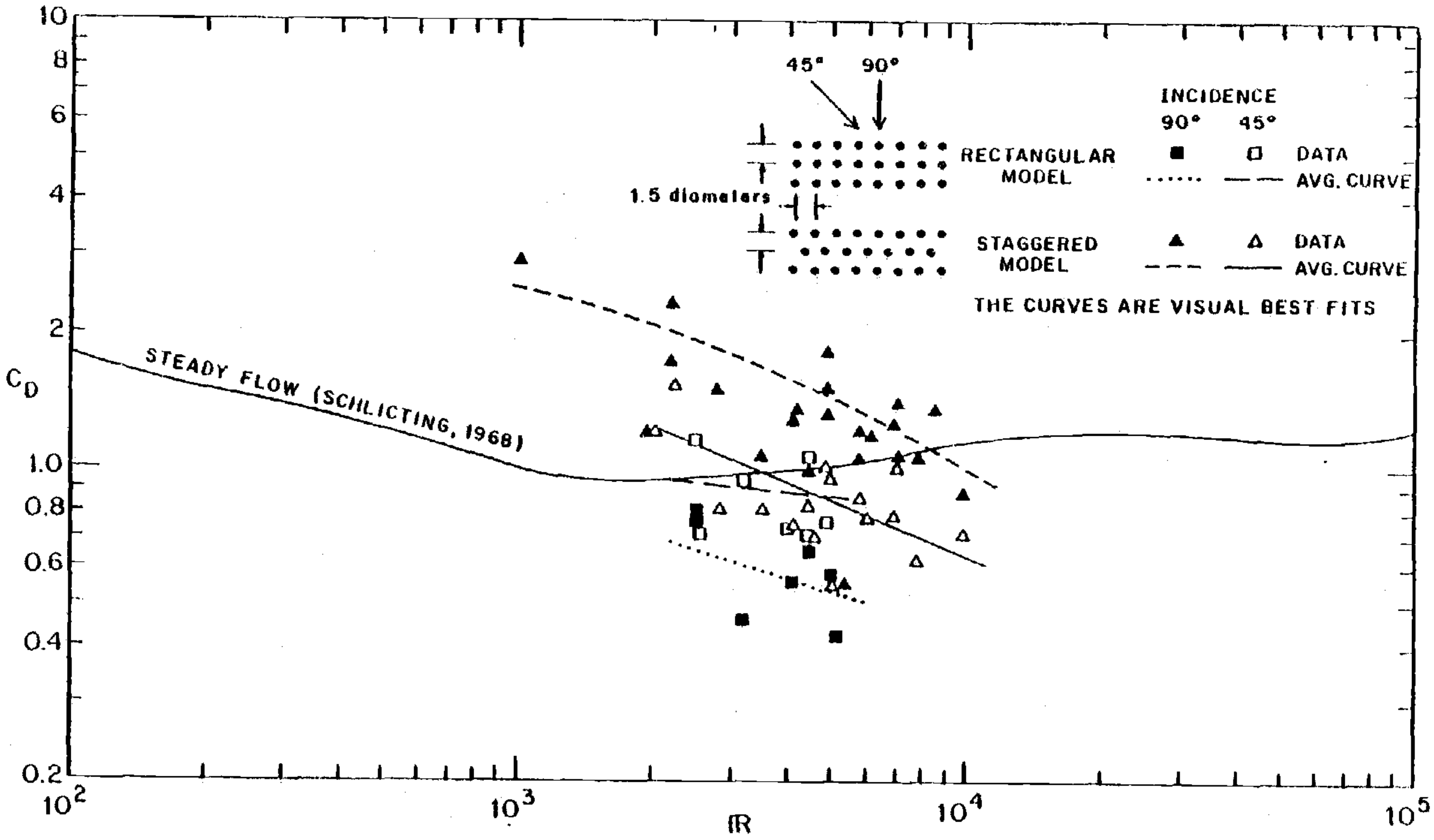

Figure 5.3. Average oscillatory form drag coefficient versus the Reynolds number for two multiple pile configurations (from Laird, 1964).

For the five pile dolphin tests, Laird arranged five cylinders in the shape of a plus symbol dolphin such that one cylinder was centrally positioned at the junction while the other four were symmetrically set at the tips of the legs of the plus symbol. This configuration was oscillated at two orientation angles; that of one leg parallel to the flow so that three cylinders were aligned in the flow direction and two were outriders, and that of flow passing at angle of 45° to both of the legs of the plus symbol. Average drag coefficients for the five cylinders of the configuration were determined as well as the lift and drag coefficients of the central cylinder.

The average drag coefficient for the five cylinders of the dolphin configuration were lower than those of a single cylinder subjected to oscillatory flow shown in Figs. 5.1 and 5.2 over the range of Reynolds numbers tested. In fact, for both angles of orientation they tended to approximate values within the scatter of the staggered model at 90° incidence shown in Fig. 5.3.

The drag coefficient of the central cylinder for flow aligned with one leg of the plus symbol configuration indicated significant shielding effects. Although the drag coefficient was relatively constant over the range of Reynolds numbers tested it was found to decrease with a decrease in spacing. The lift coefficient at this orientation was found to be generally of comparable magnitude with the drag coefficient at low Reynolds numbers and up to four times the drag coefficient at the higher Reynolds numbers of the tests.

The drag coefficient of the central cylinder for flow incident at an angle of 45° to the legs of the plus symbol was found to approximate the steady flow drag coefficient for a single cylinder over most of the test range of Reynolds numbers. However at the higher Reynolds numbers and larger spacings the drag coefficient began to decrease significantly below the single cylinder steady flow values. The lift coefficient was found to be somewhat less than the drag coefficient values at low Reynolds numbers but increased with increasing Reynolds numbers such that its value was over four times that of the drag coefficient at the highest Reynolds number tested. This lift coefficient trend is similar to that reported above for flow aligned parallel to one leg of the plus symbol and also corresponds with Laird's tests for a single isolated cylinder subjected to oscillatory flow.

5.4. The Lift Coefficient and Transverse Losses

The steady state transverse, or 'lift', force on a structural member is given by

$$F_L = C_L \rho v \frac{|v|}{2} dA_c \tag{5.4.1}$$

where

v = instantaneous velocity. . . either u or w

C_L = lift coefficient

that is, the lift force equation is identical to that of the steady flow drag force given by Eqs. (2.2.1 and 2.2.2) except for the dimensionless lift coefficient, C_L. It is not known whether or not the transverse force exerted on the structural members results in a net loss of fluid energy. Fluid energy is, for the most part, consumed due to vortex shedding and induced turbulence in the wake flow downstream from the structural member. The form drag force arises as a direct consequence of flow separation and the resulting pressure differential across the member. This force was related to irreversible fluid losses in Chapter II of this paper. The transverse force, on the other hand, arises from the unsymmetrical pressure distribution about the cylinder due to alternating vortex shedding. Consequently, this force oscillates rapidly in the transverse direction causing the elastic structural member to behave as the well known spring-mass system. There are, of course, some losses which must be associated with any such system. The question, however, is whether or not the fluid losses may be directly related to the magnitude of the lift force as calculated from Eq. (5.4.1) or whether a significant portion of the stored elastic energy of the structural member is recovered in a reversible manner by the fluid each time the transverse force changes direction. A decisive and general answer seems to be unknown at the present time. Consequently for the purposes of this investigation it will be concluded that the fluid losses may be directly related to the magnitude of the lift force as calculated from Eq. (5.4.1) and that these losses are not reversible. This conclusion is based on the fact that the lift force is a direct result of the fluid loss mechanism, i.e., it arises due to vortex shedding and the induced turbulent pressure fluctuations.

Since the lift force and the drag force equations are of the same form, the losses due to lift are incorporated into the theory by increasing the drag coefficient C_D by an appropriate amount as noted in Section 2.2. This amount corresponds to the value of the lift coefficient. Figure 5.4 depicts the lift coefficient values, as a function of the Reynolds number for constant values of the dimensionless water particle excursion, $2\xi/D$. These experimental values were obtained by Sarpkaya (1976) for single, isolated cylinders subjected to one dimensional harmonic flow. Proximity effects other than those related incidentally in Section 5.3 are not known for lift coefficients.

5.5. Summary of the Drag Coefficient, C_D

The drag coefficient, C_D, as employed in this theory, includes the fluid effects of drag, lift, and as noted in Section 2.2,

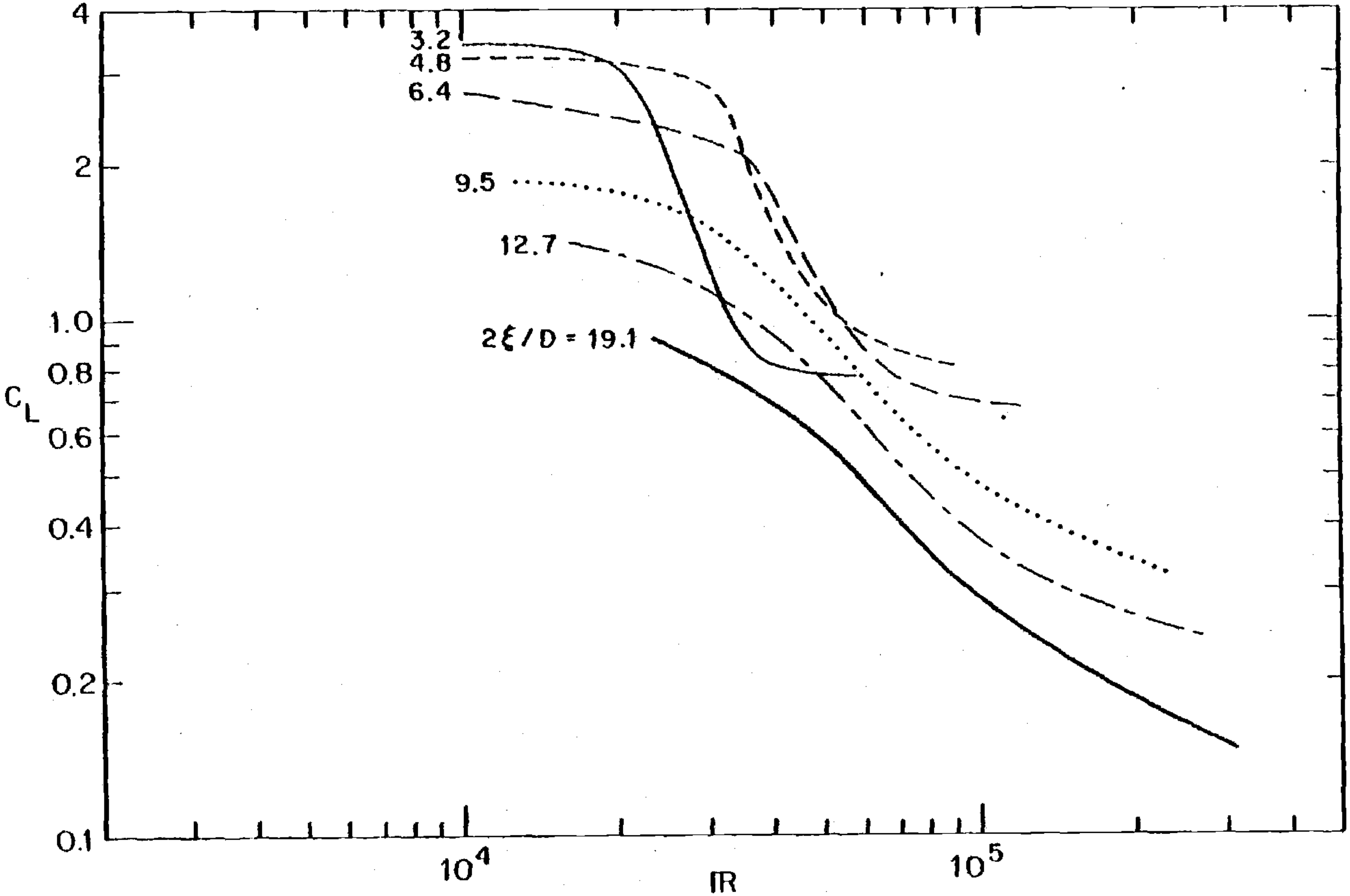

Figure 5.4. Single cylinder oscillating flow lift coefficients versus the Reynolds number for constant values of the dimensionless water particle excursion $2\xi/D$ (from Sarpkaya, 1976).

skin friction if marine fouling is a factor. Thus the name 'viscous force coefficient' might be more appropriate although the term 'drag coefficient' is retained throughout this paper. The complications involved in evaluating this coefficient due to proximity effects have been addressed in Section 5.3. It has been shown that lateral spacings of less than four diameters and/or longitudinal spacings less than 30 to 50 diameters may produce significant changes in form drag (and even possibly lift) forces. The predictive quantification of these changes, however, has not at the present time been achieved. Furthermore, experimental investigations have generally considered low blockage cases which are unsuited to the present considerations of wave related orbital water particle flow through a relatively long, or infinite, porous matrix structure. It is hypothesized by this research that the form drag forces are not reduced to such a considerable extent if flow is forced to pass through the matrix rather than diverge around it. It is recognized, however, that sheltering and turbulence effects are still a factor and that the average drag coefficient is probably reduced from that of a single isolated cylinder albeit to a lesser degree than for the low blockage cases.

For the design engineers use of the present theory, it is recommended that Figs. 5.1 and 5.4, or similar plots, be used in which the drag and lift coefficients are depicted versus the Reynolds number for the design value $2\xi/D$. The Reynolds number range and the design value $2\xi/D$ must be approximated using linear wave theory and the incident design wave conditions. Having obtained such plots for both the vertical and horizontal directions, the total drag coefficient, C_D, incorporating form drag and lift forces, is found by superimposing the form drag and lift drag plots for the design value of $2\xi/D$ to obtain a plot for the total drag coefficient, C_D, versus the Reynolds number in each the vertical and horizontal directions. The drag coefficient function described in Section 5.1.1

$$C_D = \frac{A}{\mathbb{R}} + B \tag{5.5.1}$$

is fitted to this plot in such a manner as to obtain the best fit at the higher Reynolds numbers. This is required since the greatest portion of lift and drag related dissipation occurs at higher velocities and hence higher Reynolds numbers. For this reason the choice of the constant, 'B', is critical. This research is cognizant of the fact that the drag coefficient function given by Eq. (5.5.1) does not represent the peak and valley behavior of the total drag coefficient over the full range of Reynolds numbers. However, it is felt that a median value of 'B' may be chosen easily enough which may be too low in the subcritical range and slightly too high in the transitional and supercritical ranges but which represents the average behavior of the total drag coefficient over the higher Reynolds number range .

encountered during the wave cycle. This approximating effect is entirely congruous with the linearization scheme employed in the previous section.

More complicated polynomial expressions for C_D than the one given by Eq. (5.5.1) may also be employed. However, this investigation has found that polynomials of three to four terms generally required non-integer powers of the Reynolds number when attempting to fit a moderate range of Reynolds numbers, e.g., $0 \leq \mathbb{R} \leq 10^5$. These non-integer powers made the analytical integrations of the denominators for f_{xy}, f_{xz}, f_{zx}, and f_{zy} described in the previous section impossible and thus necessitated what was felt to be an excessive expenditure for numerical integrations.

The constant, 'A', in Eq. (5.5.1) is chosen to fit the total drag coefficient curve in the low range of Reynolds numbers. Since reliable oscillatory flow lift and form drag coefficient data seems to be unavailable for Reynolds numbers less than about 10^3, 'A' should be chosen so that the drag coefficient function approximates the plot of the total drag coefficient at the lowest Reynolds numbers for which oscillatory data is available. For Reynolds numbers below the lowest Reynolds for which oscillatory lift and drag coefficients are known at the design value of $2\xi/D$, it may be assumed that the form drag coefficient approximates the steady flow values and that the lift coefficient approximates the form drag coefficient. Thus for the low range of Reynolds number in which no data is available the total drag coefficient takes on values of approximately two times the steady flow form drag coefficient. Hence the drag coefficient function given by Eq. (5.5.1) should also approximate these values at the lowest Reynolds numbers. In general, it will not be possible for Eq. (5.5.1) to approximate the total drag coefficient plot over the entire range of Reynolds numbers. Consequently the first priority is to obtain a reasonable fit at the highest Reynolds number, the second priority is to best fit the intermediate values without affecting the fit at the higher Reynolds number, and lastly, to come as close as possible to the doubled steady flow values at the lowest Reynolds numbers.

As stated previously, a quantitative description of proximity effects is not available for inclusion in Eq. (5.5.1). For structures in which proximity effects are likely to occur, several crude measures are possible for modifying Eq. (5.5.1). For example, Eq. (5.5.1) might be multiplied by some fractional constant, the value of which would be determined by the longitudinal and lateral spacing. That is, for wide lateral spacings and close longitudinal spacings the fractional constant should be low, say 0.5-0.6, to reflect the sheltering effects, while close lateral spacings and wide longitudinal spacings would require a high constant, say 0.75-0.9, to reflect more lateral interference and less sheltering. This simple technique requires an intimate familiarity with the technical literature, and a penchant for subjective intuitive estimation.

Another possible technique of evaluating the fractional constant would be to employ a figure such as Fig. 5.3 or alternative literature results of a model having rough similarity to the proposed design. The fractional constant is determined by dividing some average form drag coefficient for the model at some representatively high Reynolds number (from Fig. 5.3) by the single cylinder form drag coefficient for the design value $2\xi/D$ at the same Reynolds number (from Fig. 5.1). This ratio would then constitute the fractional multiplier to modify Eq. (5.5.1). This technique is not totally satisfactory since tests of models resembling the proposed prototype will not, in general, be available in the literature and, even if such results were available, it is likely that the experiments would have been conducted for inappropriately small blockage ratios (as in Fig. 5.3).

Finally, there is the possibility that no modification of Eq. (5.5.1) is required at all, i.e., although sheltering effects may reduce the form drag coefficient it may be that the lift coefficient increases by a corresponding amount.

Thus, the unknown nature of proximity effects on the total drag coefficient remains a topic for further research.

5.6. Added Mass Coefficient, C_m

The added mass coefficient, C_m, has been shown to be a function of the dimensionless water particle excursion and the

Reynolds number by Sarpkaya (1976), and by Garrison, Fields and May (1977). Gibson and Wang (1977) have also shown that the added mass coefficient increases significantly at and above some particular "solidification ratio" for pile groupings. However, for the relatively small diameter piles used for most coastal structures, the inertial force is small. Hence, a constant value of the added mass coefficient will not introduce appreciable error into the present analysis.

Garrison et al. (1977) and Sarpkaya (1976) have shown that the added mass coefficient is negative for isolated cylinders at Reynolds number values less than 2×10^4 and dimensionless water particle excursions greater than four. For the purposes of this investigation it is felt that a value of zero will yield sufficient accuracy for all applications in which the maximum Reynolds number does not exceed 3×10^4. For applications in which the maximum Reynolds number exceeds 3×10^4, the added mass coefficient may be approximated by a constant average value of 0.5 over the entire range of Reynolds numbers. That is

Max $\mathbb{R}$	Dimensionless Water Particle Excursion $2\xi/D$	C_m
$< 3 \times 10^4$	$2\xi/D > 4$	0
$> 3 \times 10^4$	$2\xi/D > 4$	0.5

VI. NUMERICAL PROCEDURE

6.1. Introduction

This chapter, in conjunction with the flow chart of Fig. 6.1, the computer variable definition list of Appendix C, and the program listing in Appendix D, provides a description of the numerical procedure employed for the solution of the problem being investigated. Specifically, this entails a short description of the iterative solution technique used in the main program in which initial values of the dimensionless damping coefficients, f_x, and f_z, are used to solve the $4N \times 4N$ system of equations given by Eqs. (4.2.2, 4.2.3, 4.2.5 and 4.2.6) in order to obtain the solutions C_{rn}, C_{Tn}, C_{+n}, C_{-n}. These solutions are then employed to compute the water particle velocities in Region II from which the dimensionless damping coefficients, f_x, and f_z, are calculated using the Lorentz' condition of equivalent work. These calculated values of f_x and f_z are then compared to the original estimates. The process is repeated until the values converge.

Subsequent to the main program description, short discussions of the subroutines RAPNEW, and CMPLK2 are provided in which details of the calculation of the eigenvalues k_{1n}, k_{3n}, and k_{2n}, respectively, using an iterative Newton-Raphson technique are delineated.

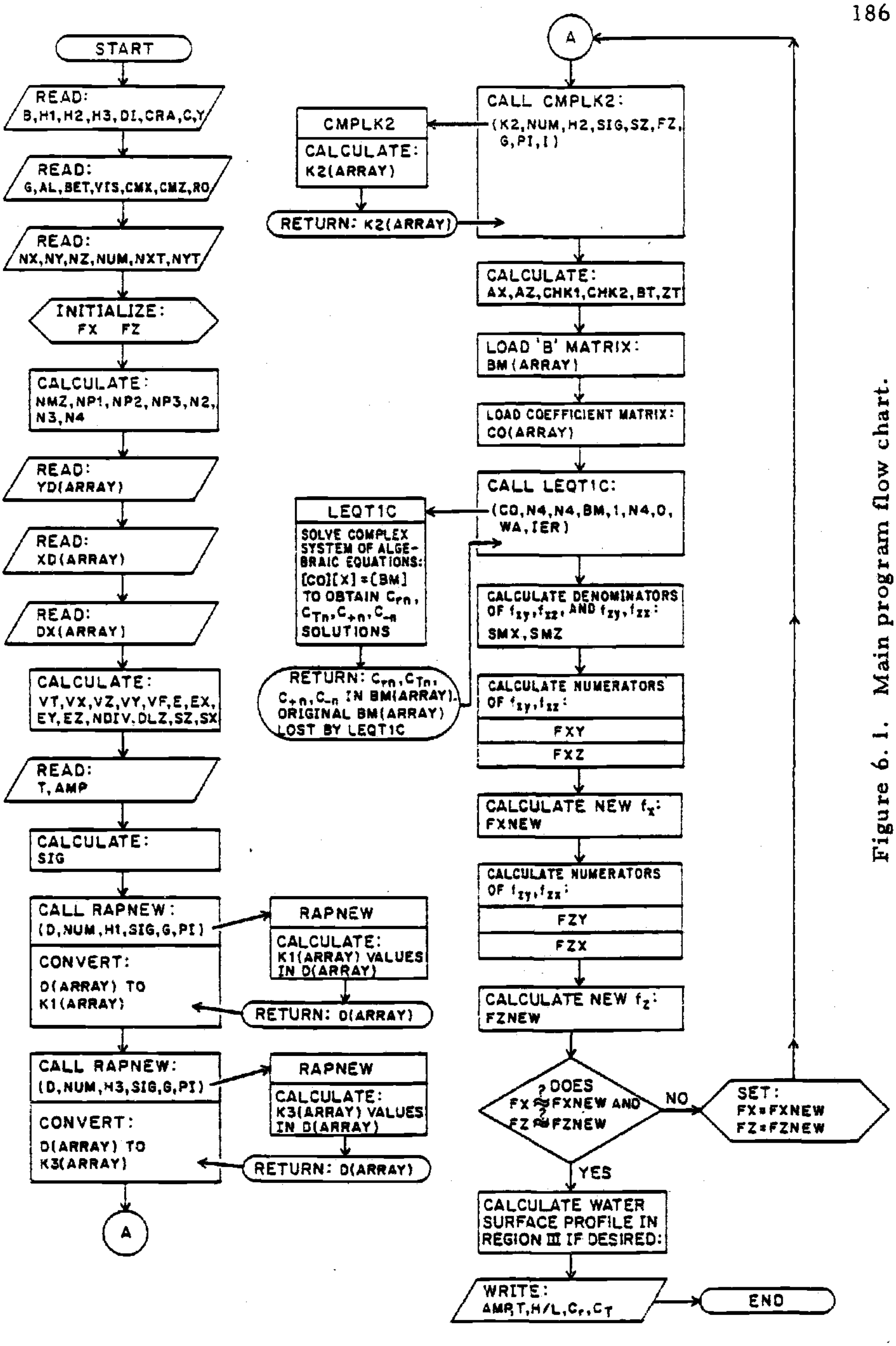

Figure 6. 1. Main program flow chart.

6. 1. 1. The Main Program

A flow chart for the main program is depicted in Fig. 6. 1 and a complete listing of the entire program is provided in Appendix D. Sufficient comment cards are provided in the listing such that, when combined with the flow chart of Fig. 6. 1 and the program variable dictionary of Appendix C, the details of the program logic should be apparent. Hence only a rudimentary description of the main program is given here.

The input variables for the program are as follows (see also Appendix C for complete definitions):

First READ statement,

(1) One-half the longitudinal width of the structure	= B
(2) The water depth in Region I	= H1
(3) The water depth in Region II	= H2
(4) The water depth in Region III	= H3
(5) Pile diameter	= DI
(6) Reflection coefficient of the Reflector-Absorber	= CRA
(7) The distance from the leeward face of the structure to the Reflector-Absorber	= C
(8) The lateral repeating distance of the structural configuration	= Y

Second READ statement,

(1) Gravitational acceleration = G

(2) First constant of the drag coefficient equation, Eq. (5.5.1) = AL

(3) Second constant of the drag coefficient equation, Eq. (5.5.1) = BET

(4) Fluid kinematic viscosity = VIS

(5) Added mass coefficient for the x-direction = CMX

(6) Added mass coefficient for the z-direction = CMZ

(6) Fluid density = RO

Third READ statement,

(1) Maximum number of x-directed members between any two adjacent vertical members = NX

(2) Maximum number of y-directed members between any two adjacent vertical members = NY

(3) The number of vertical members in the structure defined by $-b \leq x \leq b$, $-h_2 \leq z \leq 0$, $0 \leq y \leq Y$ = NZ

(4) The number at which the infinite eigen-series is truncated = NUM

(5) The total number of x-directed members in the structure defined by $-b \leq x \leq b$, $-h_2 \leq z \leq 0$, $0 \leq y \leq Y$ = NXT

(6) The total number of y-directed members in the structure defined by $-b \leq x \leq b$, $-h_2 \leq z \leq 0$, $0 \leq y \leq Y$ = NYT

Fourth READ statement,

Depth below the still water level of each y-directed structural member is read into the YD array as shown in the example Fig. 6.2. 999.9 values are read into the array to inform the program that less than the maximum number of y-directed members between two particular adjacent vertical members are present (see also 999.9 in Appendix C and Fig 6.2) = YD(NY,NZ)

Fifth READ statement,

Depth below the still water level of each x-directed structural member is read into the XD array as shown in the example Fig. 6.2. 999.9 values are read into the array to inform the program that less than the maximum number of x-directed members between two particular adjacent vertical members are present (see also 999.9 in Appendix C and Fig. 6.2) = XD(NX,(NZ-1))

Sixth READ statement,

The x-coordinate of each vertical pile within the structural volume defined by $-b \leq x \leq b$, $-h_2 \leq z \leq 0$, $0 \leq y \leq Y$.

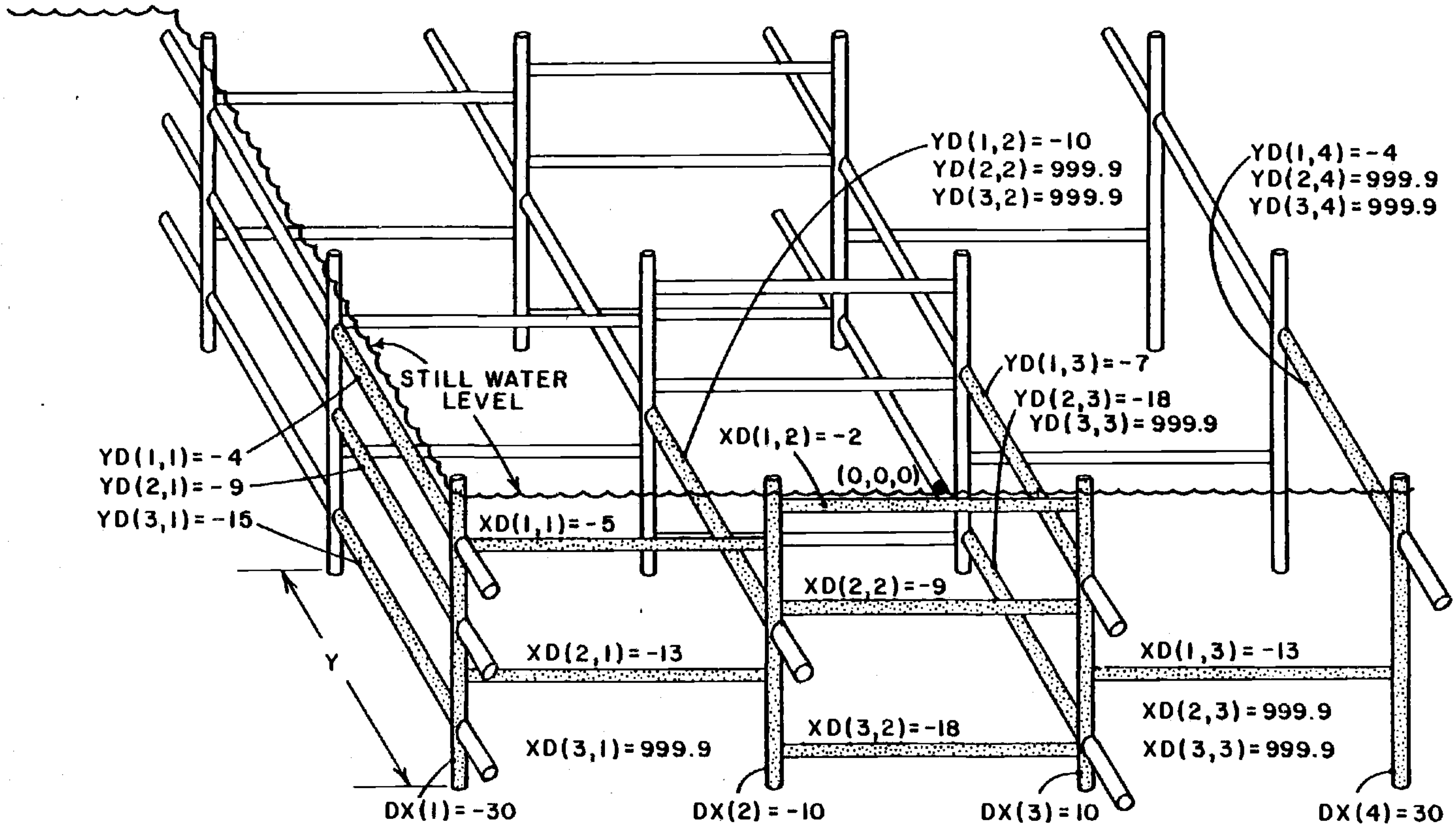

Figure 6.2. Example depicting YD(3,4), XD(3,3) and DX(4) array values.

Note that Y is the center-to-center lateral repeating distance of the structure as shown in Fig. 6.2. Thus only one row of vertical members is considered. = DX(NZ)

Seventh READ statement,

Input the incident wave period and incident wave amplitude = T, AMP

The program employs an iterative solution technique. That is the values of the horizontal and vertical dimensionless damping coefficients, f_x and f_z, are initially assumed[10] and solutions for C_{rn}, C_{Tn}, C_{+n}, C_{-n} are then obtained. These solutions allow the computation of the horizontal and vertical velocity components, from which f_x and f_z are re-calculated using the Lorentz' condition of equivalent work described in Chapter V. If the initial values and the calculated values of f_x and f_z are not close approximations of one another, i.e.,

$$f_{x1} \simeq f_{x2}$$

and

$$f_{z2} \simeq f_{z2}$$

the calculated values are retained and the solution process is

---

[10] Values of unity have been found to be reasonable first approximations for f_x and f_z for dense structures while values of 0.1 might be more appropriate for open structures, e.g., Fig. 6.2.

repeated until the dimensionless damping coefficients converge to some reasonable degree of accuracy.

Figure 6.3 depicts an example coefficient and 'B' matrix for a case in which the infinite eigen-series of Eqs. (4.2.2, 4.2.3, 4.2.5, and 4.2.6) are truncated at $N = 3$ (NUM = Program Variable $\Rightarrow$ $N = 3$). Thus a $4N \times 4N$, or 12×12, matrix is obtained since each of the system of equations may be written N times $(1 \leq m \leq N)$ as described in Chapter IV. A check mark within the matrix indicates that the coefficient of the variable listed at the top of the figure is to be calculated using the appropriate portion of the equation listed at the left hand side of the figure. The coefficient thus calculated is loaded into the program coefficient matrix, CO(L, J), where L and J are listed on the right hand side and bottom of the figure respectively.

Subsequent to the loading sequence, the CO(L, J) and BM(L) arrays are transferred to the matrix solution subroutine, LEQT1C. This subroutine is a packaged program obtained from the International Math Sciences Library system of subroutines which has been found to function quickly and efficiently. However, almost any of the commercially available <u>complex</u> matrix solution algorithms will also efficiently secure the required solutions. The solution variables C_{rn}, C_{Tn}, $C_{\tau n}$, and C_{-n} are returned by LEQT1C in the BM(L) array and the original values of the BM(L) array are lost.

Eq.	m	C_r n = 1	C_r 2	C_r 3	C_T 1	C_T 2	C_T 3	C_+ 1	C_+ 2	C_+ 3	C_- 1	C_- 2	C_- 3	L	BM(L)
(4.2.2)	m = 1	✓	O	O	O	O	O	✓	✓	✓	✓	✓	✓	L = 1	1
	2	O	✓	O	O	O	O	✓	✓	✓	✓	✓	✓	2	O
	3	O	O	✓	O	O	O	✓	✓	✓	✓	✓	✓	3 = NUM	O
(4.2.5)	1	✓	✓	✓	O	O	O	✓	O	O	✓	O	O	4 = NP1	1
	2	✓	✓	✓	O	O	O	O	✓	O	O	✓	O	5	1
	3	✓	✓	✓	O	O	O	O	O	✓	O	O	✓	6 = N2	1
(4.2.3)	1	O	O	O	✓	O	O	✓	✓	✓	✓	✓	✓	7 = NP2	O
	2	O	O	O	O	✓	O	✓	✓	✓	✓	✓	✓	8	O
	3	O	O	O	O	O	✓	✓	✓	✓	✓	✓	✓	9 = N3	O
(4.2.6)	1	O	O	O	✓	✓	✓	✓	O	O	✓	O	O	10 = NP3	O
	2	O	O	O	✓	✓	✓	O	✓	O	O	✓	O	11	O
	3	O	O	O	✓	✓	✓	O	O	✓	O	O	✓	12 = N4	O
	J =	1	2	3 NUM	4 NP1	5	6 N2	7 NP2	8	9 N3	10 NP3	11	12 N4		

Coefficient of C_r, C_T, C_+, C_-

CO(L,J) BM(L)

Figure 6.3. Coefficient and 'B' matrices for the system of simultaneous equations given by Eqs. (4.2.2, 4.2.3, 4.2.5 and 4.2.6). A check mark in the coefficient matrix indicates that the coefficient of the variable at the top of the figure is calculated by the program using the appropriate portion of the equation indicated at the left of the figure. In this example the infinite eigen-series have been truncated at N = NUM = 3; hence a 12 x 12 matrix is the result.

As previously noted, the dimensionless damping coefficients, f_x and f_z, are re-calculated using the C_{rn}, C_{Tn}, C_{+n}, and C_{-n} solutions and then compared to the initial values of the damping coefficients. If they have not converged the process is repeated until they do. Convergence has generally been found to be rapid, usually requiring four or less iterations.

Following convergence, the reflection and transmission coefficients for the structure as defined in Chapter I for the first, or propagating, wave mode are obtained as the moduli of the complex values BM(1) and BM(NP1)[11/] respectively. The reflection and transmission coefficients, when considering the evanescent as well as the propagating modes, may be obtained as the moduli of the complex computer variables CR and CT, respectively.

6.1.2. The Function Subprograms

The function subprograms CH, SH, TH, EQ, EQQ, QQ, EE, CC, U, and W are a series of functions which are used repeatedly in the program, e.g., CH = hyperbolic cosine of a complex argument. Consequently it was advantageous to refer to these functions in function subprograms. These function subprograms are described in Appendix C.

[11/] NP1 = NUM + 1 $\Rightarrow$ N + 1.

6.1.3. Subroutine RAPNEW

The eigenvalue solutions, k_{mn}, of Eq. (3.1.2)

$$\sigma^2 = gk_{mn} \text{th.} k_{mn} h_m \tag{3.1.2}$$

constitute the wave numbers in Regions I and III. There is one real solution (k_{11} and k_{31}) corresponding to the propagating wave mode ($n = 1$) in each of the two regions. Furthermore, there are an infinite number of pure imaginary solutions. This may be demonstrated by substituting the value

$$k_{mn} = ik'_{mn}$$

where

k'_{mn} is a real number

into Eq. (3.1.2) and employing the relationship

$$\text{th.}(ik'_{mn} h_m) = i \tan(k'_{mn} h_m)$$

Equation (3.1.2) becomes

$$\begin{aligned} \sigma^2 &= g(ik'_{mn})(i \tan k'_{mn} h_m) \\ &= -gk'_{mn} \tan k'_{mn} h_m \end{aligned} \tag{6.1.1}$$

From the repetitive nature of the tangent function, it is apparent that an infinite number of values of k'_{mn} will satisfy the above equation and hence an infinite number of pure imaginary values of k_{mn} $(n \geq 2)$ exist which satisfy Eq. (3.1.2).

Since Eq. (3.1.2) is transcendental in terms of the eigenvalues k_{mn}, it is necessary to employ an iterative Newton-Raphson[12/] solution technique. Briefly, this technique is applied to obtain the unknown roots, $\bar{x}$, of an arbitrary function

$$f(\bar{x}) = 0$$

An initial estimate, x_1, of the root is made and is used to find a better approximation x_2; where x_2 is the x-coordinate at which the tangent line to the curve $y = f(x)$ at $x = x_1$ crosses the x-axis. The equation of the tangent line to the curve $y = f(x)$ at x_1 is given by

$$y - f(x_1) = [x - x_1] \left[\frac{d(f(x)}{dx} \bigg|_{x=x_1} \right]$$

This line crosses the x axis at $y = 0$ and $x = x_2$ so that

$$0 - f(x_1) = [x_2 - x_1] \left[\frac{d(f(x)}{dx} \bigg|_{x=x_1} \right]$$

or

[12/] Often referred to as "Newton's Method."

$$x_2 = x_1 - \frac{f(x_1)}{\left.\frac{d(f(x))}{dx}\right|_{x=x_1}}$$

Now, let the new approximation x_2 assume the role of the initial estimate and repeat the process iteratively until x_1 and x_2 converge for some desired degree of accuracy, i.e.,

$$x_{j+1} = x_j - \frac{f(x_j)}{\left.\frac{d(f(x))}{dx}\right|_{x=x_j}} \tag{6.1.2}$$

where

$$j \text{ increases until } \frac{x_{j+1}}{x_j} \simeq 1$$

For the case being considered the arbitrary function becomes a function of k_{mn}, i.e.,

$$0 = k_{mn} \text{th.} k_{mn} h_m - \frac{\sigma^2}{g}$$

for the propagating mode $(n = 1, k_{11} \text{ or } k_{31})$ and

$$0 = k'_{mn} \tan k'_{mn} h_m + \frac{\sigma^2}{g}$$

for the evanescent modes $(n \geq 2, k_{1n} \text{ or } k_{3n})$. Substituting the above two equations into Eq. (6.1.2) yields the iterative propagating eigenvalue equation as

$$(k_{m1})_{j+1} = (k_{m1})_j - \left[\frac{(k_{m1})_j \, th.\,[(k_{m1})_j h_m] - \sigma^2/g}{th.[(k_{m1})_j h_m] + h_m (k_{m1})_j / ch^2[(k_{m1})_j h_m]}\right]$$

where

$m = 1$ or 3

and the iterative evanescent equation as

$$(k'_{mn})_{j+1} = (k'_{mn})_j - \left[\frac{(k'_{mn})_j \tan[(k'_{mn})_j h_m] + \sigma^2/g}{\tan[(k'_{mn})_j h_m] + h_m (k'_{mn})_j / \cos^2[(k'_{mn})_j h_m]}\right]$$

where

$m = 1$ or 3

$n \geq 2$

These two equations are iteratively employed in the subroutine RAPNEW where the variable k_{m1} is replaced by the subroutine array variable D(1) and k'_{mn} is replaced by D(J) for J greater than or equal to two. The initial estimate for the propagating mode is not critical as it converges rapidly even for poor estimates. Consequently a constant value of .25 has been used in RAPNEW. However in order to avoid the possibility of duplicating some of the evanescent roots and missing others it is imperative that the initial estimates be somewhat close. The initial estimate relationship

$$(k_{mn})_1 = (n-1)\pi / h_m$$

insures that all of the evanescent mode eigenvalues are found.

RAPNEW returns the D(J) array to the main program where the eigenvalues for n greater than or equal to two are established as

$$k_{mn} = i \times D(n)$$

6.1.4. Subroutine CMPLK2

The complex eigenvalues for Region II, k_{2n}, are found as solutions of Eq. (2.10.2),

$$\sigma^2 (S_z + if_z) = g k_{2n} \mathrm{th.}\, k_{2n} h_2 \tag{2.10.2}$$

using the Newton-Raphson technique described in the previous section. However, the arbitrary function in this case is written in terms of the dimensionless complex variable '$k_{2n}h_2$' such that

$$0 = k_{2n} h_2 \mathrm{th.}\, k_{2n} h_2 - \frac{h_2 \sigma^2}{g} (S_z + if_z) \tag{6.1.3}$$

The iterative eigenvalue equation employed in CMPLK2 is obtained by substituting the above function into Eq. (6.1.2) for $f(x)$ yielding

$$(k_{2n}h_2)_{j+1} = (k_{2n}h_2)_j - \left[\frac{(k_{2n}h_2)_j \text{th.}(k_{2n}h_2)_j - \dfrac{h_2\sigma^2}{g}(S_z + if_z)}{\text{th.}(k_{2n}h_2)_j + (k_{2n}h_2)_j/\text{ch.}^2(k_{2n}h_2)_j}\right]$$

As was the case in the previous section for the evanescent modes $(n \geq 2)$, the initial estimates of the k_{2n} roots are extremely critical in order to avoid missing some of the eigenvalues and duplicating others. This is particularly true of the first five wave modes in Region II. It has been found by this research that the suggested initial estimates proposed by Sollitt and Cross (1972) are not entirely satisfactory within the first five modes and thus should be used only with caution. For the purposes of this investigation, it has been advantageous to generate a disk storage file, TAPE1, on which are stored initial estimates of the first five modes of the CMPLK2 variable KH(L). These initial estimates are actually the first five roots, $k_{2n}h_2$, of Eq. (2.10.2) calculated for 35 values of the CMPLK2 dimensionless variable DIMSIG where

$$\text{DIMSIG} = h\sigma^2 S_z/g$$

and 25 values of the CMPLK2 dimensionless variable FZSZ where

$$\text{FZSZ} = f_z/S_z$$

The first five modal values of KH(L) were calculated by holding the variable DIMSIG constant and gradually increasing the variable FZSZ from zero. Thus the first set of solutions (FZSZ = 0) were actually the same as those that would have been generated by the subroutine RAPNEW (see the previous section) for which initial estimates are known. Having established the first set of the first five modal values of KH(L) for the constant value of DIMSIG, the variable FZSZ is slightly increased above zero and the first set of KH(L) is used for the initial estimates of the next set. This process was continued until all 25 values of FZSZ were used, at which time a new value of DIMSIG was employed and the process was begun again with FZSZ equal to zero. The entire process was continued until the first five modal values of KH(L) were stored for the 35 values of DIMSIG and 25 values of FZSZ. Although the process sounds lengthy, it actually entailed only slightly less than 40 seconds of computation time. This is due to the fact that the step-wise increase in FZSZ was small and thus the initial estimates were very close to the actual values allowing rapid convergence. Having stored the values of KH(L) on TAPE1 with the values of FZSZ and DIMSIG, they are referred to by CMPLK2 for initial estimates of the first five KH(L) values for various design values REFZSZ and REDMSG where

REFZSZ = design value of f_z/S_z transferred from the main program

REDMSG = design values of $h\sigma^2 S_z/g$ transferred from the main program

An example of the data stored on the TAPE1 file is given in Appendix E although this example is much coarser in terms of the DIMSIG and FZSZ increment step sizes than those actually employed in TAPE1.

CMPLK2 calculates the first 15 modal values of KH(L). Only the first five modal values require TAPE1 estimates. The remaining modes initial estimates may be calculated from the previous modes by the relationships

$$\mathrm{REAL}[\mathrm{KH(L)}]_{\substack{\text{initial}\\ \text{est.}}} = \mathrm{REAL}[\mathrm{KH(L-1)}]$$

$$\mathrm{IMAG}[\mathrm{KH(L)}]_{\substack{\text{initial}\\ \text{est.}}} = \mathrm{IMAG}[\mathrm{KH(L-1)}] + 3.2$$

where

$6 \leq L \leq 15$

since the real part of KH(L) tends toward the constant value of zero and the imaginary part increases with each mode by approximately the value of π for wave mode numbers greater than about five. CMPLK2 then calculates the values of the complex eigenvalues, K2(L), from KH(L) and returns these to the main program.

VII. THEORETICAL BEHAVIOR

7.1. Introduction

The theory has been shown to depend upon the structural geometry and the viscous and inertial matrix damping properties. A sensitivity study has been conducted with the analytical model to examine changes in wave reflection and transmission due to variations in:

(1) The dimensionless horizontal and vertical direction damping coefficients, f_x and f_z.

(2) The horizontal and vertical direction added mass coefficients, C_{mx} and C_{mz}, and the structural porosity.

(3) The dimensionless ratio of the water depth in Region II divided by one-half the longitudinal width of the structure, h_2/b, and the reflection coefficient of the reflector-absorber, C_{RA}.

(4) The dimensionless ratio of the water depth in Region II divided by the distance from the rear of the structure to the reflector-absorber, h_2/c, and the reflection coefficient of the reflector-absorber, C_{RA}.

The results of the sensitivity study are discussed in this chapter in the order listed above.

The dimensionless parameters f_x, f_z, C_{mx}, C_{mz}, ϵ, C_{RA}, h_2/b, and h_2/c are varied systematically to investigate the changes produced in the analytically computed reflection and transmission coefficients over a wide range of dimensionless wave frequencies, $\sigma^2 h/g$. The results are displayed in semi-logarithmic plots in which the linearly scaled ordinate, over the range $0 \le C_r, C_T \le 1.0$ corresponds to the reflection and transmission coefficients as defined in Chapter I of this study for the propagating mode. The abscissa, the dimensionless wave frequency, $\sigma^2 h/g$, ranges over the eight specific calculation points

$$\sigma^2 h/g = 0.05;\ 0.07;\ 0.1;\ 0.15;\ 0.25;\ 0.5;\ 1.0;\ 2.0$$

in all cases.

The calculated data points are shown on each plot and are connected by straight line segments in order to indicate trends. However, for those cases in which the reflection coefficient tends to oscillate somewhat, e.g., when C_{RA} and h_2/c are varied, these straight line connections tend to obscure the actual values of the absolute and relative maxima and minima. It is felt that this is not a significant drawback since the actual values could be found by using more $\sigma^2 h/g$ values at closer spacings. However, since general trends are the only objective of this sensitivity study, additional values of $\sigma^2 h/g$ are not justified.

In all plots, the reflection coefficient data are connected by solid lines while the transmission coefficient data are connected by broken lines.

The individual parameters varied are indicated on each figure along with the other pertinent parameters which are held constant. Unless they are the variable parameters, the values of the dimensionless damping coefficients, f_x and f_z, are chosen as 1.0 and 0.5, respectively. These values are general approximations for a wide range of structural configurations and thus are reasonable representations for this sensitivity study. The values of $h_2/b = 2.0$ and $h_2/c = 1.0$ and $C_{RA} = 0.0$ are chosen by similar reasoning. The potential flow value of unity has been chosen for the added mass coefficients C_{mx} and C_{mz} despite the fact that values of 0.5 or zero are recommended in Chapter V. The logic behind this choice is that it conforms to a well known standard and thus may facilitate future investigator's comparisons of this theory with other studies. Three different values of the structural porosity have been employed in the various portions of this sensitivity study. The values of $\epsilon = 0.92$, 0.75, and 0.66 correspond to open, intermediate, and dense pile structures respectively.

All of the analytical computations are accomplished using the NOS operating system of the Oregon State University Control Data Corporation Cyber 70 Series computer. All of the computations were conducted using equal water depths in Regions I, II, and III ($h_1 = h_2 = h_3$), although provision has been made within the model to accommodate regionally varying depths.

7.2. Variation of the Dimensionless Damping Coefficients, f_x and f_y

Figures 7.1 through 7.5 show the computed reflection and transmission coefficients for values of the dimensionless horizontal damping coefficient, f_x, which vary between 0.01 and 4.0 on each figure and values of the dimensionless vertical damping coefficient, f_z, which vary between 0.01 and 2.0 from figure to figure. Figures 7.6 through 7.10 show the data of Figs. 7.1 through 7.5 replotted where f_z varies on a particular plot while f_x varies from figure to figure. In all of these figures the reflection coefficient data are connected by solid line segments whereas the transmission coefficient data are connected by broken lines. The incident wave amplitude and the drag coefficient relationship are not indicated in the legends of the figures since these quantities have no bearing upon the solution values computed for these cases, i.e., these quantities are only necessary for the recalculation of the dimensionless damping coefficients using the Lorentz equivalent work scheme described in Chapter V. In these cases the arbitrarily established values of f_x and f_z are not recalculated using the Lorentz scheme since the sole object

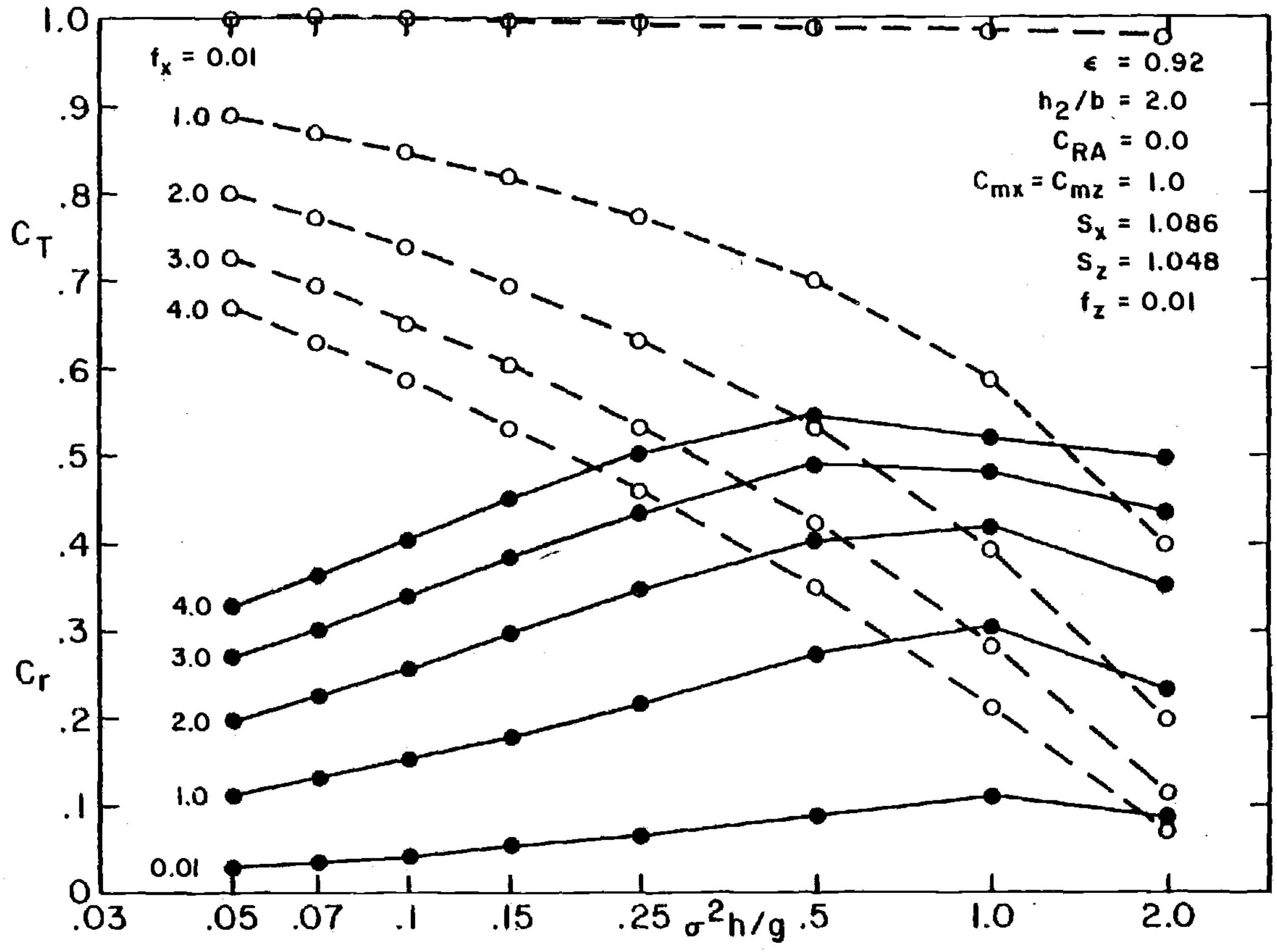

Figure 7. 1. Reflection and transmission coefficients for varying values of f_x. f_z = 0.01.

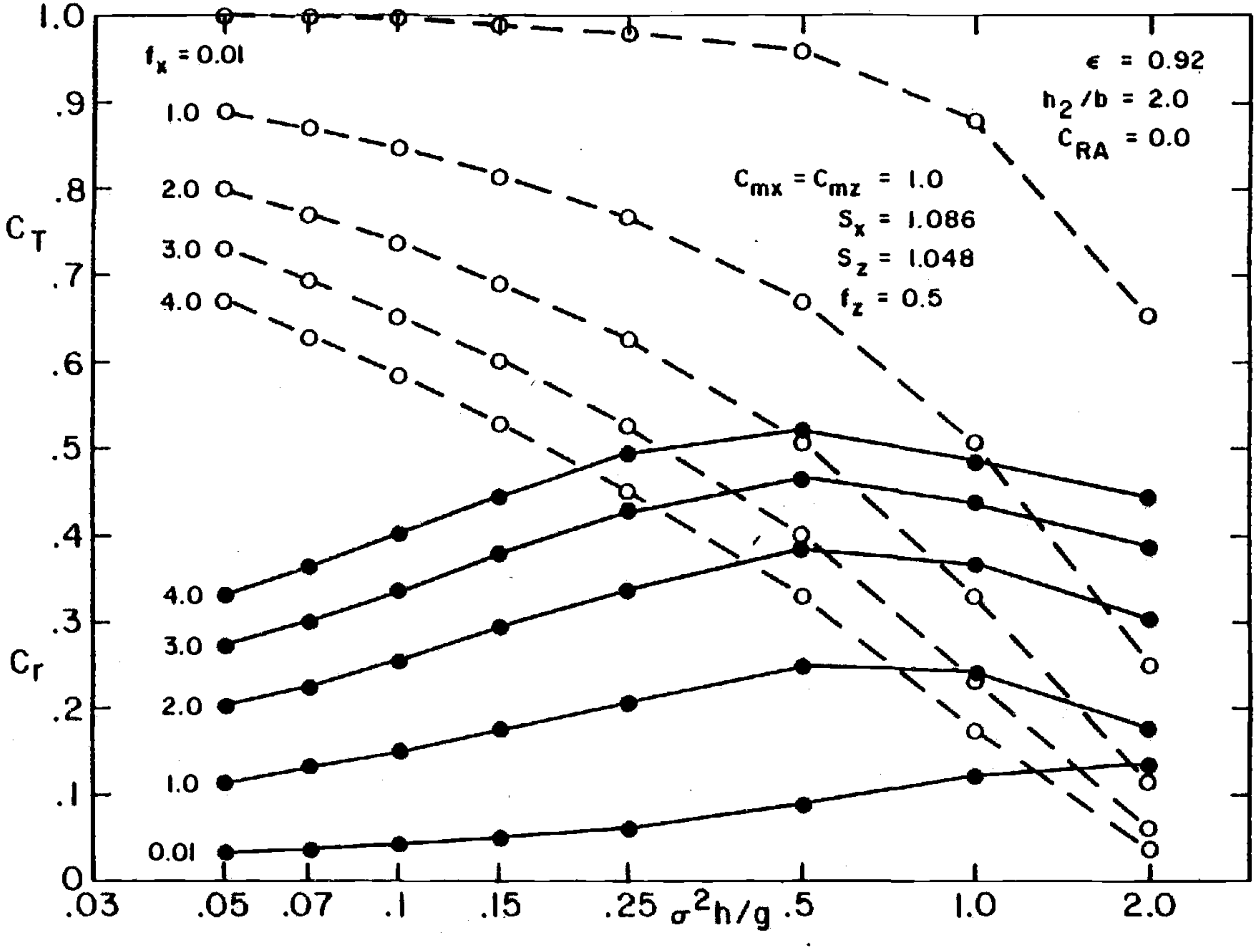

Figure 7.2. Reflection and transmission coefficients for varying values of f_x. f_z = 0.5.

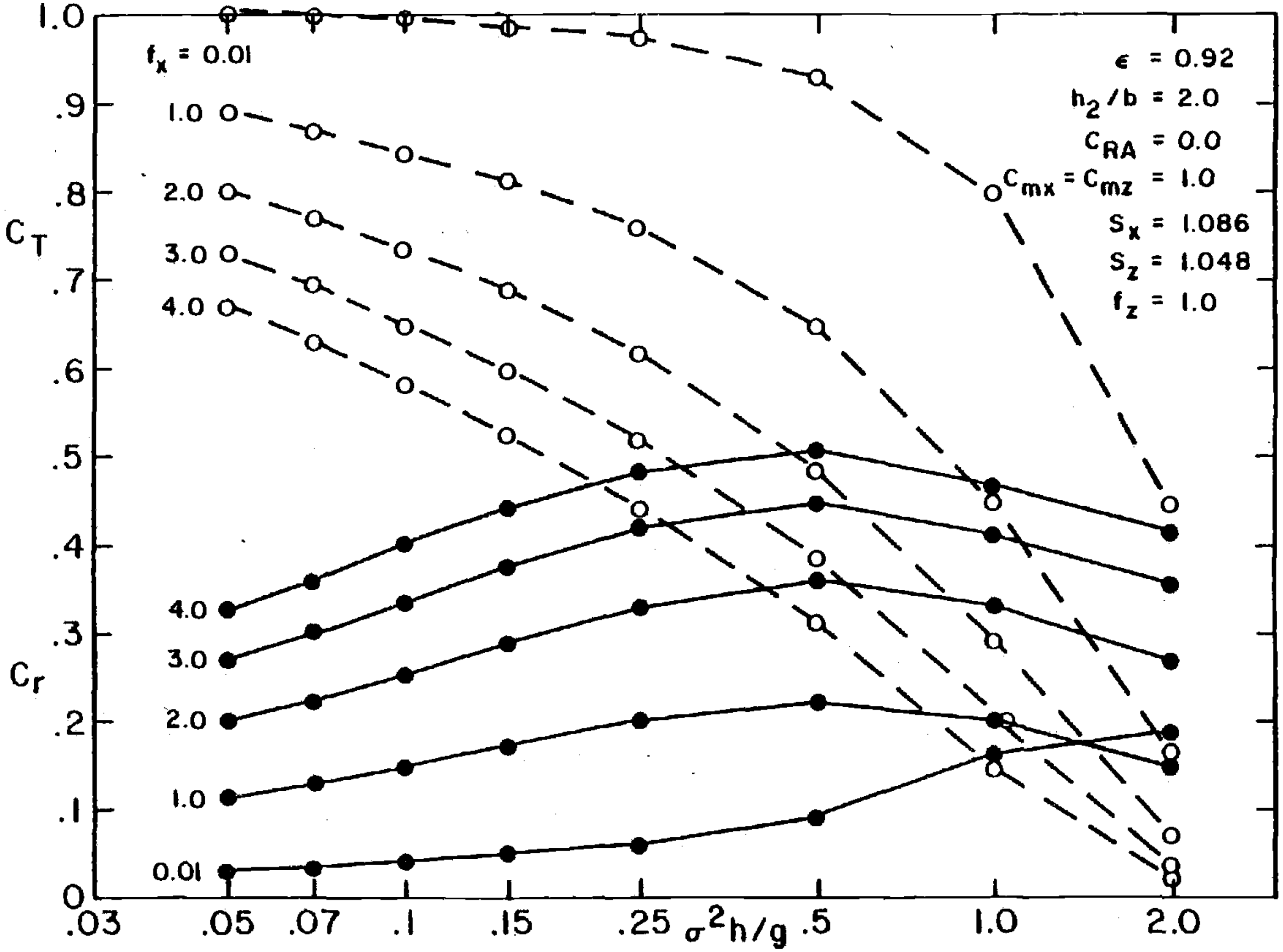

Figure 7.3. Reflection and transmission coefficients for varying values of f_x. f_z = 1.0.

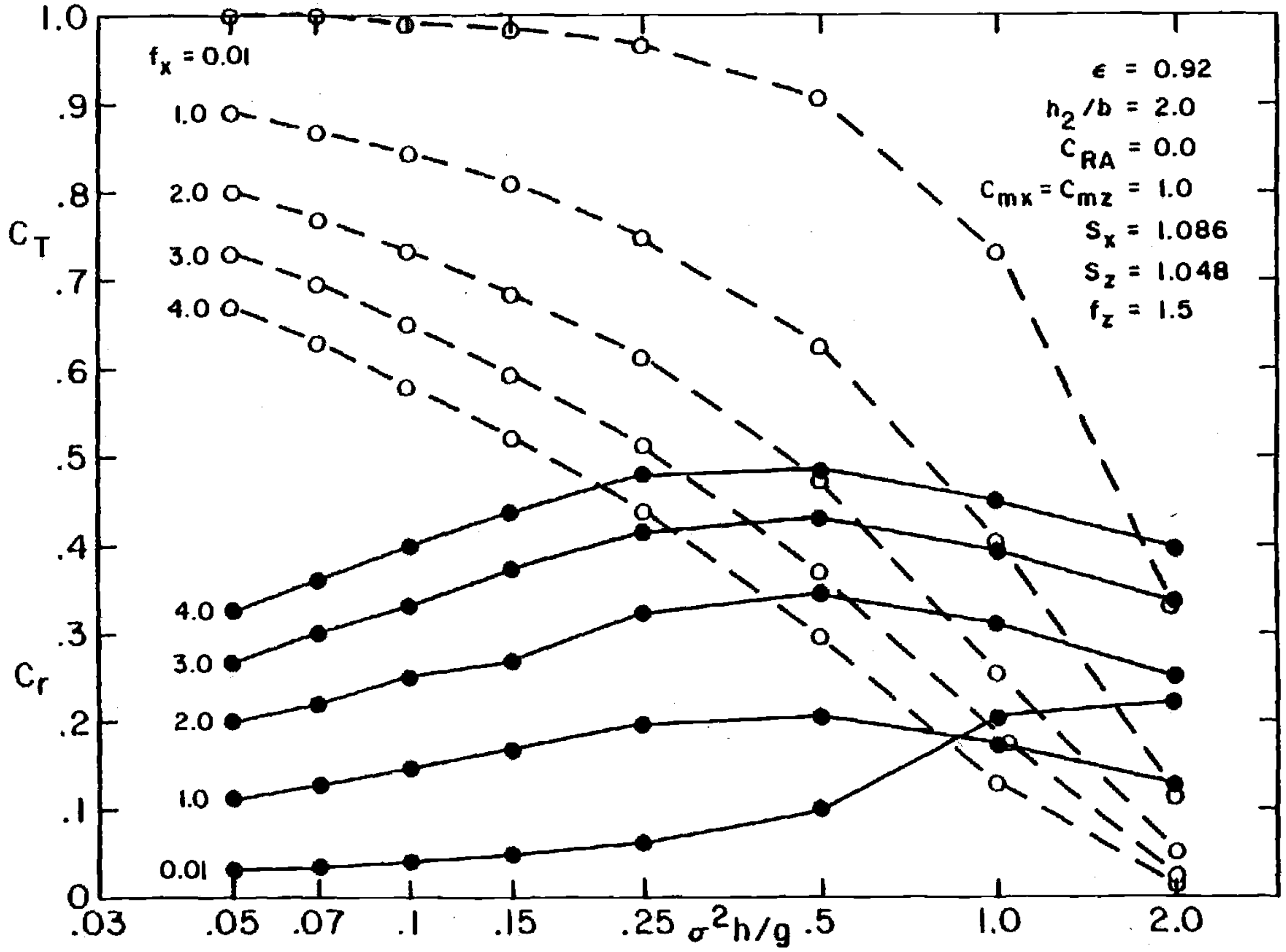

Figure 7.4. Reflection and transmission coefficients for varying values of f_x. f_z = 1.5.

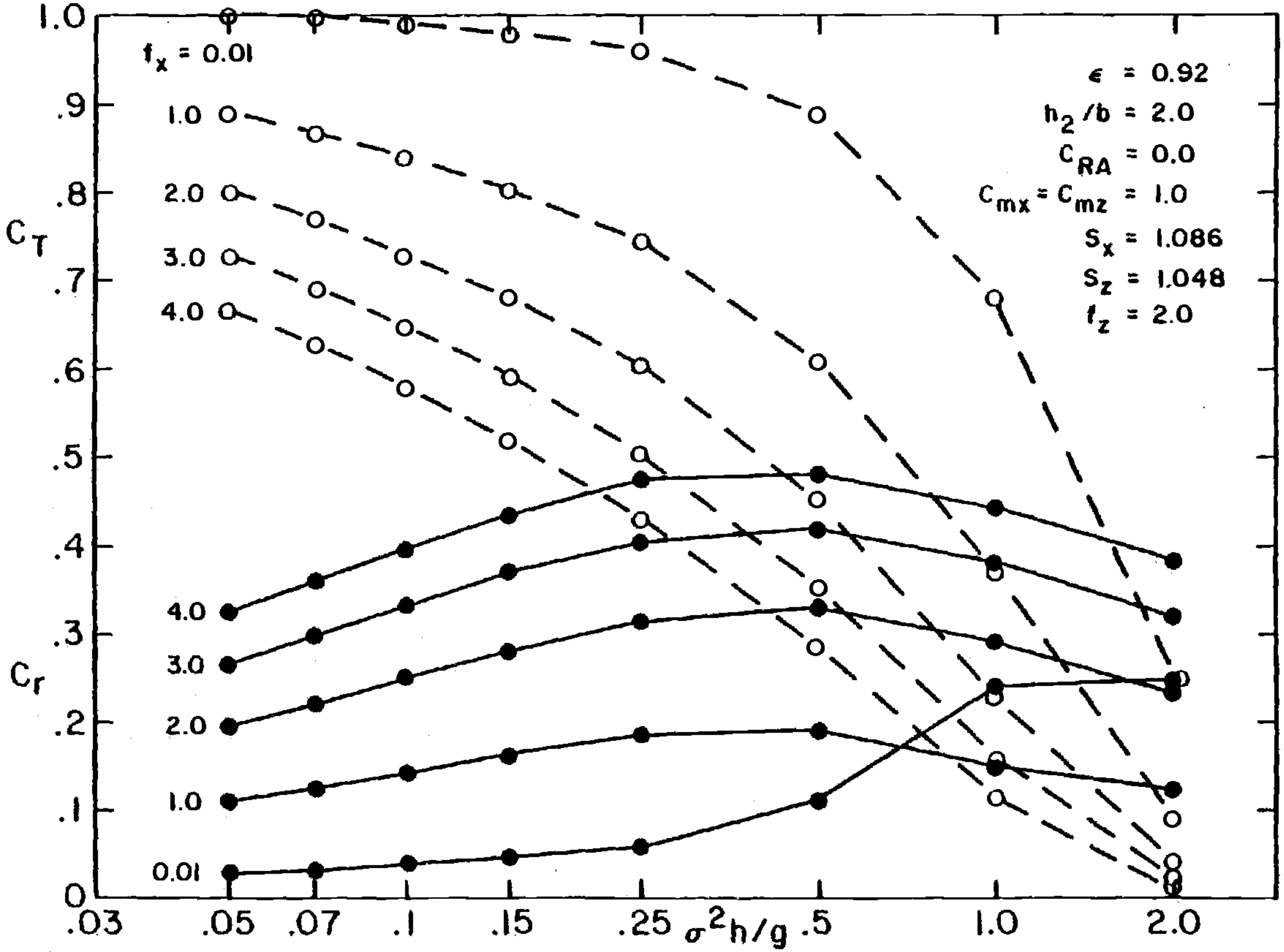

Figure. 7.5. Reflection and transmission coefficients for varying values of f_x. f_z = 2.0.

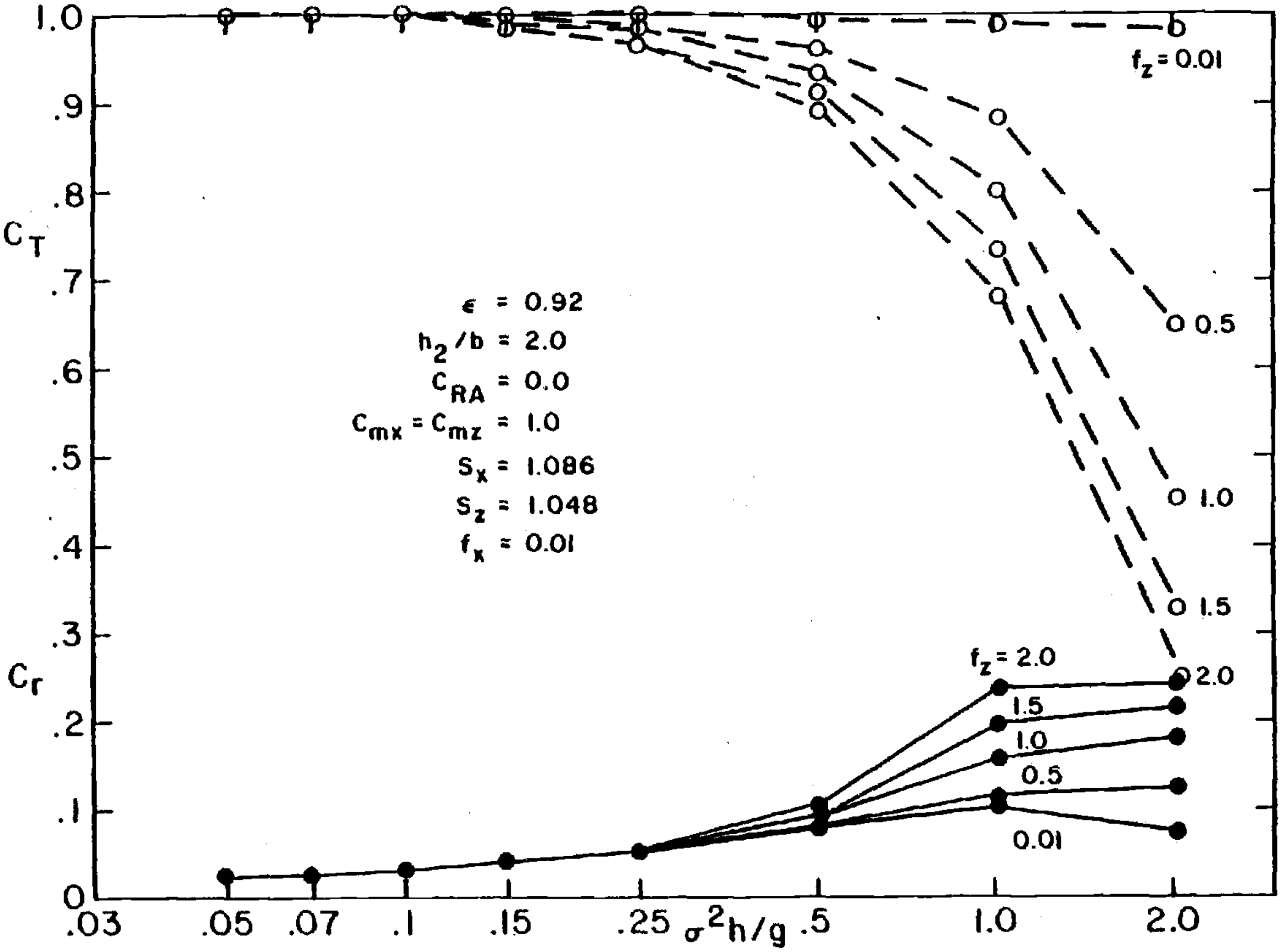

Figure 7.6. Reflection and transmission coefficients for varying values of f_z. $f_x = 0.01$.

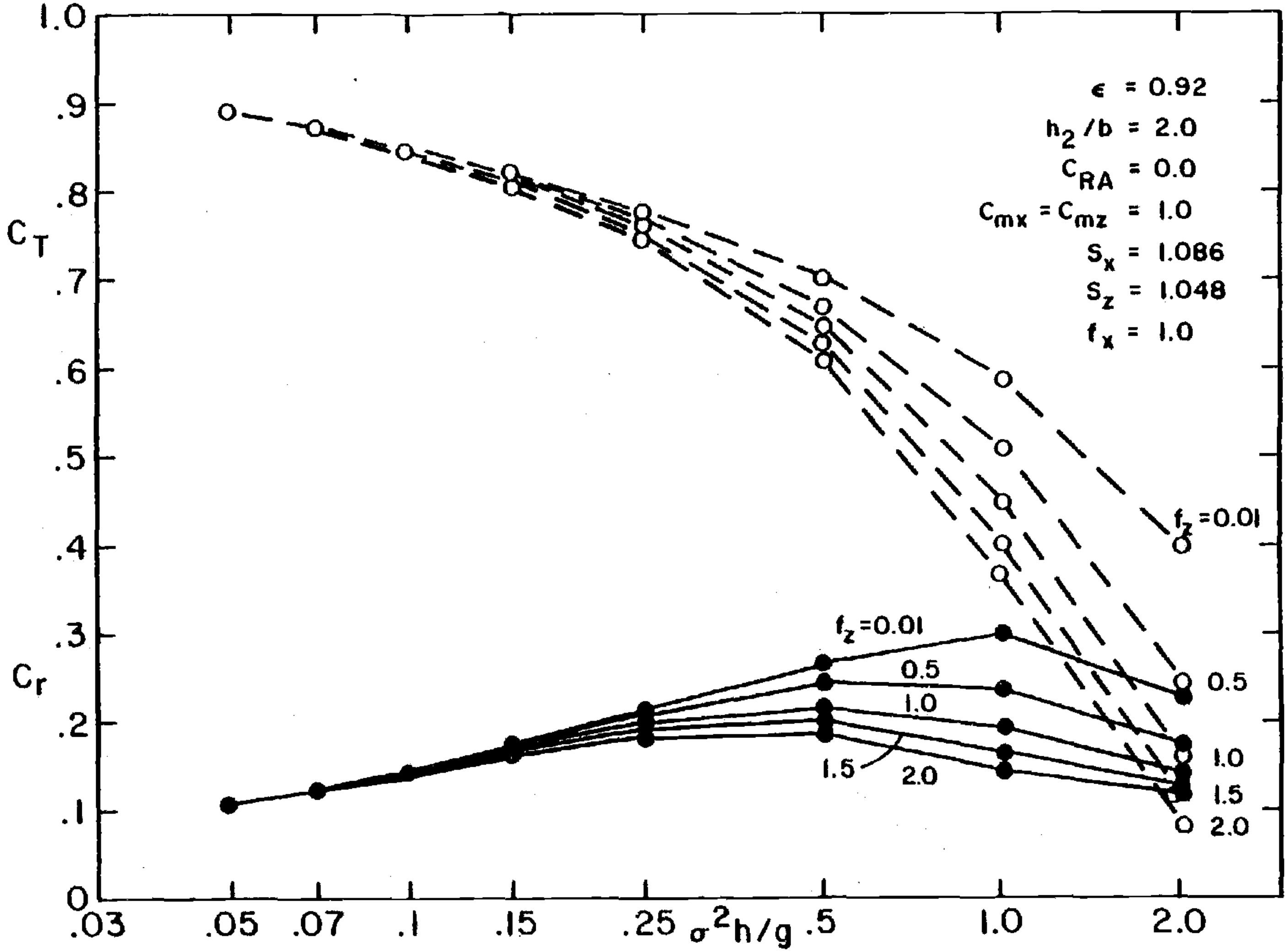

Figure 7.7. Reflection and transmission coefficients for varying values of f_z. f_x = 1.0.

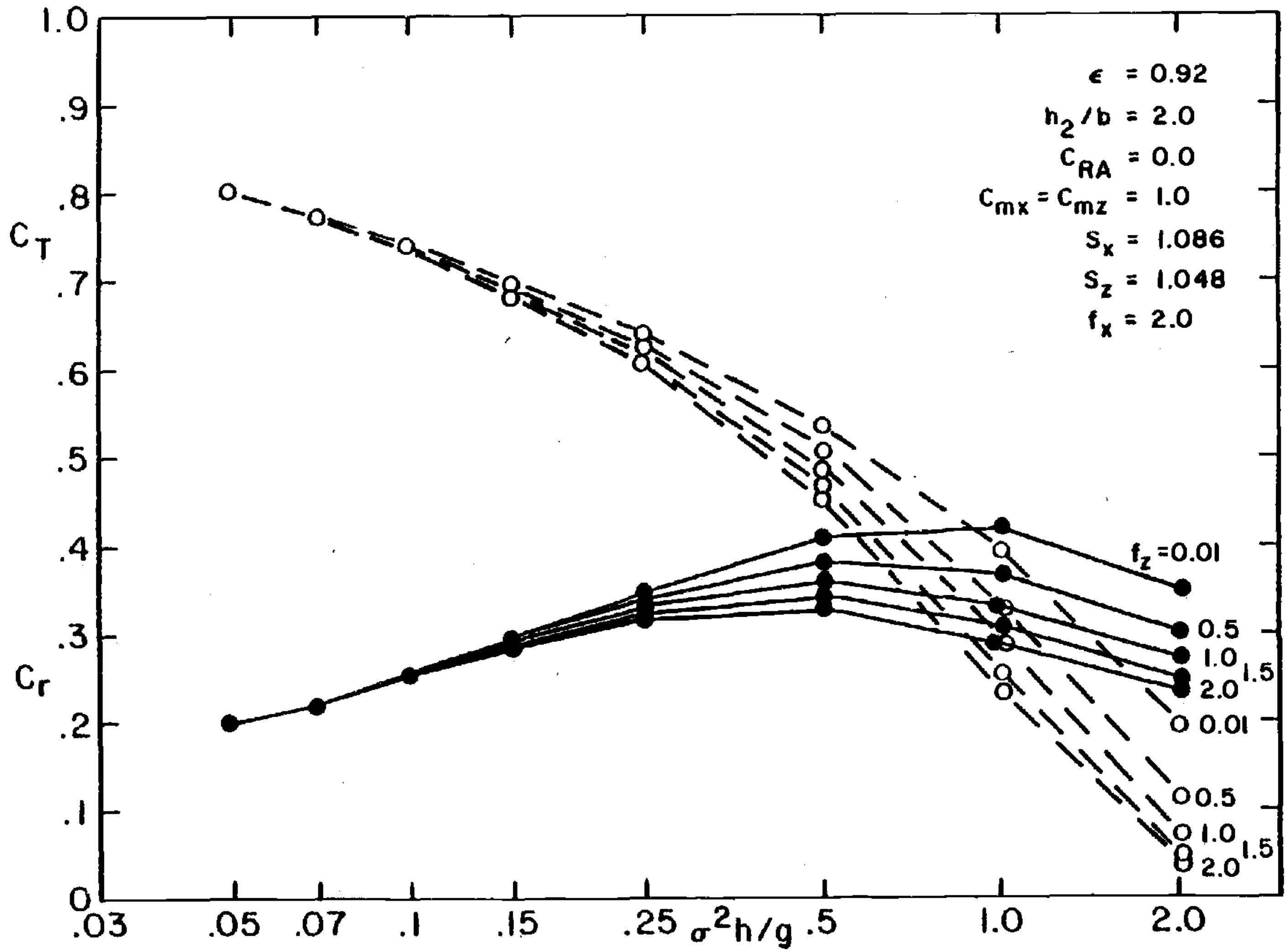

Figure 7.8. Reflection and transmission coefficients for varying values of f_z. f_x = 2.0.

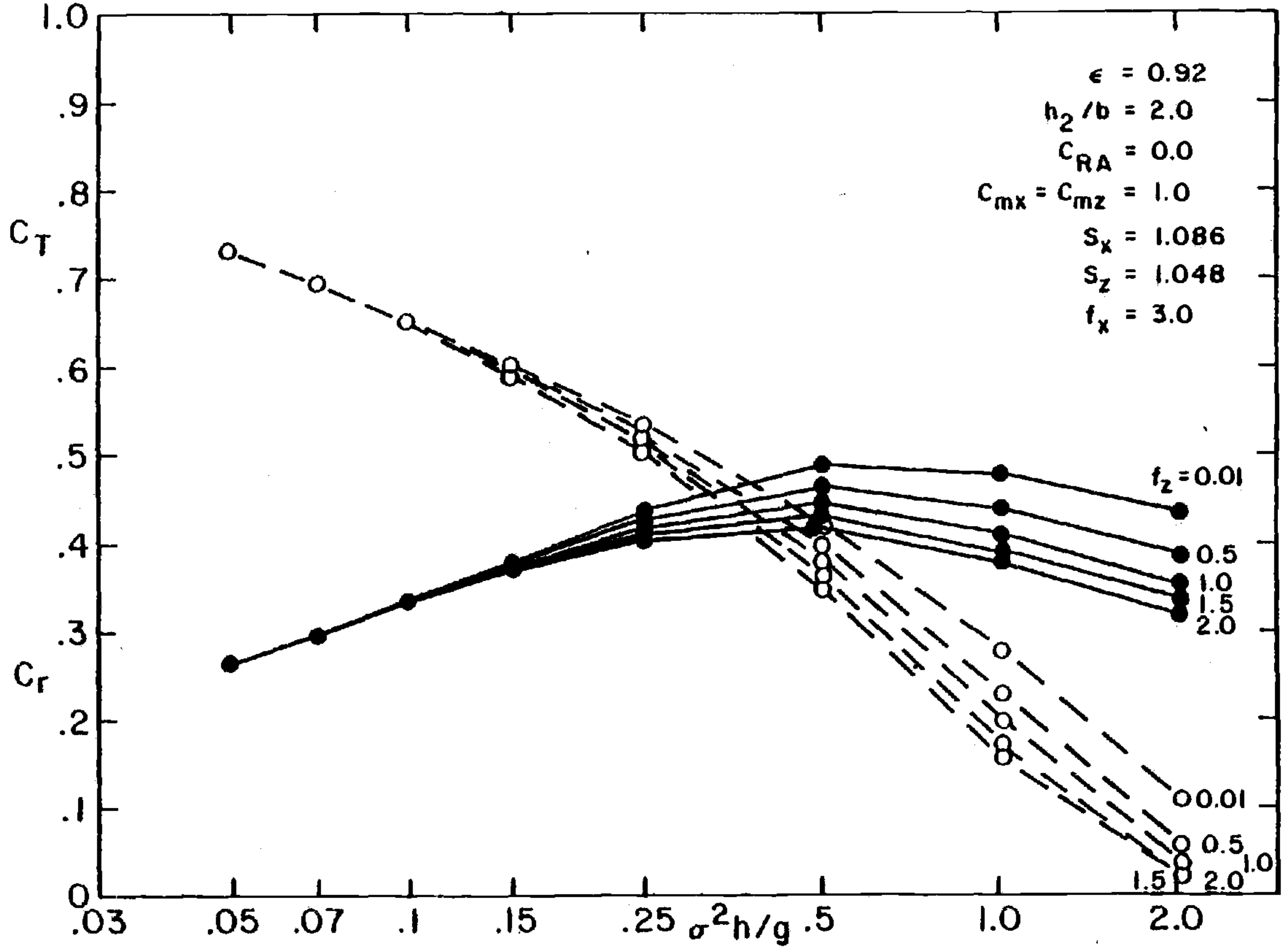

Figure 7.9. Reflection and transmission coefficients for varying values of f_z. $f_x = 3.0$.

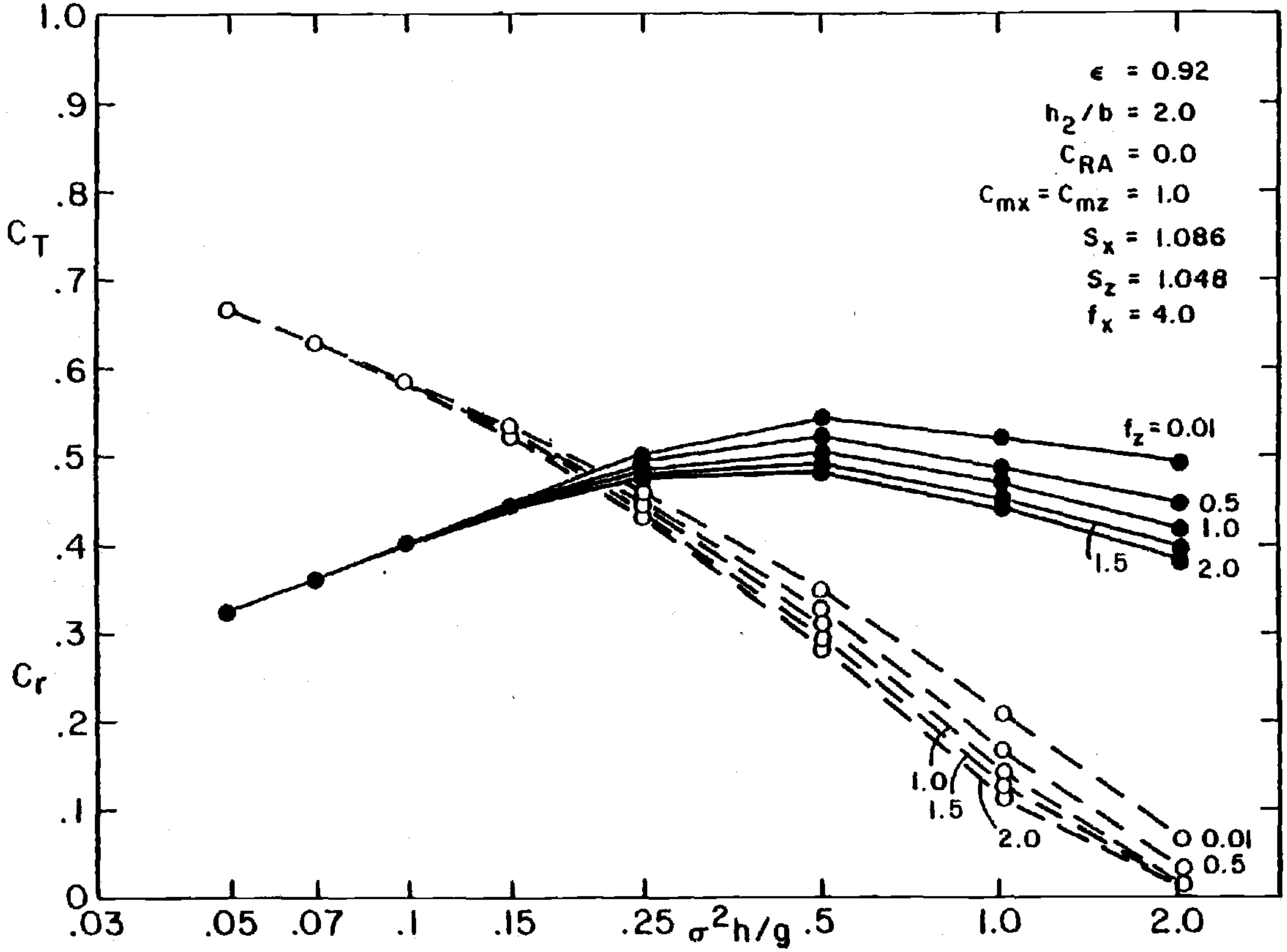

Figure 7. 10. Reflection and transmission coefficients for varying values of f_z. $f_x = 4.0$.

here is to verify how the analytical model reacts to the changing values of f_x and f_z. The value of the structural porosity is $\epsilon = 0.92$ for this portion of the sensitivity study. This value conforms to that of a fairly open structure such as that of Fig. 6.2.

As might be expected, Figs. 7.1 through 7.10 all indicate that the transmission coefficient decreases with increasing values of $\sigma^2 h/g$. In analogy, this indicates that the structure appears to be quite transparent to the long, low frequency waves, e.g., a tide, in the extreme, while the short, high frequency waves are considerably less transmissible. In addition, these same figures indicate that the transmission coefficient decreases in all cases with increasing values of the dimensionless damping coefficients, f_x and f_z, as expected. This decrease tends to be somewhat more pronounced at the intermediate and higher values of $\sigma^2 h/g$.

Contrary to the transmission coefficient behavior, the reflection coefficient data shown in Figs. 7.1 through 7.10 indicate a general peaking trend, with the maximum occurring at intermediate to higher values of $\sigma^2 h/g$. Figures 7.1 through 7.5 indicate that the reflection coefficient also generally tends to increase with increasing values of the dimensionless horizontal damping coefficient, f_x, as expected. The exceptions to the two preceding trends occur when the value of the dimensionless horizontal damping coefficient approximates zero

($f_x = .01$) and the vertical dimensionless damping coefficient is greater than f_x (see Figs. 7.2 through 7.6). These exceptions are not particularly credible since in order for f_x to approximate zero there can be almost no vertical or y-directed members and thus the x-members to which f_z corresponds must be either neutrally buoyant, or vertically supported by cables, or very infrequent vertical members.

It is somewhat surprising to note that the reflection coefficient decreases with increasing values of the dimensionless vertical damping coefficient, f_z, as shown in Figs. 7.7 through 7.10. This intuitive anomaly is also present in Figs. 7.21 through 7.25 for increasing values of the vertical added mass coefficient, C_{mz}, and, consequently, increasing values of the vertical inertial coefficient, S_z. The complexity of the simultaneous system of equations given by Eqs. (4.2.2, 4.2.3, 4.2.5 and 4.2.6) make it impossible to discern the effects of varying f_z and S_z although it is known that these constants have a direct bearing upon the values of A_z and k_{2n}. However, since the magnitude of these coefficients is indicative of the fluid resistance to wave excitation, it is unexpected that an increase in their magnitude would result in decreased wave reflection. A plausible explanation for this behavior in the increasing f_z case is that the analytical model predicts that the wavelength within the structure (determined from the real part of k_{21}) increases with increasing f_z values although $\sigma^2 h/g$ remains constant. Generally speaking, long waves are reflected less and transmitted more. However, the analytical model also predicts that the wave dissipation rate within the structure also increases with increasing f_z, thereby decreasing both the positive and negative direction propagating waves in the structure. This property tends to reduce both the reflected wave in Region I and the transmitted wave in Region III. Thus reflection is reduced with increasing values of f_z and, according to Figs. 7.7 through 7.10, the increased dissipation rate dominates the minor increase in wavelength and thus wave transmission is also reduced.

This explanation is not totally applicable to the cases of increasing S_z shown in Figs. 7.21 through 7.25 since the wavelength decreases with increasing S_z. The dissipation rate, however, increases with increasing S_z in these cases, thus, achieving the reduction in wave reflection from the interior regions of the structure.

Although the mechanism is not fully understood, the foregoing discussion leads to the conclusion that the dimensionless horizontal damping coefficient, f_x, and, as will be seen in the next section, the horizontal inertial coefficient, S_x, apparently determine the initial admissibility of a particular wave form into the structure through the seaward interface to a much higher degree than f_z or S_z. Once inside the structure, all four of these coefficients combine to determine the rate of dissipation.

There is a slightly discernible trend for the maximum, or the peak, value of the reflection coefficient to shift from $\sigma^2 h/g$ values approximating unity towards values of one-half with increasing values of the dimensionless damping coefficients. This trend is also apparent for increasing values of the inertial coefficients as will be seen in the next section.

Finally, it is interesting to note that the reflection coefficient depicted in Fig. 7.1 for f_x and f_z values approximating zero ($f_x = 0.01$, $f_z = 0.01$) attains a maximum value of about 11 percent at $\sigma^2 h/g = 1.0$. Although this might appear to be somewhat high for a structure in which viscous damping is virtually non-existent, the reflectivity may be explained by the eight percent reduction in flow volume due to the 92 percent structural porosity and, also, the inertial effects due to the finite inertial coefficient S_x.

7.3. Variation of the Added Mass Coefficients C_{mx}, C_{mz}, and the Structural Porosity, ϵ

Figures 7.11 through 7.15 depict the computed reflection and transmission coefficients for a structural porosity of 0.92 where the added mass coefficient for the x-direction assumes five different values within the range $0.0 \leq C_{mx} \leq 4.0$ on each plot. The added mass coefficient for the vertical direction takes on the same five values

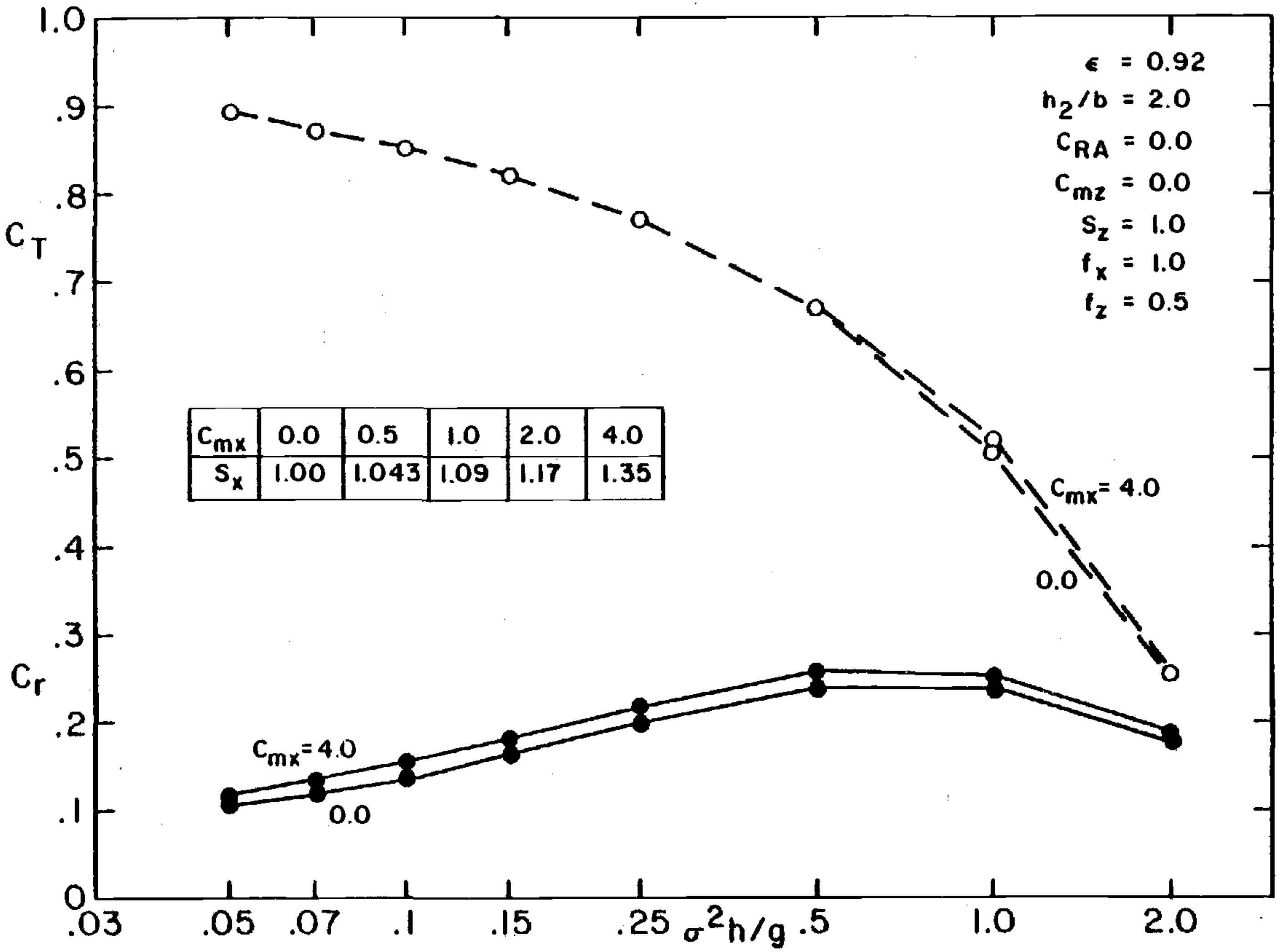

Figure 7.11. Reflection and transmission coefficients for varying values of C_{mx}, S_x. C_{mz} = 0.0, S_z = 1.0.

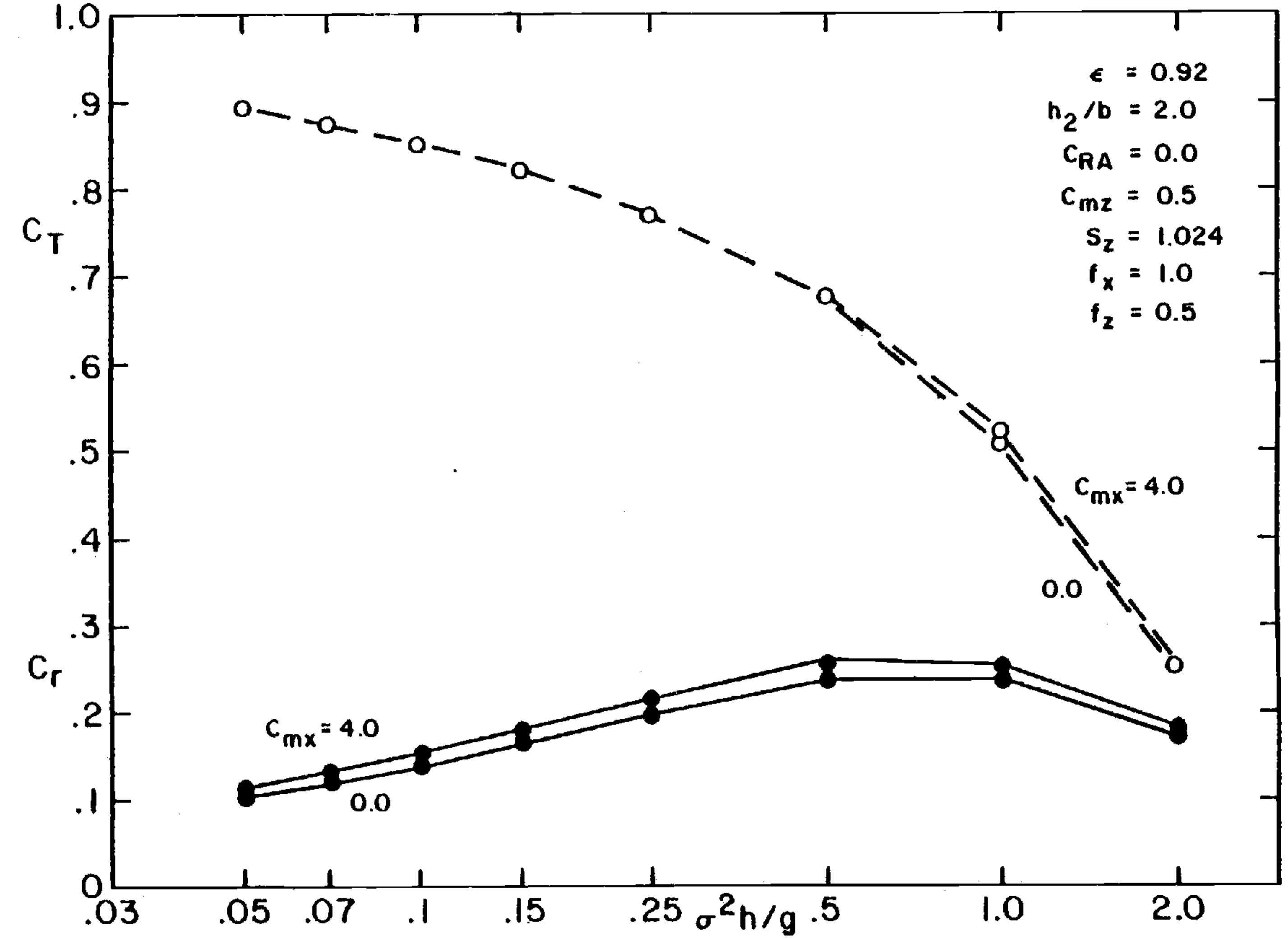

Figure 7. 12. Reflection and transmission coefficients for varying values of C_{mx}, S_x. C_{mz} = 0. 5, S_z = 1. 024.

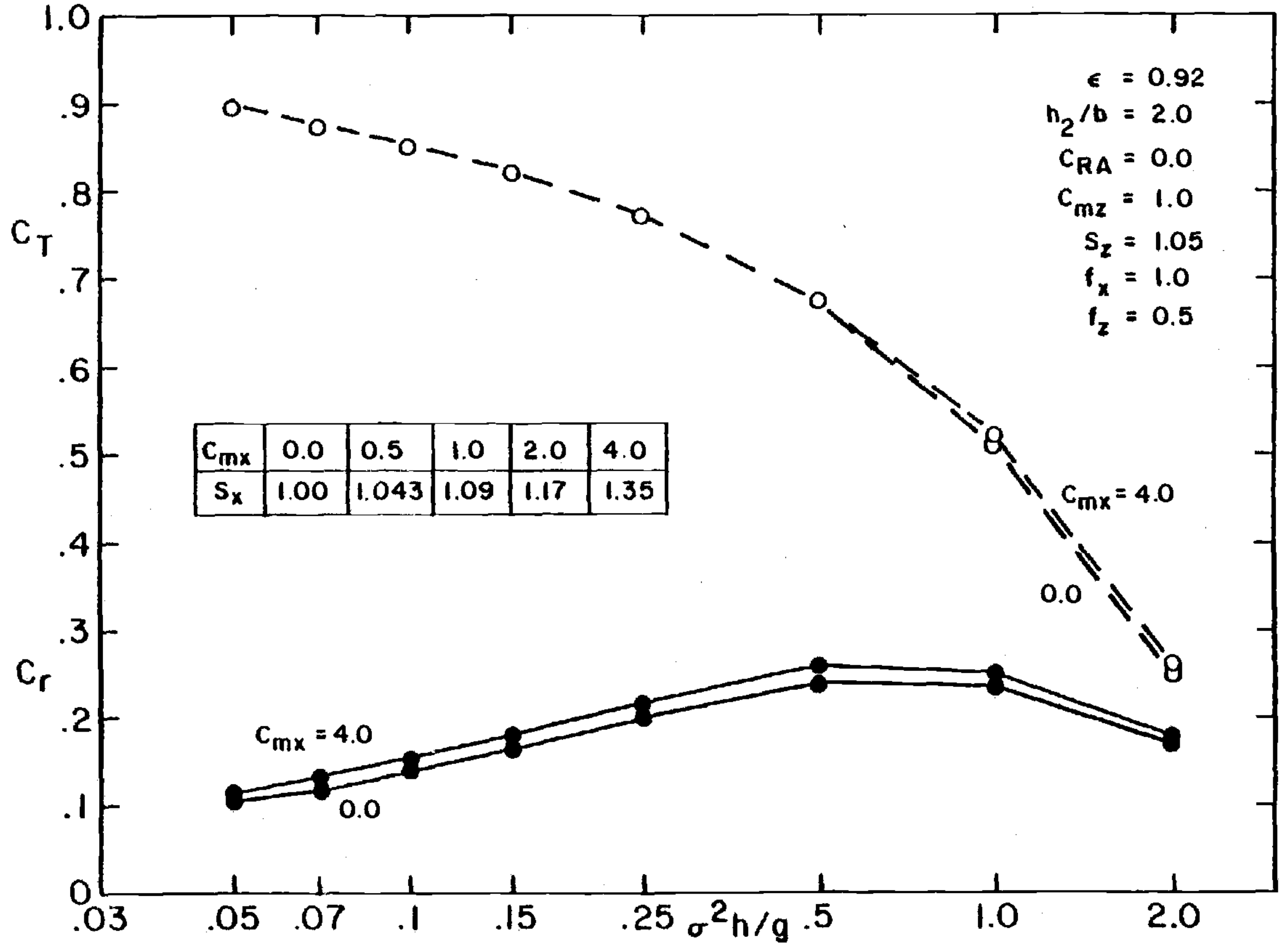

Figure 7.13. Reflection and transmission coefficients for varying values of C_{mx}, S_x. C_{mz} = 1.0, S_z = 1.05.

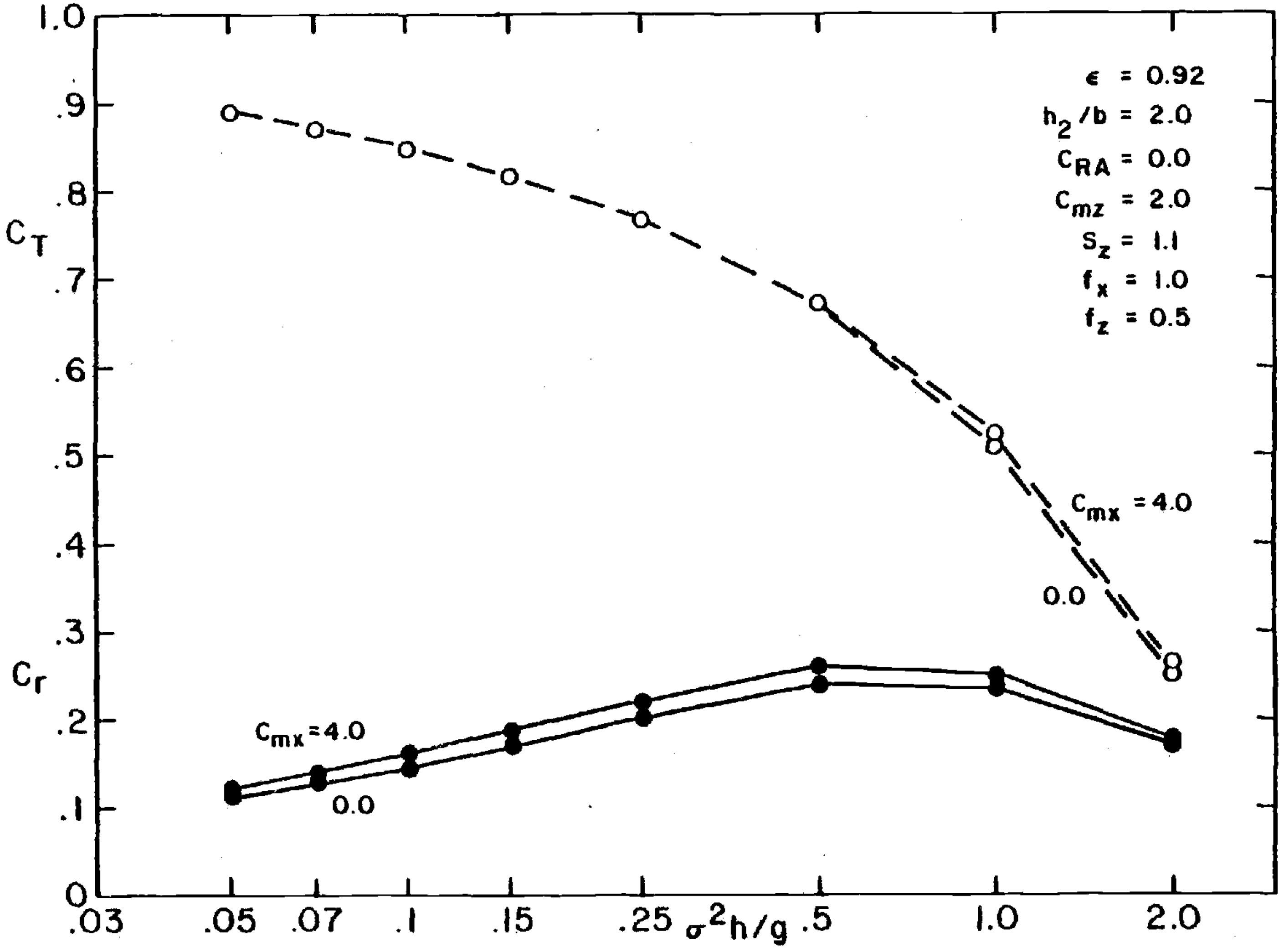

Figure 7.14. Reflection and transmission coefficients for varying values of C_{mx}, S_x. C_{mz} = 2.0, S_z = 1.1.

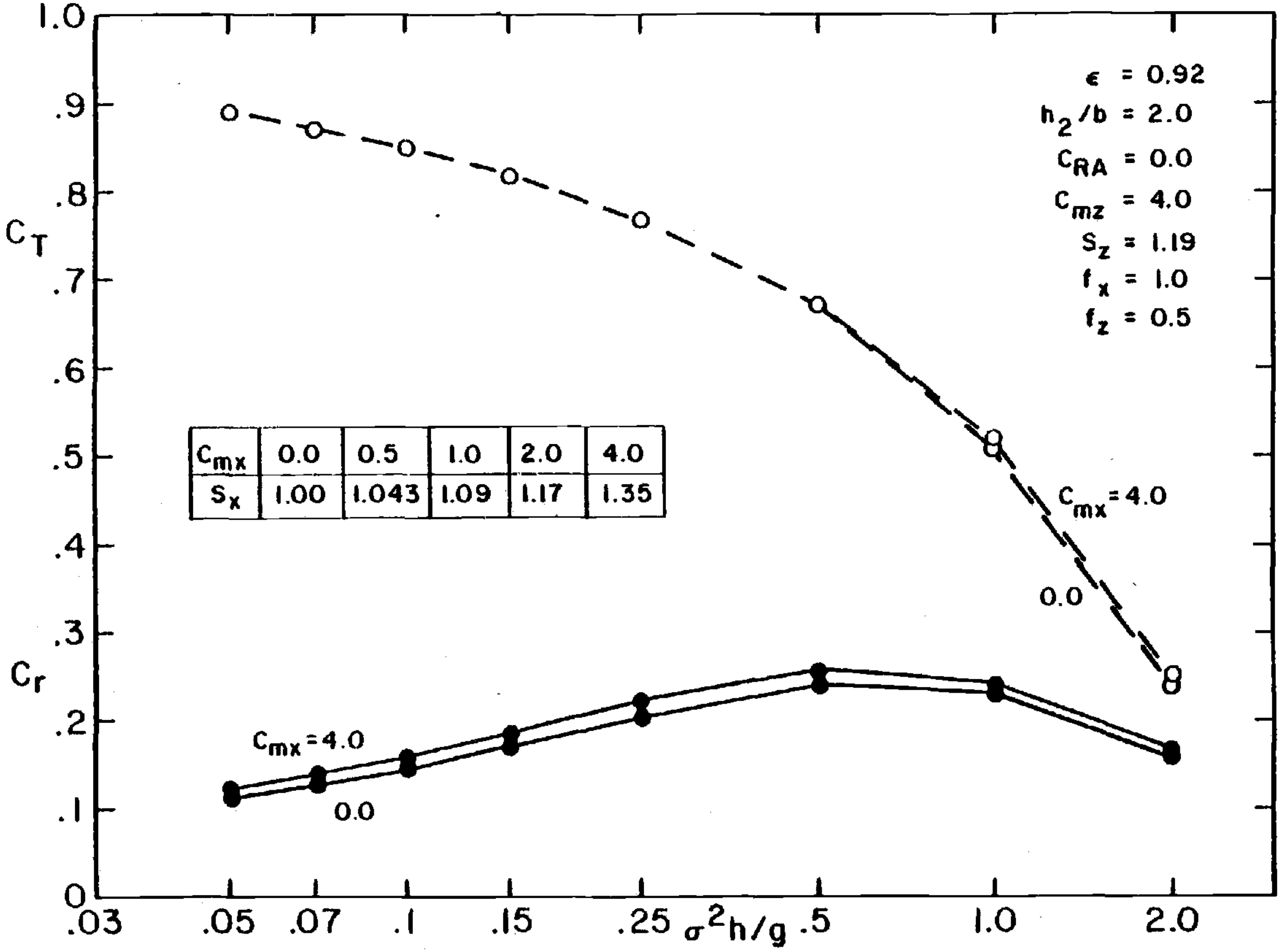

Figure 7.15. Reflection and transmission coefficients for varying values of C_{mx}, S_x. C_{mz} = 4.0, S_x = 1.19.

as C_{mx} but is varied from figure to figure. The horizontal and vertical inertial coefficients are calculated from Eqs. (2.4.3 and 2.4.4) respectively and are listed below in Table 7.1 with the added mass coefficients.

Table 7.1. $\epsilon = 0.92$.

C_{mx}:	0.0	0.5	1.0	2.0	4.0
S_x:	1.0	1.043	1.09	1.17	1.35
C_{mz}:	0.0	0.5	1.0	2.0	4.0
S_z:	1.0	1.024	1.05	1.1	1.19

These parameters as well as the structural parameters are also listed on each of the figures.

As shown in Figs. 7.11 through 7.15 variations in the computed reflection and transmission coefficients with the changes in C_{mx} and C_{mz} are almost nil. Indeed, these variations were so small that it was not possible to plot all five reflection and transmission coefficients computed at each of the eight values of $\sigma^2 h/g$ due to crowding. Consequently only the envelopes are shown on the figures. Thus, it is concluded that the analytical analysis of fairly open structures, i.e., structures of high porosity, is virtually unresponsive to the value of the added mass coefficients.

As in Figs. 7.1 through 7.10, Figs. 7.11 through 7.15 all indicate decreasing transmission coefficients with increasing $\sigma^2 h/g$ values and a peaking tendency in the reflection coefficient between the $\sigma^2 h/g$ values of 0.5 and 1.0.

Figures 7.16 through 7.20 show the computed reflection and transmission coefficients for a structural porosity of 0.66. The horizontal added mass coefficient is varied over the five values shown in Table 7.2 on each plot while the vertical added mass coefficient is varied from figure to figure over the same five values. The horizontal and vertical inertial coefficients calculated from Eqs. (2.4.3 and 2.4.4) are also shown below in Table 7.2.

Table 7.2. $\epsilon = 0.66$.

C_{mx}:	0.0	0.5	1.0	2.0	4.0
S_x:	1.0	1.23	1.45	1.91	2.81
C_{mz}:	0.0	0.5	1.0	2.0	4.0
S_z:	1.0	1.2	1.39	1.78	2.56

Other than the change in the porosities and the resulting change in the inertial coefficients, all of the structural parameters of the results portrayed in Figs. 7.16 through 7.20 are identical to those of Figs. 7.11 through 7.15. As expected, the decrease in porosity leads to a decrease in the transmission coefficient and an increase in

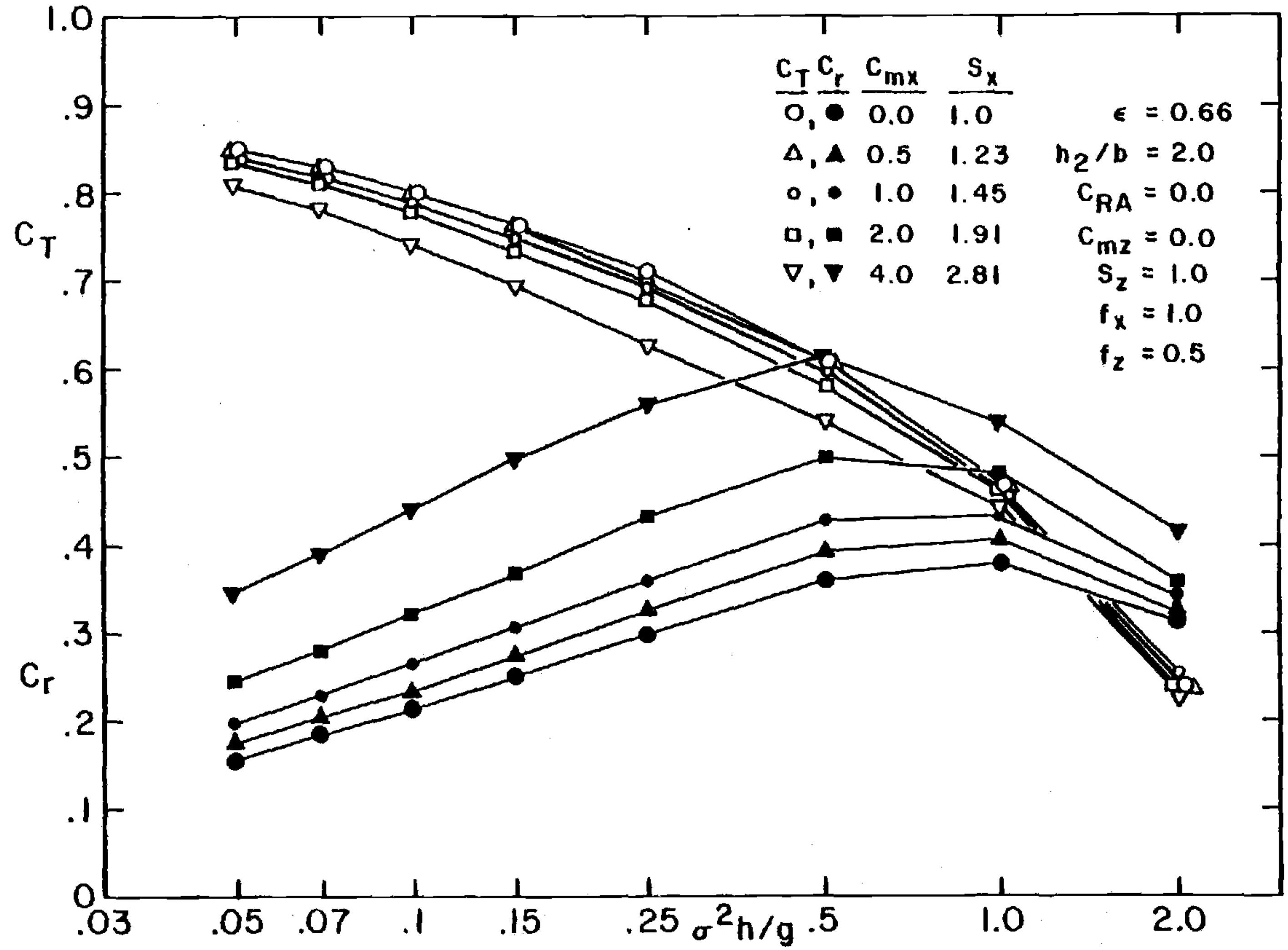

Figure 7.16. Reflection and transmission coefficients for varying values of C_{mx}, S_x. $C_{mz} = 0.0$, $S_z = 1.0$.

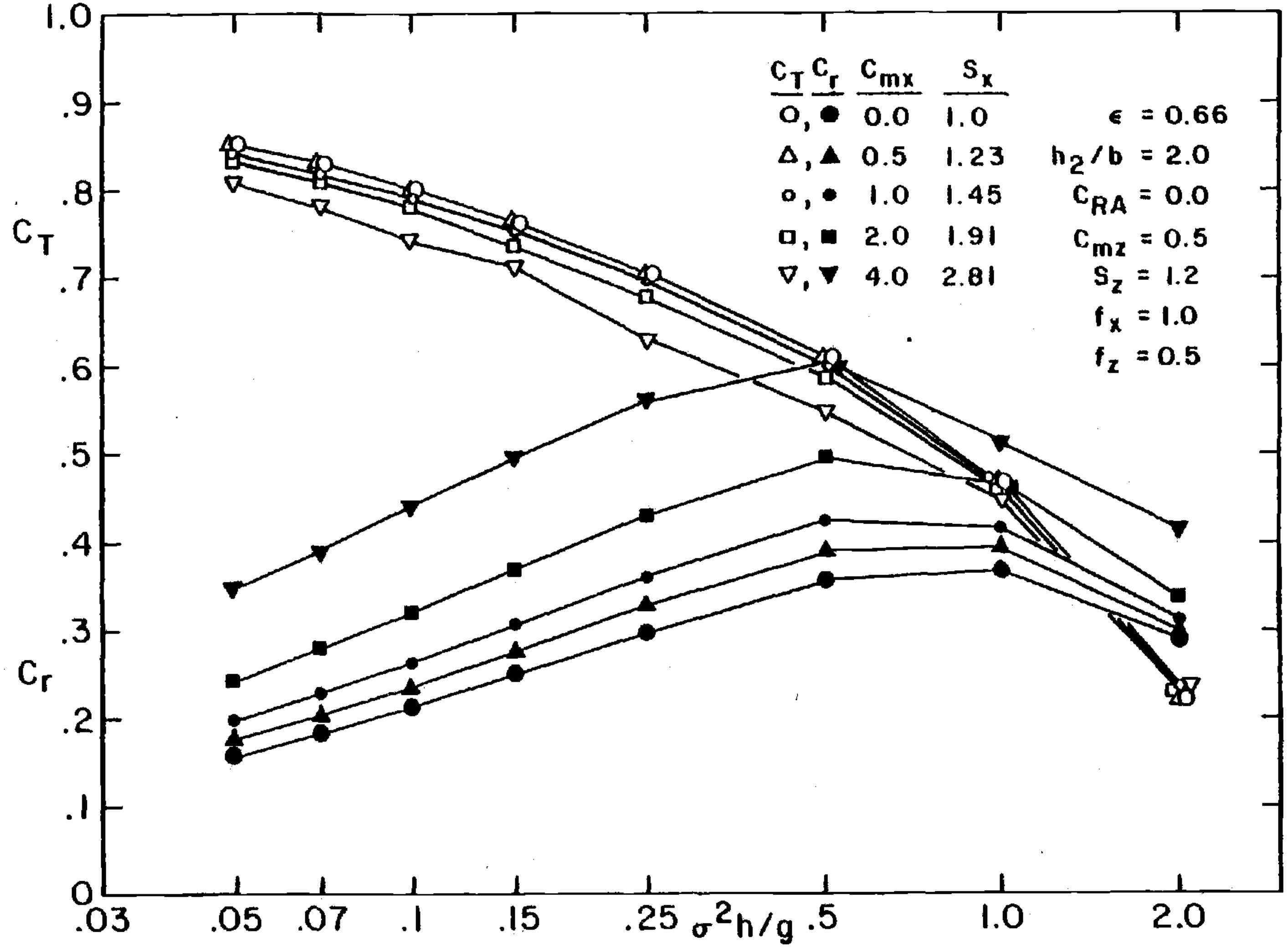

Figure 7.17. Reflection and transmission coefficients for varying values of C_{mx}, S_x. C_{mz} = 0.5, S_z = 1.2.

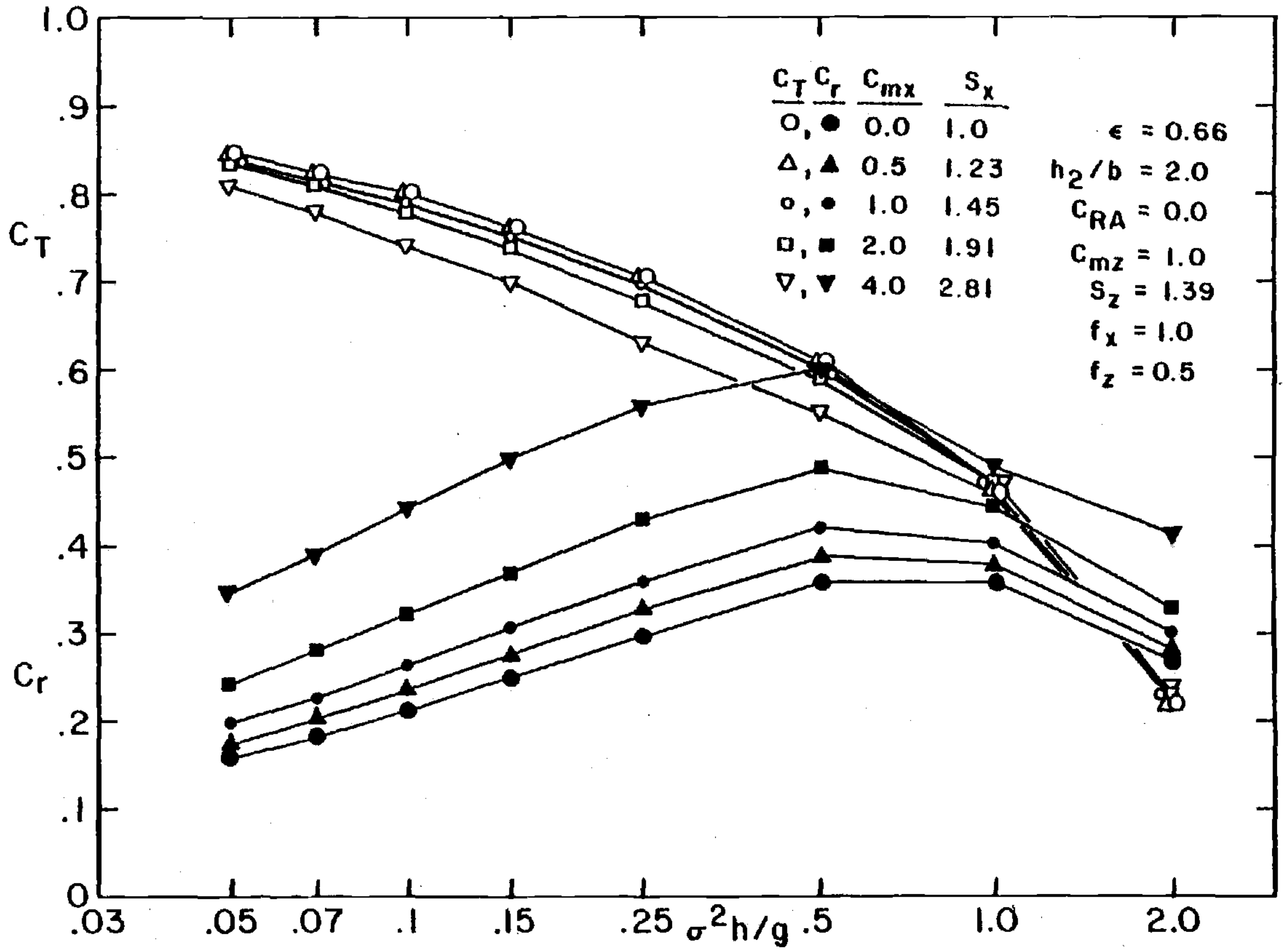

Figure 7.18. Reflection and transmission coefficients for varying values of C_{mx}, S_x. $C_{mz} = 1.0$, $S_z = 1.39$.

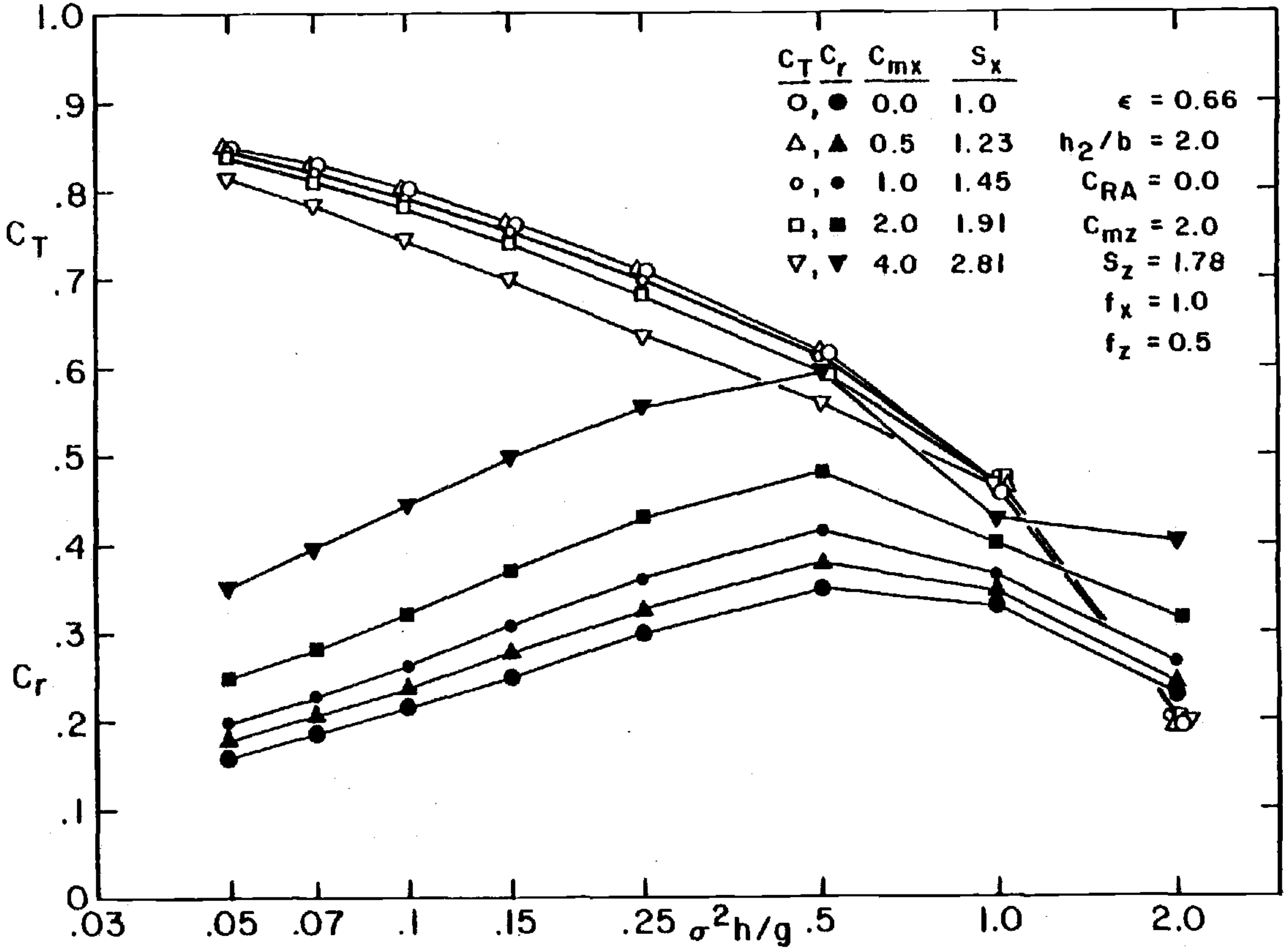

Figure 7.19. Reflection and transmission coefficients for varying values of C_{mx}, S_x. C_{mz} = 2.0, S_z = 1.78.

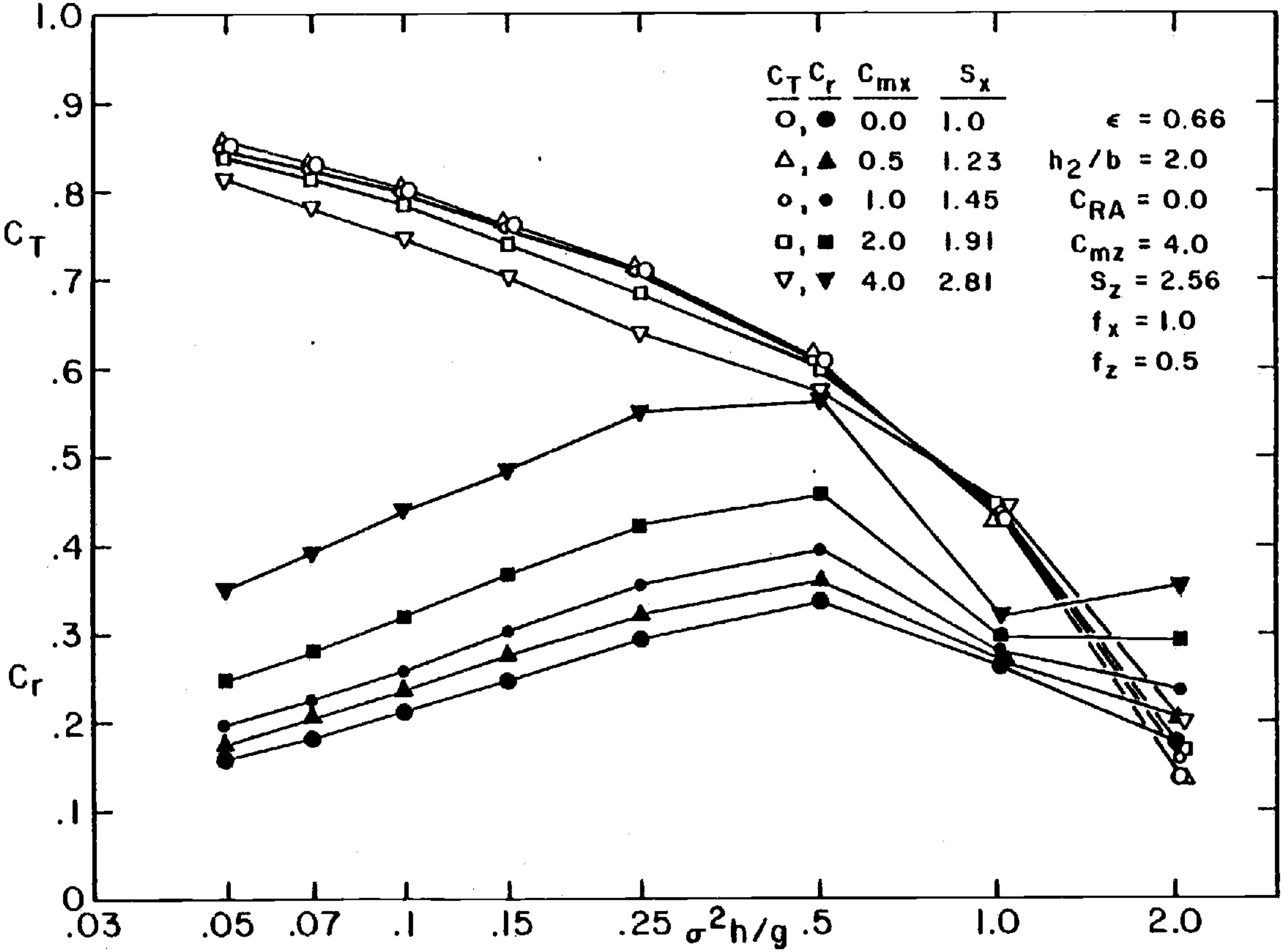

Figure 7.20. Reflection and transmission coefficients for varying values of C_{mx}, S_x. C_{mz} = 4.0, S_z = 2.56.

the reflection coefficient. However, for small values of C_{mx}, the variation in the reflection and transmission coefficients with the change in porosity is small. For large values of C_{mx}, the variation in C_T with the porosity is more pronounced at the smaller and intermediate values of $\sigma^2 h/g$ but tends toward the same C_T value at large $\sigma^2 h/g$. The change in C_r with porosity is significant at large values of C_{mx} for all $\sigma^2 h/g$ values. The reflection and transmission coefficient envelopes described by the $C_{mx} = 0.0$ and $C_{mx} = 4.0$ curves are considerably wider for the small porosity case. These changes with porosity are undoubtedly due to the resulting changes in the inertial coefficients and thus it may be concluded that the analytical model is somewhat sensitive to the value of the horizontal added mass coefficient and hence the inertial coefficient for structures of low porosity. However it should be noted in Figs. 7.16 through 7.20 that this sensitivity is not excessive when the values of the added mass coefficient recommended in Chapter V are employed, i.e., $0 \leq C_{mx} \leq .5$, since the inertial coefficient variation is small.

The computed transmission coefficients of Figs. 7.16 through 7.20 all exhibit the usual behavior, i.e., declining transmission with increasing values of $\sigma^2 h/g$ and, generally, with increasing values of C_{mx}. The exception to the latter statement occurs when $\sigma^2 h/g$ is large and C_{mz} is large; at which time C_T may increase slightly with increasing values of C_{mx}, as in Fig. 7.20.

The computed reflection coefficients of Figs. 7.16 through 7.20 all manifest the peaking tendency with peaks generally shifting from a $\sigma^2 h/g$ value of unity toward a value of 0.5 with increasing values of C_{mx} and C_{mz}. In addition, a pronounced inflection in the C_r curves is apparent when C_{mx} and C_{mz} are large and $\sigma^2 h/g$ exceeds 0.5 such that a relative minimum occurs in Fig. 7.20 for $C_{mx} = 4.0$.

Figures 7.21 through 7.25 show the data of Figs. 7.16 through 7.20 re-plotted where C_{mz} varies on each figure and C_{mx} varies from figure to figure. As was the case in Figs. 7.7 through 7.10 for the vertical dimensionless damping coefficient, the reflection coefficient curves of Figs. 7.21 through 7.25 exhibit the intuitively anomalous behavior of decreasing with increasing values of C_{mz} and, hence, increasing values of the vertical inertial coefficient. As previously reported the analytical model is predicting that fluid particle viscous and inertial damping in the vertical direction does not inhibit wave intrusion into the structure, but rather it increases energy losses and thus lowers both the reflection and transmission coefficients.

More explicitly, increasing the added mass coefficient, C_{mz}, and the dimensionless damping coefficient, f_z, for the vertical direction produces a reduction in wave reflection for relatively short

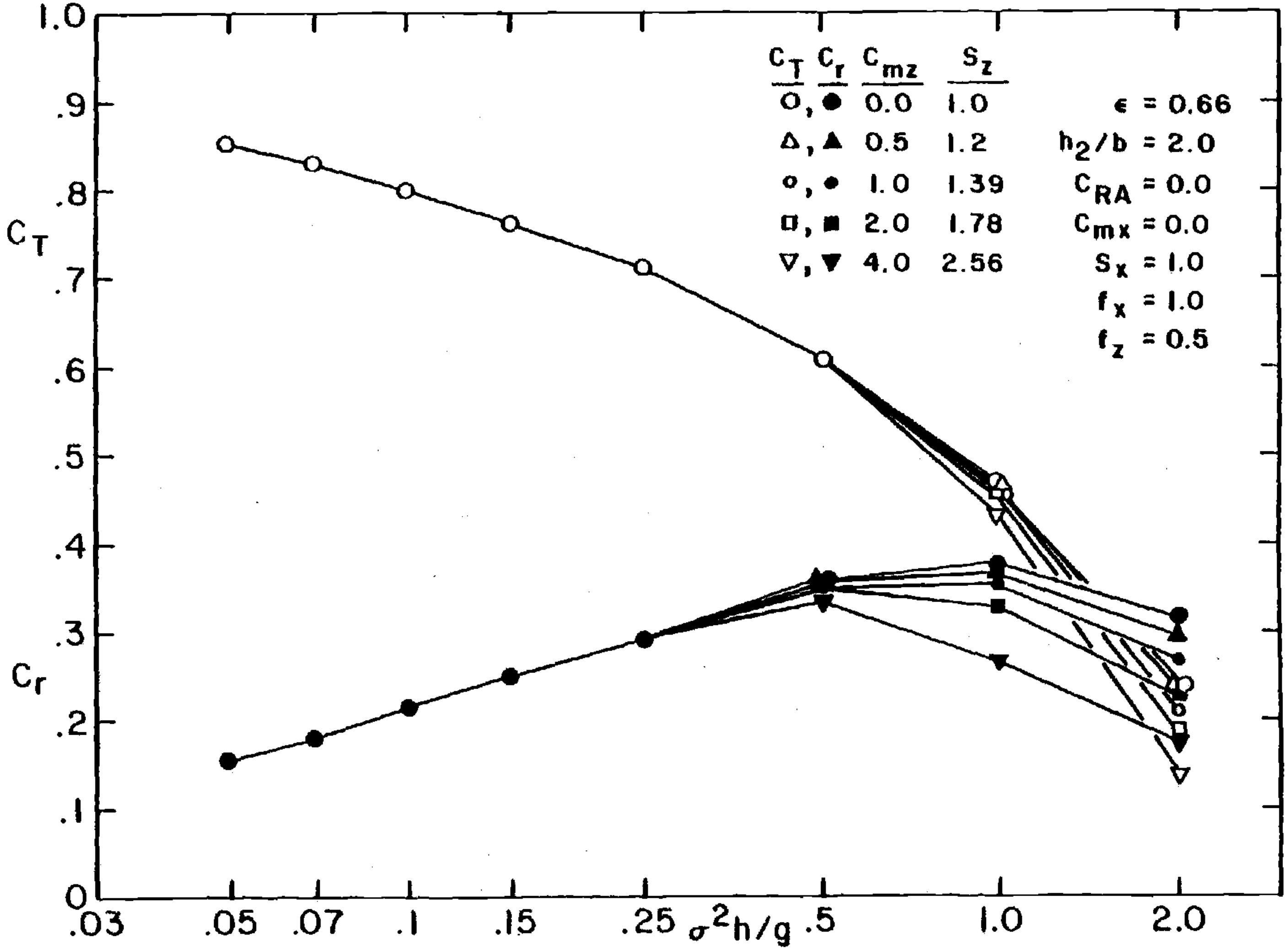

Figure 7.21. Reflection and transmission coefficients for varying values of C_{mz}, S_z. C_{mx} = 0.0, S_x = 1.0.

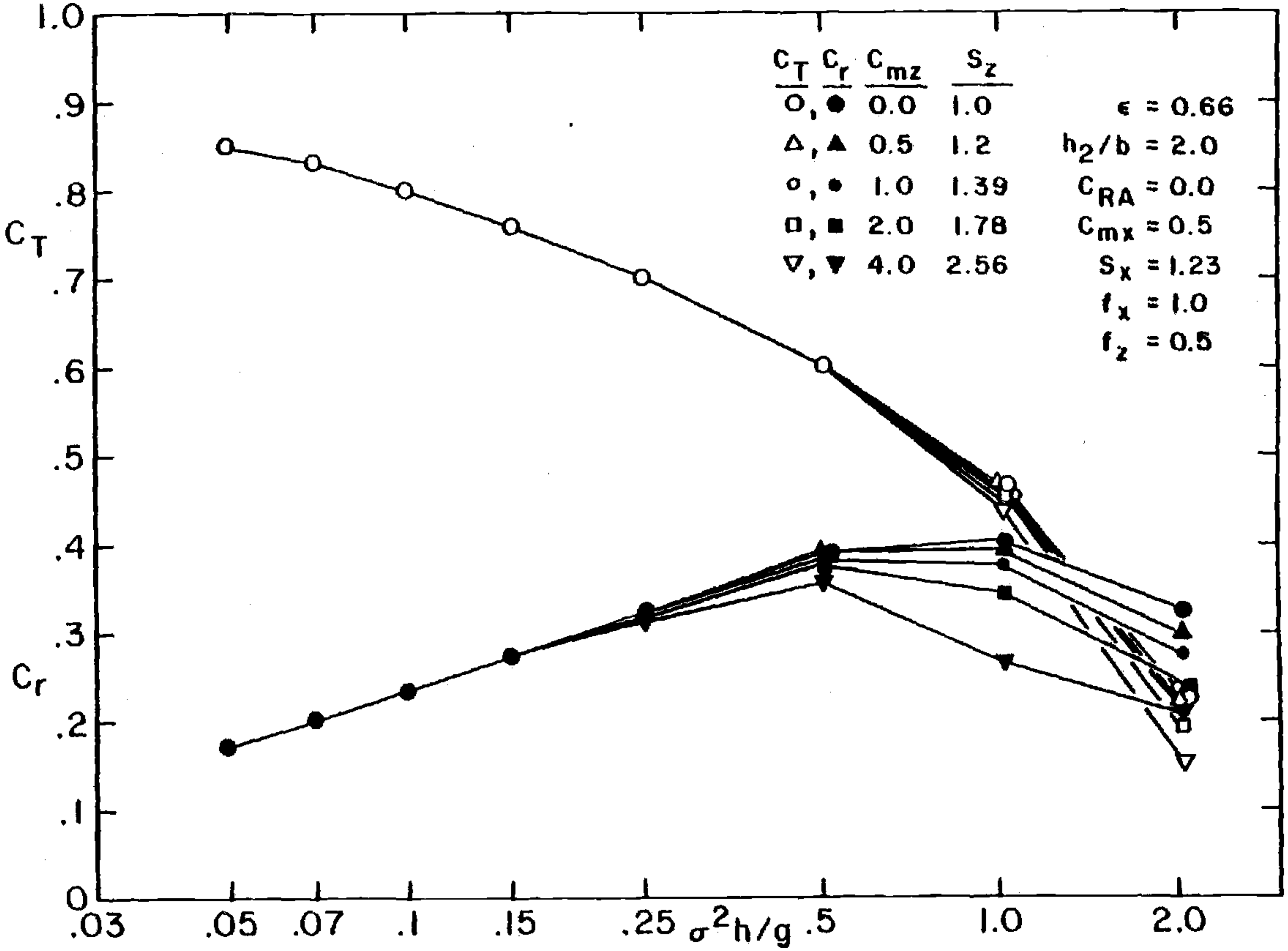

Figure 7.22. Reflection and transmission coefficients for varying values of C_{mz}, S_z. C_{mx} = 0.5, S_x = 1.23.

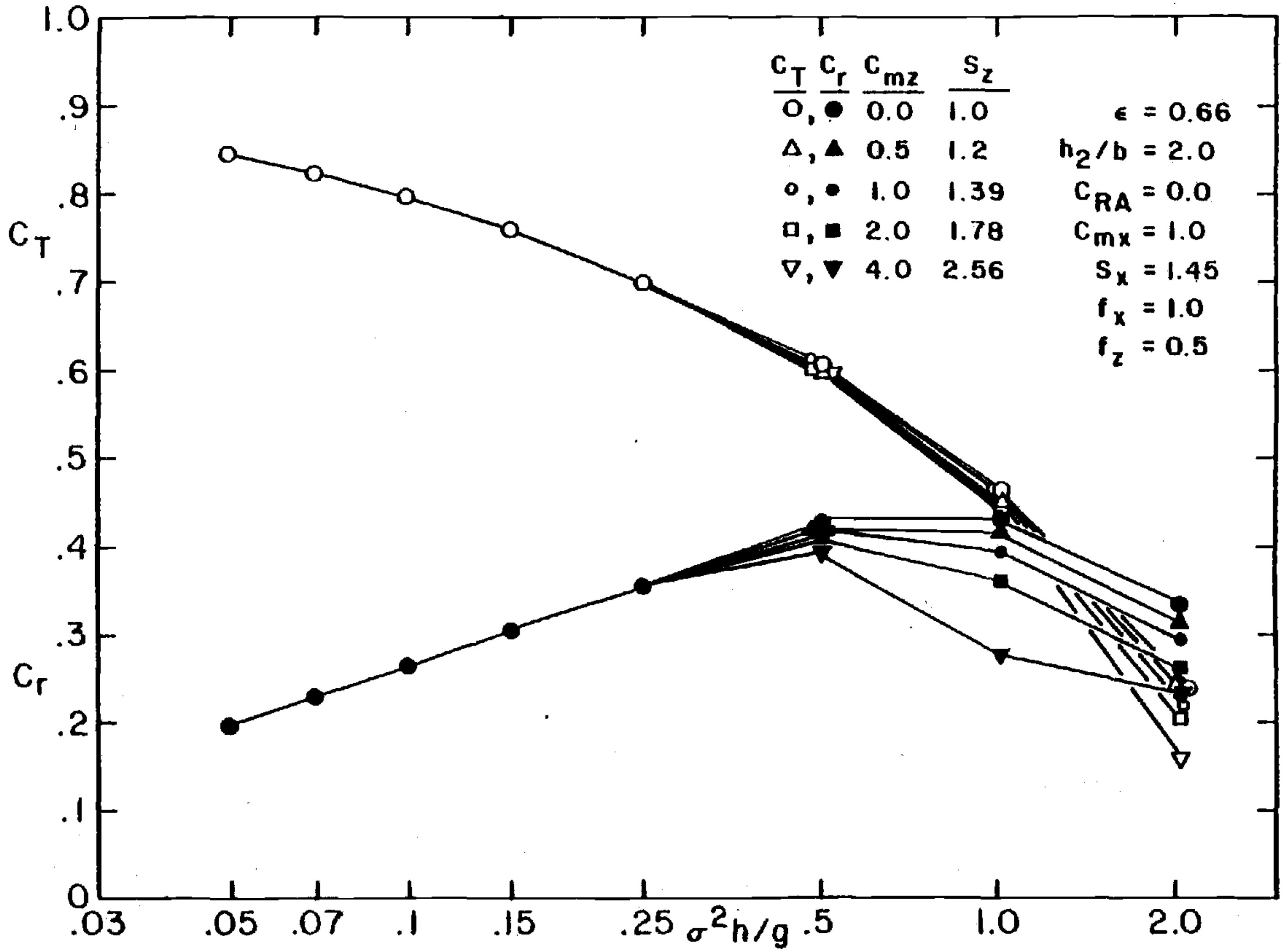

Figure 7.23. Reflection and transmission coefficients for varying values of C_{mz}, S_z. C_{mx} = 1.0, S_x = 1.45.

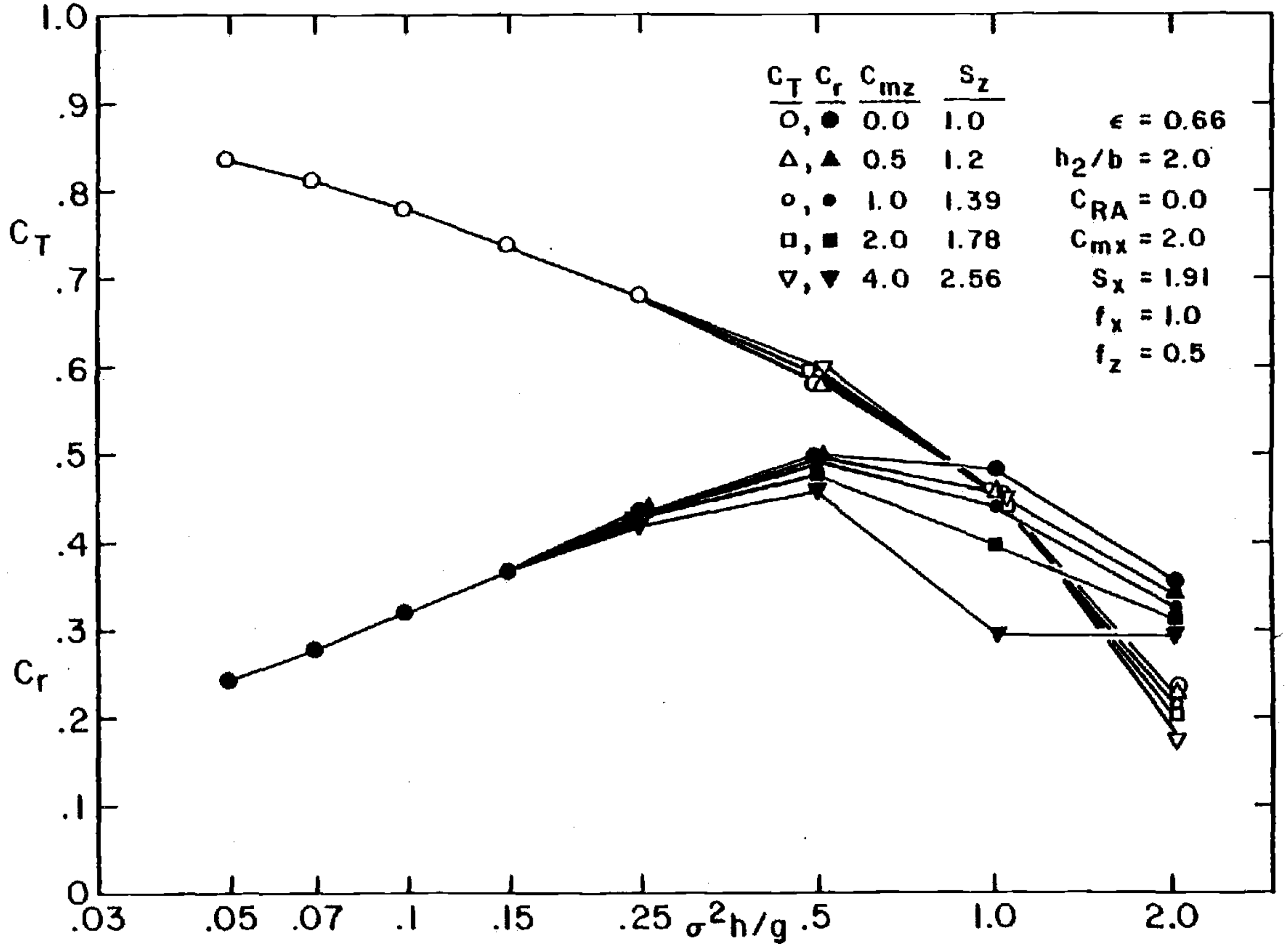

Figure 7.24. Reflection and transmission coefficients for varying values of C_{mz}, S_z. C_{mx} = 2.0, S_x = 1.91.

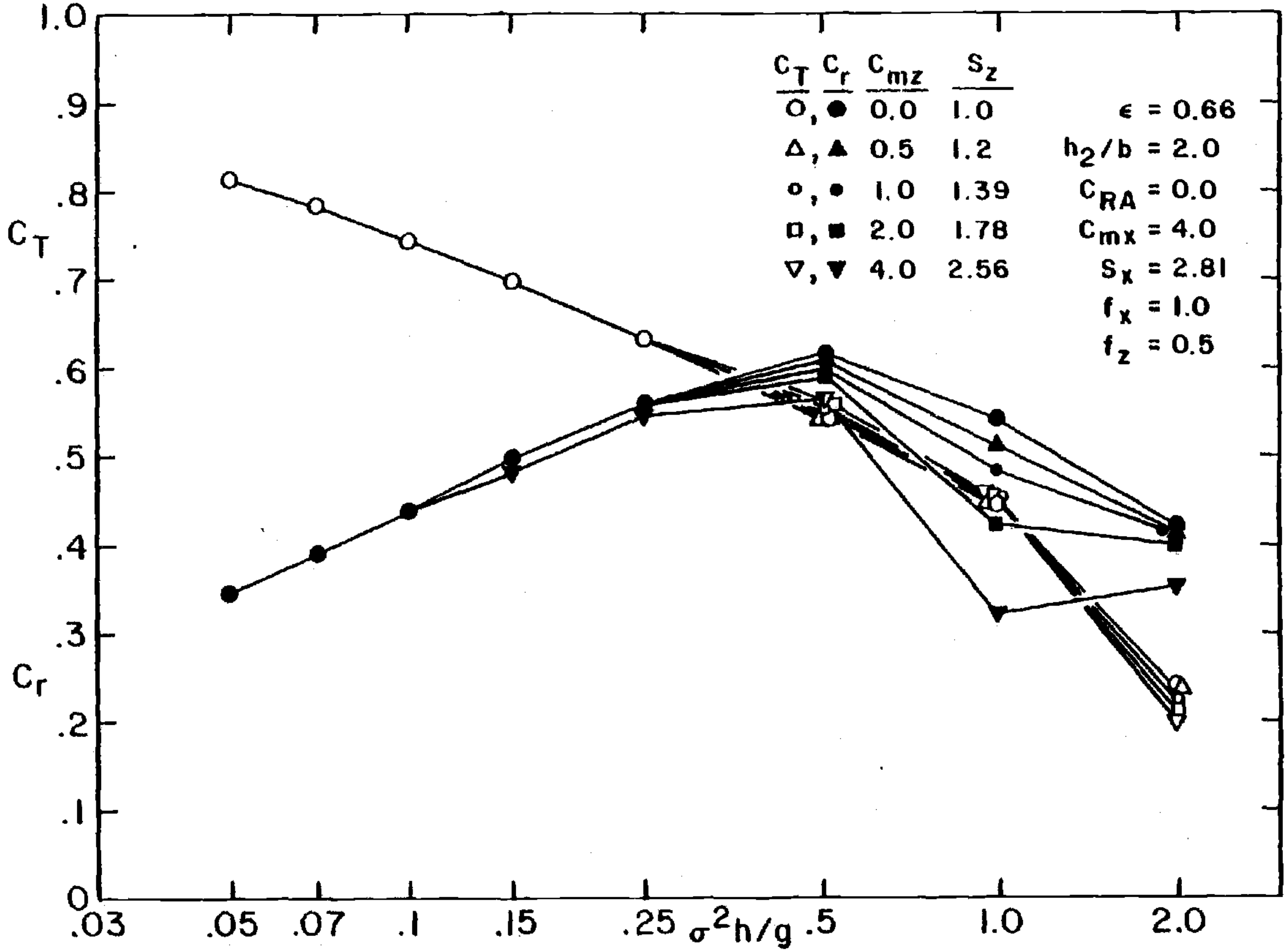

Figure 7.25. Reflection and transmission coefficients for varying values of C_{mz}, S_z. C_{mx} = 4.0, S_x = 2.81.

waves $(\sigma^2 h/g > 0.5)$. Vertical accelerations and velocities are required to develop vertical resistance forces via the added mass coefficient, C_{mz}, (or more properly the inertial coefficient, S_z) and the dimensionless damping coefficient, f_z, respectively. Vertical kinematics become an appreciable fraction of horizontal kinematics only if the wave number greatly exceeds the shallow water, long wave condition $(\sigma^2 h/g \gg 0.1)$. Thus, C_{mz} and f_z become increasingly effective at reducing wave reflection through internal wave-structure dissipation as the wave number increases. This behavior is depicted in Figs. 7.7 through 7.10 and Figs. 7.21 through 7.25. It is also apparent that the increases of the vertical added mass coefficient, C_{mz}, and the dimensionless damping factor, f_z, do not reduce wave penetration into the structure, and hence do not increase wave reflection. Rather, the wave is attenuated within the structure and internal reflections are subsequently reduced.

7.4. Variation of the Dimensionless Ratio h_2/b and the Reflection Coefficient of the Reflector-Absorber

The computed reflection and transmission coefficients are plotted in Figs. 7.26 through 7.30 for the cases in which the dimensionless ratio of the water depth in Region II, h_2, divided by the longitudinal half width of the structure, b, is varied over six different values on each figure. The range of this ratio is

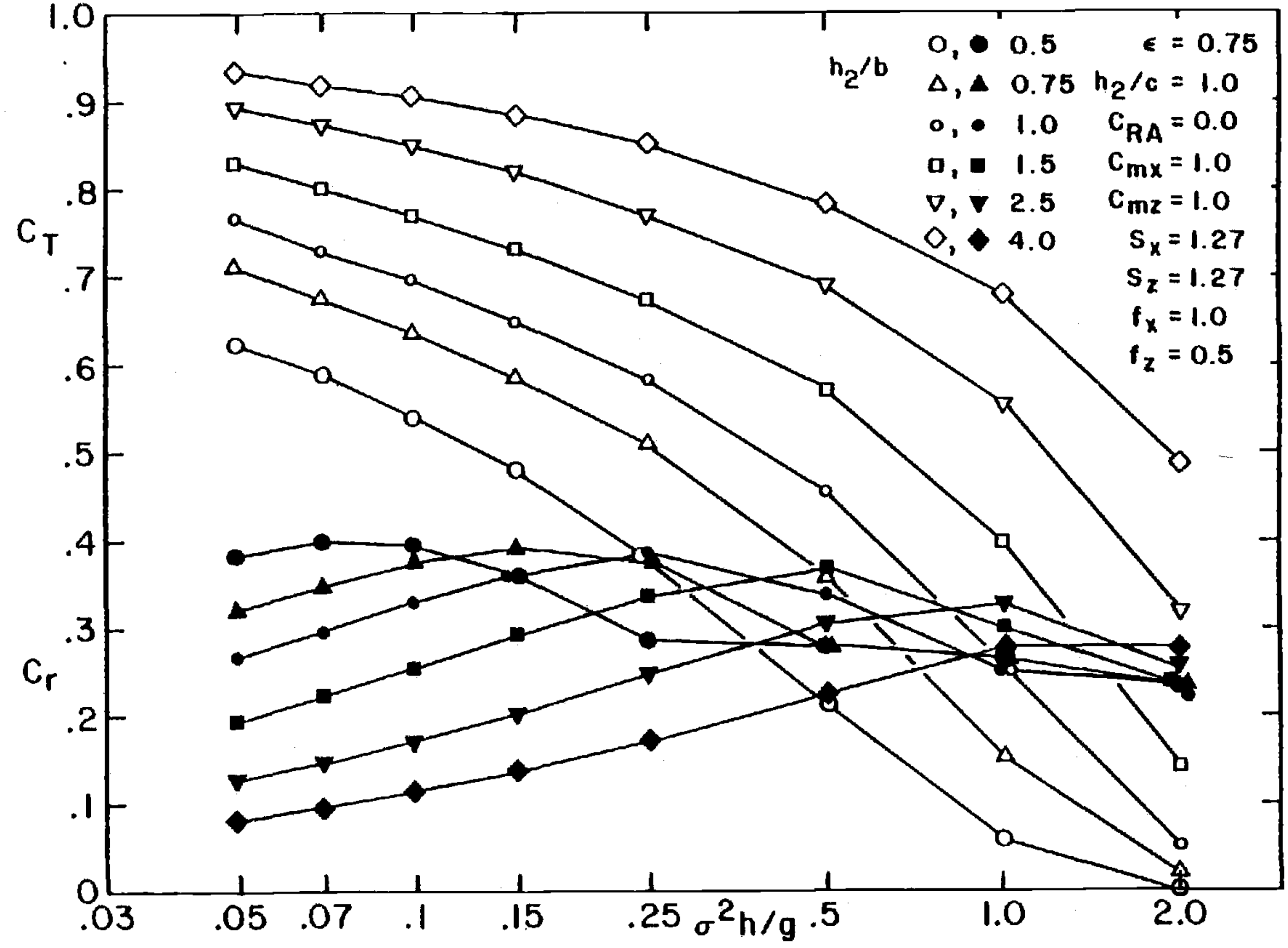

Figure 7.26. Reflection and transmission coefficients for varying values of h_2/b. $C_{RA} = 0.0$.

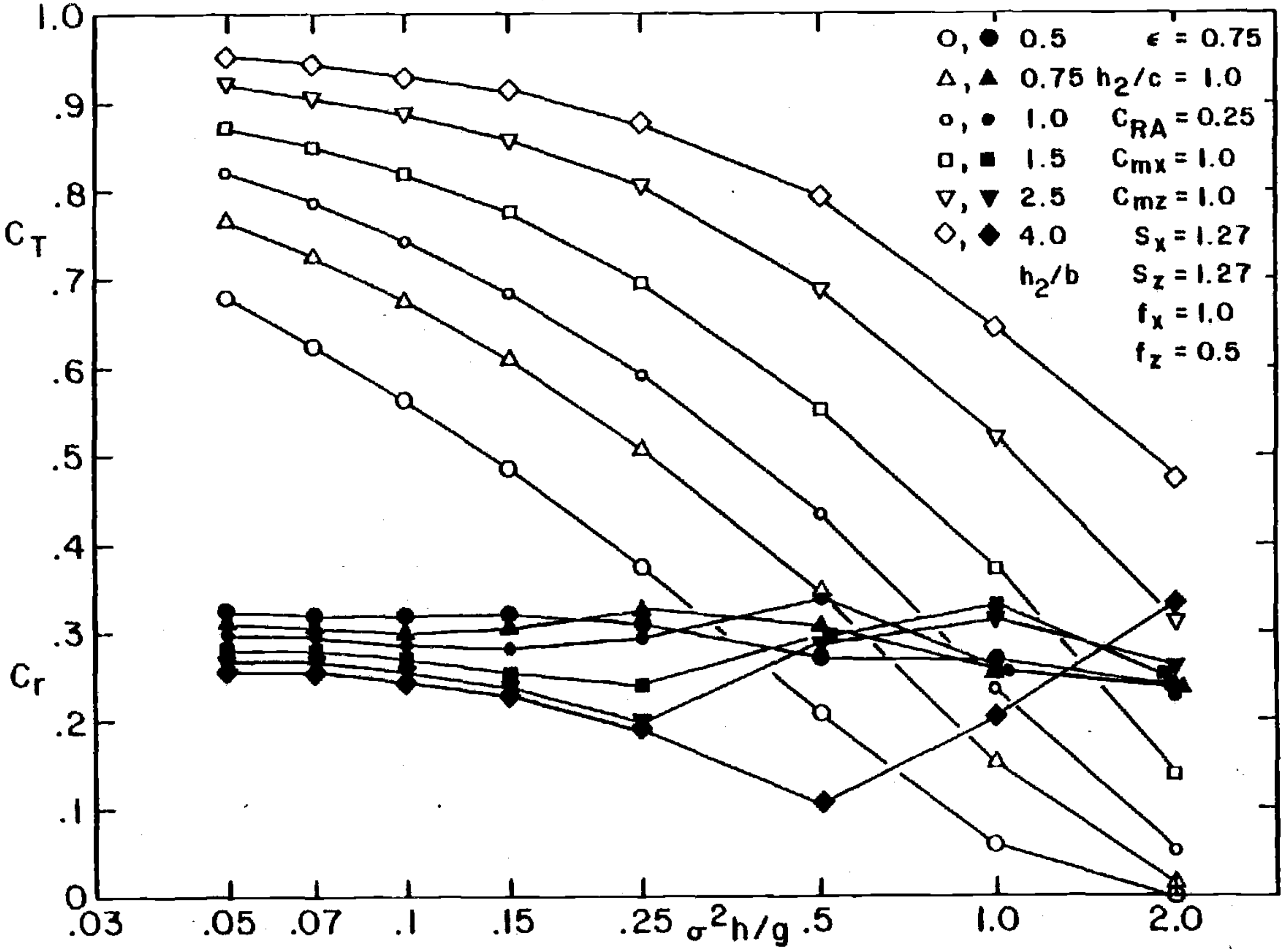

Figure 7.27. Reflection and transmission coefficients for varying values of h_2/b. $C_{RA} = 0.25$.

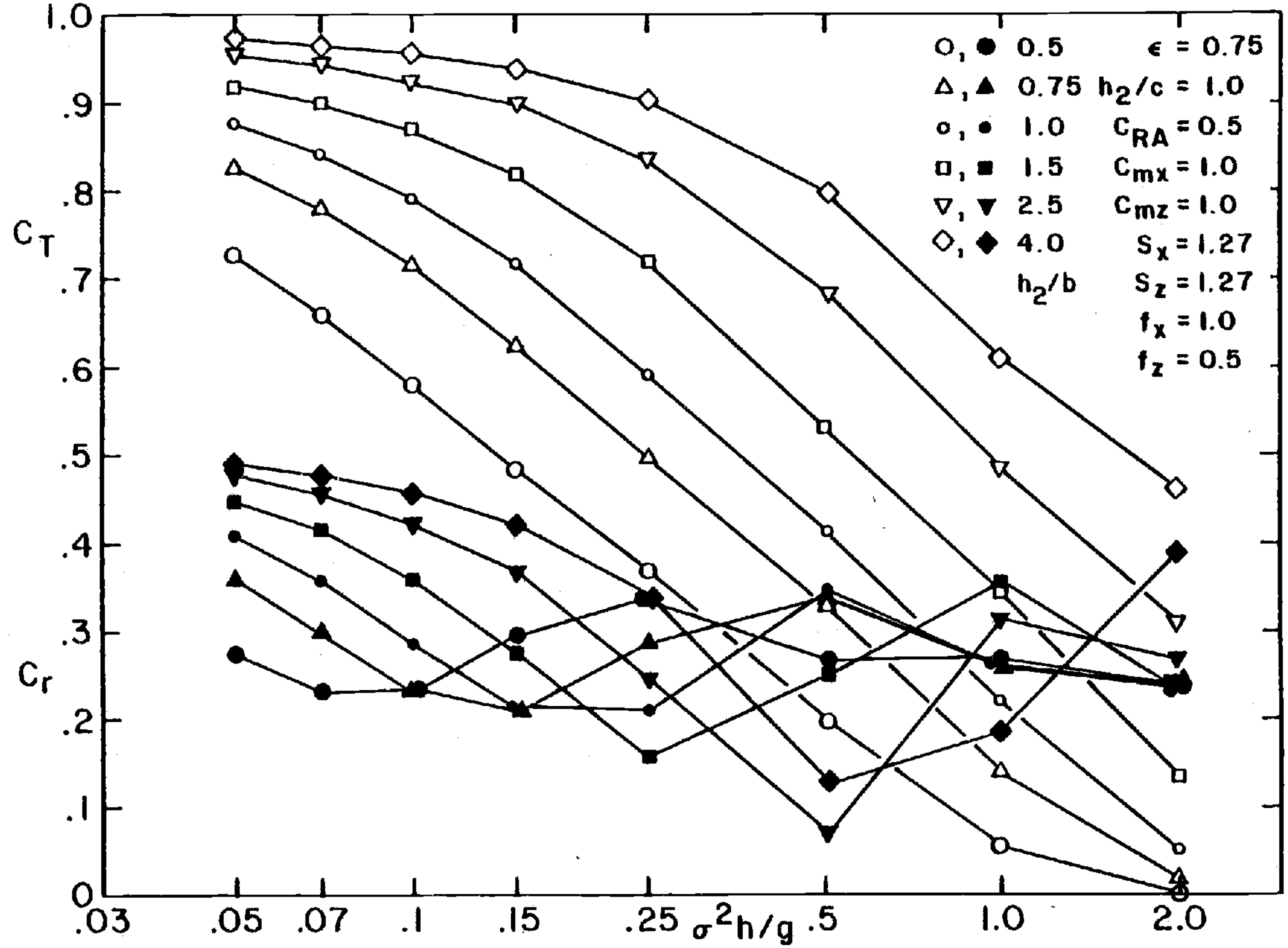

Figure 7.28. Reflection and transmission coefficients for varying values of h_2/b. $C_{RA} = 0.5$.

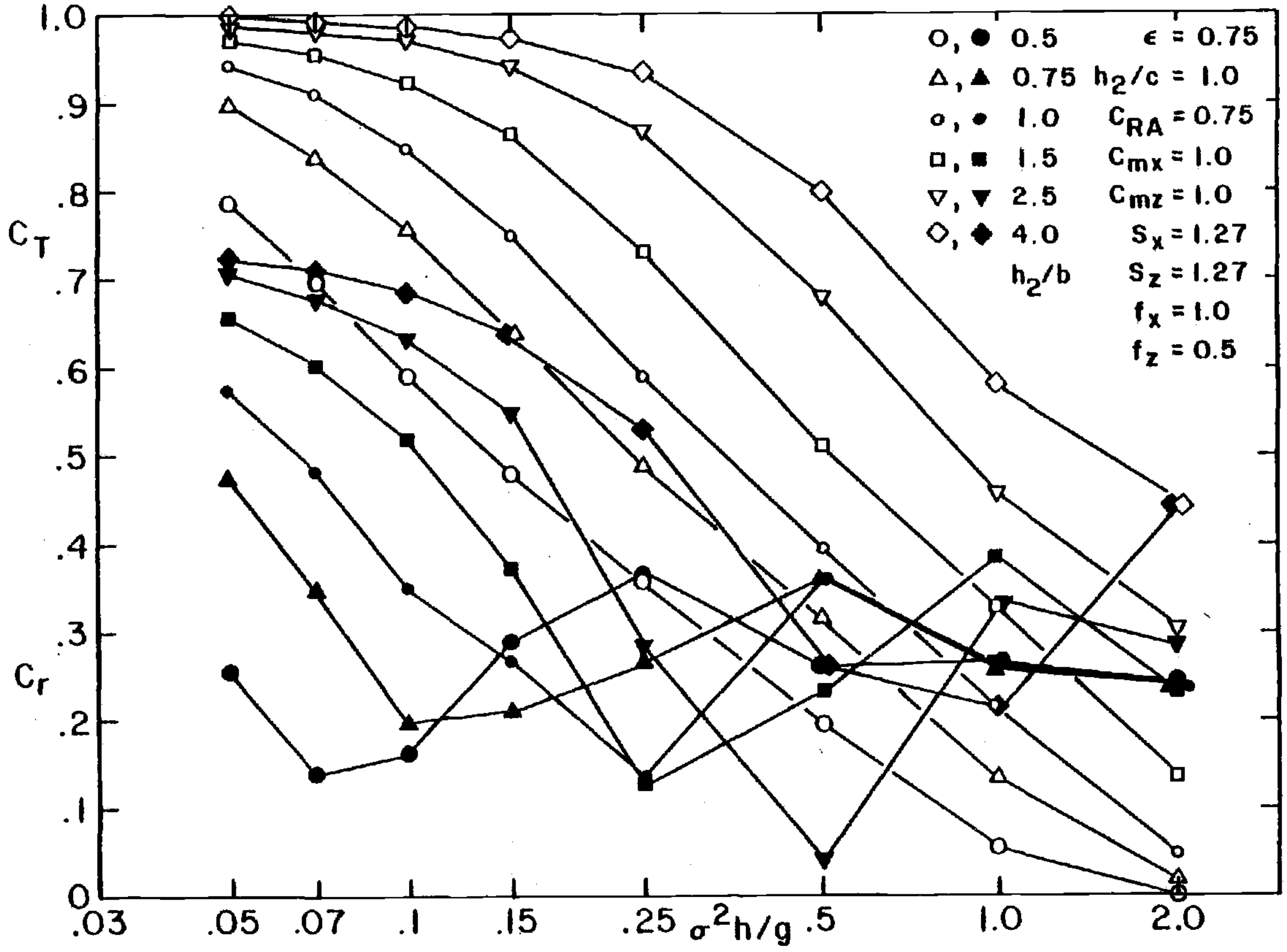

Figure 7.29. Reflection and transmission coefficients for varying values of h_2/b. $C_{RA} = 0.75$.

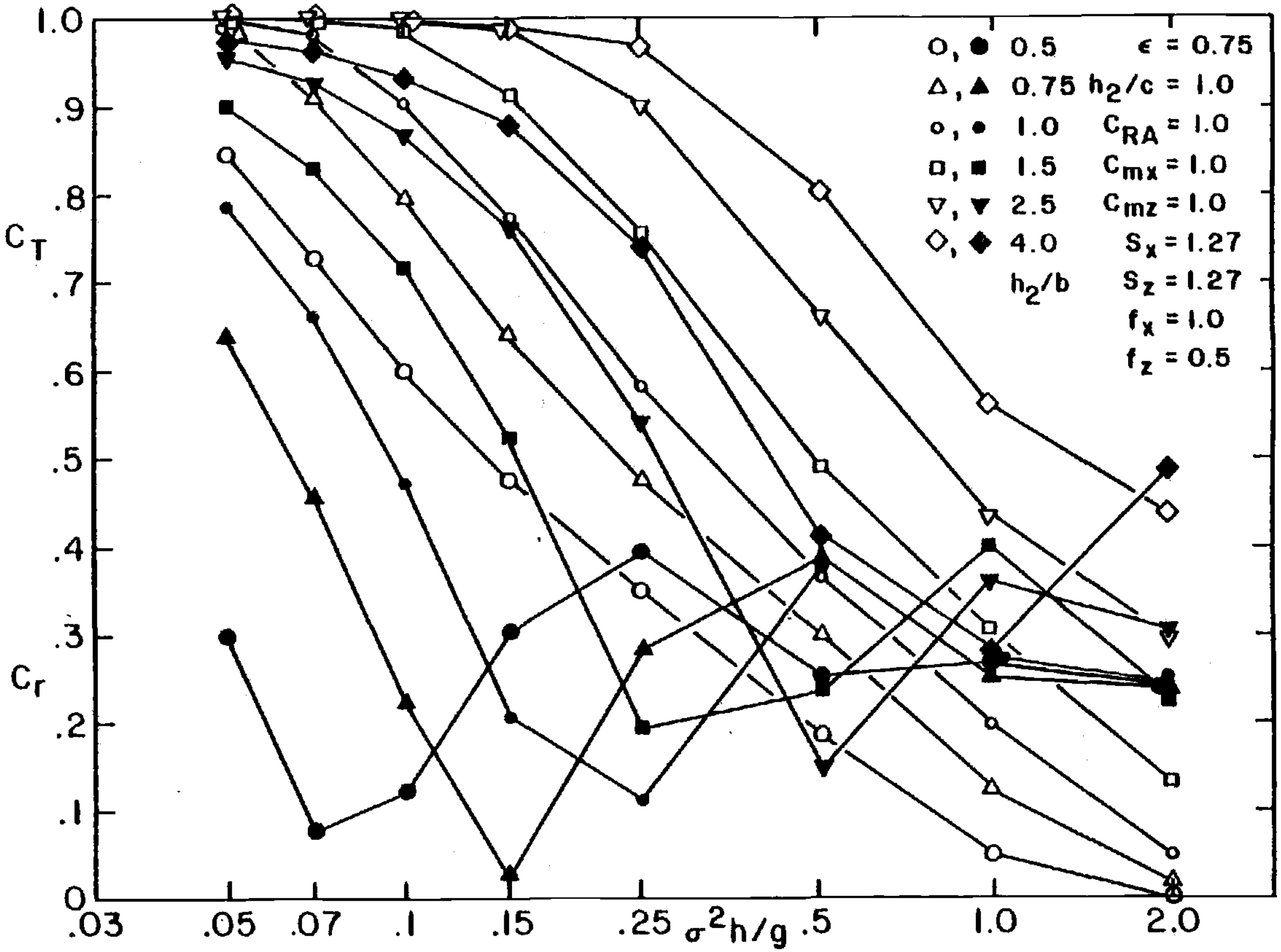

Figure 7.30. Reflection and transmission coefficients for varying values of h_2/b. $C_{RA} = 1.0$.

$.5 \leq h_2/b \leq 4.0$. The reflection coefficient of the reflector-absorber, C_{RA}, is varied from figure to figure over the range $0 \leq C_{RA} \leq 1.0$. The remaining structural parameters are held constant as indicated on each of the figures.

As reported for the analyses of Sections 7.2.1 and 7.2.2, the transmission coefficient decreases with increasing values of $\sigma^2 h/g$ and, additionally, decreases with decreasing values of h_2/b. Thus the analytical model predicts the expected behavior of increased structural transparency for long waves and also that of relatively narrow structures. It is interesting to note that the analytical model predicts a transmission coefficient slightly in excess of unity for the cases in which $C_{RA} = 1.0$ (see Fig. 7.30) and $h_2/b \geq 1.5$ at small values of $\sigma^2 h/g$. This large value of the transmission coefficient is partially due to the numerical error introduced by the truncation of the theoretically infinite eigen-series of Eqs. (4.2.2, 4.2.3, 4.2.5 and 4.2.6) at five modes. In addition, when a reflector is combined with the matrix structure energy storage in Region III becomes possible. That is, although attenuated somewhat by the structure, the incident wave provides a continuous source of energy flux into Region III. Since the analytical model does not provide for damping in Region III and since the reflection coefficient of the reflector-absorber, $C_{RA} = 1.0$, provides perfect energy reflection, it is apparent that the energy transmitted into Region III is perfectly reflected back in the seaward direction. This seaward energy flux is partially reflected at the leeward interface back towards the reflector again. This process repeats ad infinitum so that, theoretically, a portion of the initial flux of energy into Region III remains for all time. Meanwhile, the incident wave energy flux is continuous and, thus, energy is stored in Region III in terms of a large standing wave field. The large value of the transmission coefficient corresponds to the virtually undamped long wave interaction with a relatively narrow structure and the resulting energy storage in Region III.

It is also interesting to note that the transmission coefficients for the relatively wide structures $(h_2/b \leq 1.0)$ approach zero rather closely in all of these figures for the shortest waves. It appears as though these structures behave in a similar fashion to that of a low pass filter.

Figures 7.26 through 7.30 indicate that the reflection is significantly affected by both the variations in h_2/b and C_{RA}. Figure 7.26 indicates that the reflection coefficient still exhibits the peaking trend of Figs. 7.1 through 7.26 when $C_{RA} = 0$, but it also shows that both magnitude of the peak and the value of $\sigma^2 h/g$ at which it occurs are very much a function of the value of h_2/b. The maximum peak reflection coefficient of 40 percent occurs for the structure of greatest width at a value of $\sigma^2 h/g$ slightly greater than .07. Thenceforth the peaks become successively lower in magnitude and shift toward larger values of $\sigma^2 h/g$ with each decrease in the relative width (increase in h_2/b). In addition, the value of the dimensionless ratio of the longitudinal width of the structure, $2b$, divided by the incident wave wavelength, L, at these reflection peaks has been found to vary between about 0.15 and 0.18. This deviates slightly from the range $.2 \leq 2b/L \leq .25$ found by Kondo (1972) and that of $2b/L \approx .2$ by Kondo and Toma (1974). The discrepancy between Kondo's value of $2b/L$ and the present theory's may be attributable to the fact that the maximum reflection values were obtained from Fig. 7.26. However, the reflection coefficient curves were plotted on this figure by connecting the data points by straight line segments. Thus the maximum reflection may occur at a dimensionless wave frequency, $\sigma^2 h/g$, other than that of the eight data points and, therefore, be unidentifiable. However, it is noteworthy that the theory does predict that the maximum reflection is frequency (or wavelength) dependent and, furthermore, the predicted occurrence of these maximums approximates that of previous investigations.

In Fig. 7.27 the reflection coefficient curves begin to take on a peak and valley appearance which becomes more pronounced in Figs. 7.28 through 7.30. The amplitude of these C_r curve oscillations appears to increase with increasing values of C_{RA} for any given constant value h_2/b (see also Figs. 7.31 through 7.36). Due to the limiting range of $\sigma^2 h/g$ values it is difficult to judge whether or

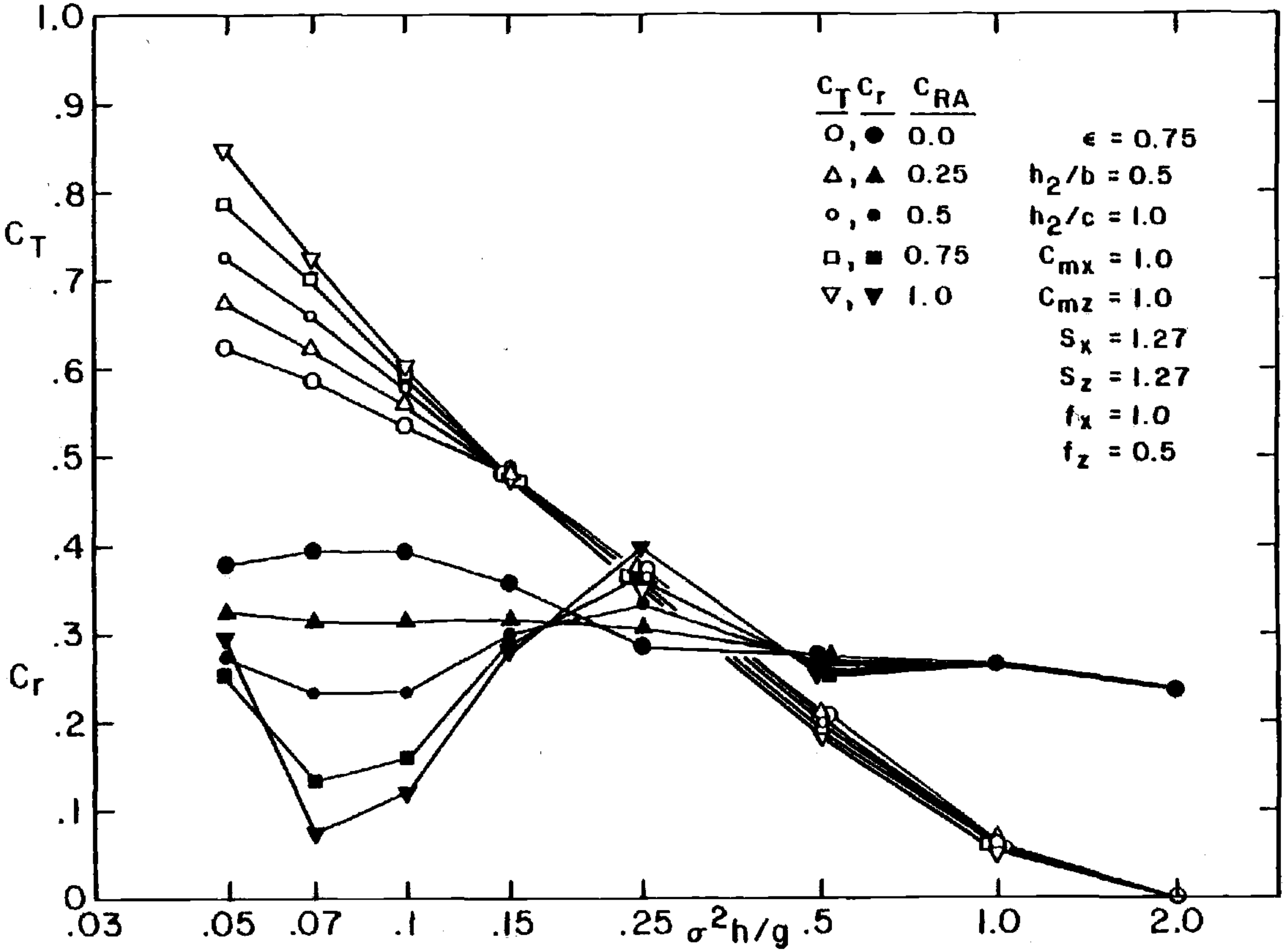

Figure 7.31. Reflection and transmission coefficients for varying values of C_{RA}. $h_2/b = 0.5$.

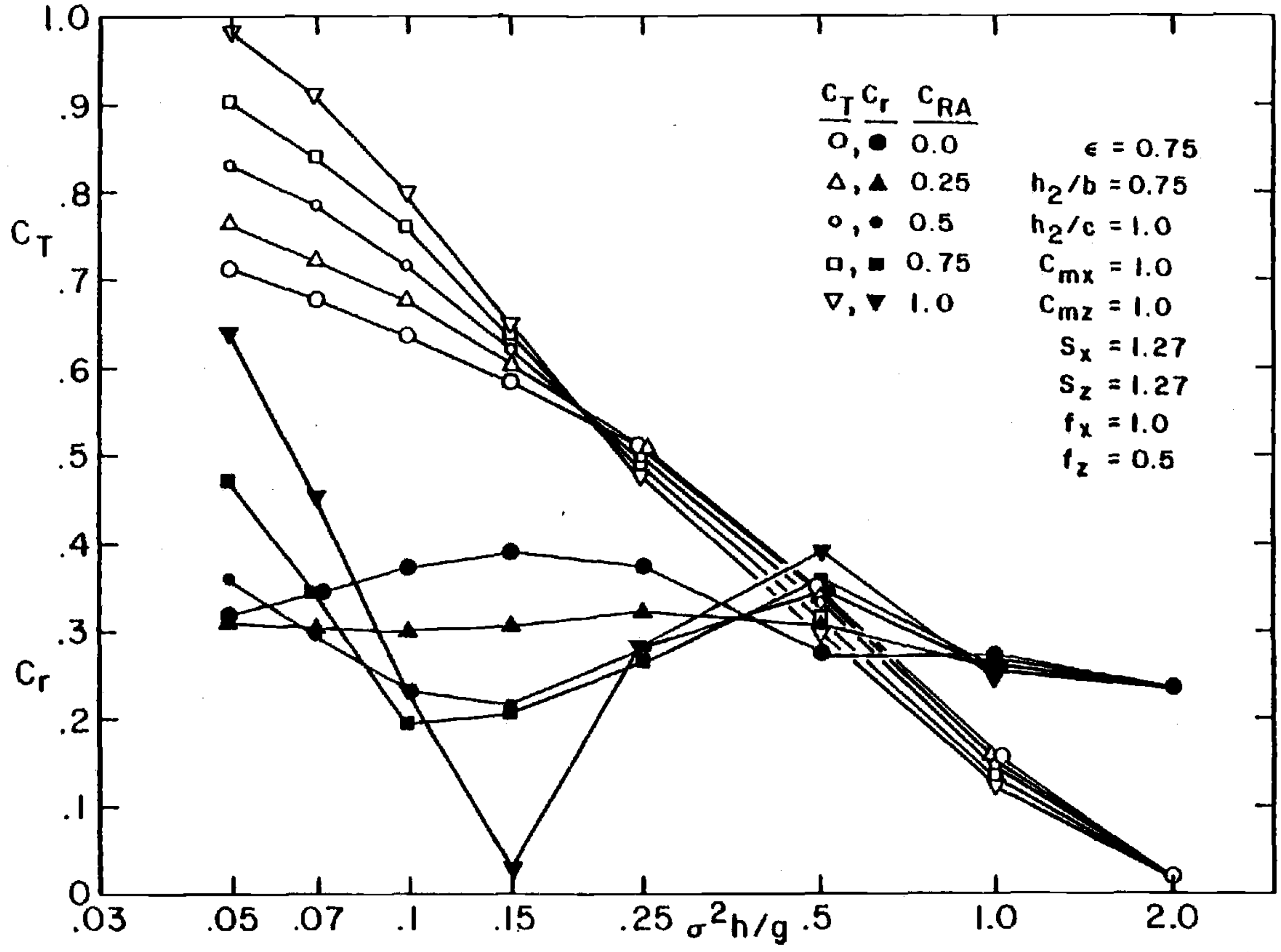

Figure 7.32. Reflection and transmission coefficients for varying values of C_{RA}. $h_2/b = 0.75$.

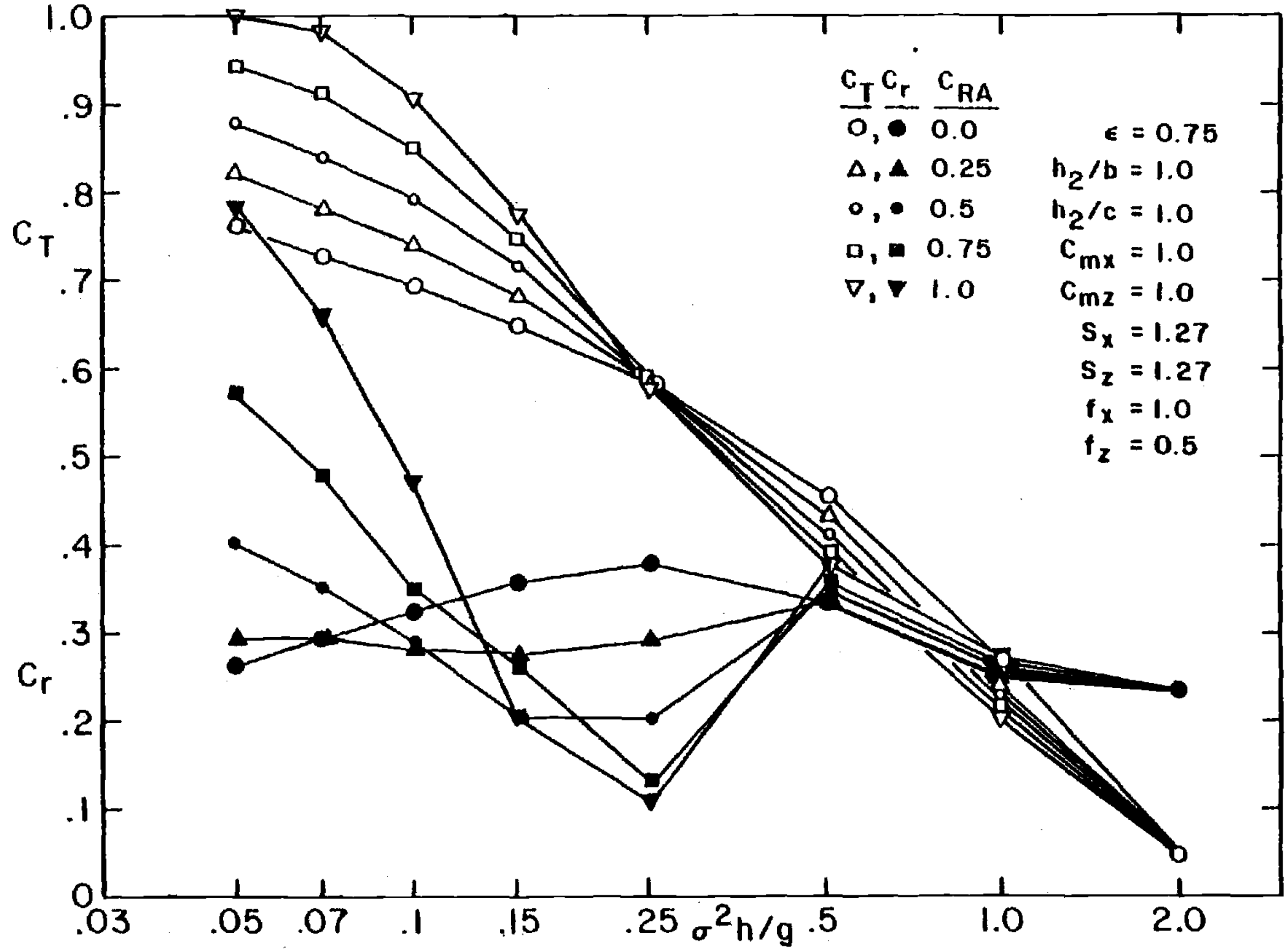

Figure 7.33. Reflection and transmission coefficients for varying values of C_{RA}. $h_2/b = 1.0$.

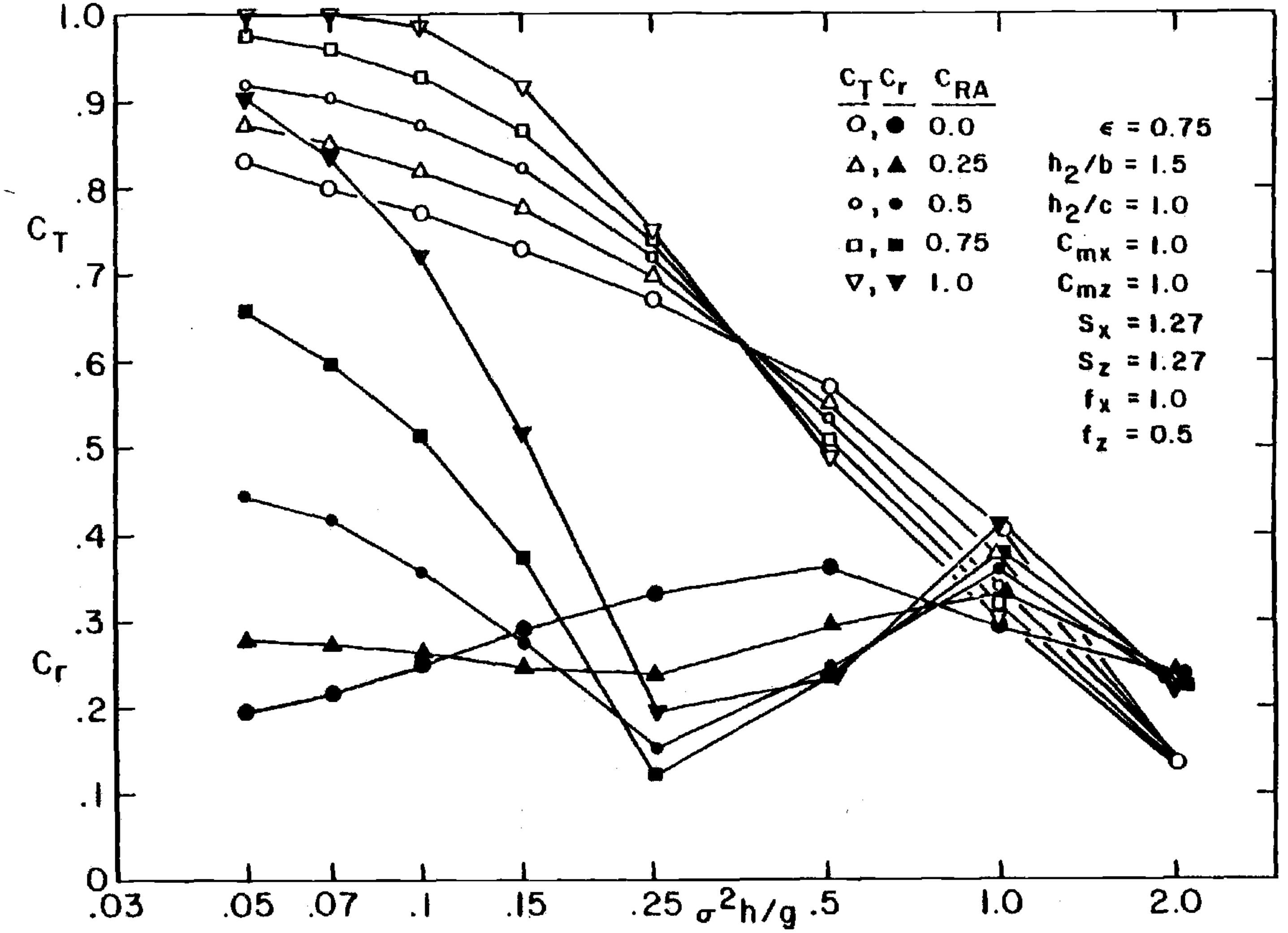

Figure 7.34. Reflection and transmission coefficients for varying values of C_{RA}. $h_2/b = 1.5$.

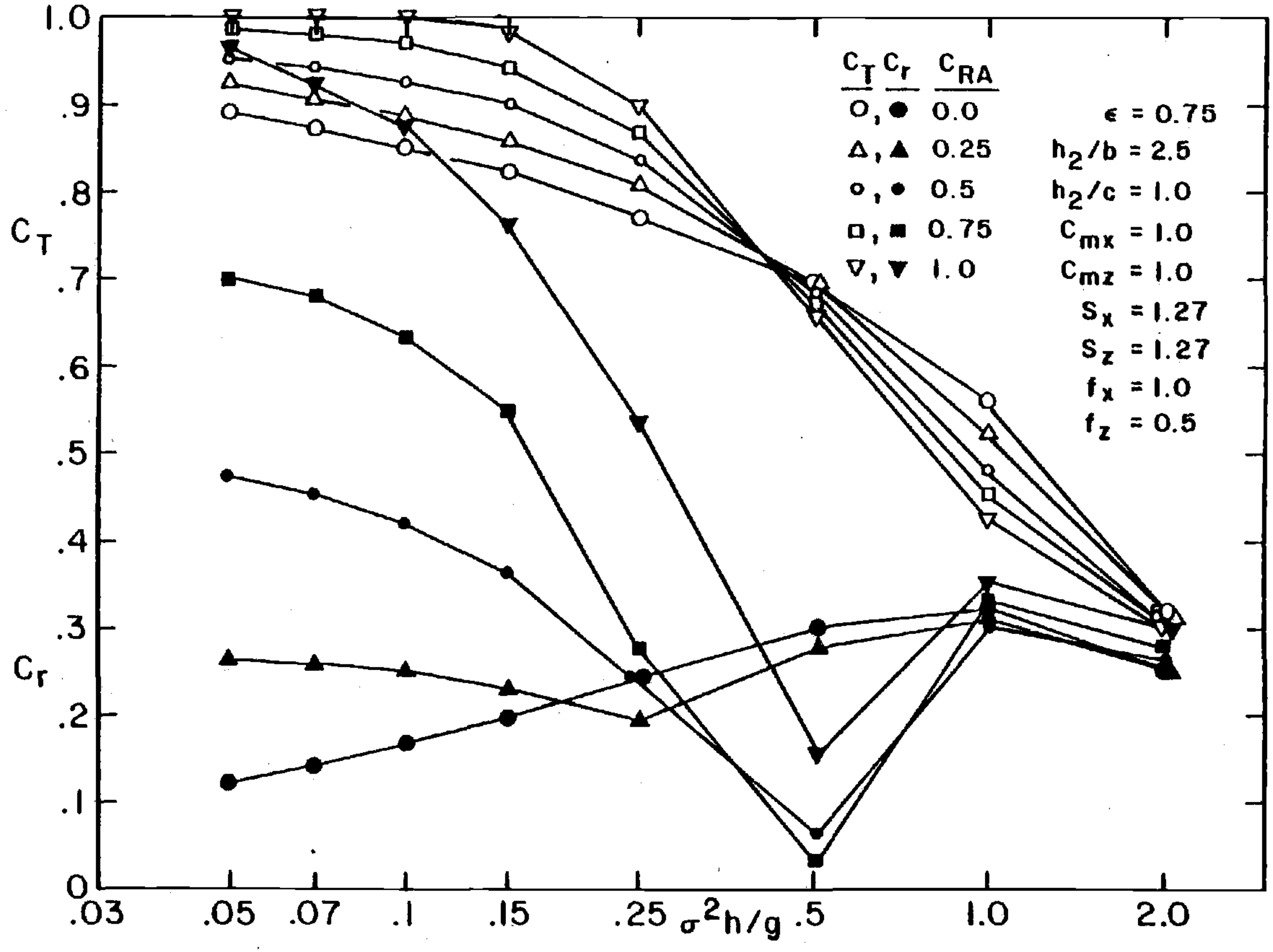

Figure 7.35. Reflection and transmission coefficients for varying values of C_{RA}. $h_2/b = 2.5$.

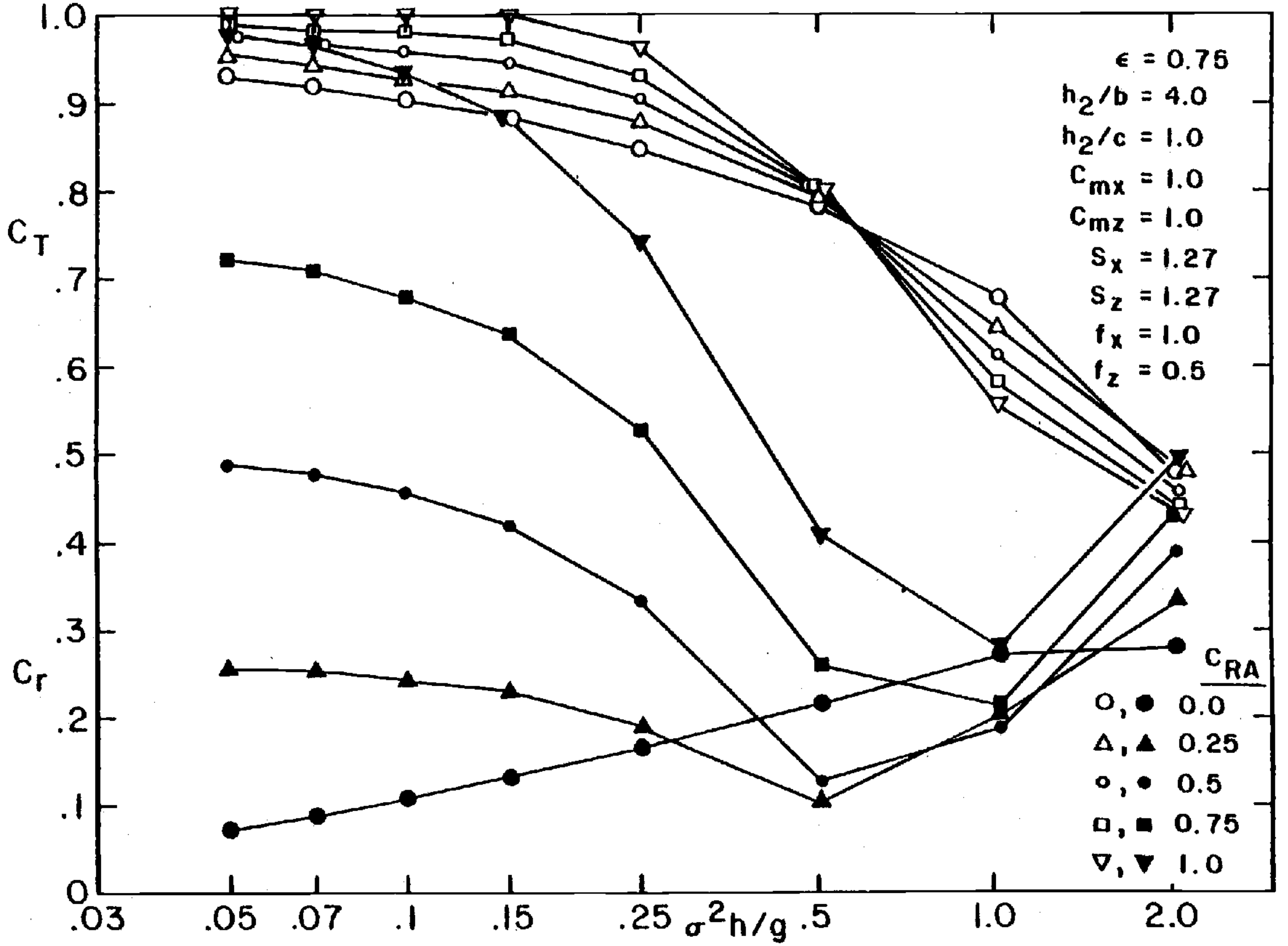

Figure 7.36. Reflection and transmission coefficients for varying values of C_{RA}. $h_2/b = 4.0$.

not the amplitude of the C_r curve oscillations increases with increasing values of h_2/b for all values of C_{RA} although it appears that this is the case for values of h_2/b up to 2.5. Finally, Figs. 7.27 through 7.30 indicate the relative maximums and minimums occur over a shorter range of $\sigma^2 h/g$ values for the smaller values of h_2/b (relatively wide structures) and that the range of $\sigma^2 h/g$ values between relative maximums and minimums increases with increasing h_2/b. From this it is concluded that relatively wide structures which are coupled with a partially or totally reflecting surface have a tendency to be moderately reflective for several different values of $\sigma^2 h/g$ but that relatively narrow structures are very reflective for one value of $\sigma^2 h/g$. Using the perfect reflection case shown in Fig. 7.30 as an example, it is hypothesized that this behavior is due to the fact that the relatively wide structure dissipates more wave energy within the structure than the relatively narrow structure. Consequently, long waves propagate through the narrow structure, reflect off of the reflector-absorber and are transmitted almost completely back through the structure and out to sea. Hence, an extremely large reflection coefficient results for the narrow structure while the exponential damping of the relatively wide structure effectively dissipates a significant portion of the wave energy, thus producing lower reflection.

Figures 7.31 through 7.36 show the data of Figs. 7.26 through 7.30 replotted where C_{RA} is varied on each figure and h_2/b varies from figure to figure. A curious feature of these figures is the fact that the transmission coefficient curves for the various values of C_{RA} on each plot appear to all intersect at a point. This point migrates towards higher values of $\sigma^2 h/g$ with increasing values of h_2/b. To the left of this point wave transmission increases with increasing values of C_{RA} while just the opposite occurs to the right of the point. That is, the structure appears more transparent to long waves and less transparent to short waves with increasing values of C_{RA}. This is probably due to superposition of wave forms traveling in the same direction with unequal amplitudes, equal frequencies, and having a variation in phase relative to one another. A similar trend is also observed in the next section for variations in h_2/c and C_{RA}.

7.5. Variation of the Dimensionless Ratio h_2/c and the Reflection Coefficient of the Reflector-Absorber

The computed reflection and transmission coefficients are plotted in Figs. 7.37 through 7.41 in a manner similar to that of Figs. 7.26 through 7.30. That is, the dimensionless ratio of the water depth in Region II divided by the distance from the rear of the structure to the reflector-absorber, h_2/c, is varied over six

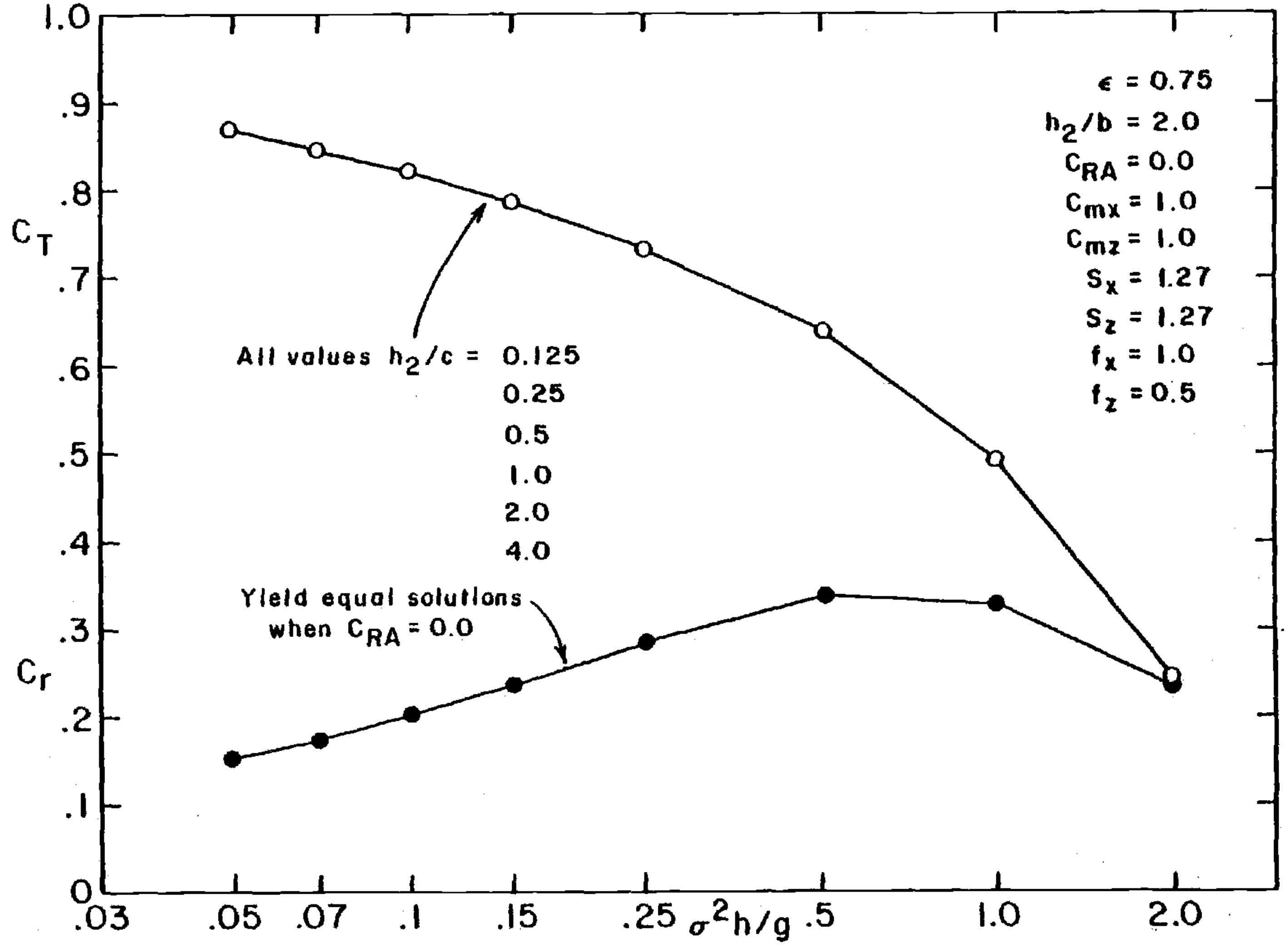

Figure 7.37. Reflection and transmission coefficients for varying values of h_2/c. $C_{RA} = 0.0$.

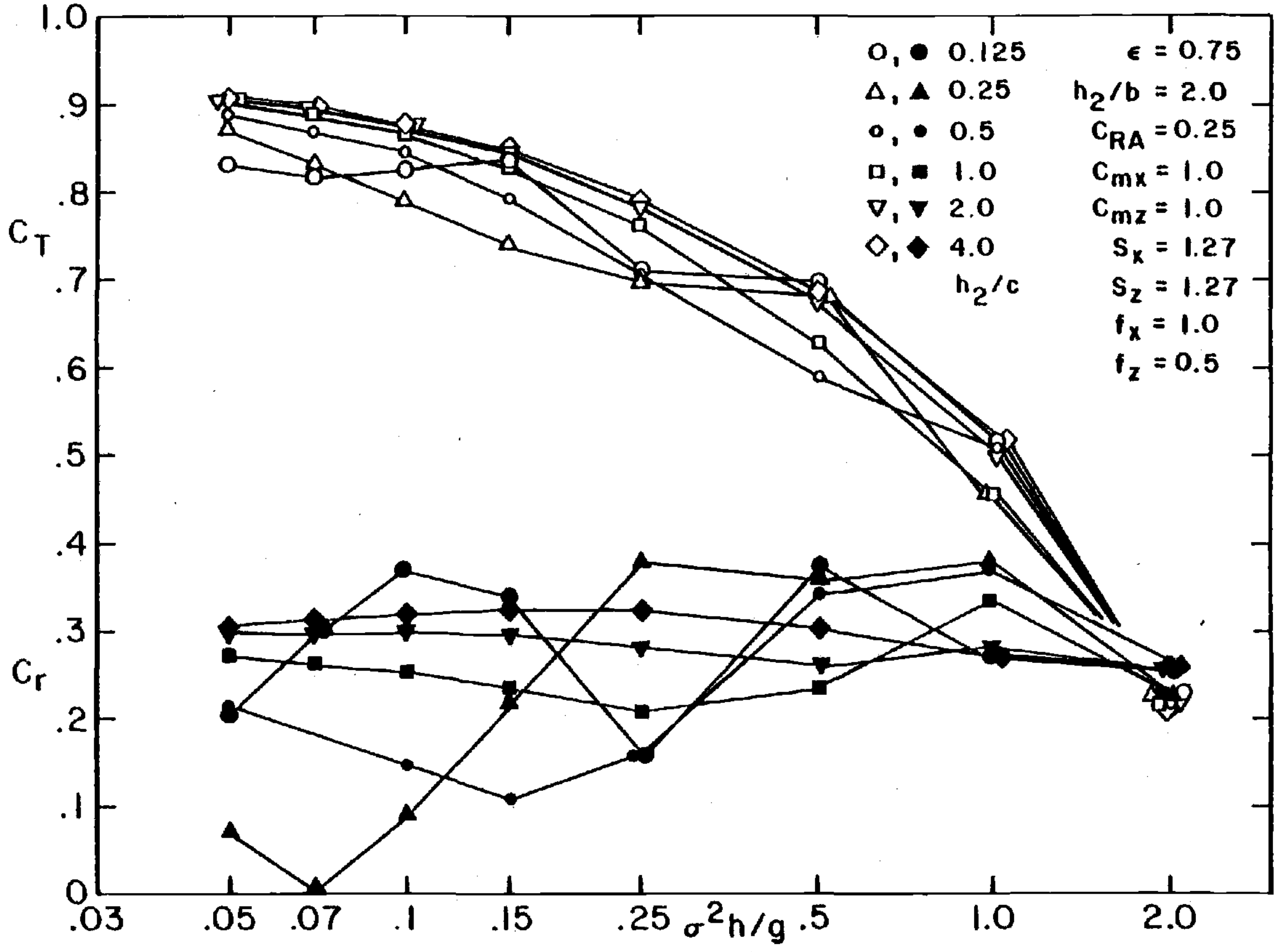

Figure 7.38. Reflection and transmission coefficients for varying values of h_2/c. $C_{RA} = 0.25$.

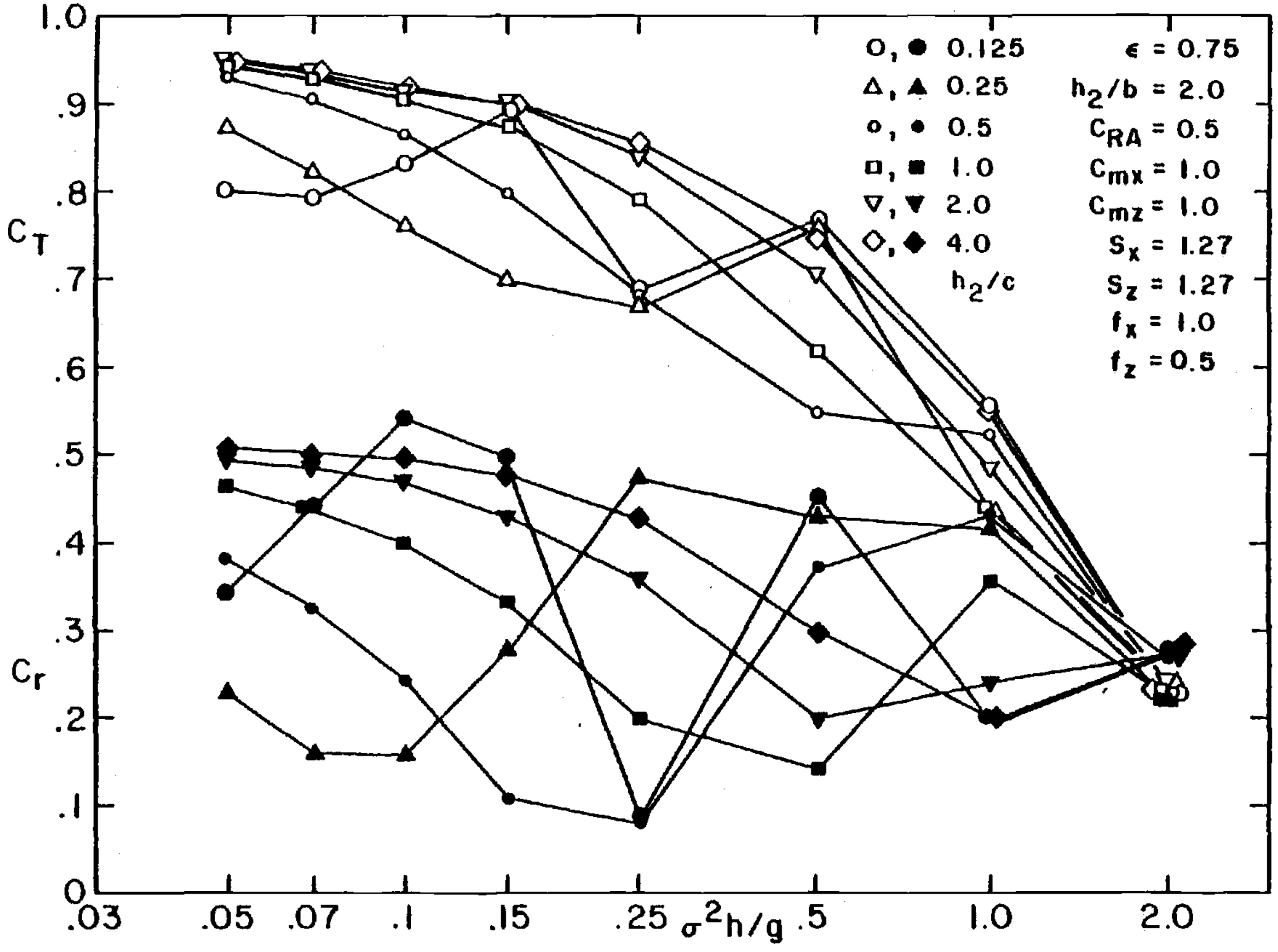

Figure 7.39. Reflection and transmission coefficients for varying values of h_2/c. $C_{RA} = 0.5$.

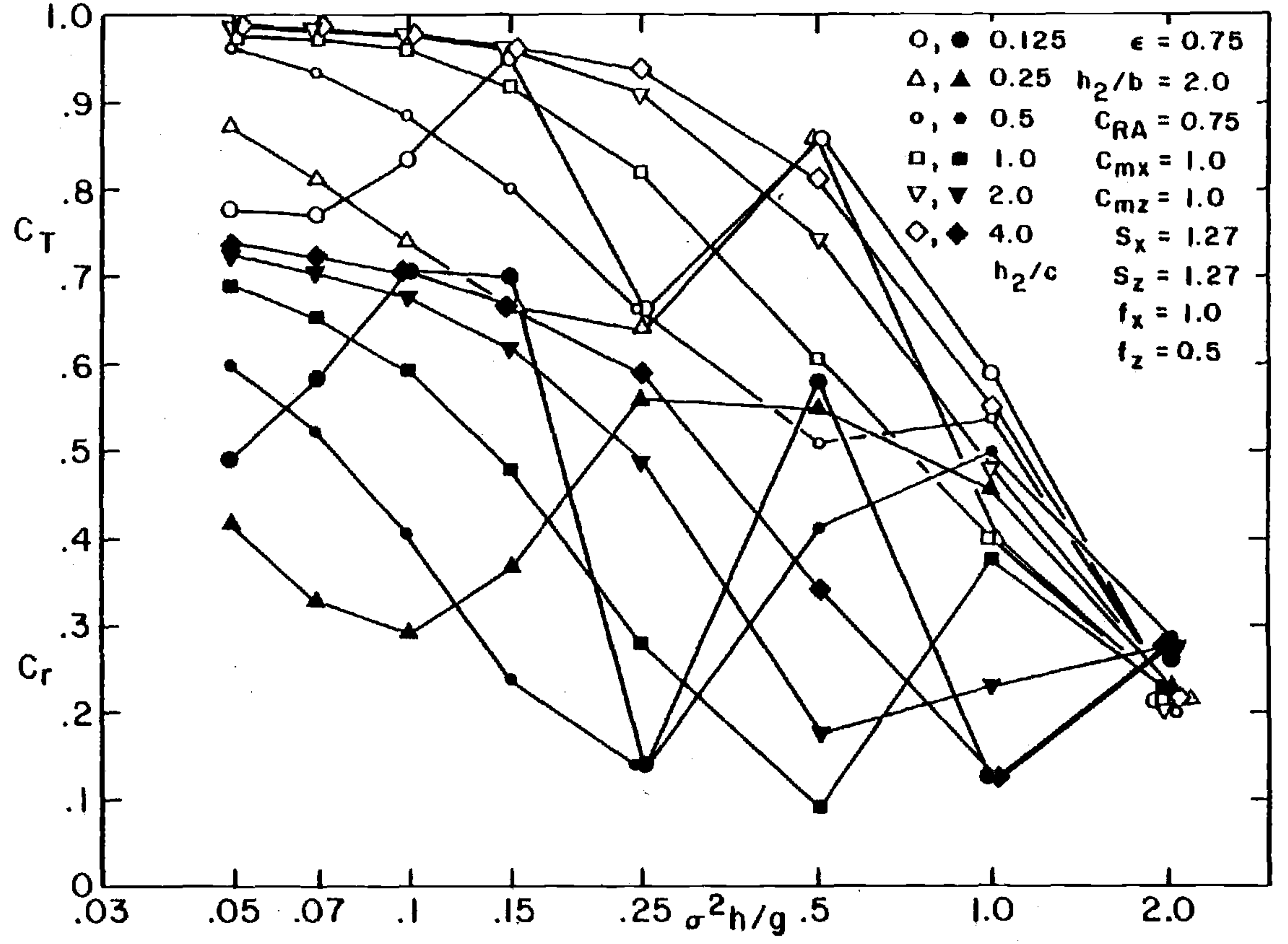

Figure 7.40. Reflection and transmission coefficients for varying values of h_2/c. $C_{RA} = 0.75$.

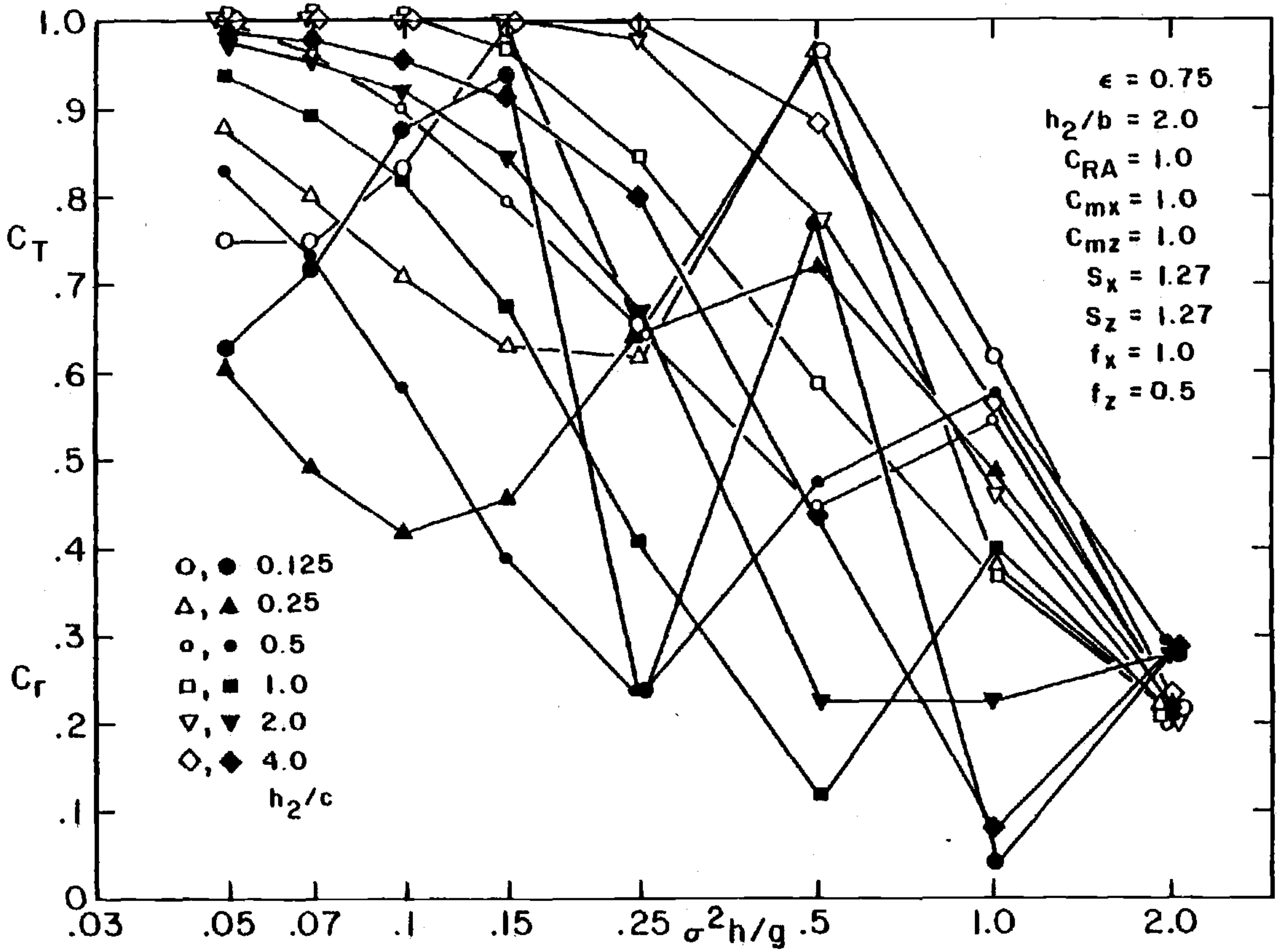

Figure 7.41. Reflection and transmission coefficients for varying values of h_2/c. $C_{RA} = 1.0$.

different values of range $0.125 \leq h_2/c \leq 4.0$ on each figure. The reflection coefficient of the reflector-absorber is varied over five different values of range $0.0 \leq C_{RA} \leq 1.0$ from figure to figure.

As expected, Figure 7.37 indicates that variations in the ratio h_2/c have no effect on the predicted values of C_r and C_T when no reflector-absorber is present and thus the model is operating correctly for this case.

The transmission coefficient curves when $h_2/c \geq 1.0$ generally approximate monotonically decreasing functions with increasing values of $\sigma^2 h/g$ in Figs. 7.38 through 7.41. Furthermore, these same curves are ordered so that the transmission coefficient decreases with decreasing values of h_2/c. However, the transmission coefficient curves, when h_2/c is less than unity, deviate from the monotonically decreasing norm and begin to exhibit a relative maxima and minima trend when $C_{RA} = 0.25$. This trend becomes progressively more exaggerated with increasing reflections from the reflector-absorber so that the structures of $h_2/c < 1.0$ appear to be quite frequency selective for wave transmission (see, for example Fig. 7.41). This selectivity is thought to be a by-product of phase shifted wave superposition in Regions II and III. Thus, it is no coincidence that the maxima and minima always occur at identical values of $\sigma^2 h/g$ from figure to figure, for each of the three particular values of $h_2/c < 1.0$, with increasing C_{RA} values from figure to figure. In addition, it has been found that these maxima tend to occur when one-half the incident wave wavelength, $L/2$, is approximately an integer multiple of c. That is, the transmission maxima for $h_2/c = 0.125$ as shown in Figs. 7.38 through 7.42 always occur at values of $L/2$ equal to approximately one and two times c. The transmission maxima for $h_2/c = 0.25$ and $h_2/c = 0.5$ occur at approximately $L/2 = c$ and $L/2 = 5c$, respectively. This dependence on one-half the wavelength might be expected for the partial standing wave field of Region III when the reflection coefficient of the reflector-absorber is greater than zero.

The reflection coefficient curves of Figs. 7.38 through 7.41 also exhibit the relative maxima and minima trend but it occurs for all values of h_2/c. Again, this trend becomes more exaggerated with increasing reflections from the reflector-absorber and this behavior is likely due to phase shifted superposition. The frequency of occurrence of relative maxima and minima for the reflection curves increases with decreasing values of h_2/c. Thus a large number of relative maxima and minima corresponding to higher order harmonics occur when the distance c is relatively large.

Figures 7.42 through 7.47 depict the data of Figs. 7.37 through 7.41 replotted where C_{RA} is varied on each figure and h_2/c varies from figure to figure. As in Figs. 7.31 through 7.36, the intersection of all of the transmission coefficient curves is apparent in Figs. 7.42 through 7.47. Again, this is thought to be directly related to a superposition phenomena.

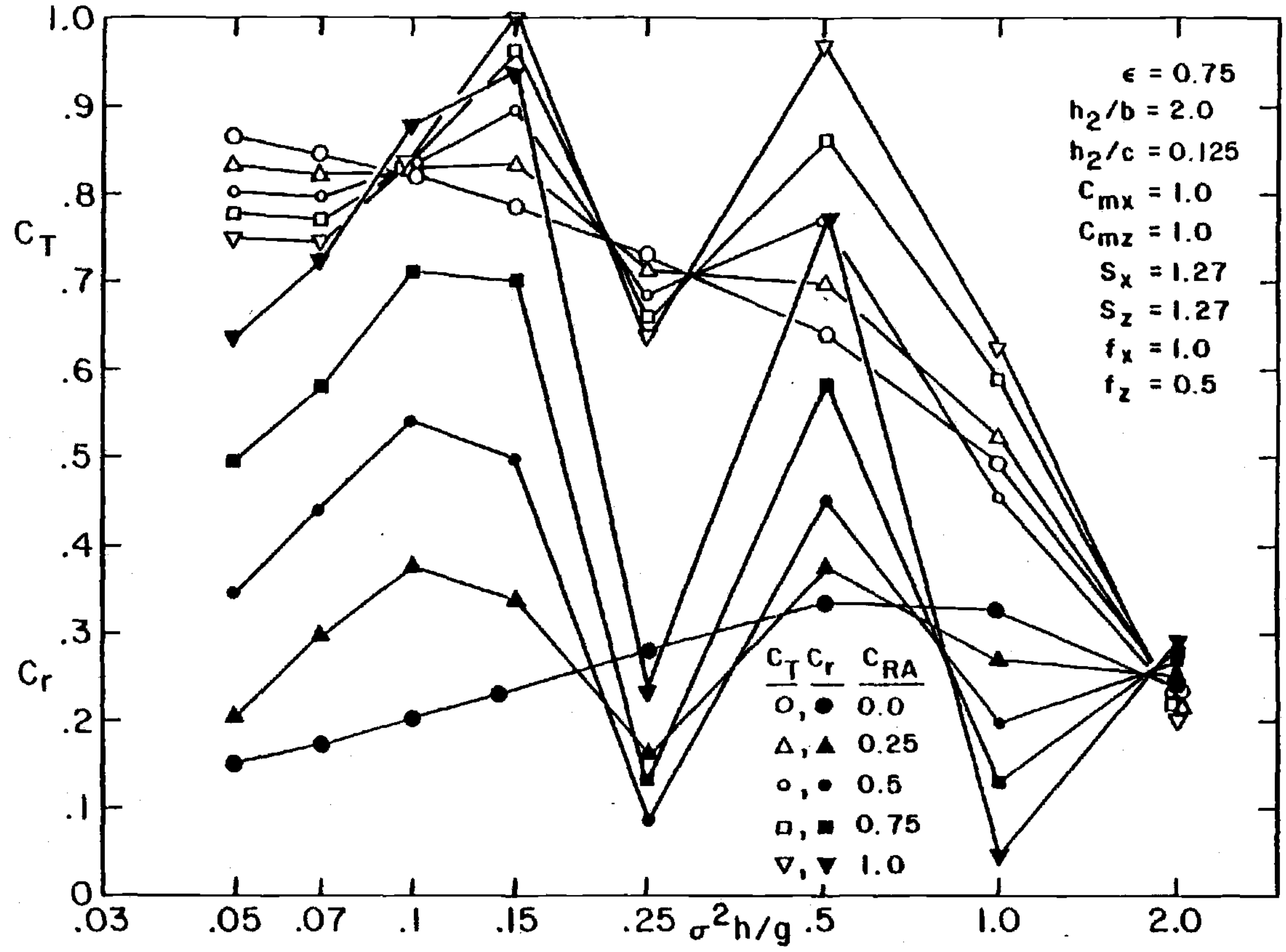

Figure 7.42. Reflection and transmission coefficients for varying values of C_{RA}. $h_2/c = 0.125$.

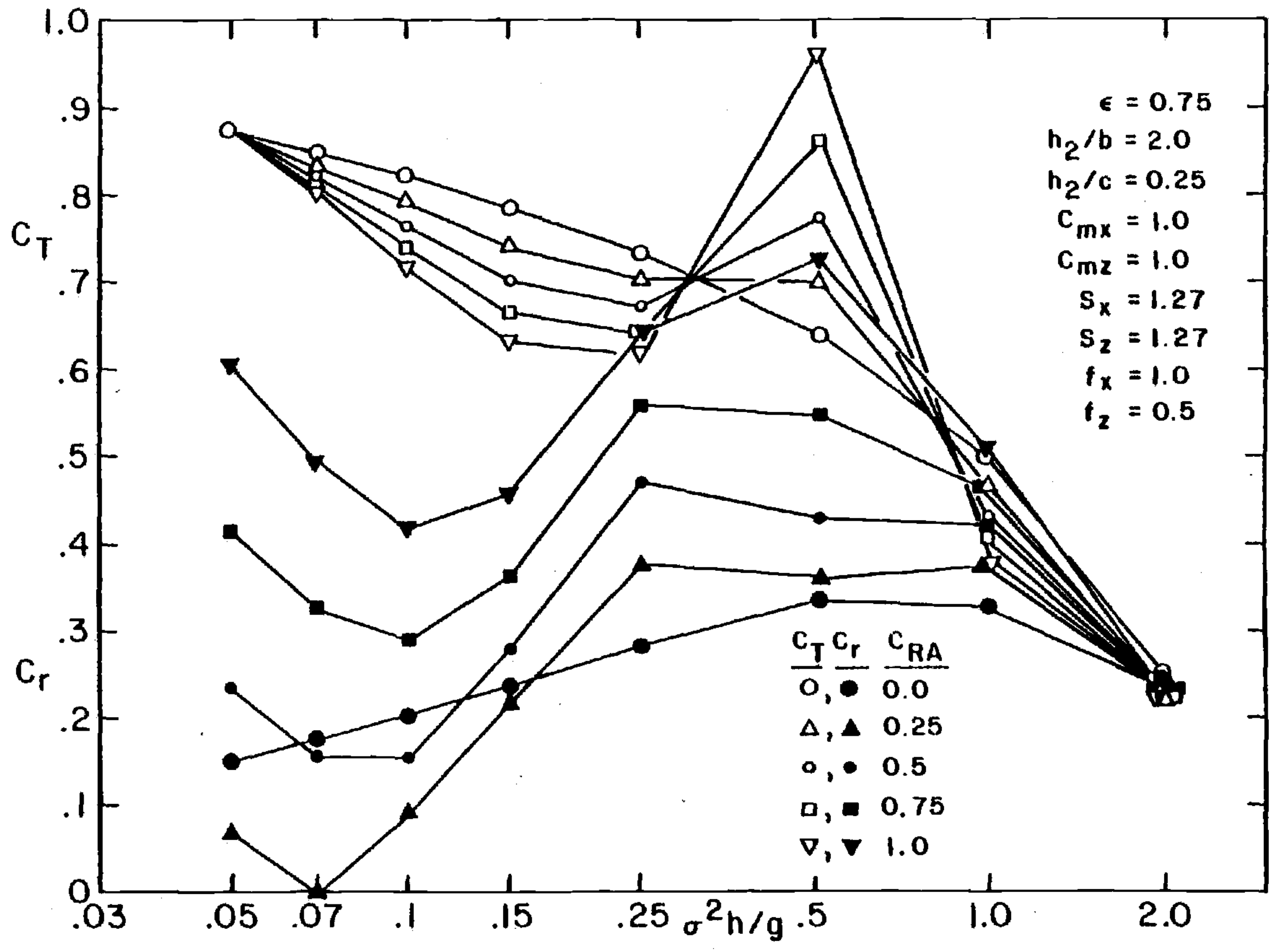

Figure 7.43. Reflection and transmission coefficients for varying values of C_{RA}. $h_2/c = 0.25$.

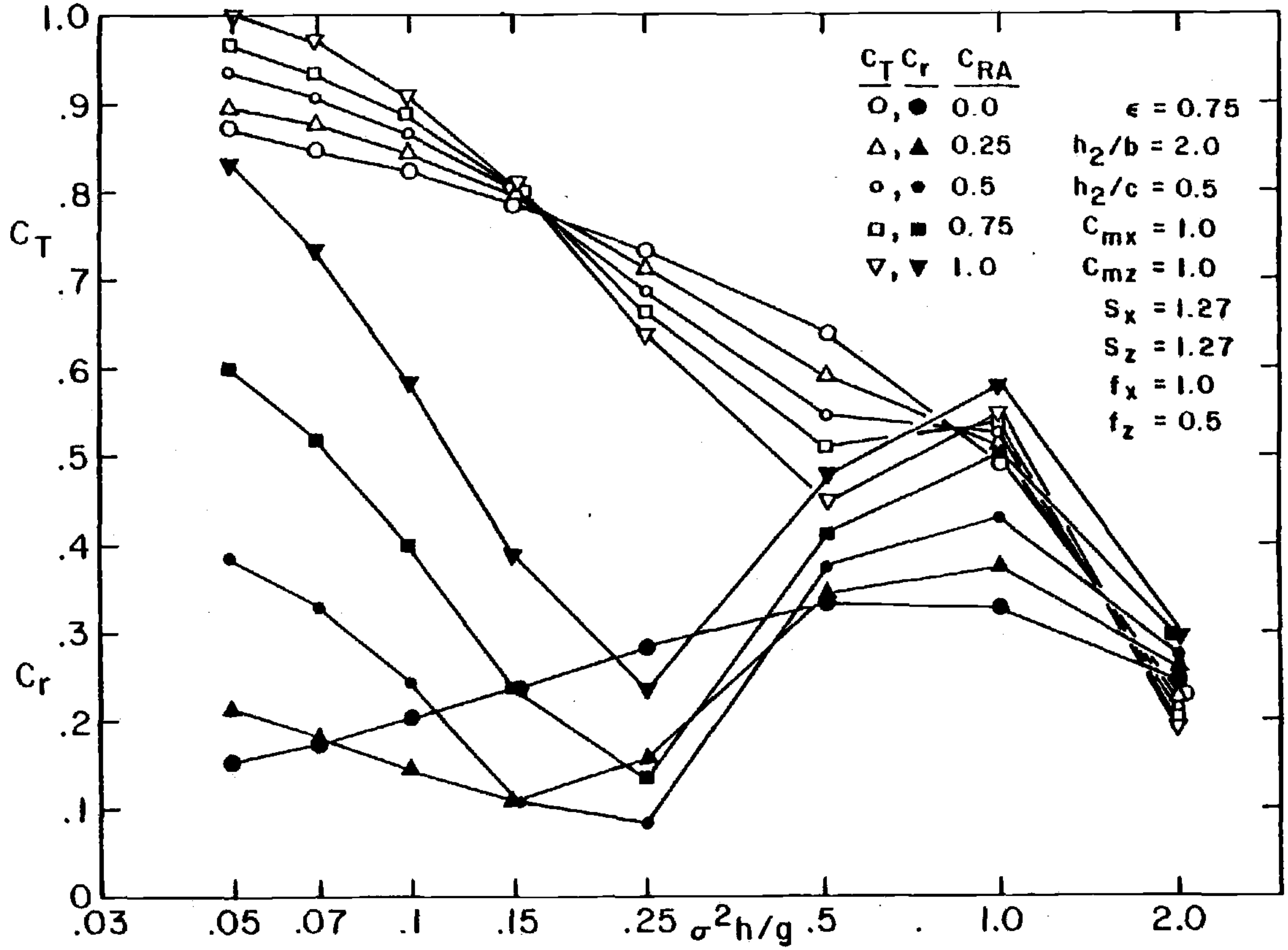

Figure 7.44. Reflection and transmission coefficients for varying values of C_{RA}. $h_2/c = 0.5$.

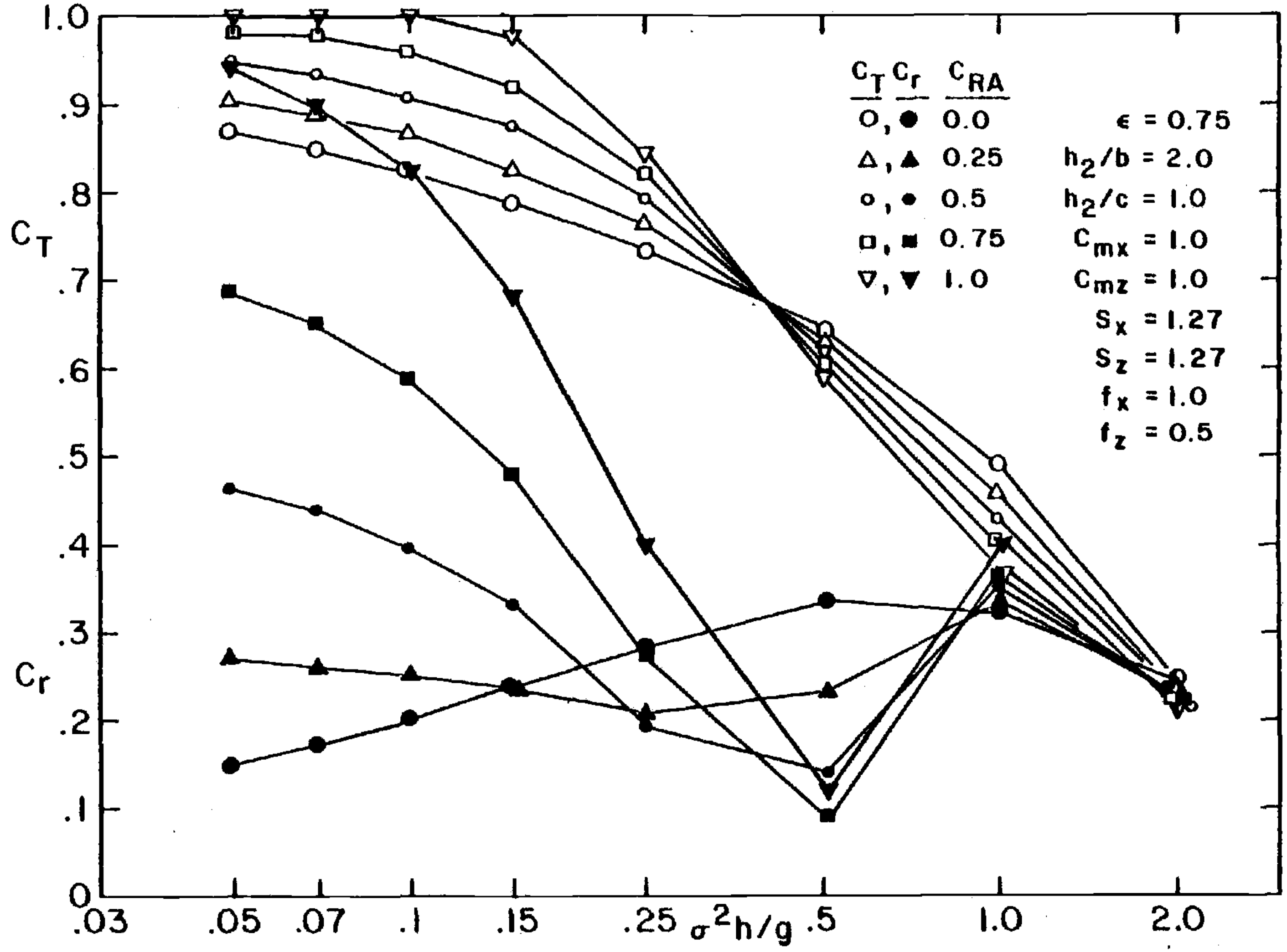

Figure 7.45. Reflection and transmission coefficients for varying values of C_{RA}. $h_2/c = 1.0$.

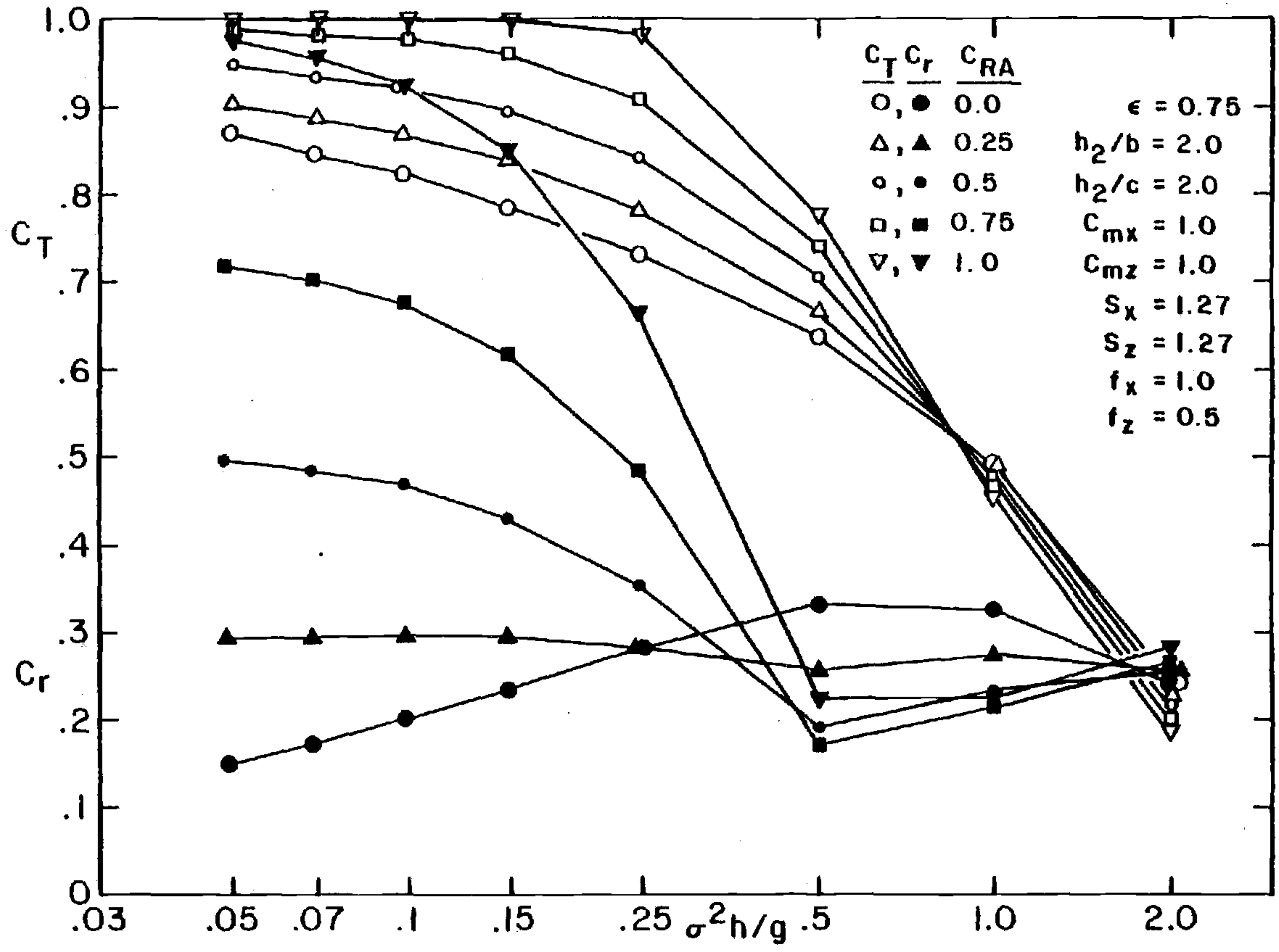

Figure 7.46. Reflection and transmission coefficients for varying values of C_{RA}. $h_2/c = 2.0$.

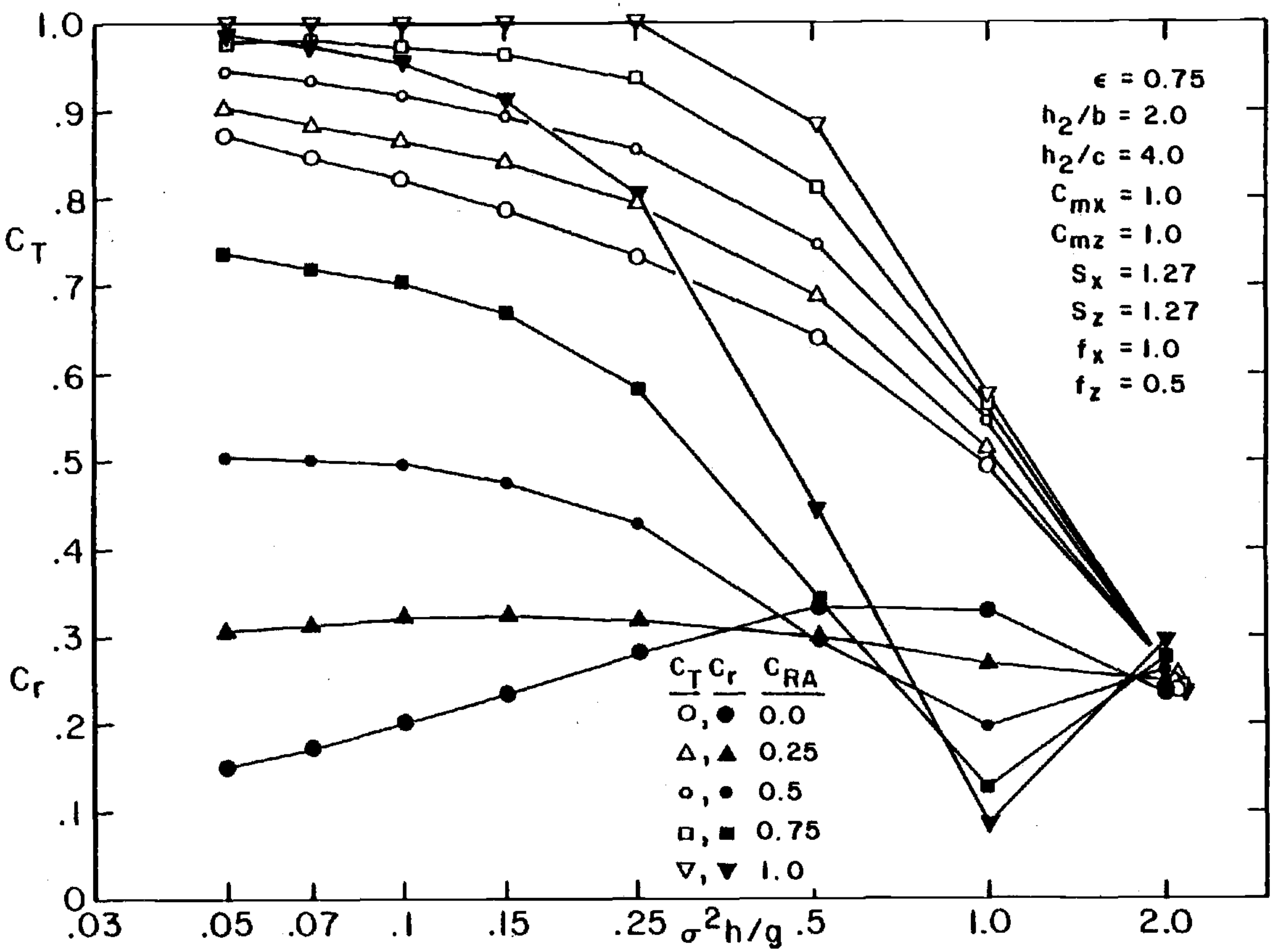

Figure 7.47. Reflection and transmission coefficients for varying values of C_{RA}. $h_2/c = 4.0$.

VIII. EXPERIMENTAL RESULTS AND THEORETICAL COMPARISONS

8.1. Introduction

In order to assess the value of the analytical model, comparisons have been made between experimentally obtained reflection and transmission coefficients and those predicted by the analytical model. This chapter provides the results of these comparisons for the experimental model studies conducted by Costello (1952), Kondo (1972) and an unpublished study by Sollitt. The model structures range from Costello's rectangular matrices of vertical piles to Kondo's orthogonal matrix of vertical and y-directed piles and finally to Sollitt's composite system of vertical piles in conjunction with an automobile tire matrix. Thus, the validity of the analytical model is assessed over a broad range of structures and under a variety of conditions.

8.2. Costello's (1952) Results vs. the Analytical Model

Sollitt and Cross (1972) compared their theoretical predictions of reflection and transmission coefficients for a two dimensional matrix of vertical piles to the data obtained experimentally by Costello (1952). Sollitt (1972) described Costello's model as follows:

> Costello (1952) conducted two-dimensional model tests on pile-array structures composed of vertical circular cylinders. . . .

The structures are composed of 3/8-inch-diameter piles spaced 1 inch on center in an orthogonal pattern of rows and columns. The resulting porosity is 89 percent. The water depth is maintained at 1.5 feet and the piles extend well above the maximum wave height. The two structures differ only in longitudinal extent; one is 24 rows long, the other is 48 rows long.

Incident and transmitted wave amplitudes are monitored with parallel-wire resistance-type wave gages. No mention or record of reflection measurements is given. The transmission coefficients are measured 3.5 feet shoreward of the test section. The incident wave characteristics are varied between the following limits: $0.01 < H_1/L < 0.12$; $1 \leq kh \leq 4$.

Sollitt's Figure 44 (1972) comparing the 1972 theory with Costello's data has been reproduced with full permission in Fig. 8.1 of this study. The reflection and transmission coefficients predicted by the present analytical model have also been superimposed upon Fig. 8.1. The only parametric variation in the two theoretical analyses is that Sollitt (1972) employed an added mass coefficient of two and a drag coefficient relationship derived from steady flow considerations of

$$C_D = \frac{10}{\mathbb{R}} + 1.2$$

The present theory used the added mass coefficients

$$C_{mx} = C_{mz} = 0.0$$

as prescribed in Sec. 5.6. It was somewhat difficult to establish the drag coefficient relationship in the manner discussed in Sec. 5.5 of

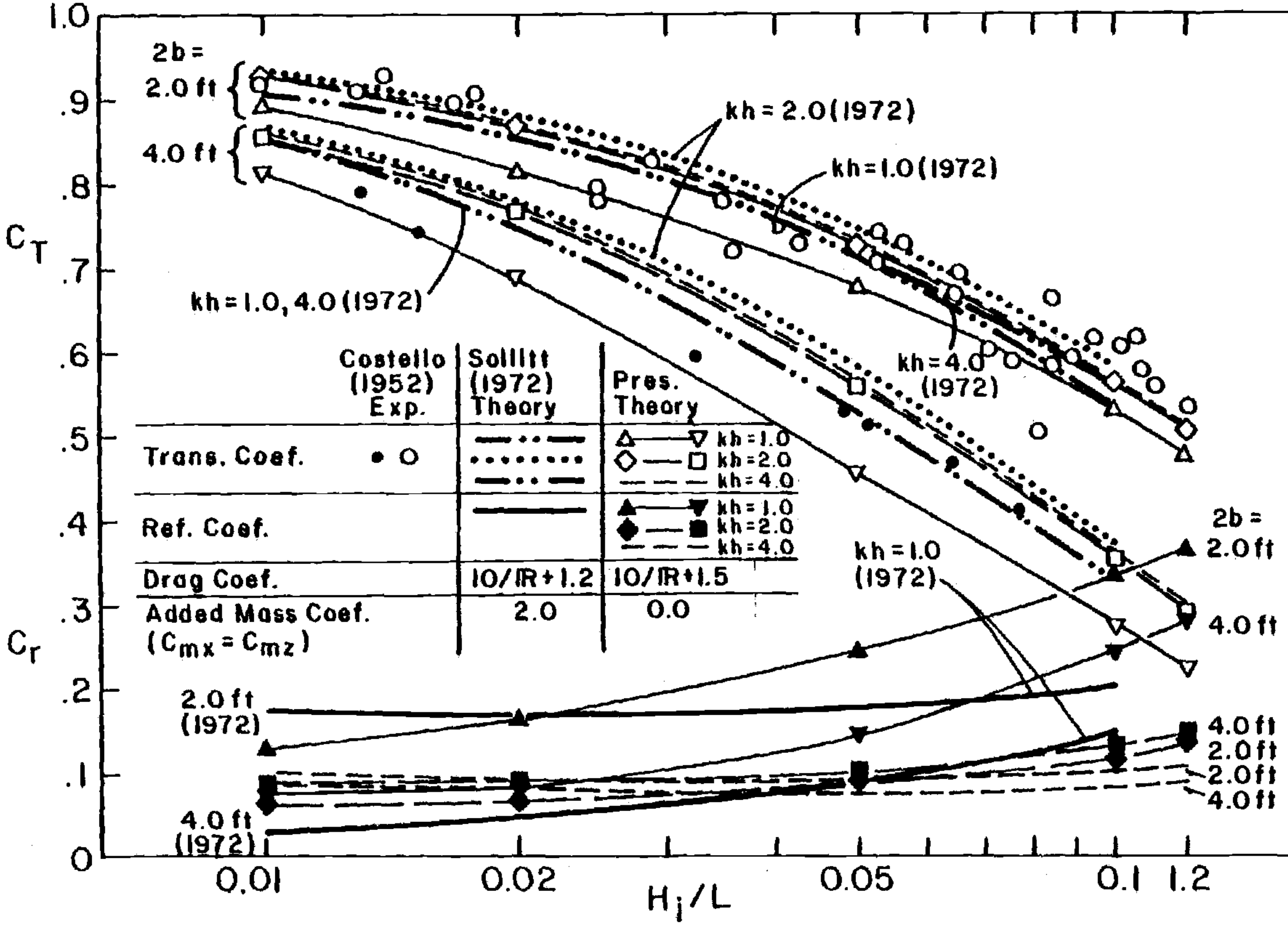

Figure 8.1. Comparison of reflection and transmission coefficients predicted by Sollitt (1972), the present theory, and experimental model study by Costello (1952). (Figure used by permission--Sollitt (1972).)

this paper due to the facts that oscillatory drag and lift coefficient data were unavailable for the low range of Reynolds numbers at which the model tests were conducted and due to the fact that proximity effects were unknown. The steady flow drag coefficient at the maximum Reynolds number encountered in the experiments was approximately unity while the nearest oscillatory data ranged from about 1.8 to 2.5 over the model study values of $2\xi/D$ and the oscillatory lift coefficient ranged from about one to three. It was felt, in a subjective manner, that the importance of the transverse force in dissipating wave energy in a rigid model at low Reynolds numbers was probably minimal and certainly did not justify superposition of a value of from one to three with the drag coefficient value. Furthermore the success enjoyed by Sollitt's (1972) theory seemed to indicate that the values of 1.8 to 2.5 from the oscillatory drag coefficient data were probably also too high. Finally, in light of the literature study related in Chapter V it was determined that a strictly steady flow emphasis was not correct. Consequently, a 'best estimate' compromise was employed in which the average of the closest oscillatory flow data over the experimental range of $2\xi/D$ was determined to be approximately two and this was averaged with the steady flow value of unity to achieve a 'B' value in Eq. (5.5.1) of about 1.5. The lift affects (if any) were not incorporated and it was hoped that this might tend to balance the failure to account for proximity effects (if any). The 'A' value of 10.0 in Eq. (5.5.1) used by Sollitt (1972) yielded a good approximation of the steady flow drag coefficient in the lower Reynolds number regime. Thus a drag coefficient relationship of

$$\frac{10}{\mathbb{R}} + 1.5 \quad .$$

was employed in the present theory's analysis of Costello's models. Lacking in sophisitication and mathematical elegance, the above described method of obtaining a drag coefficient relationship serves to illustrate the difficulty in establishing such a relationship when little or no pertinent data is available. Since oscillatory flow drag coefficient data is more readily available for circular cylinders at Reynolds numbers above 10^4, it is expected that this difficulty would not be a serious problem for prototype applications. It is, however, a recurring problem in these model applications and, as will be seen, must be dealt with by means of simple steady flow experimental evaluations for the case of the composite tire-pile structure.

The kh values corresponding to the experimental transmission coefficients are not given in Fig. 8.1 because they were not available in the 48 pile case $(2b \approx 4.0 \text{ ft})$ and because the scatter in the 24 pile case $(2b \approx 2.0 \text{ ft})$ did not indicate specific trends with regard to kh. Consequently, the present analytical model and

Sollitt's (1972) theory computed the transmission coefficients for the extreme values of kh, i.e., kh = 1.0 and kh = 4.0, to form an envelope and for one intermediate value, kh = 2.0. These are shown in Fig. 8.1 with the experimental data.

In both of the theories shown in Fig. 8.1, and as indicated by the plotted experimental data, wave transmission decreases with increasing wave steepness as expected. That is, steep waves have higher energy density levels and, thus, are more prone toward turbulent instability and energy dissipation. Consequently less of the wave is transmitted in the relative sense. Sollitt (1972) found that little or no trends were apparent for variations in kh, however, the present model predicts slightly increasing values of wave transmission with increasing values of kh although the increase in C_T is extremely small for the shorter waves. It might seem curious that the long waves (kh = 1.0) are predicted to transmit less than the shorter waves in light of the results from the preceding chapter. Those results, however, were obtained for fixed arbitrary values of the dimensionless damping coefficients. In the Fig. 8.1 results, damping coefficients are allowed to converge to values determined by the wave regime and the structural parameters via Lorentz' condition of equivalent work. In the kh = 1.0 case, the water particle velocities are higher and hence the converged dimensionless damping coefficient f_x is much larger than in either of the other two cases.

This results in increased dissipation and lower transmission for any given wave steepness.

The 48 pile case also exhibits larger values of the dimensionless damping coefficient, f_x, than that of the 24 pile case. Thus, as expected, transmission decreases with increasing numbers of piles.

The experimental transmission coefficient data, the C_T predictions of the present model, and those of Sollitt's (1972) theory are all in reasonable agreement. It is thought that the present model would correlate even more closely with Sollitt's (1972) theory had the drag coefficient relationship and the added mass coefficients been the same for both theoretical analyses.

No reflection coefficient data was available from Costello's model study for comparisons. Sollitt (1972) plotted the reflection coefficients for the single case of $kh = 1.0$ as shown in Fig. 8.1. Sollitt's results differ from those of the present model in both slope and magnitude for this case but, again, these differences are by and largely attributable to the lack of congruity in the added mass coefficients and the drag coefficient relationships.

It is interesting to note that the present theory's reflection coefficient curves for the longest wave case $(kh = 1)$ generally exceed those of the shorter waves. This occurs because the dimensionless wave frequency, $\sigma^2 h/g$, value for this case is approximately equal to 0.76. As shown in the last chapter (see Figs. 7.11

through 7.15, for example) the peak reflections generally occur between $\sigma^2 h/g$ values of 0.5 and 1.0. Since the $kh = 2$ and $kh = 4$ cases have dimensionless wave frequencies considerably in excess of this peak range, it is to be expected that the longer wave case would produce more reflection.

Although there is little difference between the present theory's 48 and 24 pile reflection coefficient curves for the shorter wave cases, the $kh = 1$ case exhibits significant variation. Surprisingly, the 48 pile configuration manifests lower reflection coefficients than the 24 pile case despite its higher value of the dimensionless damping coefficient, f_x. This is accounted for by the high interfacial porosity which admits a large portion of the incident wave. Thus a significant fraction of the reflected wave must be attributed to internal reflections within the structure. Since dissipation is greater within the 48 pile structure, it allows less of the internal reflections to escape back into Region I and, hence, reflections are diminished. This hypothetical explanation should not be construed as a generalization since reflections are complex functions of the porosities, the structural configuration, and the incident wave height and frequency. This complexity is verified by the reversal of the above description for the $kh = 2.0$ case as shown in Fig. 8.1.

The over-all assessment of the present theory's behavior with regard to Costello's (1952) experimental model must be tempered by the difficulty in establishing a drag coefficient relationship and the lack of an experimental reflection coefficient comparison. Otherwise, the present analytical model is judged to conform acceptably to Costello's model.

8.3. Kondo's (1972) Results vs. the Analytical Model

Kondo (1972) has conducted wave tank experiments to determine the reflection and transmission coefficients for a matrix structure composed of vertical and y-directed circular cylinders. The structural configuration is that of an orthogonal lattice in which each row of vertical cylinders is followed by a row of y-directed cylinders. There are eight rows of each of the vertical and the y-directed cylinders. The structure extends fully across the width of the wave tank so that wave diffraction around the structure is not a problem. The center to center longitudinal width of the structure and the diameter of the cylinders were held constant at values of 51 cm and 3.4 cm, respectively.

Reflection and transmission coefficients were measured by Kondo (1972) for three values of the wave period, two different water depths, and a host of wave heights. It is interesting to note that the reported wave heights[13/] are exceptionally small and, consequently,

---

[13/] Kondo (1972) conducted experiments using both horizontal and sloping bottoms. Only the horizontal bottom case is addressed the maximum horizontal dimensionless water particle excursions, as calculated from linear wave theory, are generally less than unity. Thus inertial effects are expected to predominate and analysis by potential or diffraction theoreies seem to be more appropriate than the Morison type approach employed herein.

Kondo's experimental data are shown in Figs. 8.2 through 8.5 along with the predicted reflection and transmission coefficient curves computed by the present analytical model. As indicated on the figures, the porosity calculated by the analytical model is 0.56 for Kondo's lattice structure. This porosity is slightly lower than the general theoretical porosity of 0.607 calculated by Kondo. However, Kondo's porosity calculation is based strictly on the theoretical pore volumes and is not subject to the slight variations with water depth when the porosity is defined as the ratio of the volume of fluid in the structure to the total volume of the structure. That is, the porosity of a pore that is filled with fluid to the top of the pore will differ from one that is filled to only one-half its height. Hence, the analytical model porosity, calculated for the water depth and lattice structure described by Kondo, differs slightly from Kondo's theoretical porosity.

---

for this comparative analysis. Consequently, all references to experimental measurements in this section refer exclusively to Kondo's horizontal bottom experiments.

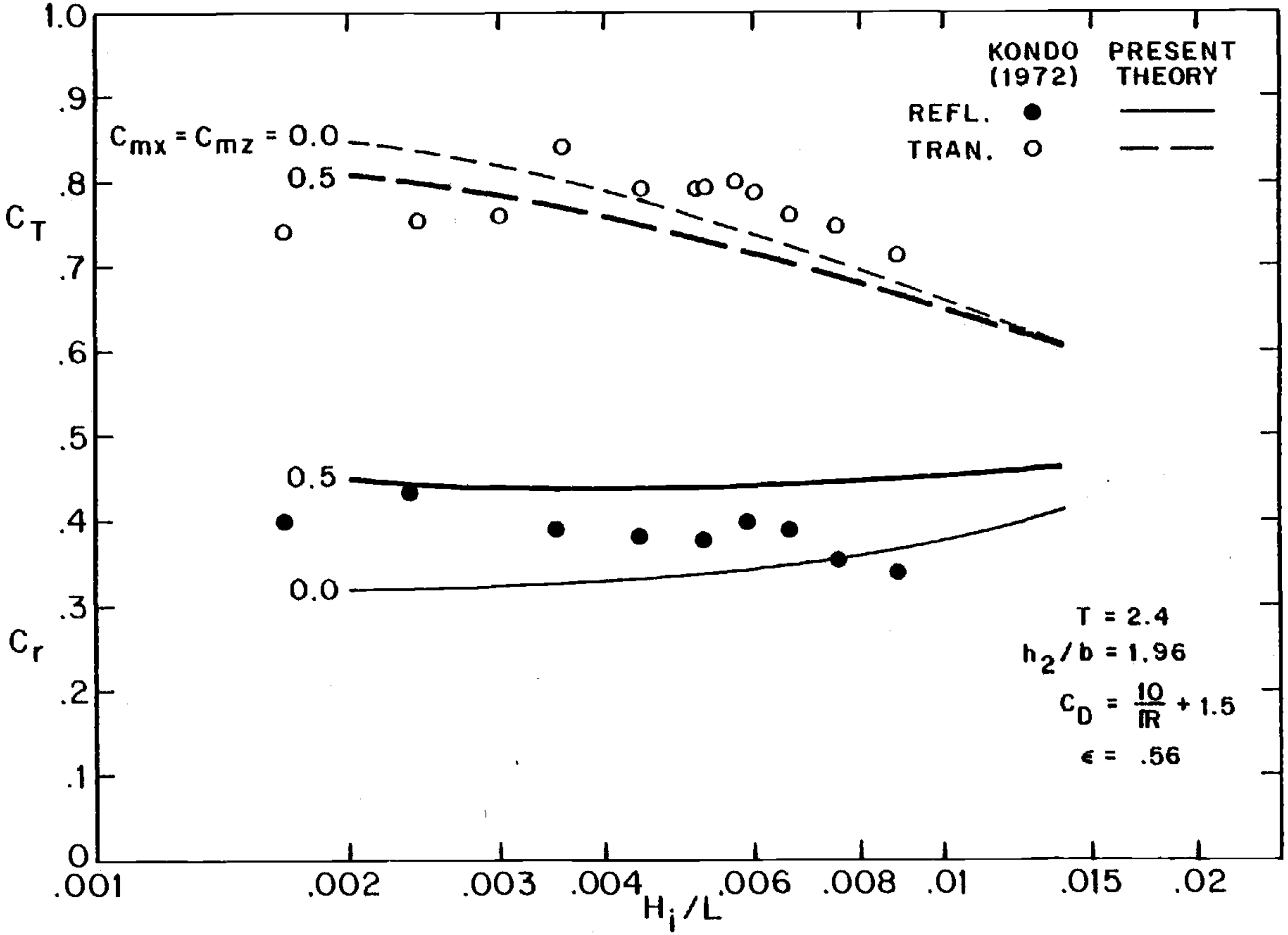

Figure 8. 2. Comparison of computed reflection and transmission coefficients with Kondo's (1972) experimental data. T = 2. 4.

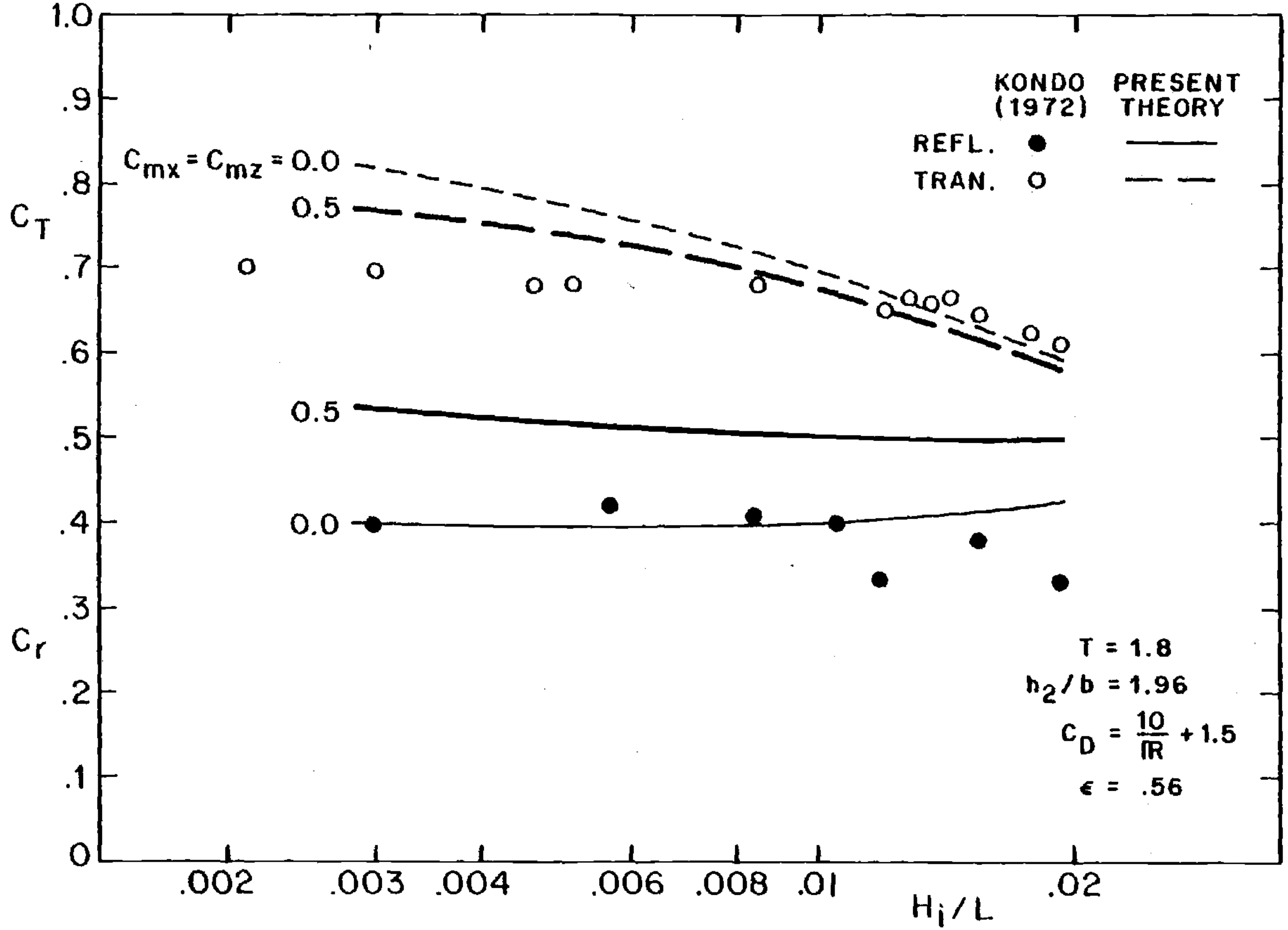

Figure 8.3. Comparison of computed reflection and transmission coefficients with Kondo's (1972) experimental data. T = 1.8.

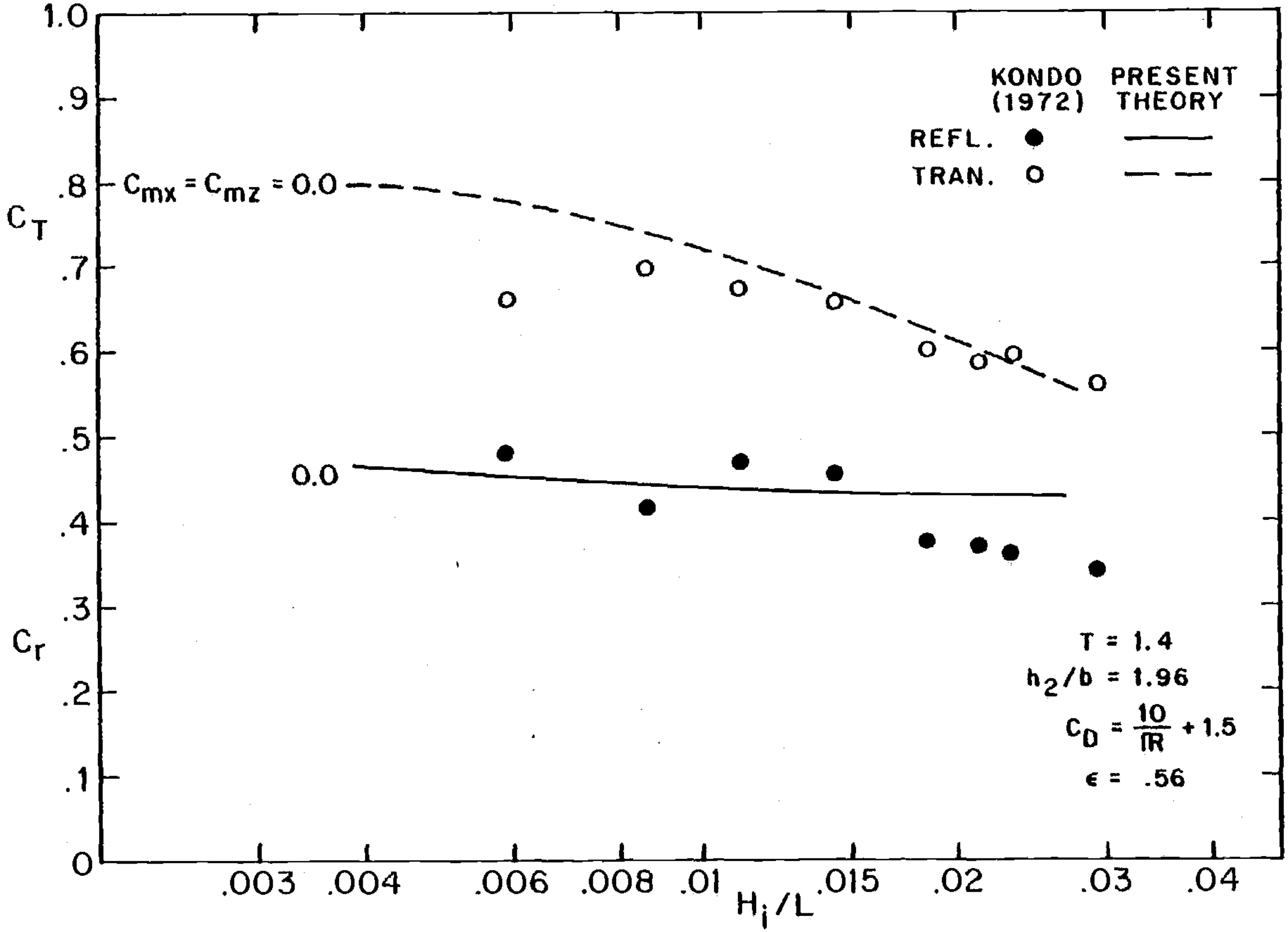

Figure 8.4. Comparison of computed reflection and transmission coefficients with Kondo's (1972) experimental data. T = 1.4.

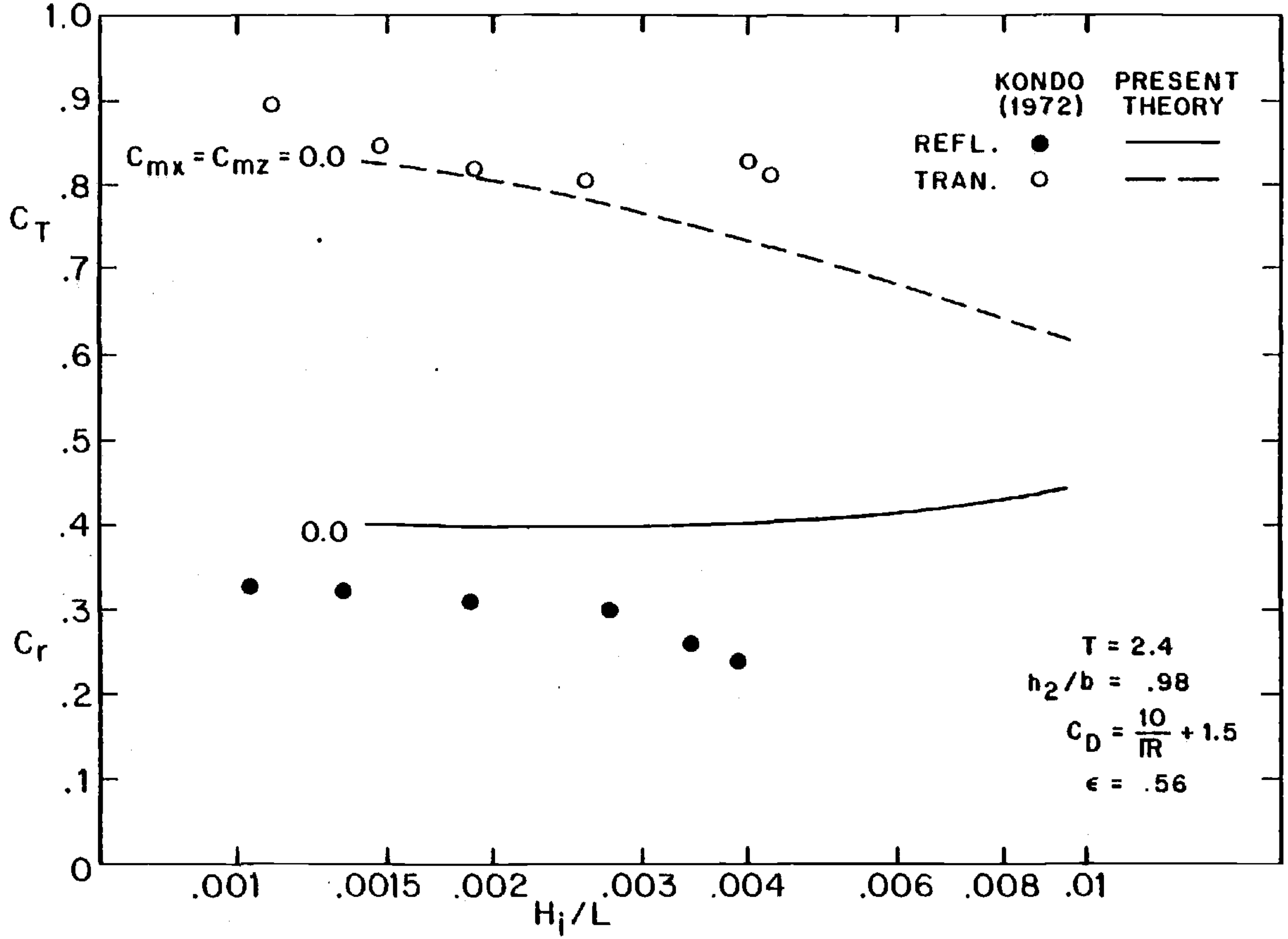

Figure 8.5. Comparison of computed reflection and transmission coefficients with Kondo's (1972) experimental data. T = 2.4, h_2/b = .98.

Vertical and horizontal added mass coefficients of 0.5, in addition to the 0.0 values prescribed in Chapter V, have been employed in the theoretical analysis of the 2.4 and 1.8 second wave cases as shown in Figs. 8.2 and 8.3. This has been done to investigate the analytical model's sensitivity to the added mass coefficients (and hence the inertial coefficients) over the inertially dominated range of Kondo's model study. It is apparent in Figs. 8.2 and 8.3 that the added mass coefficient has a significant effect on the calculated reflection coefficients over the entire range of wave steepnesses although there is a convergent trend with increasing wave steepness. This effect is also observed in the transmission coefficient curves, but to a lesser degree. Therefore, it is concluded that the analytical model is rather sensitive to the added mass coefficients under inertially dominated conditions, but this sensitivity is decreased with increasing wave steepness, i.e., increasing drag dominance.

The drag coefficient relationship employed for this analysis is again

$$C_D = \frac{10}{\mathbb{R}} + 1.5$$

The maximum Reynolds number encountered is slightly less in Kondo's experiments than in Costello's experiments described in the previous section. Thus more emphasis might be placed on the steady flow drag coefficient data rather than the above empirical equation which applies to the average of steady flow data and the terminus of oscillatory data. However, it is felt that the above relationship provided satisfactory results over the entire range of Reynolds numbers for the Costello (1952) analysis. Consequently this relationship has been employed here.

The analytically predicted reflection and transmission coefficients are compared with the experimentally obtained data of Kondo's (1972) study in Figs. 8.2 through 8.5 for the four cases of:

(1) $T = 2.4$; $h_2/b = 1.96$

(2) $T = 1.8$; $h_2/b = 1.96$

(3) $T = 1.4$; $h_2/b = 1.96$

(4) $T = 2.4$, $h_2/b = .98$

respectively. Figures 8.2 through 8.4 indicate that the predicted transmission coefficients correlate well with the magnitude and trend of the experimental data when $C_{mx} = C_{mz} = 0.0$ and the wave steepnesses are relatively high. Although these 'relatively high' waves all have dimensionless water particle excursion values less than two and often less than unity, and thus are still inertially dominated, the analytical model appears to compare favorably with these experiments regarding wave transmission. This is not true for the relatively low waves of the experiments as evidenced in all of the figures for small values of H_i/L. That is, for extreme inertially dominated conditions the analytical model disagrees with the experimental model in magnitude and/or trend with regard to wave transmission.

The predicted reflection coefficients for the first three cases generally agree in a somewhat acceptable fashion with the experimental data magnitudes over a reasonably large range of the experimental wave steepnesses. However the trend of the reflection coefficient curves does not correlate well with that of the experimental data for relatively high values of the wave steepness. That is, the predicted reflection coefficient curves are either increasing or horizontal for relatively high wave steepnesses while the experimental data tend to decrease slightly with increasing wave steepness in Figs. 8.2 through 8.4. The computed reflection coefficients do not correlate at all with the experimental data of the extreme inertially dominated case plotted in Fig. 8.5.

Thus, the overall assessment of the analytical model with regard to Kondo's experiments may be summarized as generally unfavorable transmission coefficient correlation for the lower wave steepness (extreme inertially dominated) data, good transmission coefficient agreement at the higher wave steepness data, and generally acceptable but suspect reflection coefficients over all but the lowest wave steepness data. Considering the fact that these model experiments were conducted entirely in the inertially dominated range, it is curious that the analytical model functioned as well as it did. It is hypothesized that the form of the drag coefficient relationship is in part responsible for this phenomenon since the first term of this relationship provides increased dissipation forces at lowering Reynolds numbers over that of a strictly constant drag coefficient. This behavior is analogous to the increase in the inertial force as the water particle velocities go to zero due to the 90° phase shift between acceleration and velocity components. A reliable relationship between the inertial coefficient and the Reynolds number and/or the dimensionless water particle excursion parameter is lacking. It must be concluded that the analytical model must be applied with caution under conditions of low water particle excursion parameter values.

8.4. Sollitt's (unpublished) Results vs. the Analytical Model

In accordance with Dames and Moore, Inc., job number 327-032-03, Sollitt has conducted experimental model studies to determine the transmission and reflection coefficients for:

(1) a single row of closely spaced piles;

(2) two rows of (laterally) closely spaced piles, $h_2/b = 8.0$;

(3) two rows of closely spaced piles, $h_2/b = 8.0$ (unless otherwise noted), in conjunction with a reflecting wall, $C_{RA} = 1.0$, h_2/c = variable;

(4) two rows of closely spaced piles, $h_2/b = 8.0$, with a Wave Maze® automobile tire network sandwiched between the two pile rows, and, with and without the reflecting wall.

The experiments were conducted in the indoor wave channel at Oregon State University at a constant water depth of 20 inches. A broad range of incident wave heights and periods were sampled. The results are plotted versus the wave steepness parameter H_i/L. The results have been found to be frequency dependent as well as wave steepness dependent, however, relatively few wave heights were sampled at any given wave period. Thus the plotting format of the previous section, which provided a different figure for each wave period depicts greater detail than data can provide. Consequently, the wave frequency variation is expressed on each figure by a series of tabulated integers along the underside of the upper boundary of each figure. Each integer corresponds to the dimensionless wave frequency, $\sigma^2 h/g$, of that particular data point. The smaller integer values correspond to the smaller wave periods, or higher $\sigma^2 h/g$ values, while larger integers indicate larger periods and, hence, smaller $\sigma^2 h/g$ values.

The piles were modeled using 1/2 inch diameter wooden dowels. The lateral gap spacing between the piles was held constant at 1/8 inch yielding a gap to diameter ratio of 1/4. The model pile rows extended fully across the wave tank in all cases and were aligned normal to the direction of wave advance.

The Reynolds number range of Solitt's experiments were comparable to those of Kondo (1972) and Costello (1952). Unlike Kondo's experiments, however, the dimensionless water particle excursion ranges were generally well above the inertially dominated range and thus may be considered suitable for Morison-equation-type analysis.

8.4.1. Sollitt's Single Row Model

Sollitt's experimentally obtained reflection and transmission coefficients for a single row of closely spaced piles are shown in Fig. 8.6 with the tabulated dimensionless wave frequencies, $\sigma^2 h/g$, corresponding to each data point. Since the vertical scatter range is generally less than or equal to ±0.5 with respect to the plotted data points, it is apparent that the scatter in Fig. 8.6 is primarily due to variations in the dimensionless wave frequency as well as the variation in wave steepness. For this reason, neither the experimental data nor the analytical model results approximate smooth curves and thus the display format is, necessarily, reduced to that of plotted points. Consequently, in order to compare the experimental data with the analytical results in Figs. 8.7 through 8.11, the reader merely proceeds vertically upward from a data point number along a constant line of H_i/L until the data point and the analytical result are encountered.

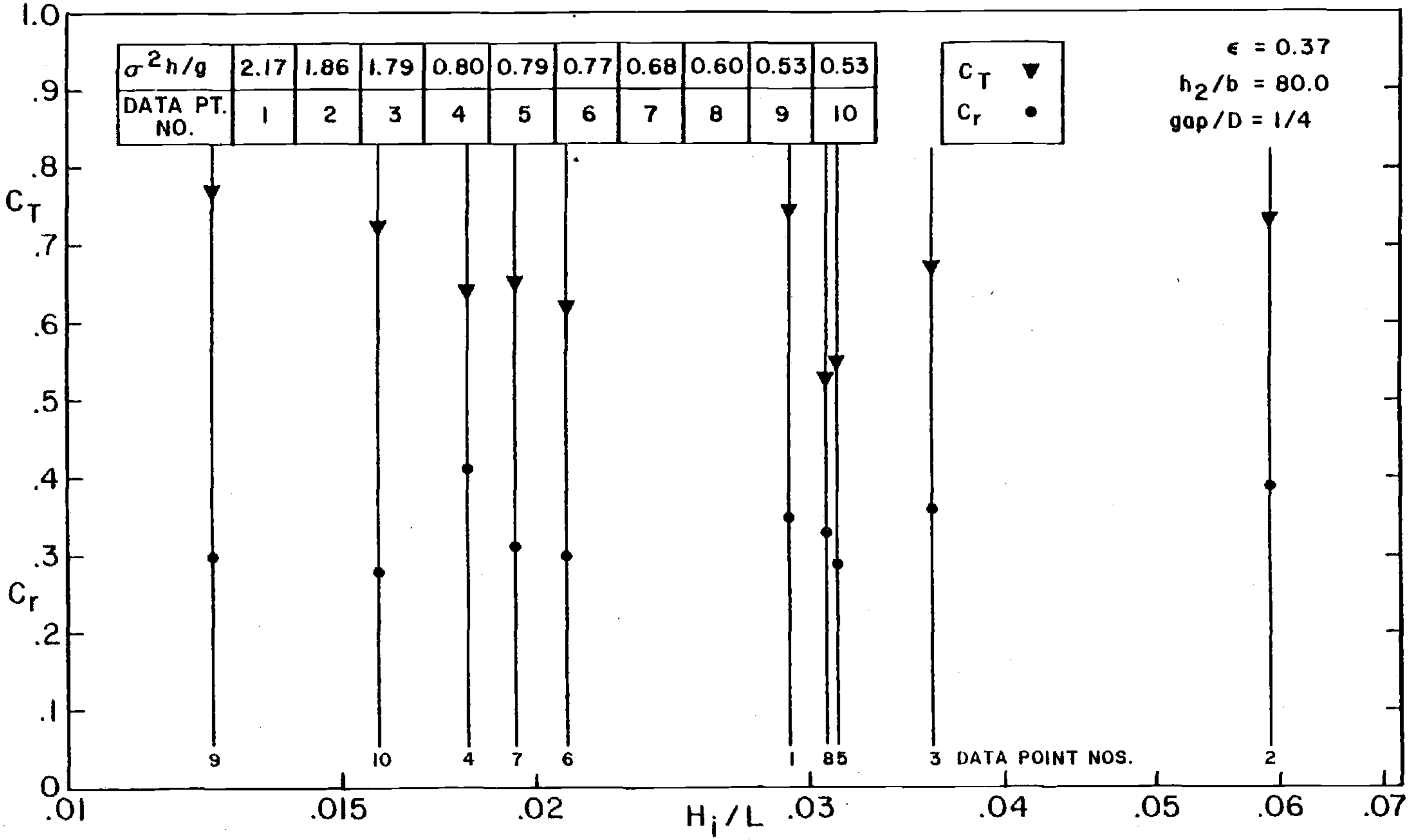

Figure 8. 6. Sollitt's experimentally obtained reflection and transmission coefficients for a single row of closely spaced piles.

The analytical model results for the case in which the drag coefficient relationship,

$$C_D = \frac{10}{\mathbb{R}} + 1.5,$$

is employed are shown in Fig. 8.7. Although this drag coefficient relationship was found to be suitable for the analyses of Costello's and Kondo's models in the two preceding sections, and due to Reynolds number similarities would be thought to be appropriate in this case as well, it is evident in Fig. 8.7 that the analytical model does not correlate well with the experiments. Since the reflection coefficient predictions underestimate and the transmission coefficient predictions generally overestimate the experimental data it is concluded that the analytical model is not accounting for sufficient wave energy dissipation within the structure when the aforementioned drag coefficient relationship is employed. Figure 8.7 also shows the effects of varying the added mass coefficient and, hence, the inertial coefficient. As would be expected for the drag dominated conditions of Sollitt's model tests, variation in these coefficients produces negligible effects in the analytical predictions.

Figure 8.8 shows the same case as Fig. 8.7 except that the drag coefficient relationship 'B'-constant is increased from 1.5 to 3.0 to provide additional dissipation. The analytical model

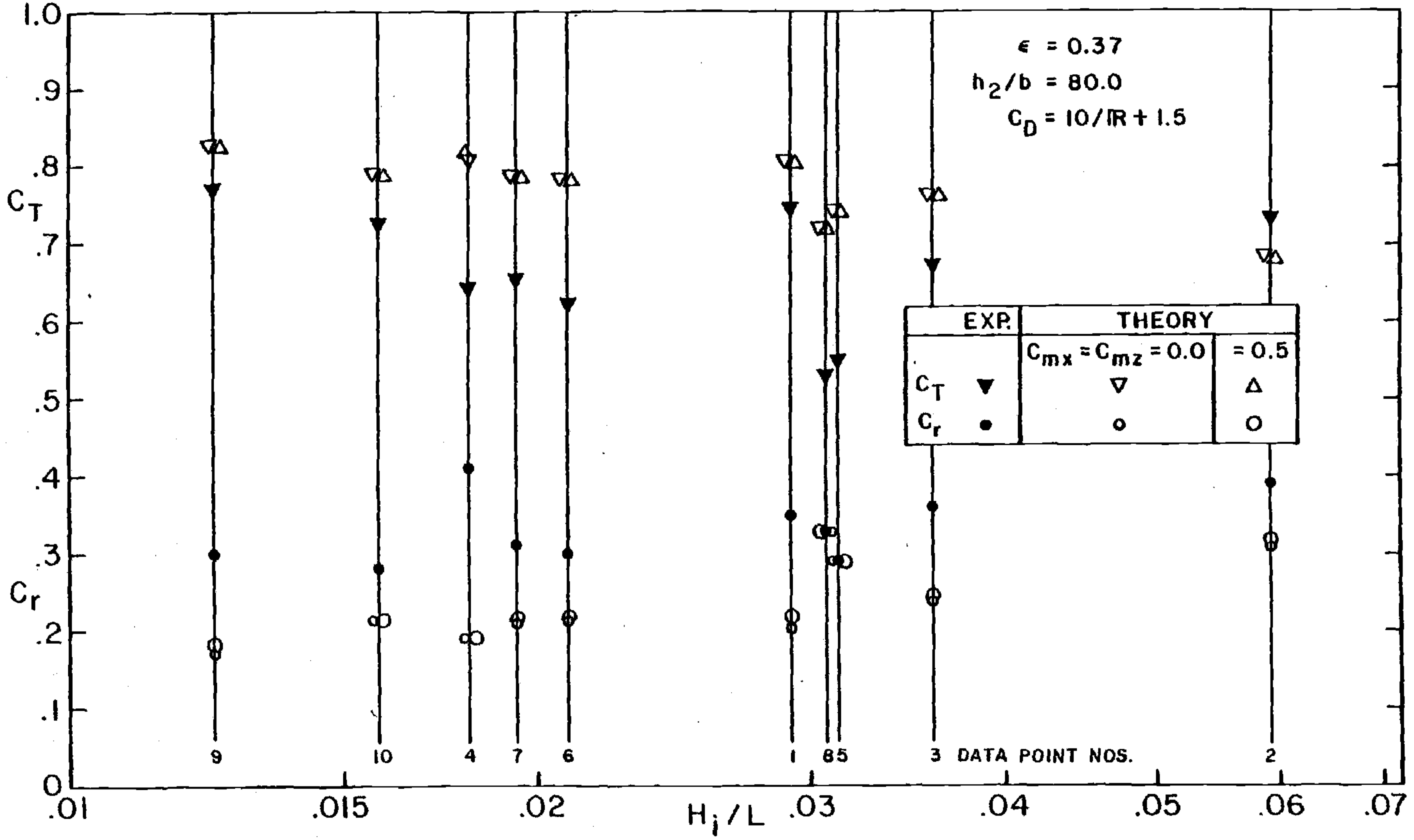

Figure 8.7. Comparison of computed reflection and transmission coefficients with Sollitt's single row model experimental data.

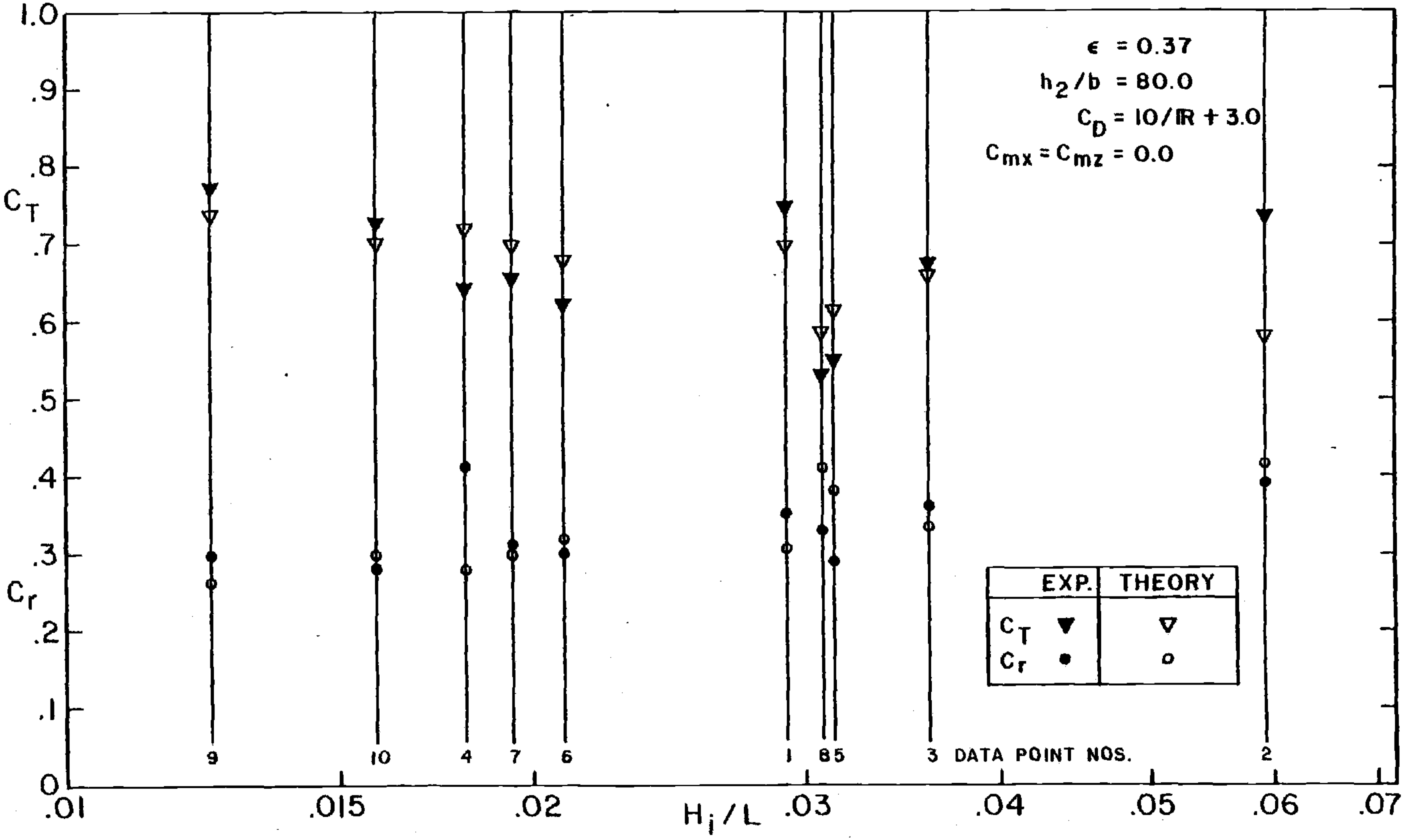

Figure 8.8. Comparison of computed reflection and transmission coefficients with Sollitt's single row model experimental data.

predictions generally compare favorably with the experimental data. The experimental transmission coefficient denoted by data point #2 ($H_i/L = .0593$) may be questionable if the hypothesis that relatively short waves and relatively steep waves transmit relatively less is to be believed. On the other hand, this hypothesis must be questioned when the transmission coefficient of the shorter, steeper wave denoted by data point 1 is compared to longer, less steep points 6, 7, 4, and 10.

It is not known with certainty why the higher drag coefficient constant is required to obtain a good fit between the theory and the experiments but it is thought that the close lateral proximity of the piles is primarily responsible for this phenomenon. However, until the physical mechanism of proximity effects is fully understood and analytically or empirically quantifiable, the drag coefficient relationship employed in Fig. 8.8 could not have been established prior to the model tests.

The concept of employing the porosity rather than the ratio of cross sectional flow areas in the horizontal mass continuity boundary conditions was addressed in Section 3.3.1. Thus the structural porosity term came to be included in the beta and zeta constants of Eqs. (3.3.7 and 3.3.8) respectively and in their orthogonalized versions, Eqs. (4.2.2 and 4.2.3) respectively. The rationale of substituting the porosity for a ratio of cross sectional flow areas might be questioned for a single row of piles and thus it was logical to investigate the porosity sensitivity. Figures 8.9 and 8.10 show the results of employing the area ratio[14/] of 0.2 calculated for this structural configuration. Figure 8.9 shows poor agreement between the theory and experiment and it is concluded that the drag coefficient relationship of

$$C_D = \frac{10}{\mathbb{R}} + 1.5$$

is too dissipative in this case, i.e., promotes too high reflection and is too inhibitive of wave transmission. Figure 8.10 indicates that the analytical model may again be 'tuned' to correlate with the experiments by decreasing the 'B'-constant of the drag coefficient relationship to 1.0 from 1.5. The analytical models of Figs. 8.8 and 8.10 correlate highly. Thus it may be concluded for the theory in this instance that a reduction in the porosity of the structure may be directly offset by a reduction in the viscous dissipation mechanism. That is, reducing the porosity tends to increase reflection at the interface while reducing the drag coefficient relationship decreases

---

[14/] Figures 8.9 and 8.10 define this area ratio as "ϵ local". This is the name of the computer program variable used in calculating the constants beta and zeta. This variable is available in the program for use with non-homogeneous structures to account for local interfacial porosity effects. It is important to realize in Figs. 8.9 and 8.10 that the term ϵ local is an area ratio and not an interfacial porosity. The interfacial porosity will, however, be employed in some of the analyses of Section 8.4.2.

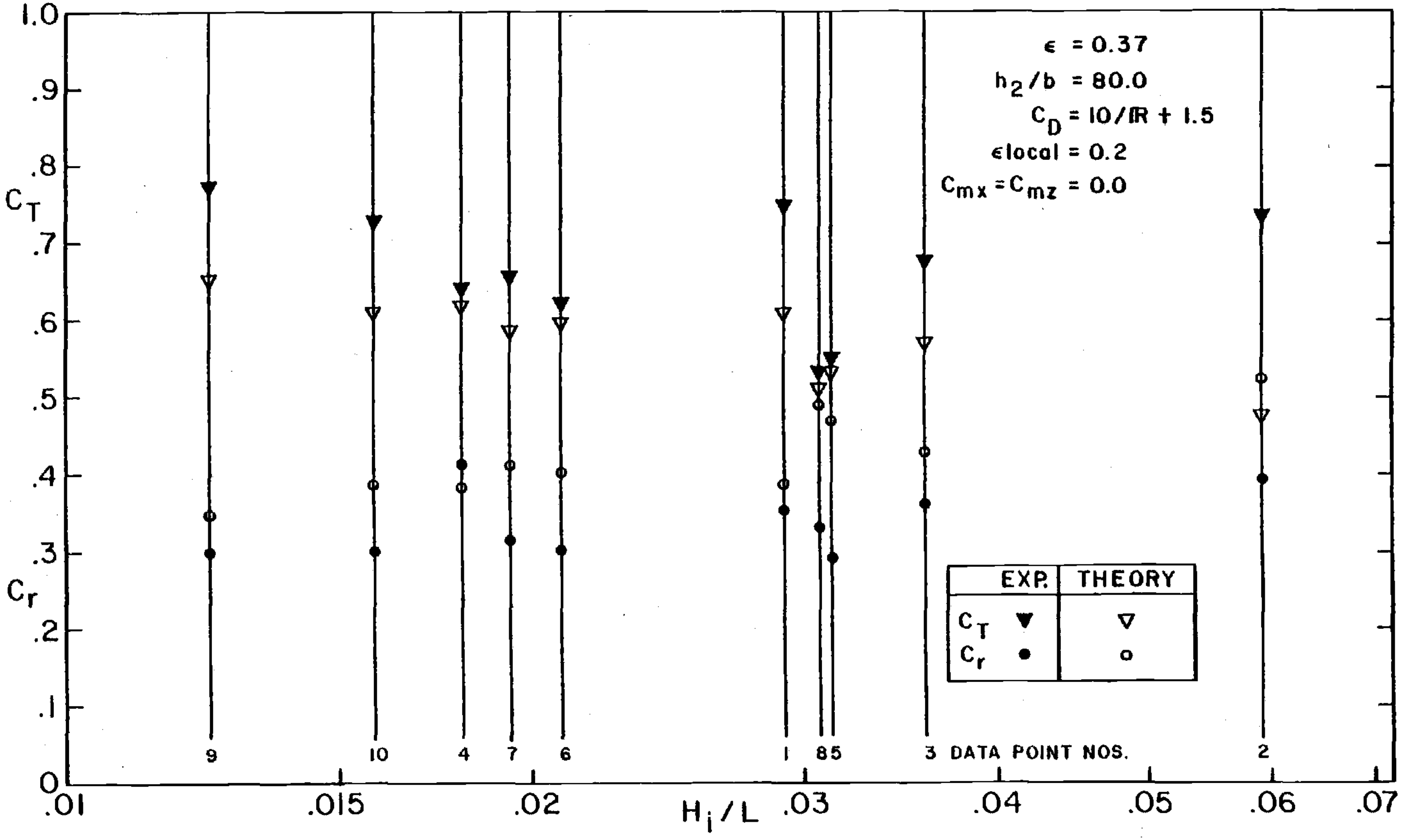

Figure 8.9. Comparison of computed reflection and transmission coefficients with Sollitt's single row model experimental data.

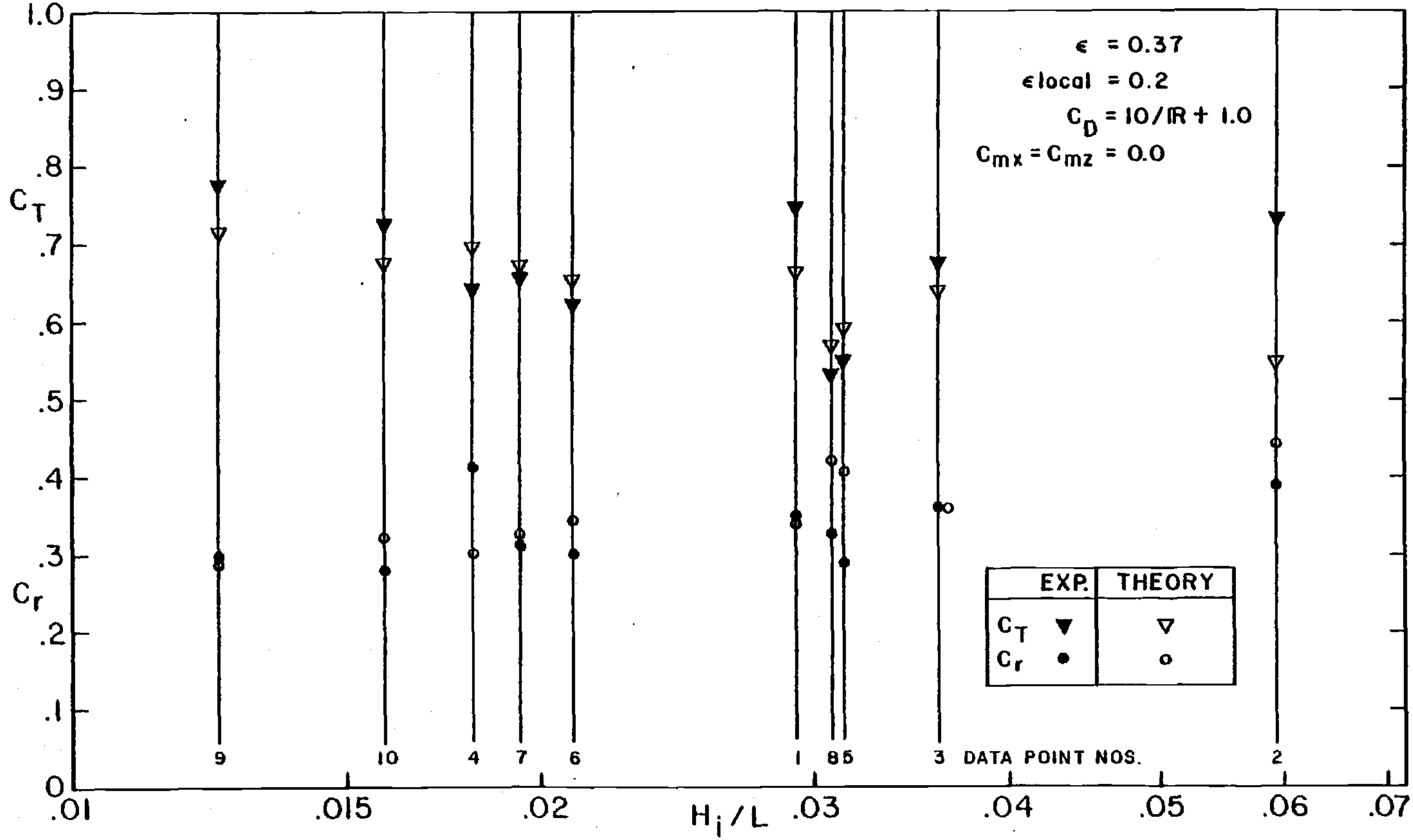

Figure 8. 10. Comparison of computed reflection and transmission coefficients with Sollitt's single row model experimental data.

the structural resistance to wave penetration and transmission thereby decreasing reflection.

It is not known whether the analysis of Fig. 8.8 or that of Fig. 8.10 more appropriately models the actual behavior of the experiments. That question, however, is of little consequence considering that both analyses had to be 'tuned' to the experimental model in order to provide satisfactory results. And although the analytical results do compare favorably to the experimental data in these two figures, it must be noted that some of the simpler, less complicated theories described in Chapter I probably would successfully approximate the experimental data with the appropriate coefficient tuning.

8.4.2. Sollitt's Two Row Model

Sollitt's experimentally obtained reflection and transmission coefficient data for a model consisting of two rows of closely spaced piles is shown in Fig. 8.11. The porosity of the structure defined by the two rows of piles is approximately 0.87. The ratio of the water depth to one-half the longitudinal width, h_2/b, is 8.0 and the gap to diameter ratio is, again, 1/4. The dimensionless wave frequencies corresponding to each of Sollitt's 18 data points are tabulated in Fig. 8.11. Again it should be noted that the scatter apparent in Fig. 8.11 is due primarily to variations in dimensionless wave frequency and wave steepness and that the experimental procedure

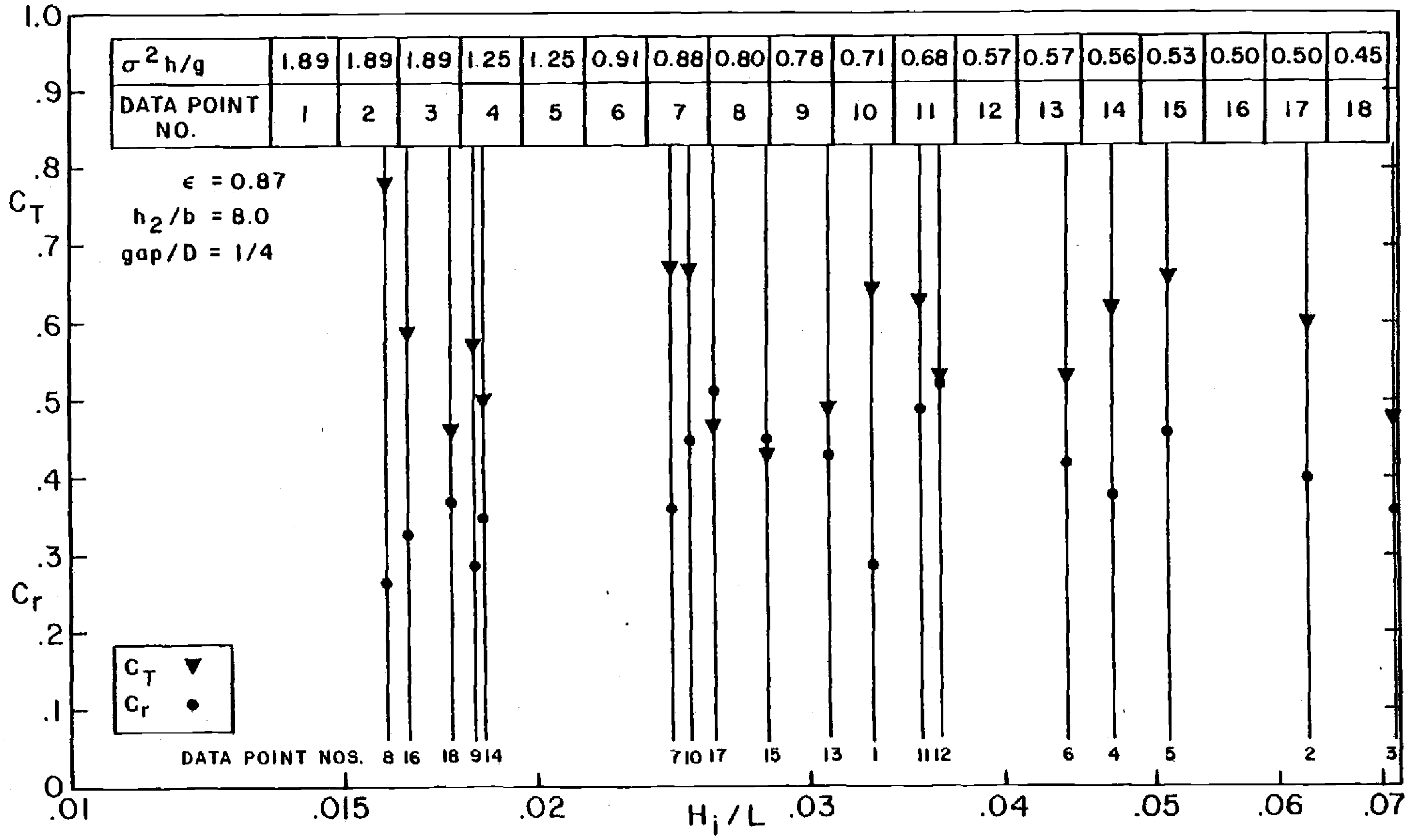

Figure 8.11. Sollitt's experimentally obtained reflection and transmission coefficients for a model consisting of two rows of closely spaced piles.

scatter associated with any given data point is less than or equal to ±.05.

Figure 8.12 depicts the theoretical predictions for the two row configuration when the general structural porosity is used in calculating the beta and zeta constants of the horizontal mass flux continuity boundary equations, Eqs. (4.2.2 and 4.2.3). Wave transmission is very high and reflection is equivalently too low for both of the indicated drag coefficient relationships employed in this analysis.

Figure 8.13 shows the same theoretical analysis as that of Fig. 8.12 except that the local interfacial porosity of 0.37 has been used in Eqs. (4.2.2 and 4.2.3). Since each row of piles conforms to the configuration used for the single row model described in the previous section, it is evident that this value of the interfacial porosity represents a true porosity. Also, the usage of $\epsilon_{local} = 0.37$ conforms to the recommendations of Sec. 3.3.1 as prescribed for nonhomogeneous structures. Unfortunately, neither of the drag coefficient relationships employed yields a generally acceptable theoretical and experimental agreement. It may be noteworthy that the predicted reflection coefficients tend toward acceptable behavior for a significant number of data points when

$$C_D = \frac{10}{\mathbb{R}} + 3.0$$

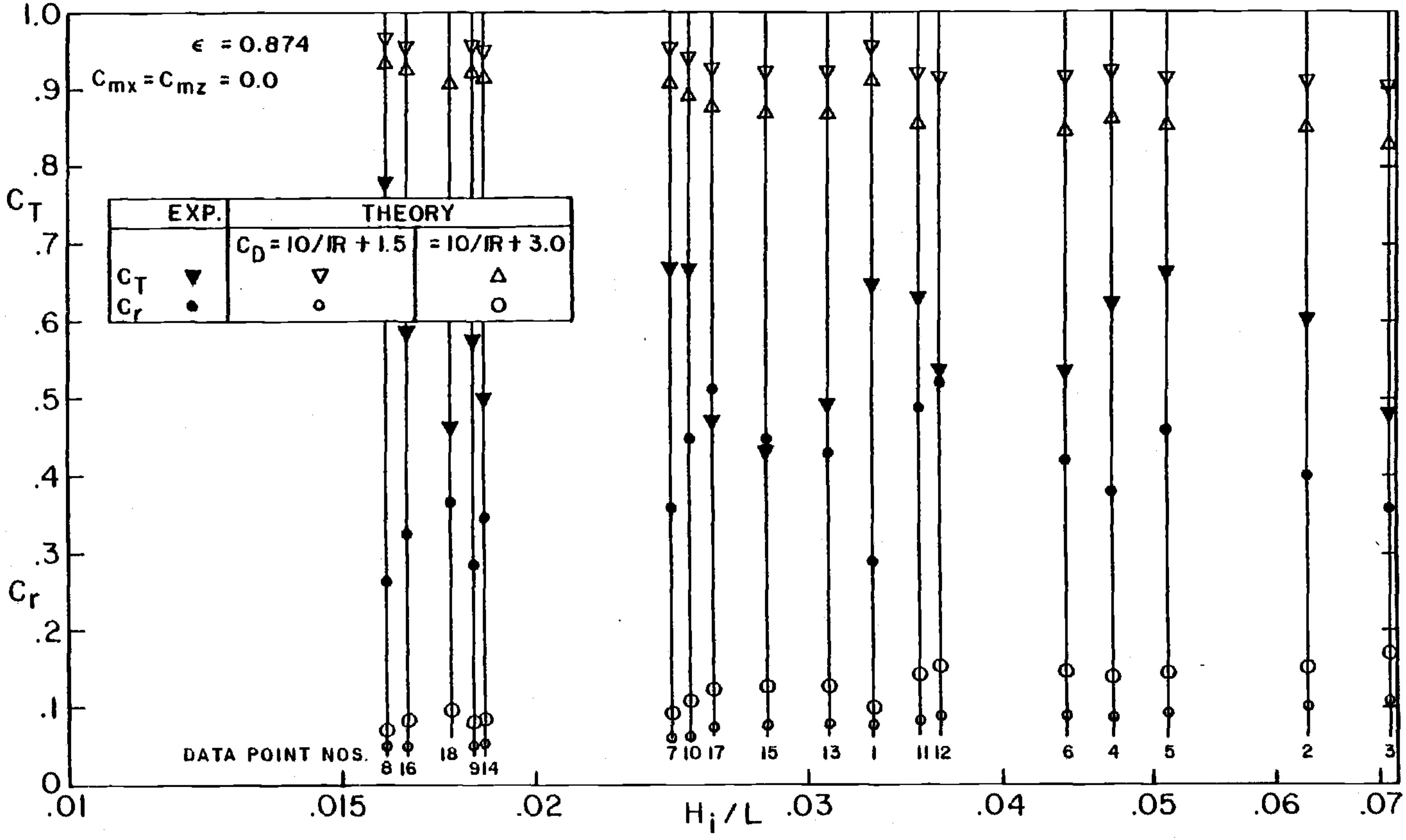

Figure 8. 12. Comparison of computed reflection and transmission coefficients with Sollitt's two row model experimental data.

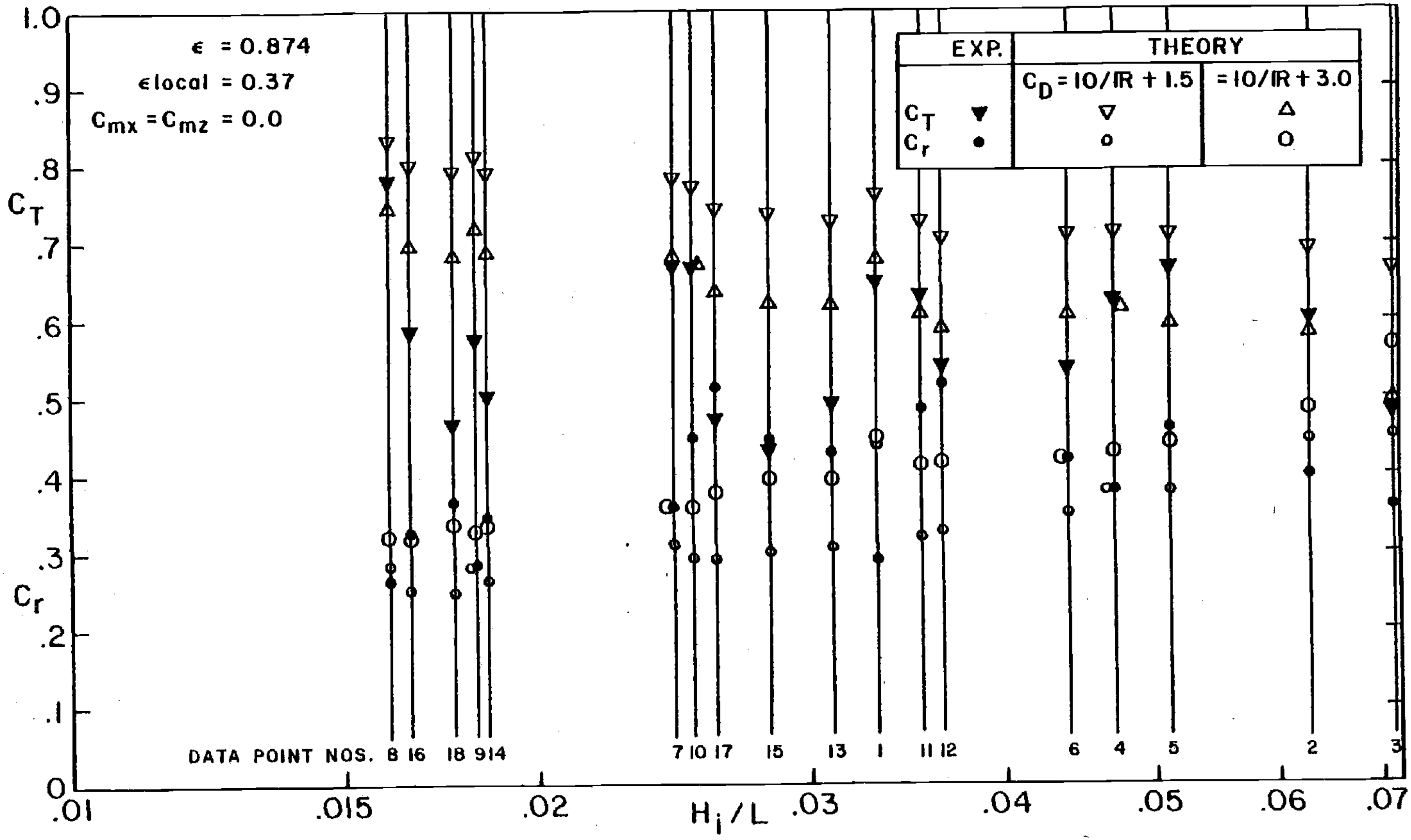

Figure 8. 13. Comparison of computed reflection and transmission coefficients with Sollitt's two row model experimental data.

The predicted transmission coefficients, on the other hand, usually overestimate the experimental data. This might be considered an indication of lack of sufficient dissipation within the analytical model. However, attempts to provide additional dissipation by increasing the drag coefficients yielded increased reflection coefficients as well as lowered transmission coefficients and hence a 'tuned' good fit was not possible using this method of analysis.

Figure 8.14 compares the theoretical and experimental results for the two row model when the ratio of cross sectional flow areas is used instead of a local interfacial porosity. Again, a smattering of poor, fair, and good correlations between the various experimental and theoretical data points is evident, but, in the overall assessment, the agreement between this analysis and the experiments must be judged as unacceptable also.

Figures 8.15 and 8.16 portray the results of analyzing the two row model with the seaward row of piles representing the structure and the leeward row of piles representing a reflector-absorber of reflection coefficient $C_{RA} = 0.33$. Since only the seaward row of piles represents the structure the analysis is exactly the same as that employed in the previous section for Figs. 8.7 and 8.8 with the exception that C_{RA} is changed from zero to 0.33. This value of C_{RA} was determined by averaging the nearly constant experimental reflection coefficient data obtained for a single row of piles as shown

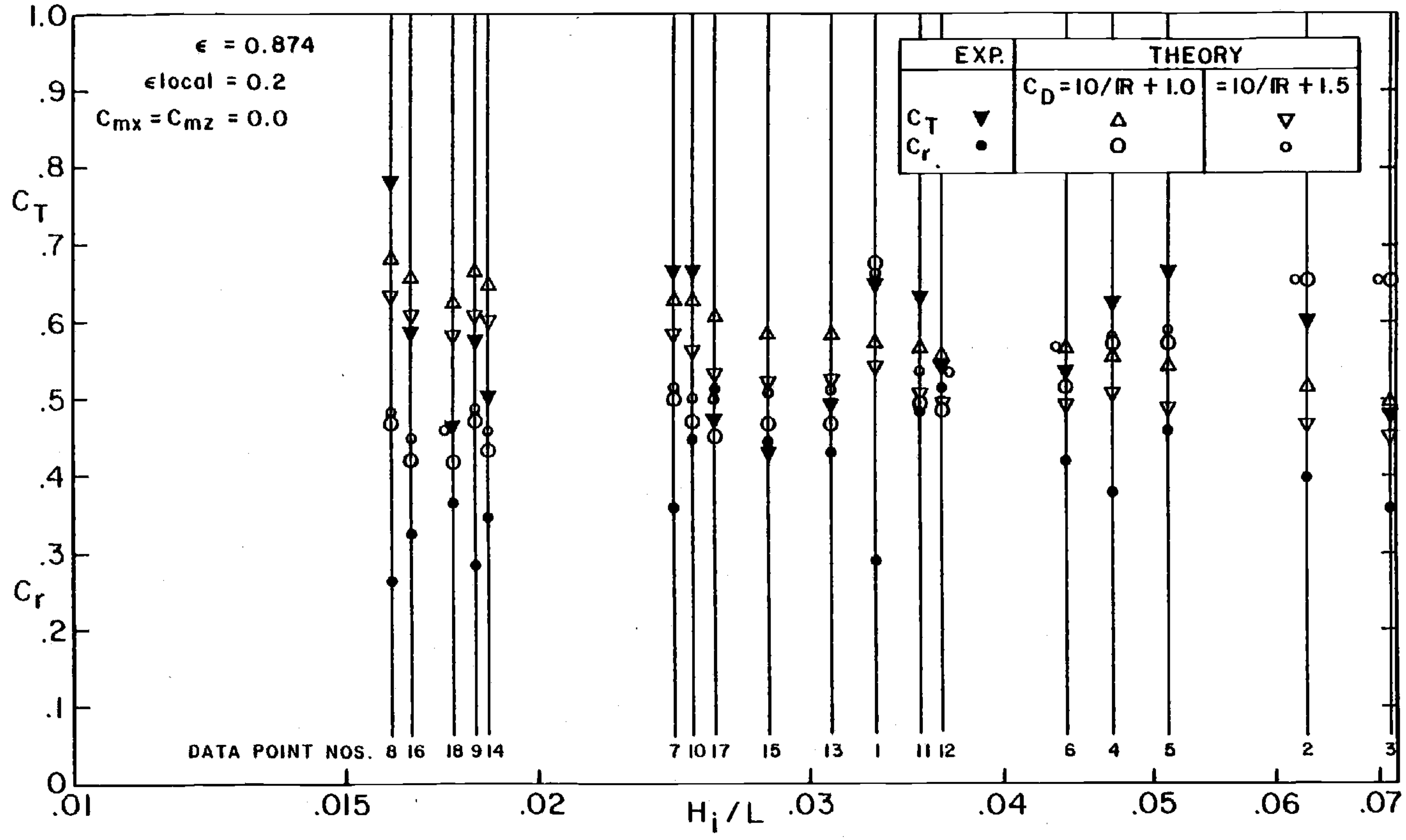

Figure 8. 14. Comparison of computed reflection and transmission coefficients with Sollitt's two row experimental data.

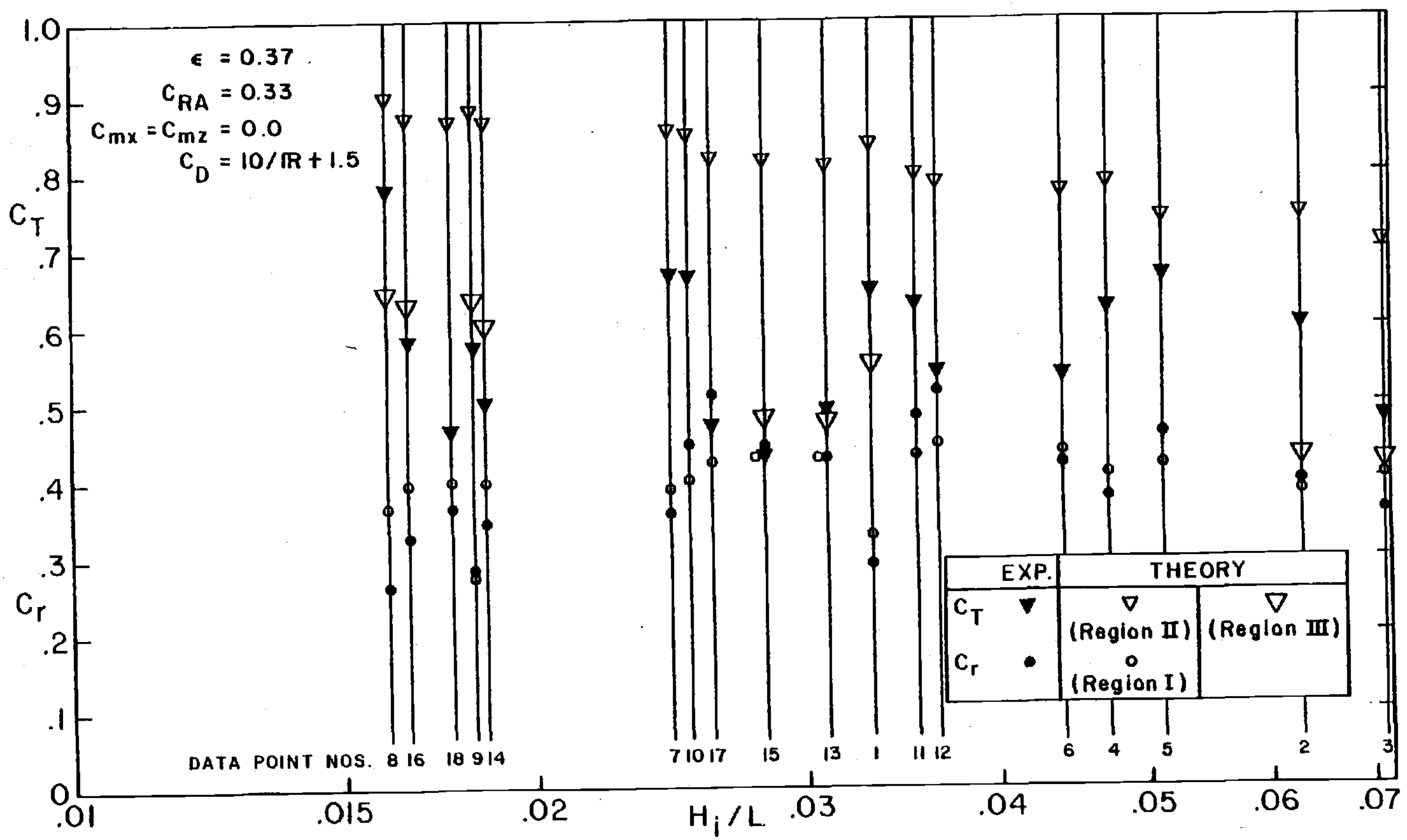

Figure 8. 15. Comparison of computed reflection and transmission coefficients with Sollitt's two row experimental data.

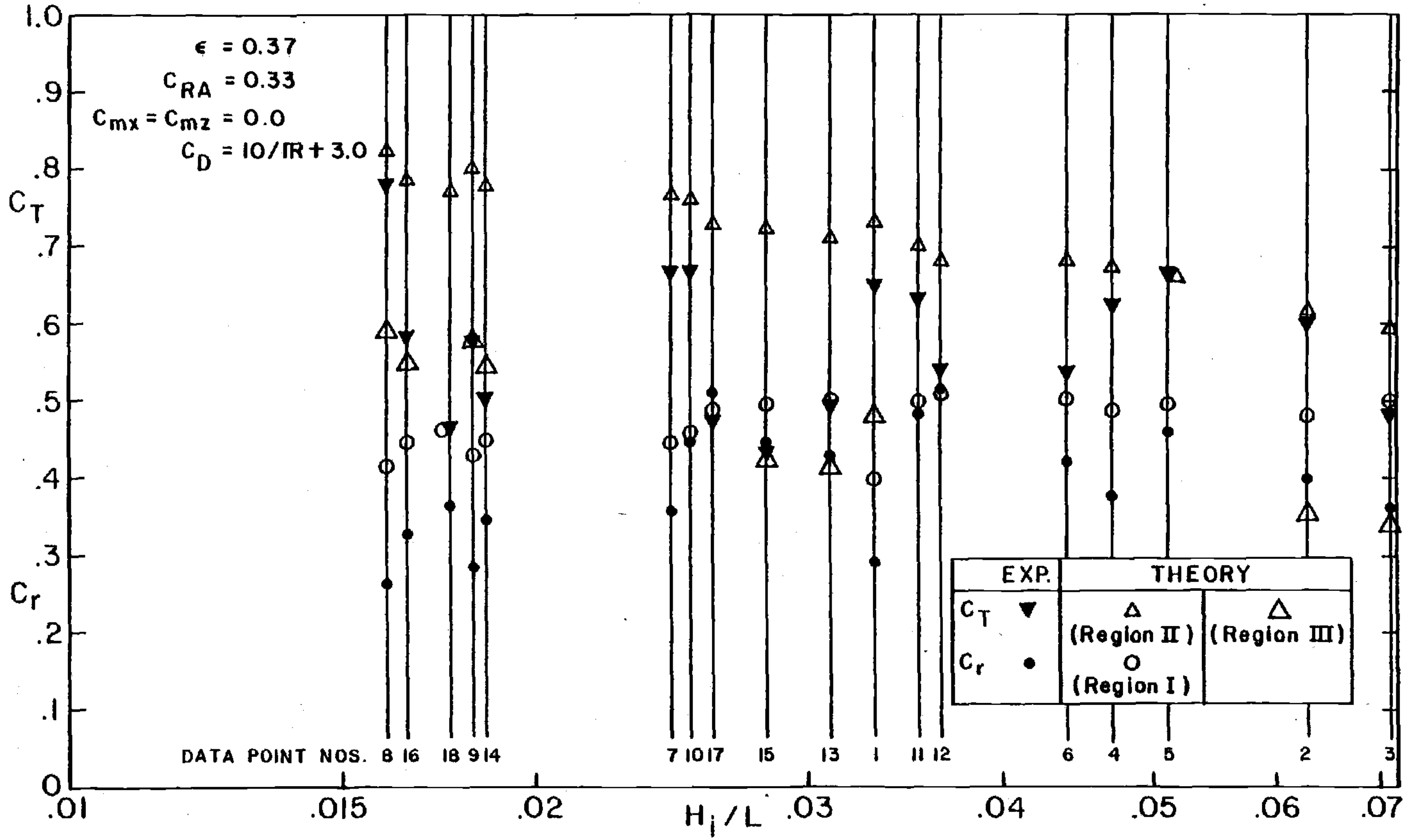

Figure 8.16. Comparison of computed reflection and transmission coefficients with Sollitt's two row experimental data.

in Fig. 8.6. The predicted reflection coefficients of Fig. 8.15 ($C_D = \frac{10}{\mathbb{R}} + 1.5$) conform very well to the experimental data. The predicted transmission coefficients can not be expected to conform to the experimental data since the theory is actually computing the wave transmission in the lee of the seaward pile row (Region II of the two row model) and the experimental wave transmission is measured in the lee of the second row of piles. In a few instances it was possible to calculate the Region III transmission coefficient from the Region II transmission coefficient and the empirical single row model transmission coefficients of Fig. 8.6. It was possible to perform this calculation only when the theoretical transmitted wave (from the Region II transmission coefficients of Fig. 8.15) approximated one of the experimental incident waves in both wave steepness and dimensionless wave frequency. When this occurred, the theoretical transmission coefficient for Region II of the two pile model was multiplied by the experimental transmission coefficient for a single row of piles to yield the Region III transmission coefficients in the lee of the back row of piles. It may seem somewhat incongruous to apply an averaging technique to the reflection coefficient data of Fig. 8.6 to obtain C_{RA} and yet only use specific occurrences of the transmission coefficient data when $\sigma^2 h/g$ and H_i/L approximately match to calculate the Region III transmission coefficients. This, however, was deemed appropriate since the transmission coefficients of Fig. 8.6

display considerably more scatter than the reflection coefficients.

The calculated Region III transmission coefficients are shown in Figs. 8.15 and 8.16. These predicted values generally agree in an acceptable fashion in Fig. 8.15. This agreement promotes the obvious question as to why the analytical model should correlate with the experiments using this method of analysis and the drag coefficient relationship of

$$C_D = \frac{10}{\mathbb{R}} + 1.5$$

when the analysis of the single row model in the previous section correlates with the experimental data using

$$C_D = \frac{10}{\mathbb{R}} + 3.0$$

One explanation is the fact that only lateral proximity effects occur in the single row model whereas some sheltering proximity effects may occur in the two row model thereby reducing the drag coefficient for the system. This, however, is thought to be only a partial explanation, and, as will be seen in the next section, the above discrepancy may also be due to the failure of the theory to appropriately model the highly localized dissipation in non-homogeneous relatively narrow structures, such as that represented by the two row experimental models.

8.4.3. Sollitt's Two Row Models with a Perfect Reflector

Sollitt has obtained reflection coefficients for four different experimental model configurations comprised of two rows of closely spaced piles in conjunction with a perfect reflecting wall. The first three model configurations employ pile rows which are identical in configuration with that of the preceding section, and, as in the preceding section, each of the two individual pile rows is identical to the single row of Section 8.4.1. Thus, $h_2/b = 8.0$, $\epsilon = 0.87$, and the ratio of the gap width to the diameter is again 1/4. Only the distance from the leeward row of piles to the reflecting wall is varied and, in order of presentation, the dimensionless distances are $h_2/c = 4.0,\ 2.0,\ 1.333$. In the fourth model, the dimensionless distance $h_2/b = 4.0$ is examined by changing the longitudinal spacing between the pile rows and, hence, the porosity of the structure is also increased to $\epsilon = 0.94$. The dimensionless distance from the leeward pile row to the reflector is $h_2/c = 2.0$ for this last case. No attempts were made to establish the transmission coefficients or measure the water surface profile between the last row of piles and the reflector in any of these models.

8.4.3a. $h_2/b = 8.0$, $h_2/c = 4.0$, $C_{RA} = 1.0$. Figure 8.17 shows the reflection coefficient data obtained by Sollitt for the indicated model configuration. The dimensionless frequency of each data point

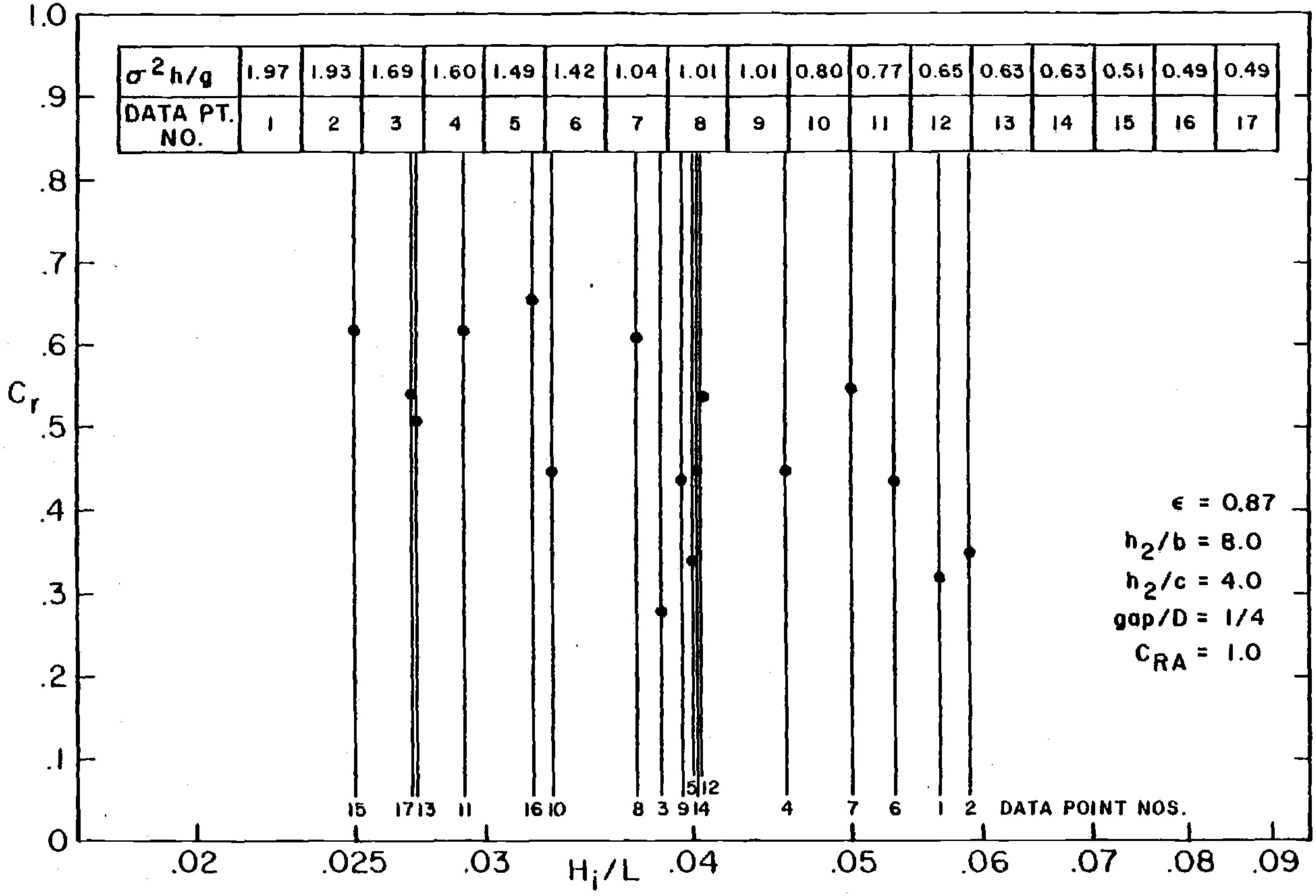

Figure 8. 17. Sollitt's experimentally obtained reflection coefficients for a two row model in conjunction with a perfect reflector. $h_2/c = 4.0$.

is also tabulated in this figure. Due to the fact that four of the data points occurred near a wave steepness of $H_i/L = 0.04$, it is necessary to further delineate these points by superimposing the data point number at each of the four data points as shown in Fig. 8.17. This has also been done for the analytically predicted reflection coefficient data as shown in Figs. 8.18 and 8.19.

Figure 8.18 depicts the analytical model reflection coefficient predictions for the two indicated drag coefficient relationships when the general structural porosity is used in the continuity of mass flux boundary condition equations, Eqs. (4.2.2 and 4.2.3). The general appearance of the predicted data is similar to that of the experiments, but it is shifted upward radically. The reason for this large discrepancy is due in part to lack of sufficient dissipation within the analytical model. Indeed, the predicted transmission coefficients (not shown) all exceed 0.94. The fact that the analytical model data exhibits similar trends to those of the experiments is somewhat encouraging. However, the fact that the variation in the drag relationship at small wave steepenss values registers little effect, and the fact that even the best theoretical data at high wave steepnesses differs considerably from the experimental data, suggest that both the 'A' and 'B' constants would have to be raised radically in order to approach a satisfactory correlation. Such an increase certainly is not to be expected or justified a-priori and probably still

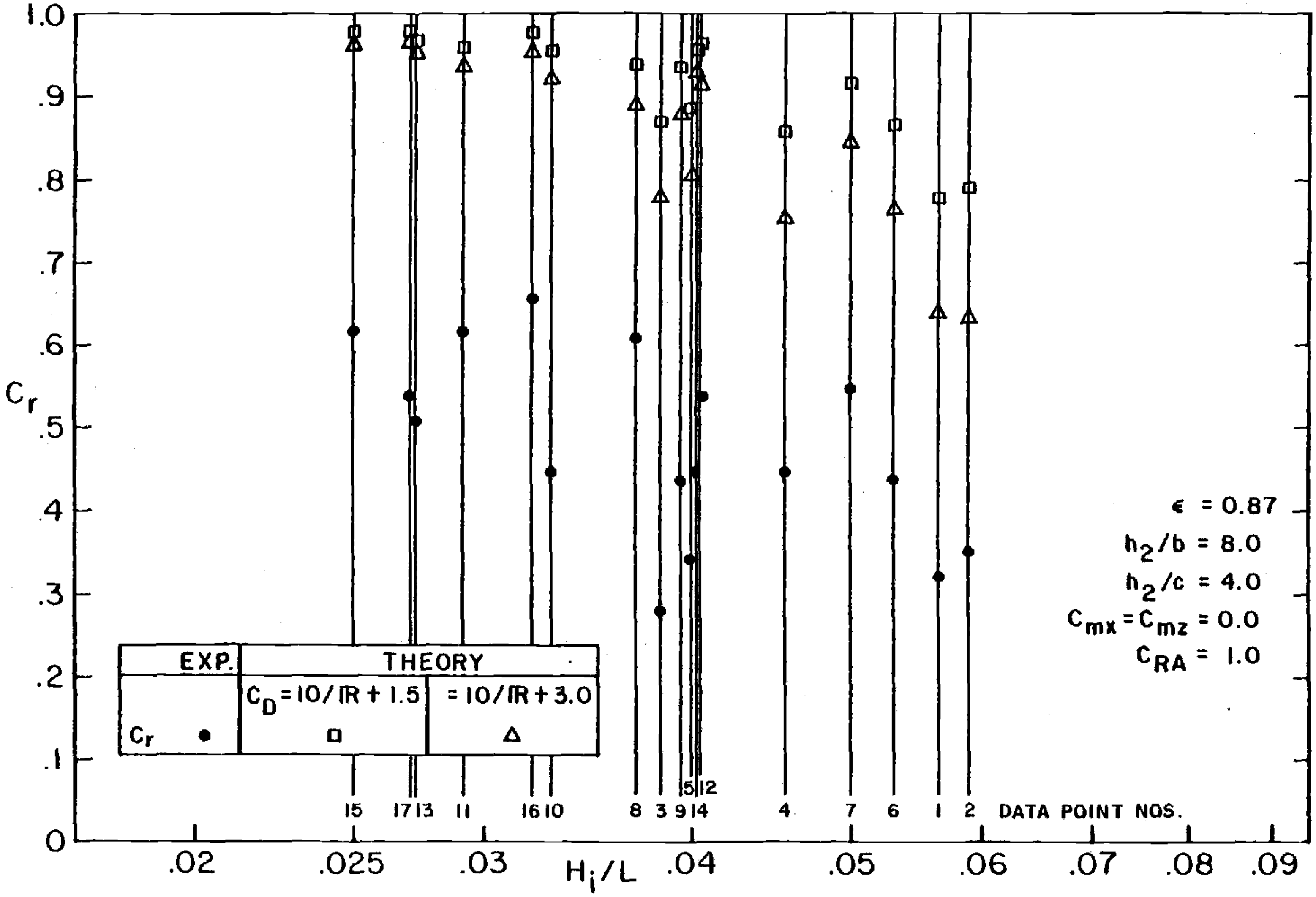

Figure 8. 18. Comparison of computed reflection coefficients with Sollitt''s experimental data for a two row model with perfect reflector. $h_2/c = 4.0$.

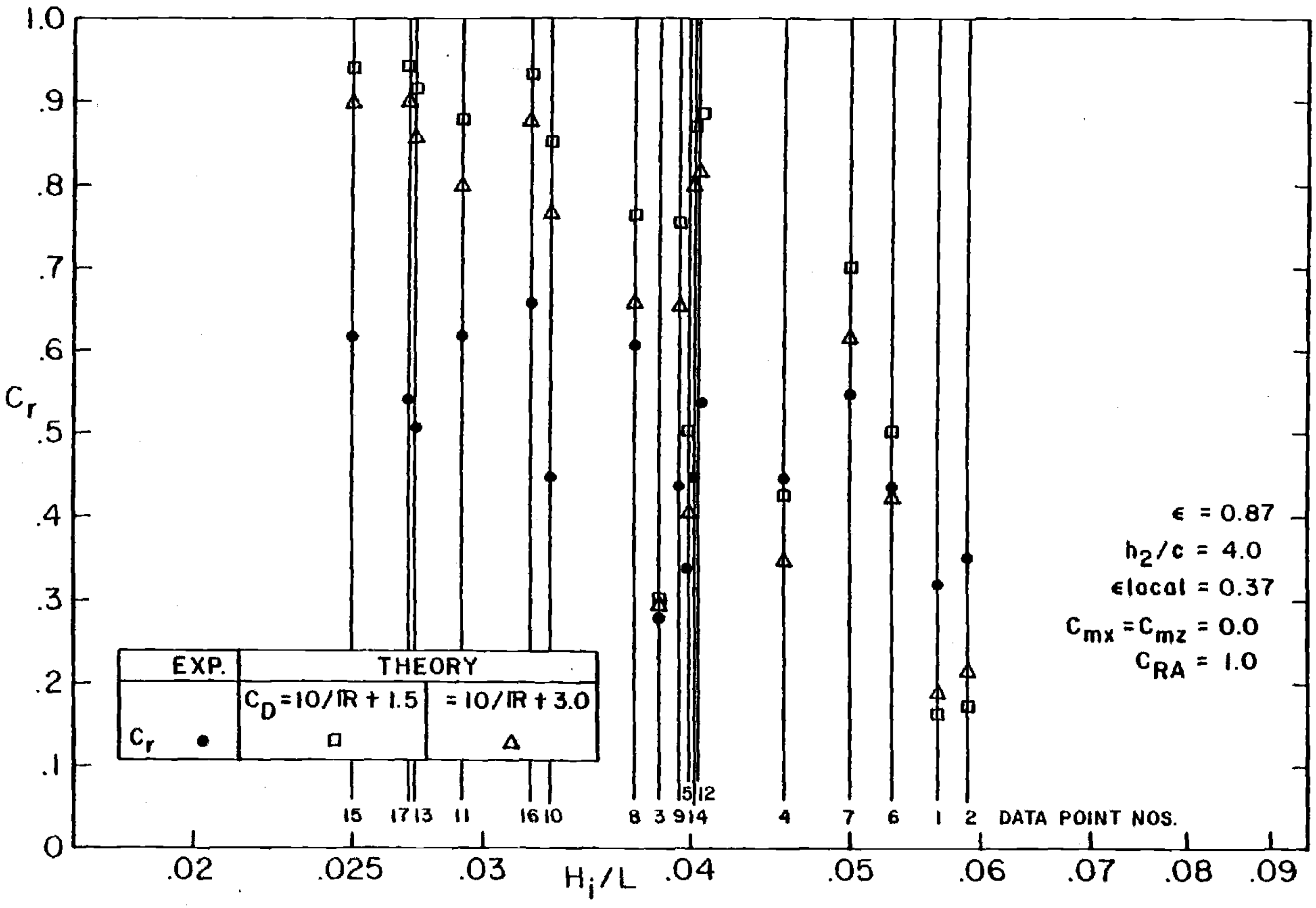

Figure 8.19. Comparison of computed reflection coefficients with Sollitt's experimental data for a two row model with perfect reflector. $h_2/b = 8.0$, $h_2/c = 4.0$.

would not yield a good fit since reflections from the seaward face of the first pile row would dominate under these conditions.

Figure 8.19 shows the theoretical results for the two indicated drag coefficient relationships when the local interfacial porosity is employed in the continuity of mass flux boundary condition equations, Eqs. (4.2.2 and 4.2.3). The slope and range of the theoretical data is considerably greater than that of Fig. 8.18, but the agreement is still generally poor with respect to the experimental data. As before, most of the theoretical transmission coefficients (not shown) are quite high, generally exceeding 0.9. Although this is, again, due in part to lack of dissipation, it can also be somewhat attritubed to multiple reflected waves and an energy build up in Region III. This is verified by the low reflection coefficients of data points 1 and 2 and their high transmission coefficients of 0.92 and 0.895 respectively. However, it must be questioned as to whether or not multiple reflected waves in Region III could completely account for such very large transmission coefficients and small reflection coefficients. That is, why should there be so little reflection at the seaward pile row and such considerable reflection and re-reflection at the rear face of the leeward pile row? The answer to this question is undoubtedly phase related, i.e., crest to crest type superposition may be occurring in Region III while crest to trough superposition takes place in Region I. This idea of improper phase relationships must also be considered, in addition to the dissipation mechanism, for probable cause in the discrepancy between the theory and the experiments.

Furthermore, Sollitt's experiments did not include a measurement of the reflection coefficient, C_{RA}, of the vertical wall reflector employed in the experimental model investigation. It has been assumed for the purposes of the theoretical investigation that the reflector is, indeed, a perfect reflector, $C_{RA} = 1.0$, in all cases. This assumption is probably slightly in error since non-linear effects, dissipation at the wall, irregularities in the surface and in the alignment of the wall, etc., all tend to decrease C_{RA} below the theoretical value of unity. It is noteworthy that such a decrease would benefit the correlation between the theory and the experiments. However, since no experimental measurements were obtained, the magnitude of this decrease is unknown. Hence variation from the theoretical value of $C_{RA} = 1.0$ cannot be rigorously justified and, thus, no other value has been employed in the theoretical analysis.

Finally, the effects of increasing the added mass coefficients were examined at a few of the experimental data points (unplotted). Increasing the added mass coefficients from 0.0 to 2.0 produced some reduction in the reflection coefficient at high wave steepnesses but had an almost negligible effect at low steepness values. No significant improvement in experimental and theoretical correlation was realized by this increase in C_{mx} and C_{mz}.

8.4.3b. $h_2/b = 8.0$, $h_2/c = 2.0$, $C_{RA} = 1.0$. Figure 8.20 shows the experimental reflection coefficient data obtained by Sollitt for the indicated model configuration. The dimensionless frequency of each data point is also tabulated on this figure.

Figure 8.21 depicts the analytical model reflection coefficients for three different drag coefficient relationships when the local interfacial porosity is used in the horizontal mass flux continuity boundary condition equations, Eqs. (4.2.2 and 4.2.3). None of the three drag coefficient relationships provide satisfactory correlation with the experimental data although each relationship has its good points. It is interesting to note that the two larger 'B'-constants in these relationships produce theoretical data trends which are concave upward over the test range of wave steepnesses.

In order to confirm whether or not the discrepancy between the theory and the experiments was purely a dissipation problem or phase related as well, a variety of drag coefficient relationships and the general porosity ($\epsilon = 0.87$), the local interfacial porosity (ϵlocal = 0.37) and the ratios of cross sectional flow areas (ϵlocal = 0.2) were employed in a multitude of analyses of this model configuration. Due to sheer numbers of graphs the results of this portion of the investigation have not been displayed here. However, it is sufficient to report that no combination provided good, general, agreement between the theory and experiments over a wide

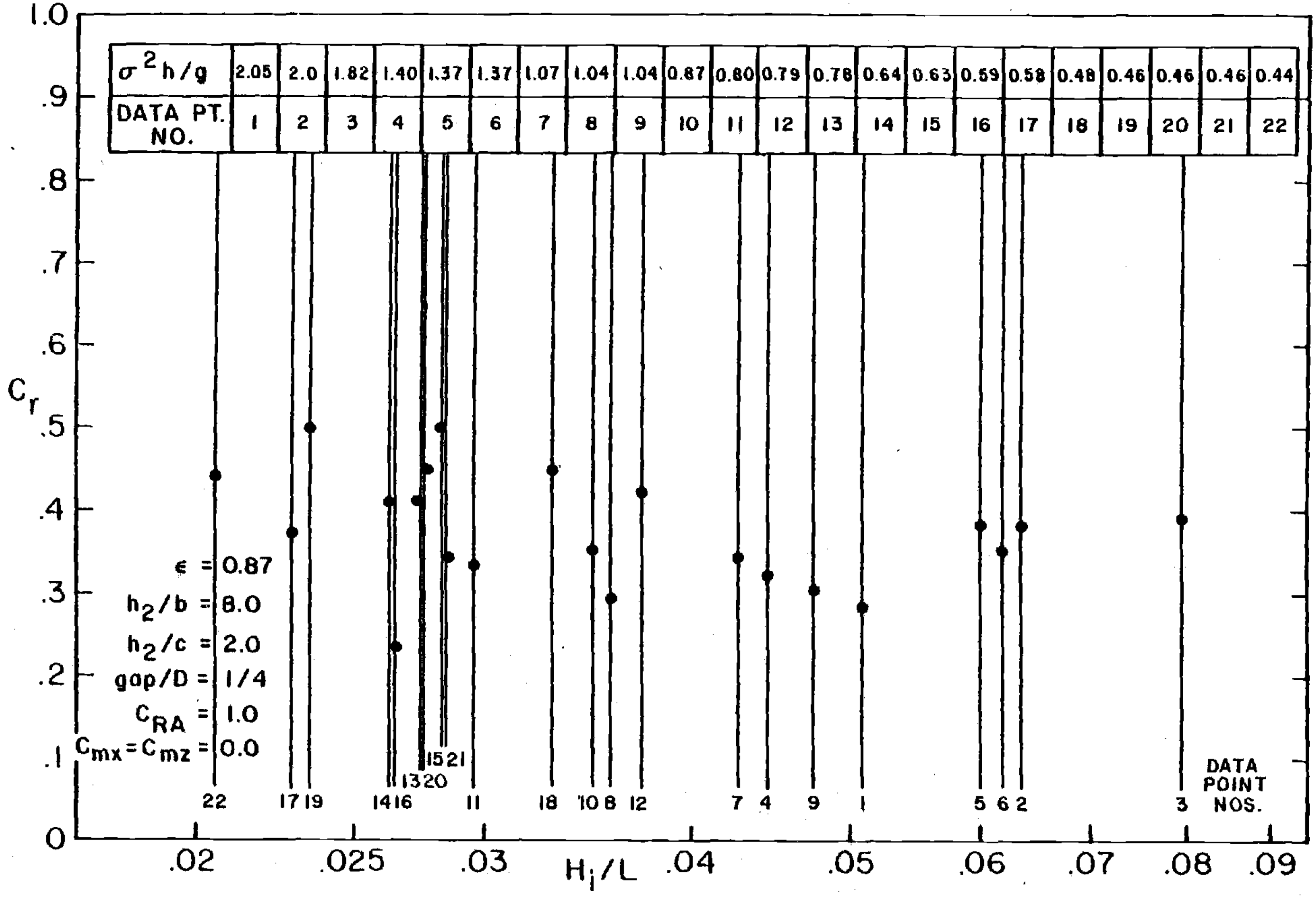

Figure 8.20. Sollitt's experimentally obtained reflection coefficients for a two row model in conjunction with a perfect reflector. $h_2/c = 2.0$.

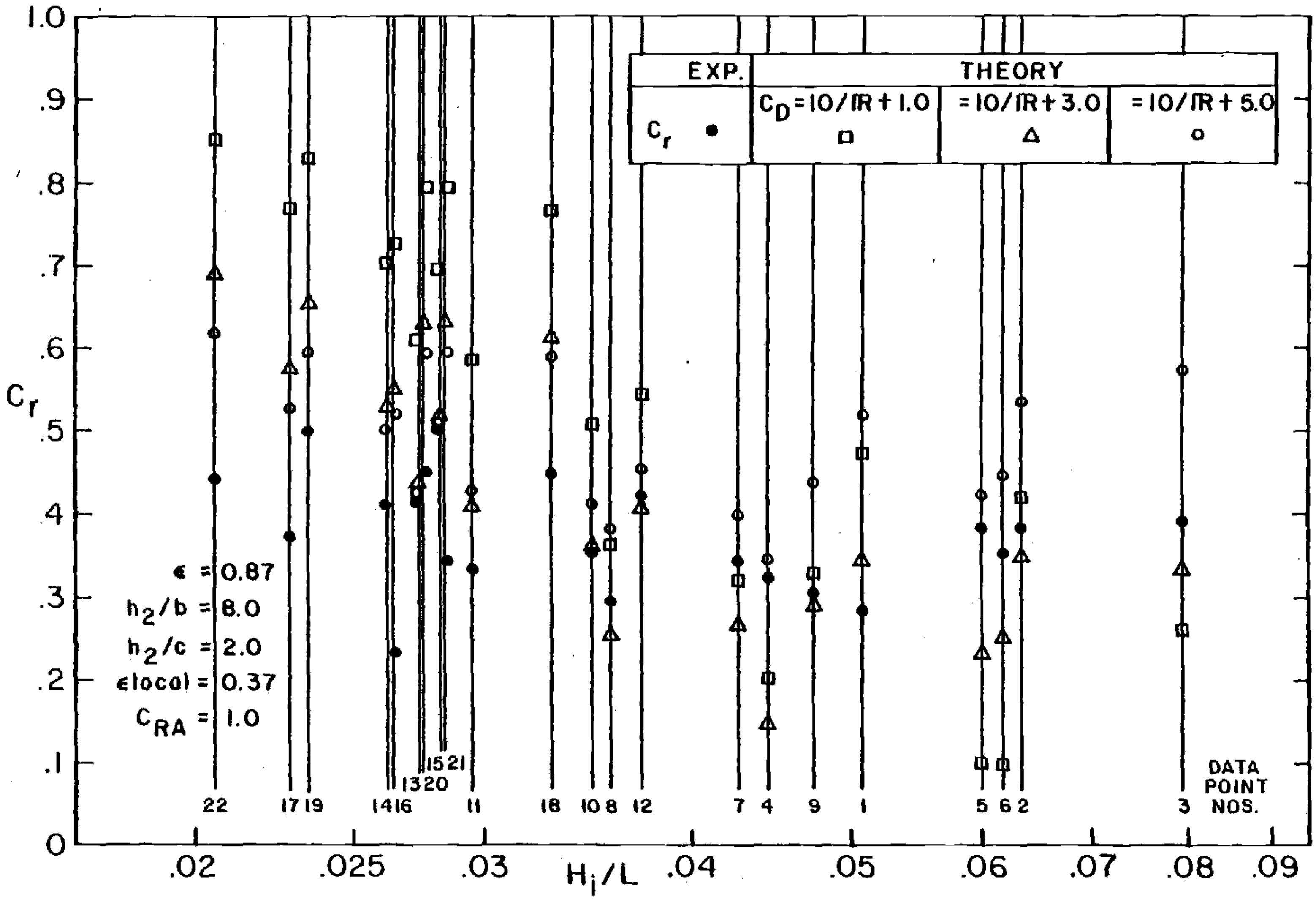

Figure 8.21. Comparison of computed reflection coefficients with Sollitt's experimental data for a two row model with a perfect reflector. $h_2/c = 2.0$.

range of wave steepnesses. That is, as in Figure 8.21, there were some good points associated with many of the analyses but no uniformly consistent correlations. Furthermore, under none of the imposed analytic conditions could a satisfactory fit be obtained with the experimental data at the four lowest dimensionless wave frequencies. This frequency related discrepancy, coupled with the wide range of dissipation conditions employed, is considered to be indicative of phase related problems.

8.4.3c. $h_2/b = 8.0$, $h_2/c = 1.33$, $C_{RA} = 1.00$. Sollitt's experimental results for the indicated model configuration are presented in Fig. 8.22 with the dimensionless wave frequencies corresponding to each data point. Referring to Figs. 8.17, 8.20, and 8.22, it is clear that the experimental reflection coefficients generally manifest a decreasing trend with increasing values of the distance 'c' from the leeward pile row to the reflector (decreasing values of h_2/c). This is particularly true for the waves of low steepness and low dimensionless wave frequency at the left side of each of the figures. This decrease in C_r with the increase in 'c' is thought to be directly related to the water storage capacity of Region III. That is, during the reflecting wall experiments, a head differential between Regions II and III was observed such that the static water level of Region III appeared to be raised somewhat. This head differential was decidedly more pronounced for the small Region III storage

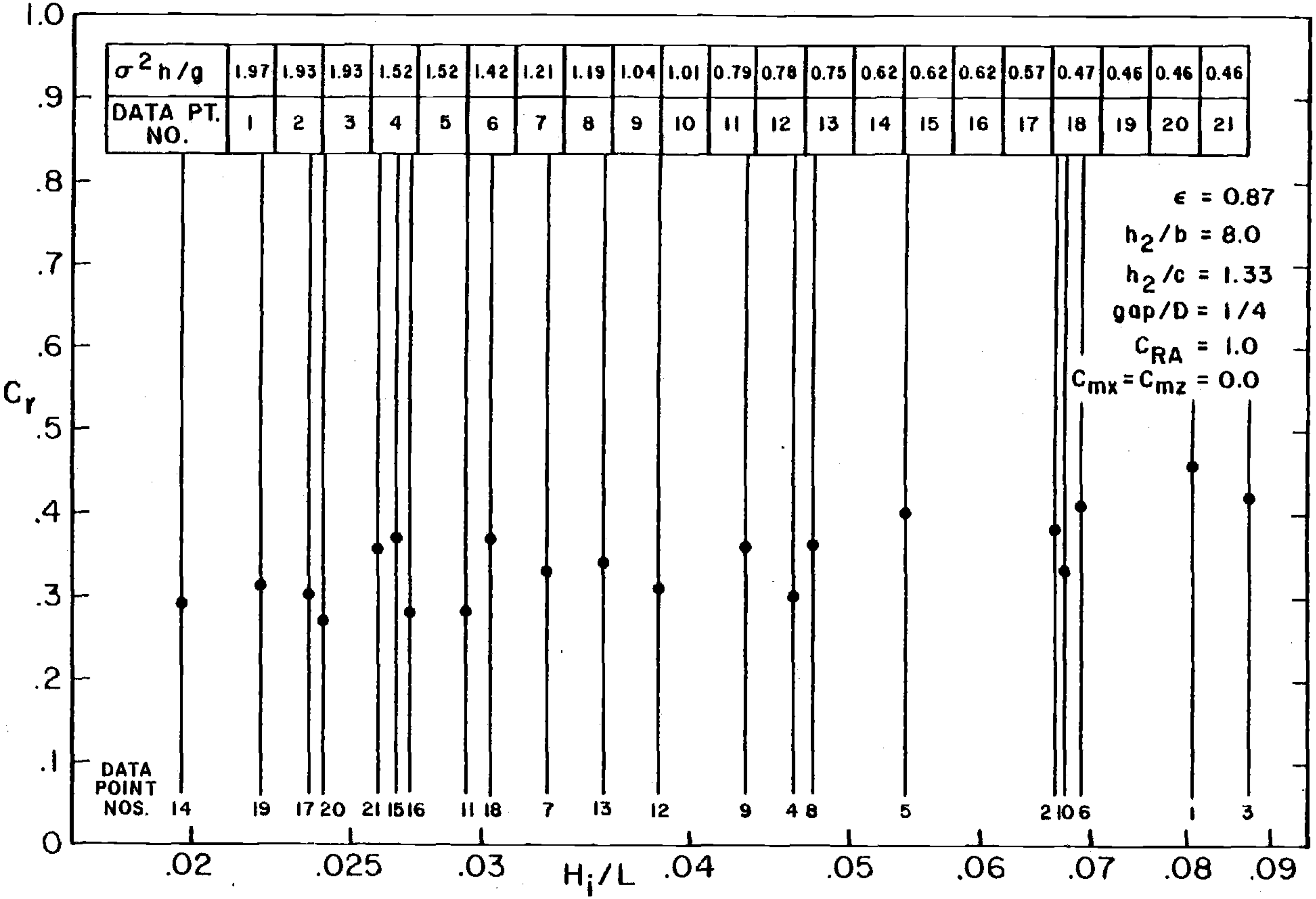

Figure 8.22. Sollitt's experimentally obtained reflection coefficients for a two row model in conjunction with a perfect reflector. $h_2/c = 1.33$.

reservoir associated with the small 'c' value of Fig. 8.17. From the trend in Figs. 8.17, 8.20 and 8.22, it is likely that the high energy density levels of the smaller reservoirs behaved as energy reflectors so that more wave energy was reflected at the second pile row interface. As 'c' increased the storage capacity of Region III increased while the head differential, the energy density level, and, hence, wave reflections all decreased. As suggested by the relative conformity of Figs. 8.20 and 8.22, there is probably some point at which further increases in 'c' have negligible effects on wave reflection. Since the distance 'c' always appeared larger to the shorter waves at the right of the figures, it is to be expected that they would be less affected by the increases in 'c'.

Since the head differential described above promotes quasi-steady jet expansion dissipation between the piles and since the analytical model does not account for these losses per se, it may be wondered if this may account for the discrepancy between the theory and these models. However, steady flow jet type losses are known to be proportional to the square of the velocity as are drag related losses. Thus, the theory could account for these losses by an increase in the drag coefficient, although, the present form of the drag coefficient relationship may not provide a good description of combined viscous drag and jet related losses over the entire Reynolds number range. Even so, if this was the only flaw in the theory with regard to Sollitt's models, the analyses described in the previous section, in which the drag coefficient constants and the porosities were varied widely, should have been able to provide a reasonable correlation with all of the experimental data. However, as was pointed out, there were at least four data points which could not be modeled by the theory under any of the imposed analytical conditions.

Figure 8.23 shows the predicted reflection coefficients when the general porosity is employed in the beta and zeta constants of Eqs. (4.2.2 and 4.2.3). Again, the theoretical data does not correlate with the experimental values.

Figure 8.24 depicts the predicted reflection coefficients when the local interfacial porosity, $\epsilon_{local} = 0.37$, is used. Surprisingly, this figure reveals that a combination of the analyses when the drag coefficient relationship 'B'-constants are equal to three and five yields reasonably acceptable results over most of the data. That is, for data points 1-4 and 16-21, $B = 3$ generally gives acceptable results, while for the remaining data points, $B = 5$ yields reasonable agreement with the experimental data. This suggests that some 'tuning' of the drag coefficient relationship for this model would probably yield an overall satisfactory correlation between theory and experiment. However, the fact that tuning is required is indicative of the fact that the model has again failed to correlate with the experiments when anticipated drag coefficient relationships are applied.

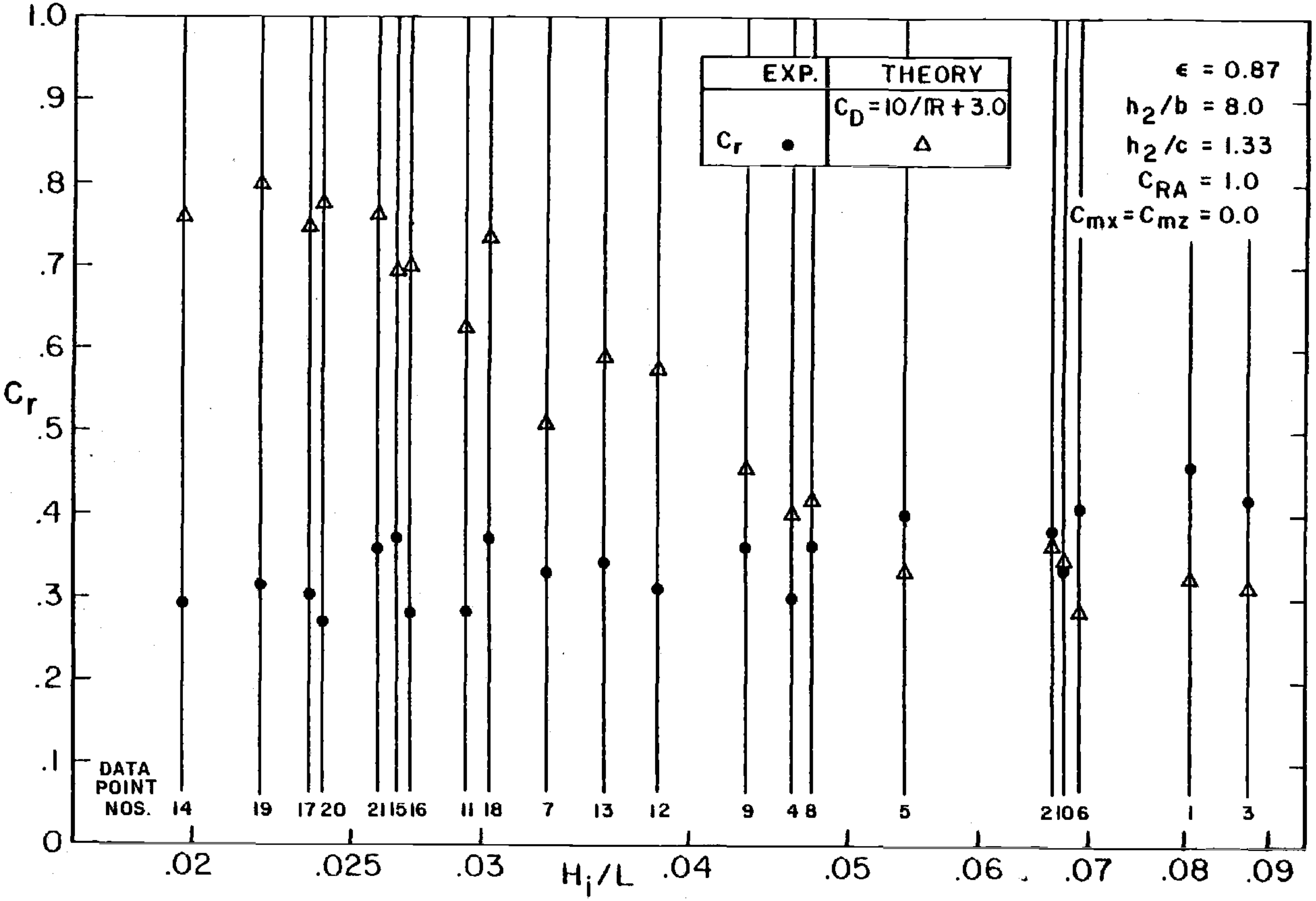

Figure 8.23. Comparison of computed reflection coefficients with Sollitt's experimental data for a two row model with a perfect reflector. $h_2/c = 1.33$.

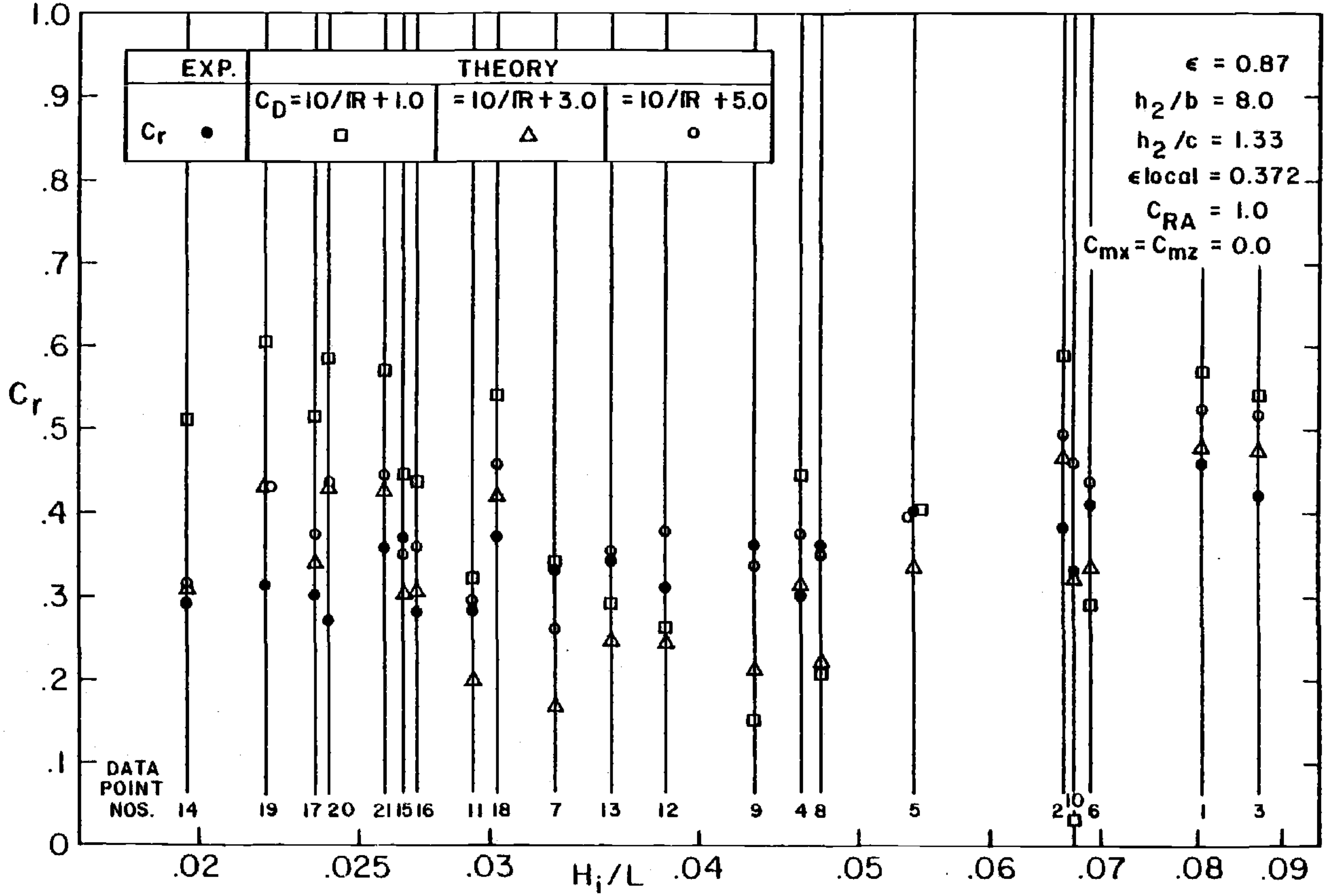

Figure 8.24. Comparison of computed reflection coefficients with Sollitt's experimental data for a two row model with a perfect reflector. $h_2/c = 1.33$.

8.4.3d. $h_2/b = 4.0$, $h_2/c = 2.0$, $C_{RA} = 1.00$. Sollitt's experimental reflection coefficients for the indicated model are shown in Fig. 8.25 with the dimensionless wave frequency information for each point. It is interesting that the results displayed in Fig. 8.25 for a two row model in conjunction with a perfect reflector are remarkably similar in both trend and magnitudes to those of the single row model with no reflector as shown in Fig. 8.6. Even the averages of both data sets are approximately equal. Assuming that the same initial wave reflection occurs at the seaward row of piles of this two row model as does at the single row model leads to the startling conclusion that the two row model dissipates all, or very nearly all, of the wave energy which penetrated into the structure. It is even more remarkable that this phenomenon occurs over a broad range of wave steepnesses and dimensionless wave frequencies.

Figure 8.26 depicts the predicted reflection coefficients for four different drag coefficient relationships and ϵlocal = 0.37. It is possible to achieve high correlation with all but the very highest and lowest data point numbers by using one or another of the indicated $\bar{C}_D$ relationships. Again, a general C_D relationship could not be predicted a-priori to obtain a good fit to all of the experimental data.

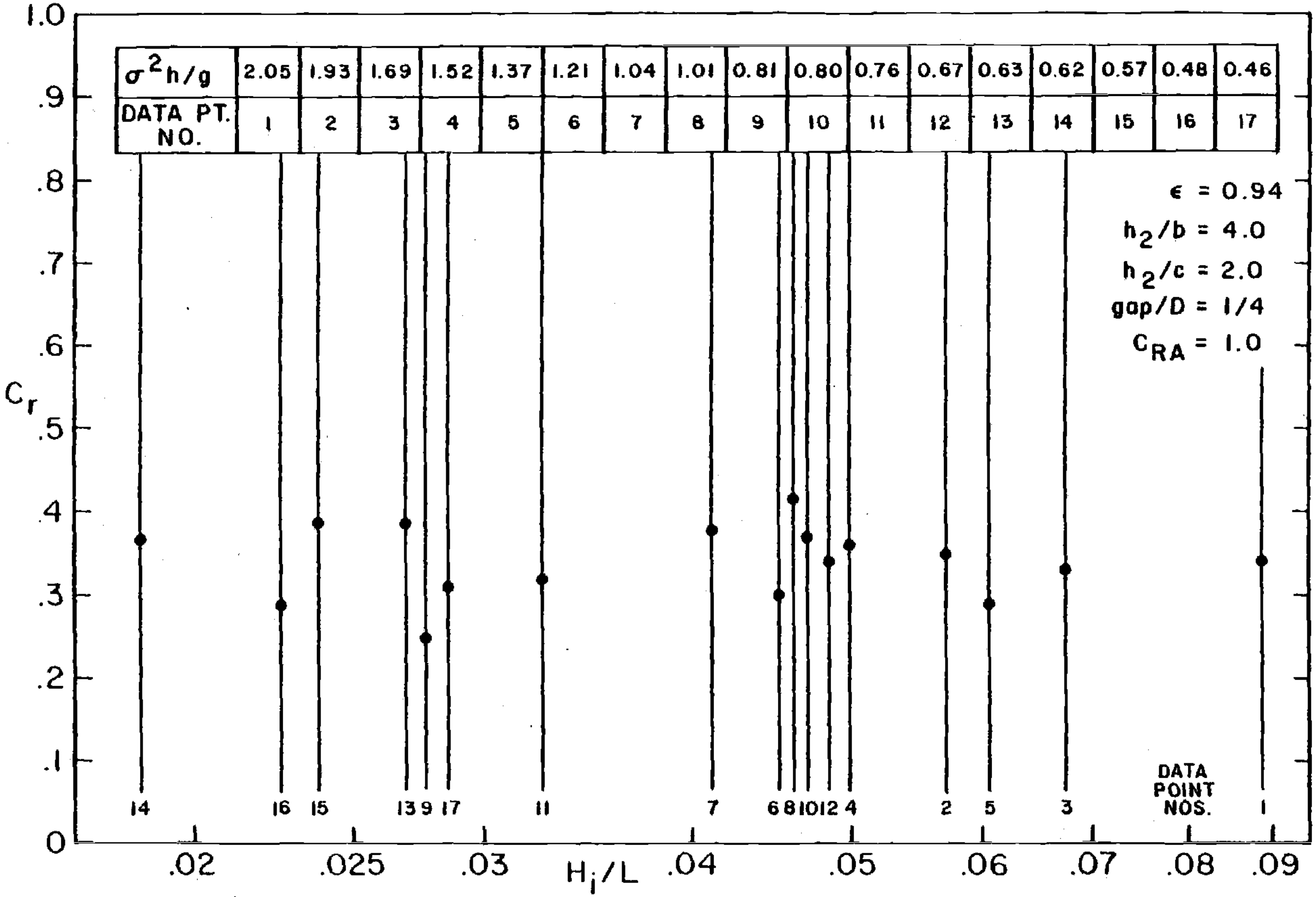

Figure 8.25. Sollitt's experimentally obtained reflection coefficients for a two row model in conjunction with a perfect reflector. $h_2/c = 2.0$, $h_2/b = 4.0$.

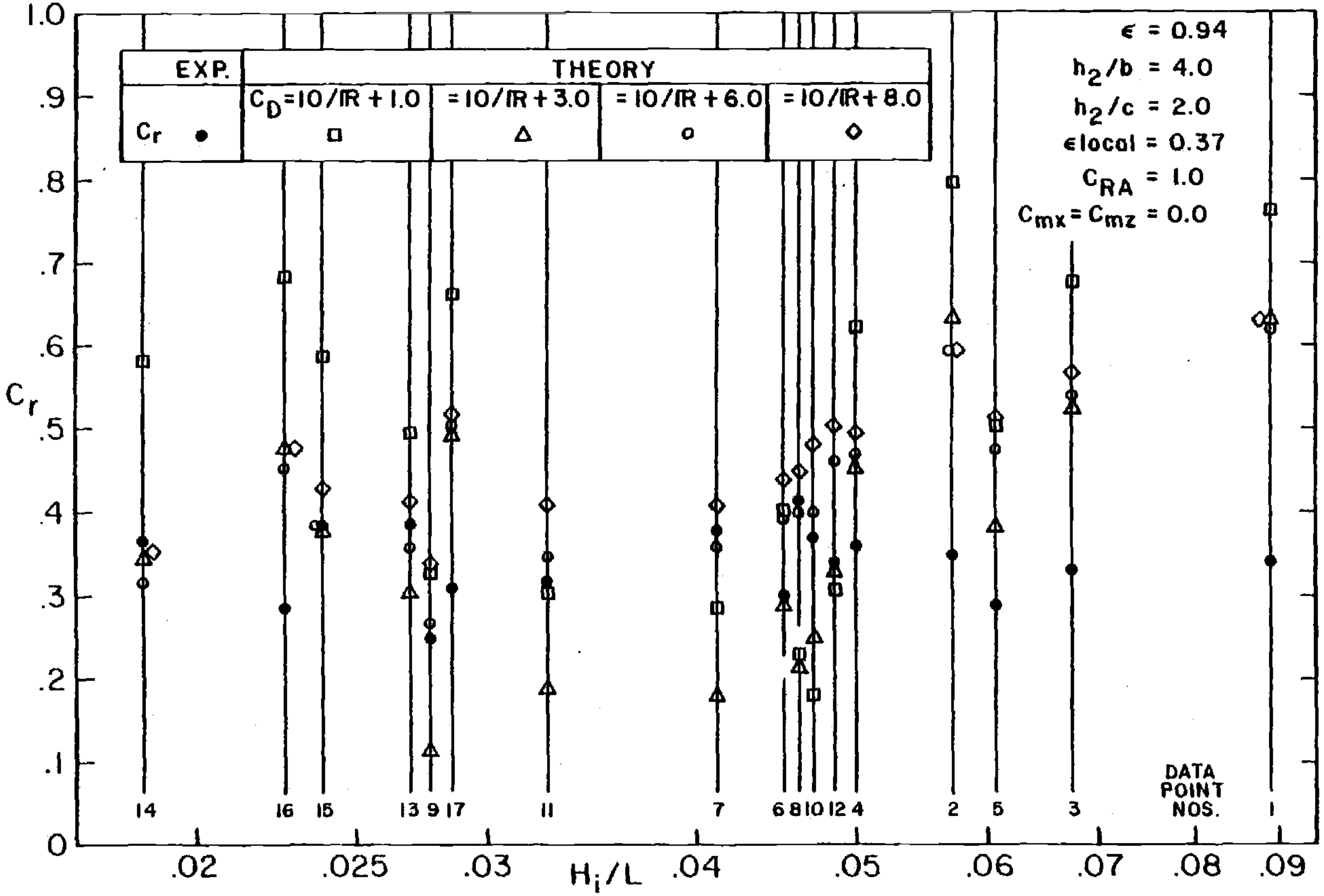

Figure 8.26. Comparison of computed reflection coefficients with Sollitt's experimental data for a two row model with a perfect reflector. $h_2/c = 2.0$, $h_2/b = 4.0$.

8.4.4. Sollitt's Two Row Models with An Automobile Tire Matrix

Sollitt has conducted experimental model studies to determine the reflection and transmission coefficients for a model comprised of two rows of closely spaced vertical piles with a Wave Maze® automobile tire maxtrix situated between the two pile rows. This two pile row configuration was identical to that described in Section 8.4.2, i.e., $h_2/b = 8.0$, and the gap width to pile diameter ratio = 1/4. The automobile tires were modeled using a soft, pliable rubber one-half inch thick by 1.75 inch outside diameter and 1 inch inside diameter. The tire matrix butted tightly against the two pile rows so that the only voids within the composite structure were those due to the gaps between the piles and those of the tire matrix itself. The general porosity for the composite structure was approximately 0.61.

Since no drag coefficient literature was available for a composite structure such as this, it was necessary to establish a drag coefficient relationship for the theoretical analysis. It was thought that a simple steady flow experiment with the composite model would prove adequate. Specifically, a steady flow flume experiment was carried out so that the head loss across the composite structure was determined from the steady flow Bernoulli equation applied at the water surface as

$$H_L = (s_f - s_b) + \frac{Q^2}{2gY_{FL}} \left(\frac{1}{s_f^2} - \frac{1}{s_b^2} \right)$$

where

H_L = head loss

s_f = water surface elevation in front of the structure

s_b = water surface elevation behind the structure

Q = the volumetric discharge rate

Y_{FL} = width of the flume

g = gravitational acceleration

Assuming that the energy dissipation was solely due to drag and drag-like phenomena (lift, expansion, contraction, jets) allowed the energy dissipation rate, or power loss, to be equated to that of the Bernoulli equation head loss, i.e.,

$$\text{Power} = F_{DRAG} \times \text{velocity} = H_L \times \gamma \times Q$$

where

F_{DRAG} = steady flow drag force

γ = fluid specific weight

or, using the steady flow drag force equation and substituting for the head loss term above,

$$\text{Power} = \rho C_D \bar{A} \frac{\bar{v}^2}{2} \bar{v} = \gamma Q \left[(s_f - s_b) + \frac{Q^2}{2gY_{FL}} \left(\frac{1}{s_f^2} - \frac{1}{s_b^2} \right) \right]$$

where

$\bar{A}$ = the average cross sectional area of the solid portion of the composite structure, i.e., $\bar{A} = Y_{FL}\bar{s}(1-\epsilon)$

$\bar{s}$ = the average water surface elevation within the structure

$\bar{v}$ = the average steady flow fluid velocity within the structure

Now employing the steady flow continuity equation to substitute for $\bar{v}$ in the above equation and solving for the drag coefficient C_D yields

$$C_D = \frac{2\bar{A}^2 g}{Q^2}\left[(s_f - s_b) + \frac{Q^2}{2gY_{FL}}\left(\frac{1}{s_f^2} - \frac{1}{s_b^2}\right)\right]$$

Thus, by measuring the volumetric flow rate and the flow depths before, at the midpoint of, and after the composite structure the steady flow drag coefficient was obtained. Experiments were conducted at several different flow rates (and, hence, several different Reynolds numbers) and due to non-homogeneity in the vertical and horizontal directions, for arrangements of the composite model simulating vertical and horizontal flow. The applicability of the steady vertical flow case to the vertical component of oscillatory flow may be subject to question since the steady flow test in this instance physically constrained the flow within the composite model. Thus, closed conduit flow was being modeled. In the oscillatory application, however, the water particles are free to diverge in and out of the structure.

The drag coefficients obtained for the composite model from the horizontal and vertical steady flow tests are plotted in Fig. 8.27 versus the Reynolds number. The length scale for the Reynolds number has been chosen as 1.33 in. since this conforms to about 1/4 the longitudinal width of the composite structure and this length will be useful for the theoretical analysis. The drag coefficient relationship for the horizontal flow test,

$$C_{Dx} = \frac{2000}{\mathbb{R}} + 19.6 \qquad (8.4.1)$$

and

$$C_{Dz} = \frac{2500}{\mathbb{R}} + 6.5 \qquad (8.4.2)$$

for the vertical flow simulation appear to approximate the experimental drag coefficients satisfactorily.

The theoretical analysis was accomplished by analyzing the composite model in sections. For the horizontal oscillatory flow analysis, the composite structure was considered to have been divided into four equally dimensioned porous slabs by passing three vertical planes (normal to the x-axis) through the structure. Thus the longitudinal dimension of each slab was 1/4 the total longitudinal width of the composite structure, or about 1.33 in. This longitudinal

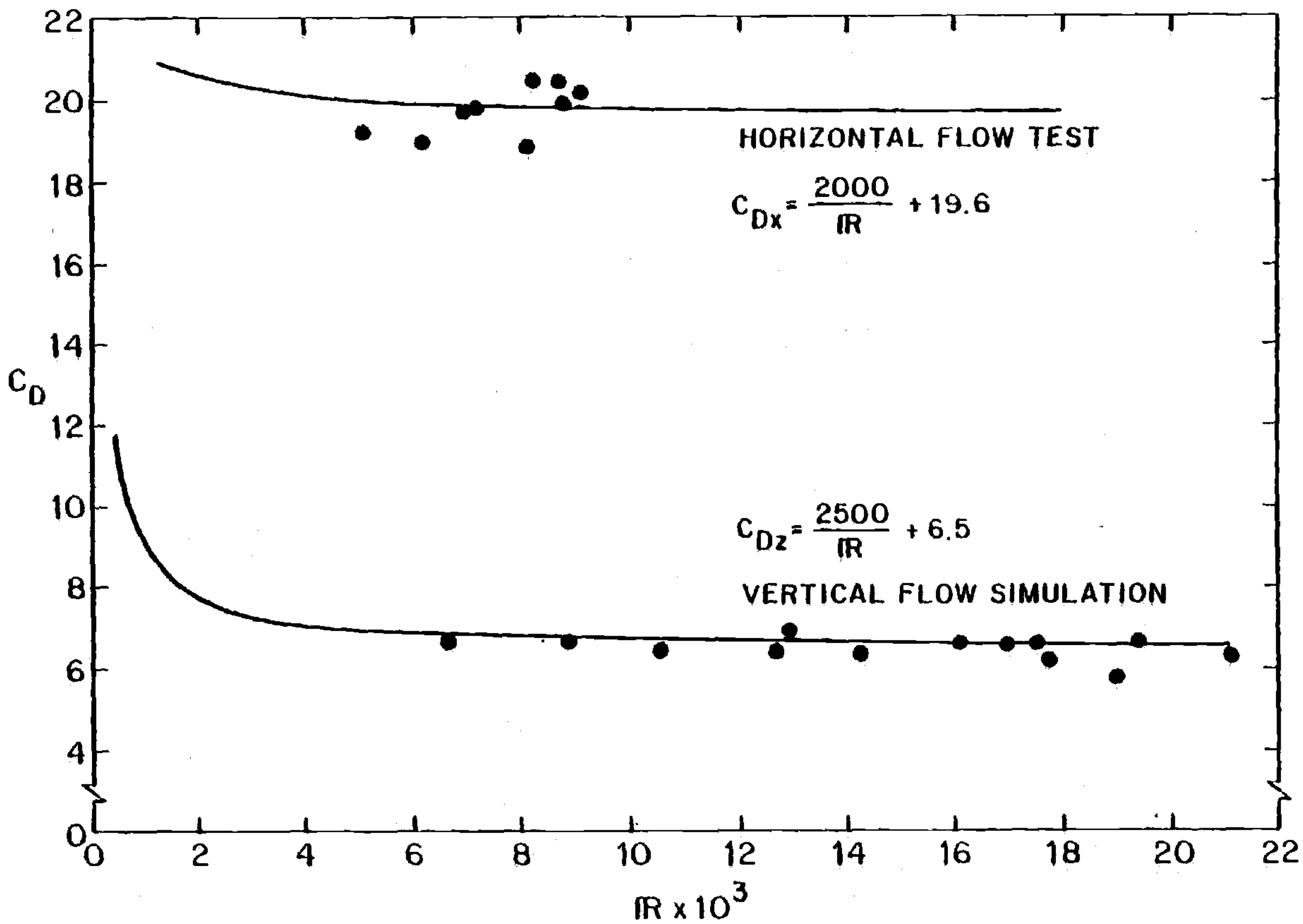

Figure 8.27. Horizontal and vertical direction drag coefficients obtained for composite structure by steady flow model tests.

quarter-width was input into the computer program as though it was the pile diameter (DI). Since the composite structure extended fully across the wave tank, the lateral width of the wave tank was input as the lateral repeating width Y of the structure.

Computation of fluid energy dissipation due to the interaction of the composite structure and the horizontal water particle velocity components can be accounted for by considering each slab as one large, vertical, porous rectangular pile <u>or</u>, subdividing each slab with horizontal planes, as several y-directed porous rectangular piles. Both methods of analysis could not be employed simultaneously since this would account for twice the actual dissipation. The vertical pile analysis was chosen. Since the steady flow drag coefficient tests were conducted on the entire model and since the model is being subdivided into four equal sections, it is necessary to divide the drag coefficient relationship of Eq. (8.4.1) by the number of sections in the direction of flow, i.e., by four. Consequently the drag coefficient relationship for the theoretical analysis of structural interaction with the horizontal component of the water particle motion is

$$C_{Dx} = \frac{2000/\mathbb{R} + 19.6}{4}$$

or

$$C_{Dx} = \frac{500}{\mathbb{R}} + 4.9$$

The application of the present form of the analytical model to the composite model analysis is compatible with the present derivation with the exception of the development of the horizontal viscous damping equations of Section 2.3.1a for vertical circular piles. Referring to this section, it is apparent that the cross sectional area of a vertical increment of a vertical pile has been calculated as

$$dA_x = dz \times D$$

where

dz = vertical incremental distance

D = pile diameter

whereas the structural cross sectional area of a composite tire-pile slab increment is

$$dA_x = dz \times Y \times (1-\epsilon)$$

Since the only specific application of this portion of the horizontal viscous damping equation is in the Lorentz equivalent work scheme of Section 5.1.1, the horizontal dissipation mechanism of the analytical model is modified to accommodate the analysis of the composite structure by multiplying Eq. (5.1.7) by the quantity

$$Y(1-\epsilon)/D$$

For the vertical component of the oscillatory flow analysis, the porous slabs are further subdivided by passing 14, evenly spaced, horizontal planes through each slab to yield 15 y-directed, porous, rectangular piles. Thus, the four slabs of the horizontal flow analysis are replaced by a total of 60 identical porous y-directed members whose vertical and longitudinal dimensions are both equal to 1.33 in. and whose lateral repeating widths, Y, are equal to the width of the wave tank. A subdivision of the composite structure into x-directed porous members could also have been employed for the analysis of the structural interaction with the vertical water particle velocity components.

Once again, since the steady flow drag coefficient results were obtained for the composite model as a whole, and since the model is being subdivided into 60 (4 longitudinal divisions by 15 vertical divisions) y-directed sections, it is necessary to divide the drag coefficient relationship of Eq. (8.4.2) by the number of sections in the flow direction. Therefore, dividing Eq. (8.4.2) by 15 yields the drag coefficient relationship for the theoretical analysis of the structural interaction with the vertical component of the water particle motion as

$$C_{Dz} = \frac{2500/\mathbb{R} + 6.5}{15}$$

or

$$C_{Dz} = \frac{167}{\mathbb{R}} + .433$$

Also, noting that the development of the horizontal viscous damping equation in Section 2.3.1d was for circular y-directed piles it is apparent that the structural cross sectional area

$$dA_z = dy \times D$$

where

dy => Y for the two dimensional problem

must be replaced by

$$dA_z = Y \times D \times (1-\epsilon)$$

Again, the vertical dissipation mechanism of the analytical model is easily modified to accommodate the analysis of the composite structure by multiplying Eq. (5.1.13) by $(1-\epsilon)$.

Although Sollitt's composite tire-pile model tests were conducted for incident wave conditions which would ordinarily indicate viscous drag forces predominating for a conventional pile matrix structure, the extension of such an assumption to the composite model may be questionable. Hence, accurate added mass coefficients were thought to be of some importance for the theoretical analysis. Consequently, a simple drop test was conducted in which an accelerometer was used to measure the acceleration of the composite model during a free fall through a column of water. Unfortunately, the model reached its terminal fall velocity so quickly that the initial (and only) accelerations were overshadowed by noise induced by the release mechanism when the model was dropped. Further contamination of the results arose from the model colliding with the sides of the test tank since close tolerances were required to eliminate end by-pass flow. The net result was judged unacceptable as the scatter range of the calculated added mass coefficients was over 100 percent. Thus it was necessary to run the analytical model for a number of arbitrary added mass coefficients in order to ascertain their effect. This has been done for equal values of C_{mx} and C_{mz} of 0.5, 0.0, -0.5 and -1.5. The negative coefficients were tried merely as a curiosity since both Garrison et al. (1977) and Sarpkaya (1976) have indicated their occurrence for cylinders at low Reynolds numbers.

The reflection and transmission coefficients obtained by Sollitt in the model experiments with the composite tire-pile matrix structure are shown in Fig. 8.28. The dimensionless wave frequency corresponding to each data point is also indicated on this figure.

The predicted reflection and transmission coefficients for the positive values of the added mass coefficients are compared to Sollitt's experimental data in Fig. 8.29. It is apparent in this figure that the variation in the added mass coefficients has a rather small effect on the results, i.e., generally decreasing both the reflection

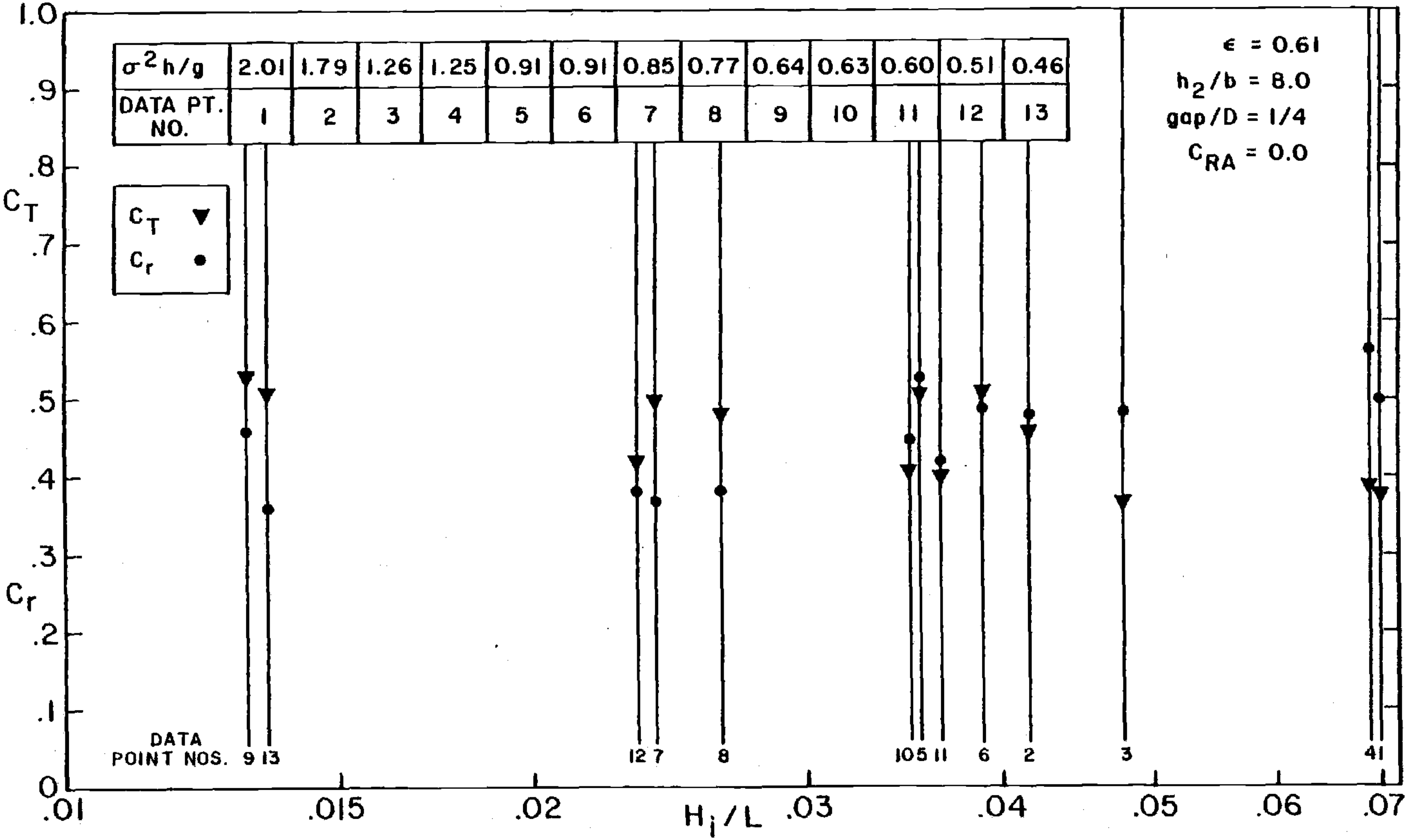

Figure 8.28. Sollitt's experimentally obtained reflection and transmission coefficients for a composite pile-automobile tire structure matrix model. $C_{RA} = 0.0$.

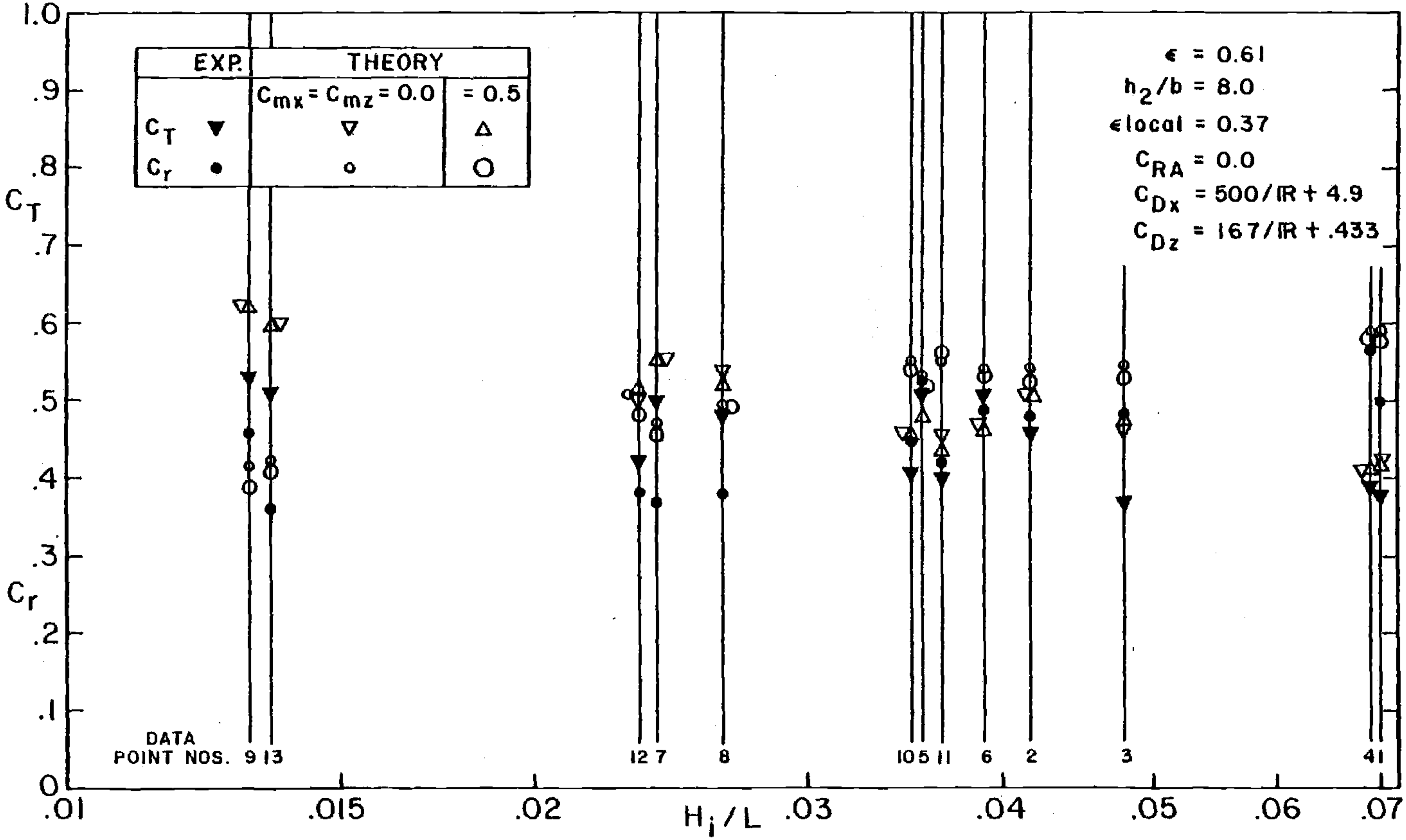

Figure 8.29. Comparison of computed reflection and transmission coefficients with Sollitt's experimental data for the composite tire-pile model.

and transmission coefficients slightly with decreasing added mass coefficients. This trend is also visible in Fig. 8.30 for the negative added mass coefficients.

The theoretical reflection and transmission coefficients correlate acceptably with a significant number of the experimental data points. However, the predicted reflection coefficients corresponding to data points 7, 8, 10, 11, and 12 are unacceptably high. The fact that all of these theoretical values over-predict the measured values for incident waves which are all of intermediate steepness and of lower dimensionless wave frequency suggests that the theory is failing to completely model the system in these instances. A definitive explanation for this discrepancy is not known. However it has been hypothesized in this investigation that a water particle is capable of 'feeling' the local environment for some distance about itself. Extending this hypothesis, water particles of low frequency steep waves, having longer excursions, would have a 'greater knowledge' of the local environment. Thus, the longer waves of data points 7, 8, 10, 11 and 12 may not actually 'see' the more reflective local interfacial porosity of 0.37 corresponding to the first pile row. Rather, they may be seeing a local porosity, based on their displacement amplitudes, which encompasses a portion of the more porous tire matrix. This would tend to decrease the initial reflection and increase the initial transmission. The increased initial transmission

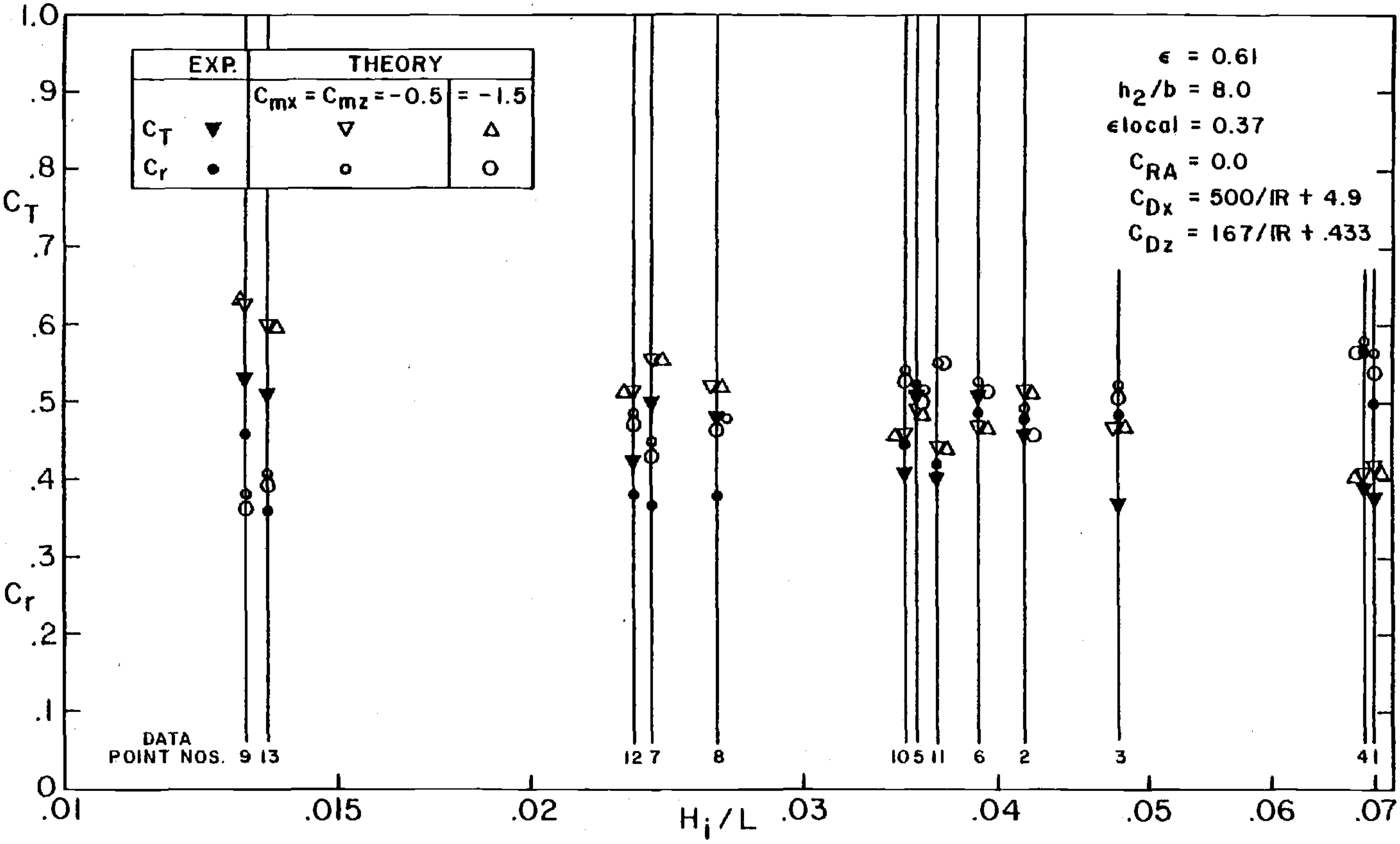

Figure 8.30. Comparison of computed reflection and transmission coefficients with Sollitt's experimental data for the composite tire-pile model.

allows higher internal velocities within the structure thereby resulting in increased dissipation so that the final transmission could conceivably remain unchanged. Further research incorporating the amplitude of the water displacements into the calculation of the interfacial porosity for non-homogeneous structures is suggested.

Figure 8.30 depicts the analytical results for negative values of the added mass coefficient. The correlation in terms of the predicted reflection coefficients is aided only slightly.

A general summary of Figs. 8.29 and 8.30 must conclude that the analytical model generally achieves a reasonable approximation of the experiments and often yielded predictions which were within the limits of experimental error. This correlation was achieved using drag coefficients obtained from steady flow model tests and added mass coefficients obtained from the literature for cylindrical piles. The fact that the application of these coefficients to the analysis of the composite tire-pile matrix structure yielded reasonable correlation is encouraging.

Figure 8.31 shows Sollitt's experimentally obtained reflection coefficients when a perfect reflector is positioned at a dimensionless distance $h_2/c = 4.0$ behind the composite tire-pile matrix. That is, with the exception of the tire matrix, the model configuration is identical to that described in Section 8.4.3a. Comparison of Fig. 8.31 with Fig. 8.17 indicates that the tire matrix tends to increase

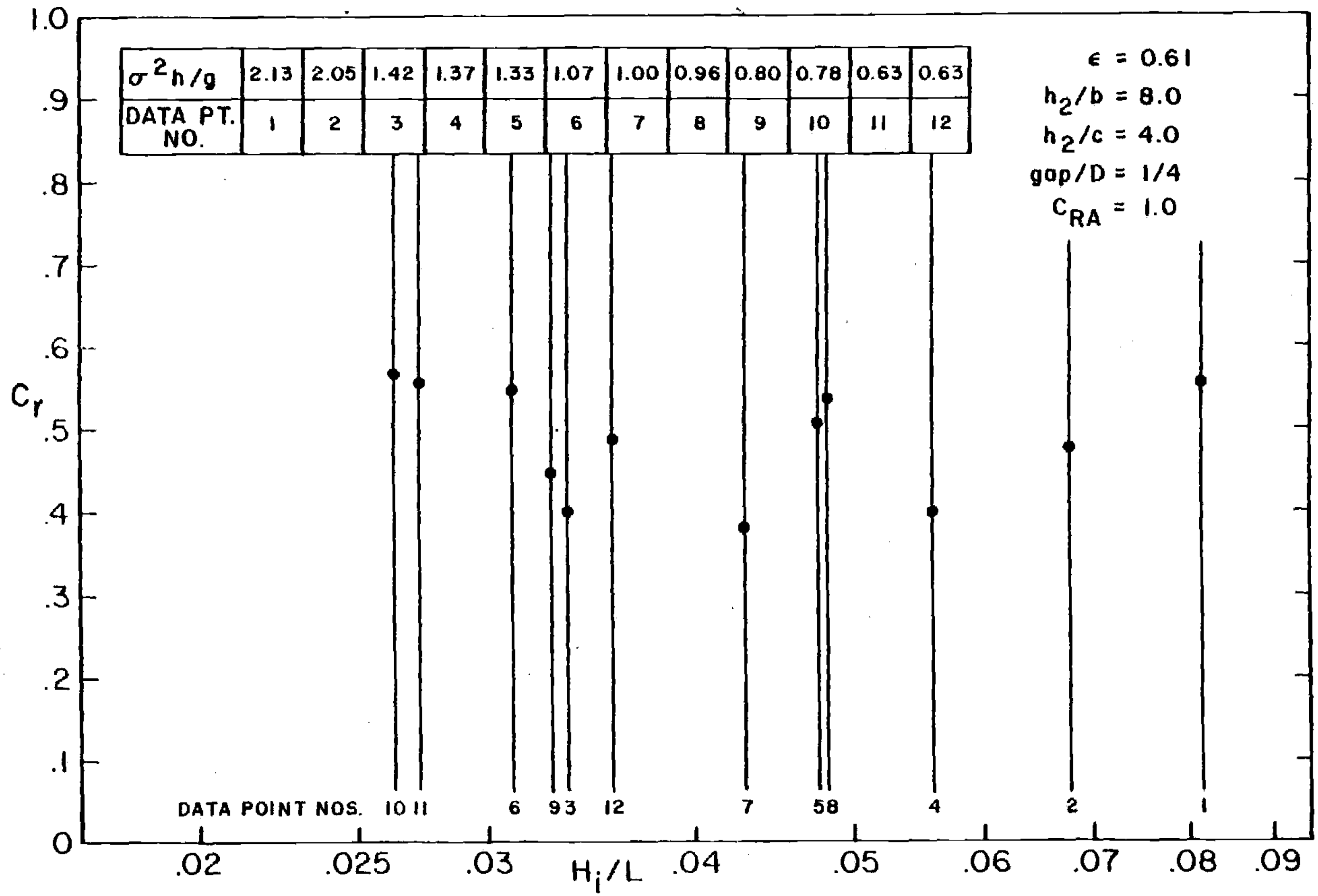

Figure 8.31. Sollitt's experimentally obtained reflection coefficients for a composite tire-pile matrix model in conjunction with a perfect reflector. $C_{RA} = 1.0$, $h_2/c = 4.0$.

the reflection of the steeper waves and decrease that of the less steep waves.

Figure 8.32 depicts the predicted reflection coefficients for the configuration described above. As was the case in Fig. 8.29, the theory over-predicts the actual reflection for waves of low frequency and intermediate steepness ($H_i/L = .026$ is considered intermediate with respect to Fig. 8.29). This over-prediction was also observed for the analysis without the tire matrix as shown in Fig. 8.19. The theory generally correlates with the experimental data in an acceptable fashion for the first six data points of Fig. 8.32 while the discrepancy for the last six points might be improved by an interfacial porosity based on the displacement amplitude of the longer waves.

Figure 8.33 shows Sollitt's experimentally obtained coefficients when a perfect reflector is positioned at a dimensionless distance $h_2/c = 1.33$ behind the tire-pile structure. Thus, the model configuration is analogous to that described in Section 8.4.3c. Comparison of Fig. 8.33 with Fig. 8.22 indicates that the general trend remains similar but that the inclusion of the tire matrix increases the wave reflection. This increase in reflection is attributed to the decrease in porosity rather than a change in the internal dissipation.

Figure 8.34 compares the theoretical reflection coefficients for the perfect reflection case when $h_2/c = 1.33$ to the experimental

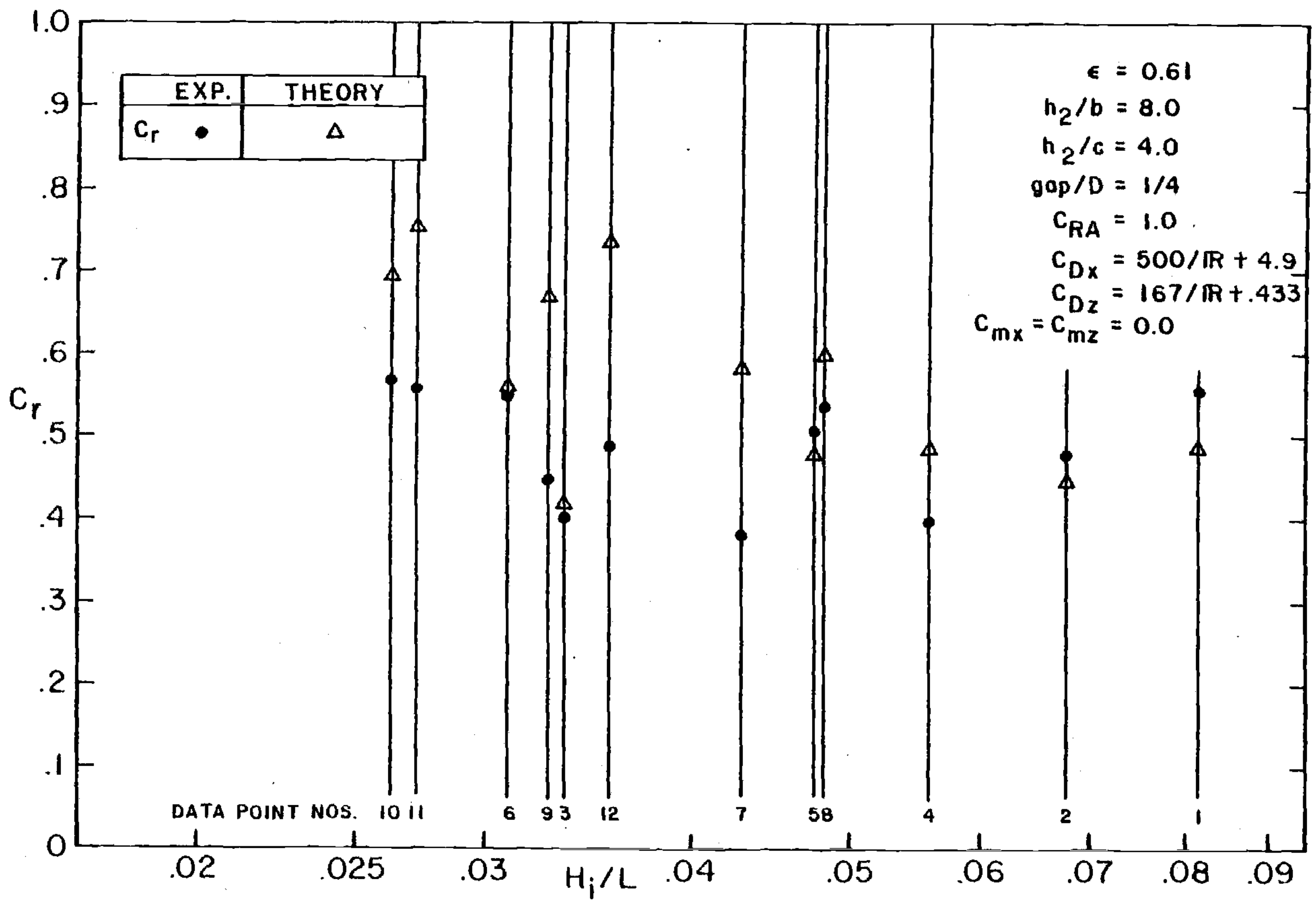

Figure 8.32. Comparison of computed reflection coefficients with experimental data for the composite tire-pile model with a perfect reflector. $C_{RA} = 1.0$, $h_2/c = 4.0$.

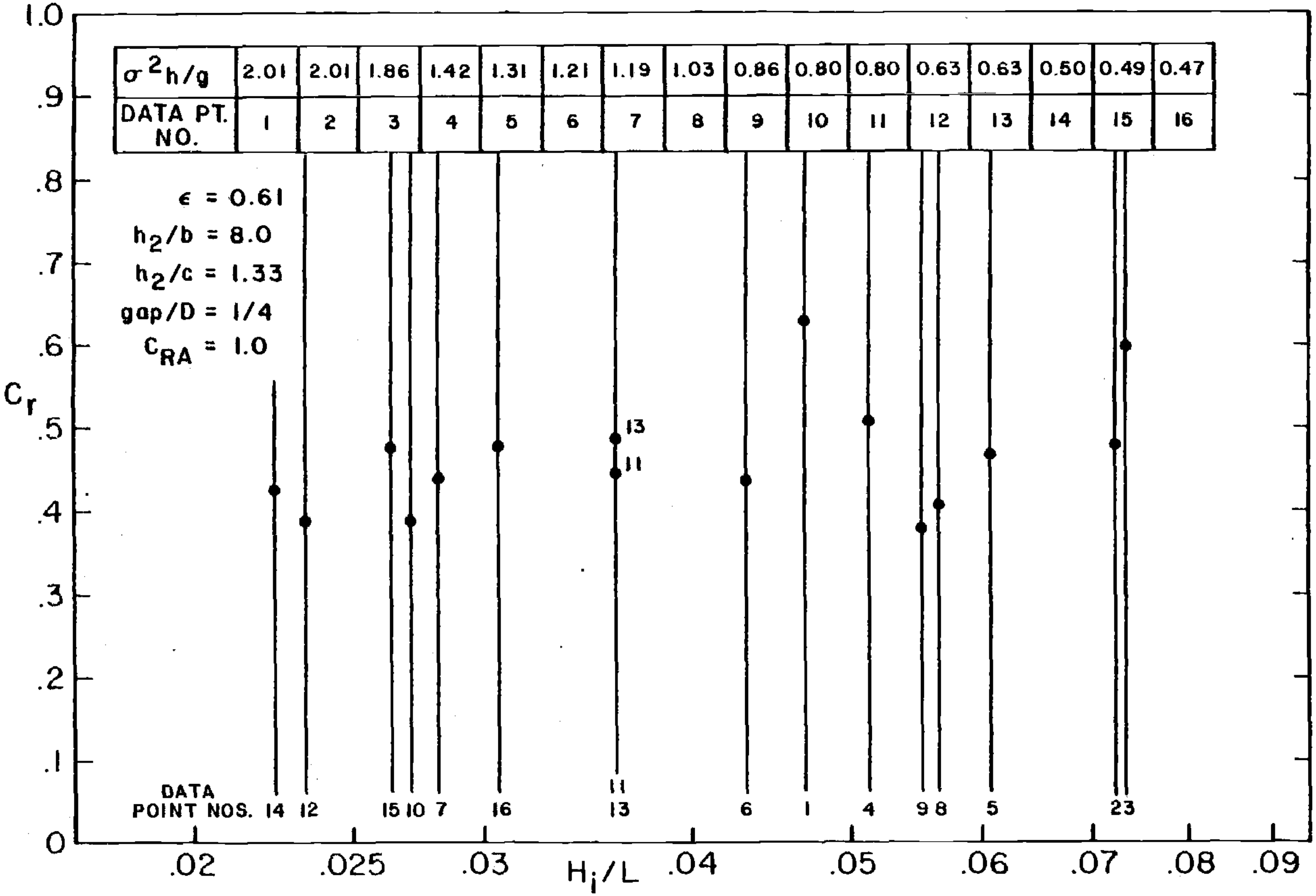

Figure 8.33. Sollitt's experimentally obtained reflection coefficients for a composite tire-pile matrix model in conjunction with a perfect reflector. $C_{RA} = 1.0$, $h_2/c = 1.33$.

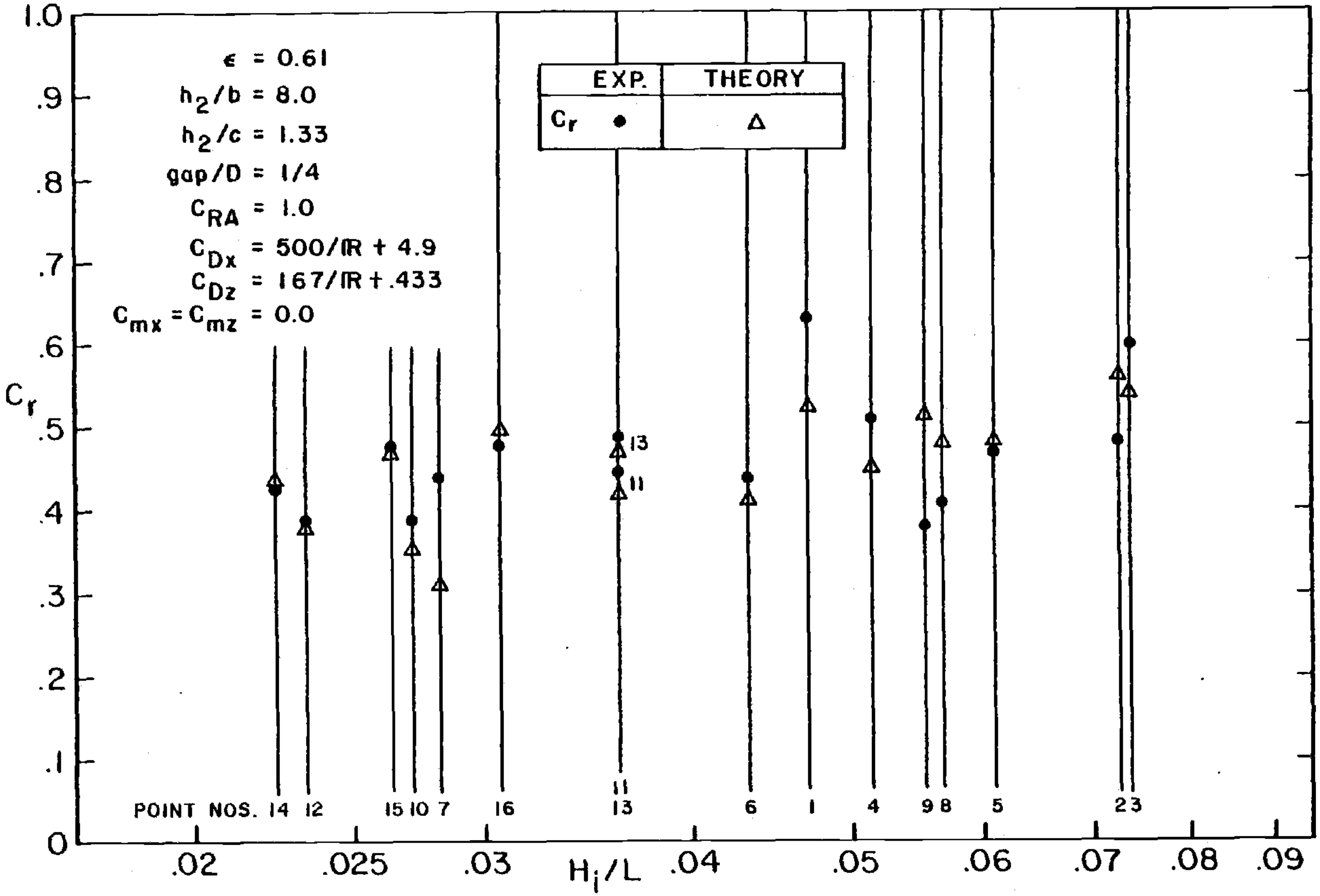

Figure 8.34. Comparison of computed reflection coefficients with experimental data for the composite tire-pile model with a perfect reflector. $C_{RA} = 1.0$, $h_2/c = 1.33$.

data. The correlation over the entire range of wave steepnesses is quite good. It is not known why the waves of intermediate steepness and low frequency are well modeled in this instance as opposed to those of Figs. 8.29 and 8.32. However, the correlation in this case and that of Fig. 8.29 are quite satisfactory.

8.5. Summary of Theoretical and Experimental Correlation

In general, the analytical model has achieved reasonable correlation with experimental models that are relatively wide and homogeneous. Also, acceptable correlation is obtained for the analysis of structures which are inhomogeneous but longitudinally continuous. Experimental configurations employing a perfect reflector are well modeled only when the distance, c, from the rear of the structure to the reflecting wall approaches the magnitude of the water depth. The analytical model generally does not correlate well with relatively narrow experimental models with reflection barriers and with inhomogeneous, longitudinally discontinuous structures.

IX. SUMMARY AND CONCLUSIONS

9.1. Theoretical Approach

The problem of a small amplitude, harmonic, monochromatic, two dimensional wave normally incident upon a laterally continuous, regularly repeating matrix structure has been analytically modeled. The analysis employs modifications of the longitudinal and vertical Navier-Stokes equations of motion in which damping has been provided by Morison-type resistance forces. The equations of motion are linearized with respect to the velocity components by means of longitudinal and vertical dimensionless damping coefficients. These coefficients are defined to obtain equivalent energy dissipation by both the linear and non-linear viscous damping forces during one wave cycle. A velocity potential is defined for use in the linearized equations of motion so that, employing the small amplitude wave assumptions, a modified Laplace-type partial differential equation is obtained. Making use of the kinematic and dynamic free surface coundary condition and the horizontal, impermeable, bottom boundary condition from linear wave theory, infinite eigen-series solutions for the velocity potential and pressure fields within the structure and the seaward and leeward regions adjoining the structure are achieved. The boundary conditions of horizontal mass flux continuity and pressure continuity are applied at the seaward and leeward structural interfaces to obtain a coupled system of complex algebraic equations. This system of equations is orthogonalized with respect to the vertical coordinate thereby eliminating the depth dependency. The unknown, complex, amplitude coefficients of the system are rendered dimensionless by division by the incident wave amplitude and the solutions for the resulting reflection, transmission and interior coefficients are obtained through the use of an iterative numerical algorithm.

9.2. Summary of Theoretical Behavior

The general theoretical behavior of the transmission coefficient, C_T, may be summarized as:

a) C_T generally decreases with increasing dimensionless wave frequencies, $\sigma^2 h/g$. The exception occurs when the distance to the reflector-absorber is less than the water depth, in which case C_T exhibits relative maxima and minima. These maxima and minima occur as functions of $\sigma^2 h/g$ and the distance between the structure and the reflecting wall, c, such that c is approximately some integer multiple of one-half the incident wavelength.

b) C_T decreases with increasing values of both the horizontal and vertical dimensionless damping coefficients, f_x and f_z.

c) C_T generally decreases as the horizontal added mass coefficient, C_{mx}, increases and, hence, as S_x increases. The exception occurs when the vertical added mass coefficient, C_{mz}, and $\sigma^2 h/g$ are both large at which time the trend reverses.

d) C_T is virtually insensitive to variations in C_{mz} for all structural porosities tested and is insensitive to C_{mx}, as well, at high structural porosities.

e) C_T decreases as the structural porosity decreases.

f) C_T decreases as the structural width, $2b$, increases relative to the water depth, h_2.

g) C_T decreases with decreasing values of C_{RA} for small to intermediate values of $\sigma^2 h/g$ (long to intermediate waves) and $h_2/c \geq 1.0$. This trend reverses for intermediate to large values of $\sigma^2 h/g$ (intermediate to short waves) with the reversal point migrating towards higher $\sigma^2 h/g$ values as h_2/c increases from unity. Multiple reversals are possible when $h_2/c < 1.0$.

The general theoretical behavior of the reflection coefficient, C_r, may be summarized as:

a) C_r exhibits a peaking tendency at intermediate to high values of $\sigma^2 h/g$ in the absence of a reflector-absorber. C_r on either side of the peak decreases monotonically. The maximum C_r shifts toward lower $\sigma^2 h/g$ with increasing values of f_x, f_z, C_{mx}, and C_{mz} and has generally been found to occur at a $\sigma^2 h/g$ value such that $0.16 \leq 2b/L \leq 0.18$.

b) C_r increases as f_x and $C_{mx}(S_x)$ increase.

c) C_r generally decreases as f_z and $C_{mz}(S_z)$ increase.

d) C_r is virtually insensitive to changes in C_{mx} and C_{mz} when the structural porosity is large.

e) C_r increases as the structural porosity decreases.

g) C_r exhibits relative maxima and minima as functions of $\sigma^2 h/g$, b, and c when the reflection coefficient of the reflector-absorber, C_{RA}, is non-zero. The relative amplitudes of these maxima and minima become more exaggerated with increases in C_{RA} and, in general, with increases in h_2/b and decreases in h_2/c. Relatively narrow structures exhibit high C_r for long wave conditions while relatively wide structures are more frequency selective and tend to be only moderately reflective of some particular long and intermediate waves.

9.3. Summary of Application Instructions

Detailed instructions for the use of the analytical model via the computer program are provided in Chapter VI and Appendices C, D, and E. A summary of the required data for the application of the analytical model is provided here. The variable names indicated in this section correspond to the computer program variables while the variable name in parentheses corresponds to the variable used within the text of this report.

9.3.1. The Geometric Variables

The application of the theory requires that the structural geometry and the local bathymetry be known. Hence, an existing or proposed design configuration and location must be known. Specifically, the required geometric variables are the:

(1) distance from the center of structure to the seaward and leeward edges, B (b).

(2) water depths in the seaward and leeward regions adjoining the structure and that within the structure, H1 (h_1), H3 (h_3), H2 (h_2) respectively. Note that the water depths are not required to be equal in each of the three regions.

(3) pile diameter DI (D). The program is presently written for a constant pile diameter for all members, however, only minor modifications are required to accommodate a pile diameter which varies from member to member.

(4) distance from the leeward edge of the structure to the reflector-absorber, C (c).

(5) lateral distance over which the structural configuration repeats itself, Y (Y).

(6) maximum numbers of laterally and longitudinally directed structural members between any two vertical members, NY and NX, respectively.

(7) total numbers of laterally, longitudinally, and vertically directed structural members within the structural volume defined by $-b \leq x \leq b$, $-h_2 \leq z \leq 0$, and $0 \leq y \leq Y$, NYT, NXT, and NZ, respectively.

(8) z-coordinates of the centerlines of each of the laterally and longitudinally directed members, YD[ARRAY] and XD[ARRAY], respectively. The x-coordinate is not required since it is assumed that these members are located between vertical members and the x-coordinate is known for each vertical member. The coordinates of each member are required for the local velocity calculation in the vicinity of each member.

(9) x-coordinate of the centerline of each vertical member, DX[ARRAY].

9.3.2. The Empirical and/or Experimental Variables

The input variables required for the application of the analytical model which are, or have been, either empirically, experimentally or historically obtained are the:

(1) gravitational acceleration, G (g).

(2) fluid density and kinematic viscosity, RO (ρ) and VIS (ν), respectively.

(3) reflection coefficient of the reflector-absorber, CRA (C_{RA}).

(4) drag coefficient constants, AL (A) and BET (B), as specified in Chapter V.

(5) the added mass coefficients for the x and z-directions, CMX (C_{mx}) and CMZ (C_{mz}), respectively, as specified in Chapter V.

(6) the number of terms at which each of the infinite eigen-series of the system of complex algebraic simultaneous equations is truncated, NUM (N). Values of Num = 5 have been found to yield acceptable accuracy in this study.

9.3.3. Design Wave Variables

The wave variables required are the incident wave period, T (T), and the incident wave amplitude, AMP (a_i). However, since the maximum wave reflection, transmission, and attenuation may be of interest for a particular design configuration it is recommended that a wide range of incident wave steepnesses and wave frequencies be examined as opposed to exclusive consideration of a single design wave condition.

9.3.4. Computational Requirements

The programmed analytical model has been shown to achieve rapid convergence for all of the structures examined in this study. The maximum computational and processing time required for the calculation of any data point set for the most complex structure analyzed in this study was less than 20 octal seconds per data point (both the reflection and transmission coefficients constituting a data point). Since the program has been structured for 'debugging' efficiency rather than computational efficiency, further savings are obtainable by re-structuring the program, although, this is not recommended.

9.4. Assessment of Theoretical and Experimental Comparisons with Suggestions for Future Investigations

The analytical model has been shown to correlate acceptably with the longitudinally wide, homogeneous, vertical pile models of Costello's (1952) experimental investigation. However, Costello's results did not include reflection measurements and the correlation is, therefore, solely for the measured and predicted wave transmissions.

The theoretical results have shown reasonable agreement with Kondo's (1972) measured reflection and transmission coefficients for a longitudinally wide, homogeneous, orthogonal lattice composed of vertical and laterally directed circular cylinders. The predicted transmission coefficients generally correspond to the measured values at all but the lowest wave steepness and most inertially dominated data. The computed reflection coefficients generally compare favorably with Kondo's data in a magnitude sense but must be viewed critically with regard to trend at the higher experimental wave steepness values. Since the experiments were conducted at very small ratios of the water particle excursion to the pile diameter, inertial dominance is to be expected. This is well modeled by the theory's sensitivity to the added mass and, hence, inertial coefficients. Further research to establish the added mass coefficient as a function of the Reynolds number and the dimensionless water particle excursion, in analogy with the drag coefficient, is required.

Both the analysis of Costello's models and that of Kondo's model entailed some difficulty in establishing a drag coefficient relationship using the method prescribed in Chapter V. This was due to the lack of applicable oscillatory drag coefficient data at the low Reynolds numbers of the experiments. This problem was also apparent in the analysis of Sollitt's models. However, sufficient data is available in the literature for most prototype applications and, thus, further research at low Reynolds numbers is not warranted.

The analytical model has been shown to be in good agreement with Sollitt's model composed of a single row of laterally closely spaced vertical piles. This correlation, however, was achieved only by 'tuning' the model to the data by increasing the drag coefficient above its expected value. This increase might be attributed to proximity effects although further research is required to establish a definitive relationship for the prediction of proximity effects in an 'a priori' manner. The theory has been found to be appropriately insensitive to the inertial terms for the drag dominated conditions of Sollitt's experiments.

The analysis of Sollitt's model composed of two rows of laterally closely spaced vertical piles indicates fair agreement between the theory and the experiment only when the structure is analyzed as though the first row of piles represents the structure and the second row represents a partial reflector. It is concluded that the spatial averaging of the theoretical dissipation mechanism is not well suited to the highly localized dissipation of such an inhomogeneous two row experimental model. However, the step-wise analysis using the predicted data for a single row of piles in conjunction with a partial reflector could be extended to handle multiple rows of laterally closely spaced and longitudinally widely spaced vertical piles.

Additional model studies would be required to verify the validity of such an approach.

Comparison of the analytical results with those obtained experimentally by Sollitt for two closely spaced vertical pile row models in conjunction with a perfect reflector indicate only fair to poor correlation. That is, no correlation was obtained for the structures in which the longitudinal distance between the pile rows was small and the distance from the leeward pile row to the reflector was small to moderately large. Fair correlation was obtained for the structures in which the distance between the pile rows or the distance to the reflector was increased. However this correlation was achieved only after rigorous 'tuning' of the drag coefficient relationship. The failures of the analytical model in these cases has been attributed to an increase in the still water level in the region between the leeward pile row and the reflector. This increased head results in variations of internal reflections from within the structure which are not accounted for by the analytical model.

Generally reasonable correlation between the analytical model and Sollitt's experiments involving a composite automobile tire-circular vertical pile matrix have been obtained when no reflector is present. However, a discrepancy has been noted between the predicted and experimental reflection coefficients for the longer waves. It is felt that an alternative approach in which the interfacial porosity of these longitudinally continuous but inhomogeneous structures would be defined as a function of the water particle displacements could reduce these discrepancies. This constitutes an area in which further research is required.

When a perfect reflector is tested in conjunction with Sollitt's composite tire-pile matrix models, the analytical model again generally over predicts the reflection coefficients for the longer waves when the distance from back of the composite structure to the reflector is small. Correlation with the shorter steeper wave data is reasonable. Upon increasing the distance from the composite structure to the reflector, the predicted reflection coefficients are found to concur with Sollitt's experimental data over the range of experimental wave steepnesses. The fact that reasonable agreement is obtained for at least two of the composite model configurations leads to the conclusion that drag relationships obtained from steady flow model tests are acceptable when oscillatory data is not available in the literature.

A general assessment of the analytical model's performance must conclude that acceptable results may be expected for structures which are homogeneous and relatively wide, or, for structures which are inhomogeneous but longitudinally continuous. When a reflector is present, the application of the theory is recommended only for structures in which the distance from the rear of the structure to the reflector approaches or exceeds the water depth. Use of the theory is not recommended for relatively narrow structures with reflection barriers, or, inhomogeneous, longitudinally discontinuous structures.

The above assessment is tempered by the availability of reliable drag and added mass coefficients for the structure. Steady flow model tests have been shown to provide rapid and reasonably reliable data for the determination of drag coefficients for use in the theory.

This study has shown that the fairly open pile configurations of most harbor related facilities yield little wave attenuation. Significant attenuation is only attained for structures which exhibit a structural density beyond that required in terms of wave, foundation, and application loadings. Enhancement of common structural configurations using scrap materials to promote increased wave attenuation appears to be feasible and the analysis of these composite structures has been shown to be within the capabilities of the analytical model. Further research in this area should prove beneficial.

Additional recommended studies include, experimental model comparisons for models which include laterally directed, longitudinally directed, and/or diagonally directed members. Also, further research is required to provide an analytical description of the static head increase between the rear of the structure and the reflector when the distance between the two surfaces is small.

Finally, additional research is required to obtain deterministic relationships for proximity effects, and the effect of transverse forces on fluid energy dissipation.

BIBLIOGRAPHY

Abramowitz, M., and Stegun, I. A., eds., Handbook of Mathematical Functions with Formulas, Graphs, and Mathematical Tables, Dover Publications, Inc., New York, N.Y., pp. 85, 1970.

Ball, D.J., and Cox, N.J., "Hydrodynamic Drag on Groups of Flat Plates", Jr. of the Waterway, Port, Coastal and Ocean Div., A.S.C.E., Vol. 104, WW2, pp. 163-73, May, 1978.

Berkhoff, J.C.W., and van der Weide, J., "Wave Forces on a Row of Cylindrical Piles of Large Diameter", Pre-print paper presented at the 16th International Conference on Coastal Engr., Hamburg, Germany, Publication no. 206, October, 1978.

Costello, R.D., "Damping of Water Waves by Vertical Circular Cylinders", Trans., Amer. Geophysical Union, Vol. 33, #4, pp. 513-19, Aug., 1952.

Dalton, C., and Szabo, J.M., "Drag on a Group of Cylinders", Jr. of Pressure Vessel Technology, Trans. of the A.S.M.E., Vol. 99, pp. 152-57, Feb., 1977.

Dinoy, A.A., "Friction Factor and Reynolds Number Relationship in Flow through Porous Media", M. Engr. Thesis, Asian Inst. of Tech., Bangkok, Thailand, 1971.

Garrison, C.J., Field, J.B., and May, M.D., "Drag and Inertia Forces on a Cylinder in Periodic Flow", Jr. of the Waterway, Port, Coastal and Ocean Div., A.S.C.E., Vol. 103, WW2, pp. 193-204, May, 1977.

Gibson, R.J., and Wang, H., "Added Mass of Pile Group", Jr. of the Waterway, Port, Coastal, and Ocean Div., A.S.C.E., Vol. 103, WW2, pp. 215-23, May, 1977.

Goda, Y., and Ippen, A.T., "Theoretical and Experimental Investigation of Wave Energy Dissipators Composed of Wire Mesh Screens", Mass. Inst. of Tech. Hydrodynamics Lab. Rep. #60, Aug., 1963.

Grune, J., and Kohlhase, S., "Wave Transmission through Vertical Slotted Walls", Proc. of the 14th Coastal Engr. Conf., A.S.C.E., Copenhagen, Denmark, pp. 1906-23, June, 1974.

Hansen, O.N-E., Jacobsen, V., and Lundgren, H., "Hydrodynamic Forces on Composite Risers and Individual Cylinders", Paper # OTC 3541, 11th Annual Offshore Technology Conf., Houston, Tx., pp. 1607-21, Ap. 30-May 3, 1979.

Hartmann, ., "Das Stabgitter in Instationärer Strömungsbewegung", Mitt. des Instituts für Wasserbau, und Wasserwirtschaft, Technische Uniwersitat, Berlin, Heft 69, 1969.

Hattori, M., "Transmission of Water Waves through Perforated Wall", Coastal Engr. in Japan, J.S.C.E., Vol. 15, pp. 69-79, 1972.

Hayashi, T., Hattori, M., Kano, T., and Shirai, M., "Hydraulic Research on the Closely Spaced Pile Breakwater", Proc. of the Tenth Conf. on Coastal Engr., A.S.C.E., Tokyo, Japan, pp. 873-84, 1966.

Hayashi, T., Hattori, M., and Shirai, M., "Closely Spaced Pile Breakwater as a Protection Structure Against Beach Erosion", Coastal Engr. in Japan, J.S.C.E., Vol. 11, pp. 149-60, Dec., 1968.

Ijima, T., Eguchi, Y., and Kobayashi, A., "Theory and Experiment on Permeable Breakwater and Quay Wall", Kyushu Univ. Coastal Engr. Res. Lab, Tech. Rep. #3, Fukuoka, Japan, April, 1971.

Ijima, T., Chou, C.R., and Yumura, Y., "Wave Scattering by Permeable and Impermeable Breakwater of Arbitrary Shape", Proc. of the 14th Coastal Engr. Conf., A.S.C.E., Copenhagen, Denmark, pp. 1886-1905, June, 1974.

Ijima, T., Tanaka, E., and Okuzono, H., "Permeable Seawall with Reservoir and the Use of 'Warock' ", Proc. of the 15th Coastal Engr. Conf., A.S.C.E., Honolulu, Hawaii, pp. 2623-42, 1976.

Ijima, T., Chou, R.C., and Yoshida, A., "Method of Analyses for Two-Dimensional Water Wave Problems", Proc. of the 15th Coastal Engr. Conf., A.S.C.E., Honolulu, Hawaii, pp. 2716-36, 1976.

Ippen, A.T., ed., Estuary and Coastline Hydrodynamics, McGraw-Hill Book Co., Inc., New York, N.Y., 1966.

Kamel, A. M., "Water Wave Transmission through and Reflection by Pervious Coastal Structures", U.S. Army Engineers Waterways Exper. Sta. Research Rep. H-69-1, Vicksburg, Miss., Oct., 1969.

Keulegan, G. H., and Carpenter, L. H., "Forces on Cylinders and Plates in an Oscillating Fluid", National Bureau of Standards Report #4821, Nat. Bur. of Standards, Washington, D. C., 1956.

Kondo, H., "An Analytical Approach to Wave Transmission through Permeable Structures", Coastal Engr. in Japan, J. S. C. E., Vol. 13, pp. 31-42, + 1 errata, 1970.

Kondo, H., and Toma, S., "Reflection and Transmission for a Porous Structure", Proc. of the 13th Coastal Engr. Conf., A. S. C. E., Vancouver, Canada, pp. 1847-66, July, 1972.

Kondo, H., and Toma, S., "Breaking Wave Transformation by Porous Breakwaters", Coastal Engr. in Japan, J. S. C. E., Vol. 17, pp. 81-91, 1974.

Kondo, H., Toma, S., and Yano, K., "Laboratory Study on Pervious Core Breakwaters", Proc. of the 15th Coastal Engr. Conf., A. S. C. E., Honolulu, Hawaii, pp. 2643-61, 1976.

Kondo, H., Toma, S., and Kasai, K., "An Analytical Approach to Predict the Transmission and Reflection Coefficients for Multi-Layered Porous Breakwaters", Memoirs of the Muroran Inst. of Technology, Science and Engr., Vol. 9, No. 1, ca. 1976 (in Japanese).

Laird, A. D. K., "Wave Forces on Piling", Governmental Research Report # AD606502, U. S. Dept. of Commerce, Office of Technical Services, June, 1964.

Laird, A. D. K., "Flexibility in Cylinder Groups Oscillated in Water", Jr. of the Waterways and Harbors Div., Proc. of the A. S. C. E., Vol. 92, WW3, pp. 69-85, Aug., 1966.

Lean, G. H., "A Simplified Theory of Permeable Wave Absorbers", Jr. of Hydraulic Res., I. A. H. R., Vol. 5, No. 1, pp. 15-30, 1967.

Lé Mehauté, B., "Perméabilitité des Diques en Enrochment aux Oudes de Gravitité Périodiques", La Houille Blanche, No. 2, pp. 148-179, 1958.

Lorentz, H. A., "Report of the State Committee Zuidersee 1918-1926", (Dutch text), Den Haag, Alg, Landsdrukkerij, 1926.

Madsen, O. S., "Wave Transmission through Porous Structures", Jr. of the Waterways, Harbors, and Coastal Engr. Div., A.S.C.E., Vol. 100, WW3, pp. 169-88, Aug., 1974.

Madsen, O. S., and White, S. M., "Wave Transmission through Trapezoidal Breakwaters", Proc. of the 15th Coastal Engr. Conf., A. S. C. E., Honolulu, Hawaii, pp. 2662-76, 1976.

Madsen, O. S., and White, S. M., "Energy Dissipation on a Rough Slope", Jr. of the Waterways, Harbors and Coastal Engr. Div., A. S. C. E., Vol. 102, WWI, pp. 31-48, 1976a.

Massel, S. R., "Interaction of Water Waves with Cylinder Barrier", Jr. of Waterways, Harbors, and Coastal Engr. Div., A. S. C. E., Vol. 102, WW2, pp. 165-87, May, 1976.

McCorquodale, J. A., "Wave Energy Dissipation in Rockfill", Proc. of the 13th Coastal Engr. Conf., A. S. C. E., Vancouver, Canada, pp. 1885-1901, July, 1972.

Morison, J. R., O'Brien, M. P., Johnson, J. W., and Schaaf, S. A., "The Force Exerted by Surface Waves on Piles", Petroleum Trans., Amer. Inst. of Mining Engrs., Vol. 189, pp. 149-154, 1950.

Nagai, S., "Researches on Steel-Pipe Breakwater", Proc. of the Tenth Conf. on Coastal Engr., A. S. C. E., Tokyo, Japan, pp. 850-72, 1966.

Nagai, S., "Perforated Vertical Wall Breakwater", The Dock and Harbor Authority, London, pp. 194-198, Oct., 1976.

Nagai, S., and Kakuno, S., "Slit-Type Breakwater: Box-Type Absorber", Proc. of the 15th Coastal Engr. Conf., A. S. C. E., Honolulu, Hawaii, pp. 2697-716, 1976.

Nasser, M. S., and McCorquodale, J. A., "Wave Motion in Rockfill", Jr. of Waterways, Harbors, and Coastal Engr. Div., A. S. C. E., Vol. 101, WW2, pp. 145-59, May, 1975.

Numata, A., "Laboratory Formulation for Transmission and Reflection at Permeable Breakwaters of Artificial Blocks", Coastal Engr. in Japan, J. S. C. E., Vol. 19, pp. 47-58, 1976.

Robertson, J. M., Hydrodynamics in Theory and Application, Prentice-Hall, Inc., Englewood Cliffs, N. J., 1965.

Sarpkaya, T., "Vortex Shedding and Resistance in Harmonic Flow about Smooth and Rough Cylinders at High Reynolds Numbers", Report # NPS-59SL76021, Naval Post Graduate School, Monterey, Ca., Feb., 1976.

Sarpkaya, T., "Hydrodynamic Forces on Various Multiple-Tube Riser Configurations", Paper # OTC 3539, 11th Annual Offshore Technology Conf., Houston, Tx., pp. 1603-06, Ap. 30-May 3, 1979.

Sawaragi, T., and Iwata, K., "Effect of Structural Shape on Wave Run-Up and Wave Damping", Coastal Engr. in Japan, J. S. C. E., Vol. 13, pp. 55-74, 1970.

Sawaragi, T., and Iwata, K., "On Wave Deformation due to Permeable Structures", Coastal Engr. in Japan, J. S. C. E., Vol. 16, pp. 107-22, 1973.

Schlicting, H., Boundary Layer Theory, 6th ed., McGraw-Hill Book Co., New York, N. Y., pp. 16, 1968.

Shore Protection Manual, U. S. Army Coastal Engineering Research Center, Fort Belvoir, Va., 2nd Ed., 1975.

Sollitt, C. K., and Cross, R. H., "Wave Reflection and Transmission at Permeable Breakwaters", Mass. Inst. of Tech. Water Resources and Hydrodynamics Lab. Rep. # 147, March, 1972.

Terrett, F. L., Osorio, J. D., and Lean, G. H., "Model Studies of a Perforated Breakwater", Proc. of the 11th Conf. on Coastal Engr., A. S. C. E., London, England, pp. 1104-20, 1968.

Thomas, Jr., G. B., Calculus and Analytic Geometry, 4th edition, Addison-Wesley Publishing Co., Reading, Mass., pp. 674, 1968.

Todd, F.H., "Model Experiments on Different Designs of Breakwaters", The Civil Engineer in War, Vol. 2, Docks and Harbors, Inst. Civil Engineers, pp. 243-55, 1948.

Tominaga, M., and Sakamoto, T., "Study of Wave Transformation by Permeable Structures", Rept. of the Public Works Res. Inst., Japan, No. 137, pp. 117-40, 1970.

Ward, J.C., "Turbulent Flow in Porous Media", Jr. of the Hydraulics Div., A.S.C.E., Vol. 90, # HY5, pp. 1-12, Sept., 1964.

Wiegel, R.L., "Transmission of Water Waves Past a Rigid Thin Vertical Barrier", Jr. of Waterways and Harbors Div., Proc. A.S.C.E., 86, WWI, Paper 2413, March, 1960.

Wiegel, R.L., Oceanographical Engineering, Prentice-Hall Inc., Englewood Cliffs, N.J., 1964.

Wylie, C.R., Advanced Engineering Mathematics, McGraw-Hill Book Co., New York, N.Y., 1975.

Yamamoto, T., and Nath, J.H., "High Reynolds Number Oscillating Flow by Cylinders", A.S.C.E. reprint from Proc. of the 15th Coastal Engr. Conf., A.S.C.E., Honolulu, Hawaii, pp. 2321-2340, 1976.

Zdravkovich, M.M., "Review of Flow Interference between Two Circular Cylinders in Various Arrangements", Jr. of Fluids Engr., Trans. of the A.S.M.E. (Series I), Vol. 99, pp. 618-33, Dec., 1977.

APPENDICES

APPENDIX A

The velocity potential in Region II is given by Eq. (3.2.1) as

$$\phi_{2n} = -g[a_{+n} e^{i[\sqrt{A_x/A_z}\, k_{2n}(x+b)]} + a_{-n} e^{-i[\sqrt{A_x/A_z}\, k_{2n}(x-b)]}]$$

$$\times \left[\frac{ch.\, k_{2n}(h_2+z)}{ch.\, k_{2n}h_2} \right] e^{-i\sigma t} \qquad (3.2.1)$$

The bracketed arguments of the spatial exponential functions are, in general, complex since the eigenvalue k_{2n} is generally complex and, since

$$A_x = f_x\sigma - i\sigma S_x$$

and

$$A_z = f_z\sigma - i\sigma S_z$$

are both complex, the square root of the ratio A_x/A_z must also be complex. Hence the spatial exponentials will take on the general form

$$e^{\alpha}[\cos\lambda + i\sin\lambda]$$

where

α = real part of the complex argument of the spatial exponentials

λ = imaginary part of the complex argument of the spatial exponentials

From the above form, it is apparent that the argument of the exponent, α, must be a negative number if wave amplification within the structure is to be avoided.

Since the range of the x-variable in Region II is $-b \leq x \leq b$, the value of $(x+b)$ is always positive or zero; on the other hand, the value of $(x-b)$ is always negative or zero thereby cancelling the negative sign in front of the a_{-n} term spatial exponential argument. Due to the similarity of the two x-dependent terms in Eq. (3.2.1), only the complex argument

$$i\sqrt{A_x/A_z}\,k_{2n}(x+b) \tag{A. 1}$$

need be examined to determine the sign of α.

The real and imaginary portions of the eigenvalues, k_{2n}, returned by the CMPLK2 subroutine are always positive. While it may be shown that the negatives of the real and imaginary portions also satisfy the complex dispersion equation, Eq. (2.10.2), there is no justification for choosing negative complex wave numbers, k_{2n}, and hence the positive values are retained. Therefore let

$$k_{2n} = c + id \tag{A. 2}$$

where

c, d = real and positive

With the sign of the eigenvalues, k_{2n}, fixed as positive, only the sign of the square root of the complex ratio A_x/A_z remains to be determined. This is accomplished by letting

$$\sqrt{A_x/A_z} = p + iq \tag{A.3}$$

where

p, q = real numbers whose signs have yet to be determined

and by making the substitutions indicated by Eqs. (A.2 and A.3) in Eq. (A.1), i.e.,

$$i\sqrt{A_x/A_z}\,k_{2n}(x+b) = i(p+iq)(c+id)(x+b)$$

Simplifying the complex algebra yields

$$i\sqrt{A_x/A_z}\,k_{2n}(x+b) = (x+b)(pd+qc) + i(x+b)(pc-dq)$$

where

$$-(x+b)(pd+qc) = \alpha$$

Now, since the quantities $(x+b)$, c, and d are all real and positive, it is apparent that the negative value of α will be preserved and waves will decay within the structure under any of the following three conditions;

(a) p and q are both positive

(b) p is negative, q is positive and qc > pd

(c) q is negative, p is positive and pd > qc

To examine the quantities p and q, it will be helpful to expand the complex square root of the ratio A_x/A_z such that

$$\sqrt{\frac{A_x}{A_z}} = \sqrt{\frac{\sigma(f_x - iS_x)}{\sigma(f_z - iS_z)}} = \sqrt{\frac{(f_x f_z + S_x S_z) + i(f_x S_z - f_z S_x)}{f_z^2 + S_z^2}}$$

Now let

$$\gamma = \frac{A_x}{A_z} = m + in$$

where

$$m = \frac{f_x f_z + S_x S_z}{f_z^2 + S_z^2}$$

$$n = \frac{f_x S_z - f_z S_x}{f_z^2 + S_z^2}$$

Using DeMoivre's theorem

$$\sqrt{\frac{A_x}{A_z}} = \gamma^{1/2} = \sqrt{(m^2 + n^2)^{1/2}} (\cos \tfrac{1}{2}\theta + i \sin \tfrac{1}{2}\theta)$$

where

$$\theta = \tan^{-1} \frac{n}{m}$$

or, substituting for m, n, and θ in the above expression yields

$$\sqrt{\frac{A_x}{A_z}} = \left[\left(\frac{f_xf_z+S_xS_z}{f_z^2+S_z^2}\right)^2 + \left(\frac{f_xS_z-f_zS_x}{f_z^2+S_z^2}\right)^2\right]^{1/4}$$

$$\times\left\{\cos\frac{1}{2}\left[\tan^{-1}\left(\frac{f_xS_z-f_zS_x}{f_xf_z+S_xS_z}\right)\right] + i\sin\frac{1}{2}\left[\tan^{-1}\left(\frac{f_xS_z-f_zS_x}{f_xf_z+S_xS_z}\right)\right]\right\}$$

The real fourth root of the first bracketed quantity may be chosen either positive or negative. Since one-half the principle range of the arctangent function yields a range of the cosine argument between $-\pi/4$ and $\pi/4$, the cosine term will always be positive. Referring to the phase diagram below

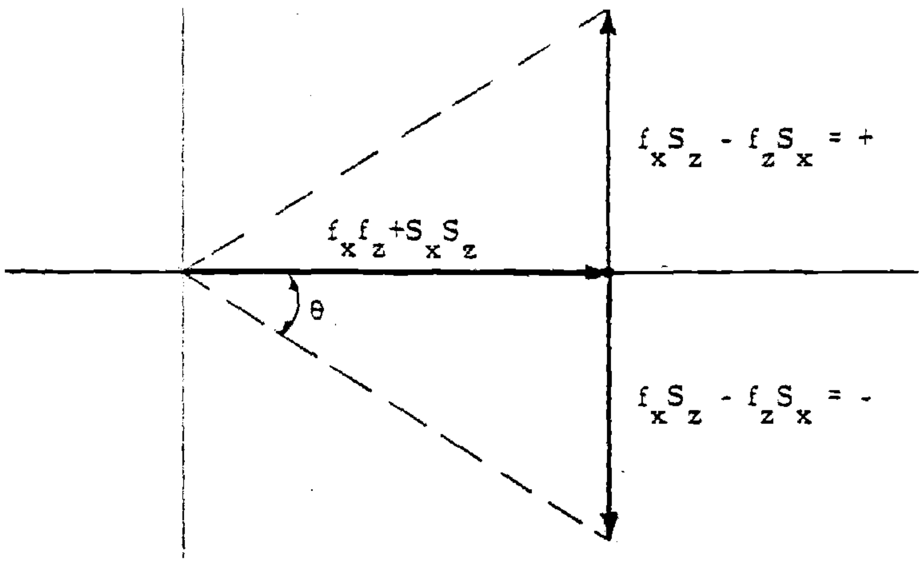

it is apparent that the sine term will be either positive or negative depending on whether the quantity

$$f_xS_z - f_zS_x$$

is positive or negative. If this quantity is positive, and hence the sine term is positive, then the positive real fourth root of the bracketed term is chosen so that the terms p and q are both positive and thus α will be negative in accordance with the previously specified condition (a).

If the quantity

$$f_x S_z - f_z S_x$$

is negative, and hence the sine term is negative, then the sign of the real fourth root is chosen to satisfy conditions (b) or (c), i.e.,

$$\underbrace{\mathrm{Imag}(k_{2n})}_{d}\underbrace{\left[\left(\frac{f_x f_z + S_x S_z}{f_z^2 + S_z^2}\right)^2 + \left(\frac{f_x S_z - f_z S_x}{f_z^2 + S_z^2}\right)^2\right]^{1/4} \cos\frac{1}{2}\left[\tan^{-1}\left(\frac{f_x S_z - f_z S_x}{f_x f_z + S_x S_z}\right)\right]}_{p}$$

$<$ (cond. (b); choose neg. real fourth root)

$>$ (cond. (c); choose pos. real fourth root)

$$\underbrace{\mathrm{Real}(k_{2n})}_{c}\underbrace{\left[\left(\frac{f_x f_z + S_x S_z}{f_z^2 + S_z^2}\right)^2 + \left(\frac{f_x S_z - f_z S_x}{f_z^2 + S_z^2}\right)^2\right]^{1/4} \sin\frac{1}{2}\left[\tan^{-1}\left(\frac{f_x S_z - f_z S_x}{f_x f_z + S_x S_z}\right)\right]}_{q}$$

Choosing the sign of the fourth root as prescribed above assures wave decay in Region II and thus allows the theory to conform to observed physical phenomena.

APPENDIX B

B.1. $\int ch.(a+bs)ch.(c+fs)ds$

Employing the method of integration by parts let

$$u = ch.(a+bs) \qquad dv = ch.(c+fs)ds$$

$$du = bsh.(a+bs)ds \qquad v = \frac{1}{f}sh.(c+fs)$$

then

$$\int ch.(a+bs)ch.(c+fs)ds$$

$$= \frac{1}{f}ch.(a+bs)sh.(c+fs) - \frac{b}{f}\int sh.(c+fs)sh.(a+bs)ds$$

To evaluate the integral on the extreme R.H.S. of the above equation the method of integration by parts is employed again. Letting

$$u = sh.(a+bs) \qquad dv = sh.(c+fs)ds$$

$$du = bch.(a+bs)ds \qquad v = \frac{1}{f}ch.(c+fs)ds$$

then

$$\int ch.(a+bs)ch.(c+fs)ds$$

$$= \frac{1}{f}ch.(a+bs)sh.(c+fs) - \frac{b}{f^2}sh.(a+bs)ch.(c+fs) + \frac{b^2}{f^2}\int ch.(a+bs)ch.(c+fs)ds$$

Subtracting the integral on the extreme R.H.S. of the above equation from both sides and simplifying yields

$$(1-\frac{b^2}{f^2})\int ch.(a+bs)ch.(c+fs)ds$$

$$=\frac{1}{f}ch.(a+bs)sh.(c+fs)-\frac{b}{f^2}sh.(a+bs)ch.(c+fs)$$

Dividing both sides of the above equation by $(1-b^2/f^2)$ yields

$$\int ch.(a+bs)ch.(c+fs)ds$$

$$=\frac{[\frac{1}{f}ch.(a+bs)sh.(c+fs)-\frac{b}{f^2}sh.(a+bs)ch.(c+fs)]}{(1-b^2/f^2)}$$

Now, multiplying the R.H.S. of the above equation by (f^2/f^2) yields the required integral as

$$\int ch.(a+bs)ch.(c+fs)ds$$

$$=\frac{fch.(a+bs)sh.(c+fs)-bsh.(a+bs)ch.(c+fs)}{f^2-b^2}$$

B.2. $ch.^2 a(b+s)ds$

Letting

$$r = bs$$

$$dr = ds$$

then, by substitution,

$$\int ch.^2 a(b+s)ds = \int ch.^2 (ar)dr$$

But, by hyperbolic identity

$$ch.^2 (ar) = \frac{1}{2} ch.(2ar) + \frac{1}{2}$$

so that, by substitution,

$$\int ch.^2 a(b+s)ds = \frac{1}{2}\int ch.(2ar)dr + \frac{1}{2}\int dr$$

Performing the integrals on the R.H.S. of the above equation yields

$$\int ch.^2 a(b+s)ds = \frac{sh.(2ar)}{4a} + \frac{r}{2}$$

or, substituting for r, the required integral is obtained as

$$\int ch.^2 a(b+s)ds = \frac{sh.\,2a(b+s)}{4a} + \frac{b+s}{2}$$

B.3. $\int sh.(a+bs)sh.(c+fs)ds$

Employing the method of integration by parts, let

$$u = sh.(a+bs) \qquad dv = sh.(c+fs)ds$$

$$du = bch.(a+bs)ds \qquad v = \frac{1}{f}ch.(c+fs)$$

then

$$\int sh.(a+bs)sh.(c+fs)ds$$

$$= \frac{1}{f}sh.(a+bs)ch.(c+fs) - \frac{b}{f}\int ch.(c+fs)ch.(a+bs)ds$$

To evaluate the integral on the extreme R.H.S. of the above equation the results of integration B.1 may be employed or the method of integration by parts may be used again. The latter is chosen although the result is the same. Therefore, letting

$$u = ch.(a+bs) \qquad dv = ch.(c+fs)ds$$

$$du = bsh.(a+bs)ds \qquad v = \frac{1}{f}sh.(c+fs)$$

the above equation becomes

$$\int \text{sh.}(a+bs)\text{sh.}(c+fs)ds$$

$$= \frac{1}{f}\text{sh.}(a+bs)\text{ch.}(c+fs) - \frac{b}{f^2}\text{ch.}(a+bs)\text{sh.}(c+fs) + \frac{b^2}{f^2}\int \text{sh.}(a+bs)\text{sh.}(c+fs)ds$$

Subtracting the integral on the extreme R. H. S. from both sides of the above equation and simplifying yields

$$(1 - \frac{b^2}{f^2}) \int \text{sh.}(c+fs)ds$$

$$= \frac{1}{f}\text{sh.}(a+bs)\text{ch.}(c+fs) - \frac{b}{f^2}\text{ch.}(a+bs)\text{sh.}(c+fs)$$

Dividing both sides of the above equation by $(1-b^2/f^2)$ and then multiplying the resulting R. H. S. by (f^2/f^2) yields the required integral as

$$\int \text{sh.}(a+bs)\text{sh.}(c+fs)ds$$

$$= \frac{f\text{sh.}(a+bs)\text{ch.}(c+fs) - b\text{sh.}(c+fs)\text{ch.}(a+bs)}{f^2 - b^2}$$

APPENDIX C

The following listing correlates variable names used within the narrative and those of the computer program listing (see Appendix D). Whenever possible, pertinent equation numbers within the narrative are given for the 'Narrative Variables'. Otherwise the pertinent section numbers in which the variable is defined are noted. Definitions are supplied as necessary.

MAIN PROGRAM

Program Var.	Narrative Var. (Eq. No.; Sec. No.)	Definition
AL	A (Eq. 5.5.1; Sec. 5.1.1)	First constant of the drag coefficient expression.
AMP	a_i (Eq. 3.2.5; Sec. 3.2.2)	Incident wave amplitude.
AX	A_x (Eqs. 2.5.1, 2.5.4; Sec. 2.5)	$A_x = f_x\sigma - i\sigma S_x$.
AZ	A_z (Eqs. 2.5.2, 2.5.6; Sec. 2.5)	$A_z = f_z\sigma - i\sigma S_z$.
A1	Not used	Defined in Program for computational expediency in calculating denominators of f_{xz}, f_{xy}, f_{zx}, f_{zy}.
A2	Not used	
A3	Not used	
A4	Not used	
A5	Not used	
A6	Not used	
A7	Not used	
B	b (Fig. 1.1, Sec. 1.1)	1/2 the longitudinal width of the structure.
BET	B (Eq. 5.5.1; Sec. 5.1.1)	Second constant of the drag coefficient expression
BM	Not used explicitly	The R.H.S., or 'B' matrix side, of the general matrix equation $[A][X] = [B]$. 'BM' is therefore the column vector matrix composed of ones and zeroes corresponding to the system of equations described by Eqs. (4.2.2, 4.2.3, 4.2.5 and 4.2.6).
BT	β (Eq. 3.3.7; Sec. 3.3.1)	$\beta = \dfrac{-i\sigma\epsilon\sqrt{A_x/A_z}}{A_x}$.

Program Var.	Narrative Var. (Eq. No.; Sec. No.)	Definition
B1	Not used	Defined in program for computational expediency in calculating the denominators of f_{xz}, f_{xy}, f_{zx}, f_{zy}.
B2		
B3	Not used	
B4	Not used	
B5	Not used	
B6	Not used	
C	c (Fig. 1.1, Sec. 1.1)	Distance from the rear of the structure to the reflector-absorber.
CHK1	Not used	$\text{CHK1} = \sqrt{A_x/A_z}$.
CHK11	ch. $(k_{11}h_1)$	
CHK2	Not used	$\text{CHK2} = \sqrt{A_x/A_z}\Big/A_x$.
CM	$\Sigma_{n=1}^{N} C_{-n}$ (Eq. 4.2.2; Sec. 4.2)	Complex dimensionless amplitude coefficient corresponding to the superposition of all waveforms within the structure referenced to x = b oriented in the negative direction. $\text{CM} = \Sigma_{n=1}^{N} a_{-n}/a_i$.
CMX	C_{mx} (Eq. 2.2.3; Secs. 2.2 and 5.6)	Added mass coefficient for the x-direction.
CMZ	C_{mz} (Eq. 2.2.4; Secs. 2.2 and 5.6)	Added mass coefficient in the z-direction.
CO	Not used explicitly	The 'coefficient matrix', or 'A' matrix, of the general matrix equation $[A][X] = [B]$. 'CO' is therefore the coefficient matrix corresponding to the system of simultaneous equations given by Eqs. (4.2.2, 4.2.3, 4.2.5, 4.2.6).
CP	$\Sigma_{n=1}^{N} C_{tn}$ (Eq. 4.2.2; Sec. 4.2)	Complex dimensionless amplitude coefficient corresponding to the superposition of all waveforms within the structure referenced to x = -b oriented in the positive direction. $\text{CP} = \Sigma_{n=1}^{N} a_{tn}/a_i$.
CR	$\Sigma_{n=1}^{N} C_{rn}$ (Eq. 4.2.2; Sec. 4.2)	Complex dimensionless amplitude coefficient corresponding to the superposition of all waveforms in Region I referenced to x = -b oriented in the negative direction. $\text{CR} = \Sigma_{n=1}^{N} a_{rn}/a_i$. Since CR is obtained from the

Program Var.	Narrative Var. (Eq. No.; Sec. No.)	Definition
		superposition of <u>all</u> the aforementioned waveforms it includes the evanescent modes as well as the propagating mode. The reflection coefficient defined for the structure in Sec. 1.1 is obtained as the modulus value of the complex quantity C_{r1}. The solutinn values C_{rn} are returned from the complex matrix solution algorithm LEQT1C as the first N values of the 'BM' matrix. The original values of the 'BM' are lost by the matrix solver. Thus the reflection coefficient for the structure with regard to the propagating mode only is found by taking the modulus of BM(1), i.e., $\lvert C_{r1}\rvert \Rightarrow \lvert BM(1)\rvert$.
CRA	C_{RA} (Eq. 4.2.3; Secs. 4.2, 1.1)	Real, known, reflection coefficient of the reflector-absorber.
CT	$\Sigma_{n=1}^{N} C_{Tn}$ (Eq. 4.2.3; Sec. 4.2)	Complex dimensionless amplitude coefficient corresponding to the superposition of <u>all</u> waveforms in Region III referenced to x = b oriented in the positive direction. CT = $\Sigma_{n=1}^{N} a_{Tn}/a_i$. Since CT is obtained from the superposition of all of the aforementioned waveforms, it includes the evanescent modes as well as the propagating modes. The solution values C_{Tn} are returned from the complex matrix solution algorithm LEQT1C as the second N values of the 'BM' matrix. The transmission coefficient as defined in Sec. 1.1 is found as the modulus of the complex quantity BM(N+1), i.e., $\lvert C_{T1}\rvert \Rightarrow \lvert BM(N+1)\rvert$ (see also CR).
C1	Not used	Defined in program for computational expediency in calculating the denominators of f_{xz}, f_{xy}, f_{zx}, f_{zy}.
C2	Not used	
C3	Not used	
C4	Not used	
C5	Not used	
D	Not used	Array values corresponding to k_{1n} and k_{3n} returned as eigenvalue solutions of Eq. (3.1.2) by the Newton-Raphson technique subroutine RAPNEW.
DI	D (Fig. 1.2)	Pile diameter.

Program Var.	Narrative Var. (Eq. No.; Sec. No.)	Definition
DIV	Not used	Either 1/20 or 1/40. Used to determine the number of points between the leeward edge of the structure and the reflector-absorber at which the water surface profile is evaluated.
DLX	dx (Eq. 5.1.15; Sec. 5.1.4)	Delta x increment used in the numerical evaluation of the numerator of Eq. (5.1.15).
DLZ	dz (Eq. 5.1.7; Sec. 5.1.1)	Delta z increment used in the numerical evaluation of the numerator of Eq. (5.1.7).
DX(#)	Not used	One dimensional array containing the x-coordinate of each vertical member within the structural volume defined by $-b \leq x \leq b$, $-h_2 \leq z \leq 0$, $0 \leq y \leq Y$.
E	ϵ (Eq. 2.3.1; Sec. 2.3)	Porosity of the structure.
ELOCAL	ϵ_{local} (see Sec. 3.3.1, Chap. VIII)	Local interfacial porosity for non-homogeneous structures.
EX	ϵ_x (Eq. 2.3.2; Sec. 2.3)	Ratio of the volume of all structural members whose longitudinal axis runs in the x-direction to the total volume of the structure.
EY	ϵ_y (Eq. 2.3.3; Sec. 2.3)	Ratio of the volume of all structural members whose longitudinal axis runs in the y-direction to the total volume of the structure.
EYY	Not used	Computational constant.
EZ	ϵ_z (Eq. 2.3.4; Sec. 2.3)	Ratio of the volume of all vertical structural members to the total structural volume.
FX	f_x (Eq. 2.3.7; Sec. 2.3.1c)	Total dimensionless damping coefficient for the x-direction.
FXNEW	Not used	Recalculated value of FX in iterative solution.
FXY	Numerator of f_{xy} (Eqs. 2.3.6, 5.1.12; Secs. 2.3.1b, 5.1.2)	The numerator of the dimensionless damping coefficient for x-directed flow past y-directed structural members.
FXYY	Not used	Dummy summation variable for calculation of FXY.

Program Var.	Narrative Var. (Eq. No.; Sec. No.)	Definition
FXZ	Numerator of f_{xz} (Eqs. 2.3.5, 5.1.7; Secs. 2.3.1a, 5.1.1)	The numerator of the dimensionless damping coefficient for x-directed flow past vertical structural members.
FZXX	Not used	Dummy summation variable for calculation of FXZ.
FZ	f_z	Total dimensionless damping coefficient for the z-direction.
FZNEW	Not used	Recalculated value of FZ in iterative solution.
FZX	Numerator of f_{zx} (Eqs. 2.3.9, 5.1.15; Secs. 2.3.1e, 5.1.4)	The numerator of the dimensionless damping coefficient for vertical flow past x-directed structural members.
FZXX	Not used	Dummy summation variable for calculation of FZX.
FZY	Numerator of f_{zy} (Eqs. 2.3.8, 5.1.13; Secs. 2.3.1d, 5.1.3)	The numerator of the dimensionless damping coefficient for vertical flow past y-directed structural members.
FZYY	Not used	Dummy summation variable for calculation of FZY.
G	g (Sec. 2.6)	Gravitational acceleration.
HL	Not used	Wave steepness H/L.
H1	h_1 (Fig. 1.1)	Water depth in Region I.
H2	h_2 (Fig. 1.1)	Water depth in Region II.
H3	h_3 (Fig. 1.1)	Water depth in Region III.
I	i (Sec. 2.1)	The imaginary constant; $i = \sqrt{-1}$.
IER	Not used	Error control parameter for the complex matrix solution algorithm LEQTIC.
J	Not used	Do loop integer variable.
K	Not used	Do loop integer variable. Counter variable.
KDIV	Not used	Number of segments an x-directed pile is divided into for the numerical integration of the numerator of Eq. (5.1.15).

Program Var.	Narrative Var. (Eq. No.; Sec. No.)	Definition
K1(#)	k_{1n} (Eqs. 2.8.2, 3.1.2)	Complex column vector array corresponding to one real (propagating mode) and N-1 pure imaginary (evanescent modes) eigenvalue solutions of Eq. (3.1.2) in Region I. Commonly termed as the wave number in Region I.
K1ONE	k_{11} (Eq. 3.2.5; Sec. 3.2.2)	Propagating wave number in Region I.
K2(#)	k_{2n} (Eqs. 2.8.2, 2.10.2; Sec. 2.10)	Complex column vector array corresponding to the N complex eigenvalue solutions of Eq. (2.10.2) in Region II. The wave number in Region II.
K3(#)	k_{3n} (Eqs. 2.8.2, 3.1.2)	Complex column vector array corresponding to one real (propagating mode) and N-1 pure imaginary (evanescent modes) eigenvalue solutions of Eq. (3.1.2) in Region III. The wave number in Region III.
L	Not used	Do loop integer variable.
LEQT1C	Not used	Complex matrix solution subroutine from the International Math Sciences Library numerical programs package.
M	Not used	Do loop integer variable. Counter variable.
N	Not used	Do loop integer variable.
NC	Not used	Number of points at which the water profile in the domain $b \leq x \leq b+c$ is evaluated in the lee of the breakwater.
NDIV	Not used	Number of segments into which a vertical structural member is divided for the numerical integration of the numerator of Eq. (5.1.7).
NMZ	Not used	The number of vertical structural members within the structural volume defined by $-b \leq x \leq b$, $-h_2 \leq z \leq 0$, $0 \leq y \leq Y$, minus 1. Corresponds to the number of longitudinal gaps between the vertical members.
NN	Not used	Do loop integer variable.
NP1	N+1	One plus the value at which the infinite eigen-series is truncated at.

Program Var.	Narrative Var. (Eq. No.; Sec. No.)	Definition
NP2	2N+1	One plus two times the value at which the infinite eigen-series is truncated at.
NP3	3N+1	One plus three times the value at which the infinite eigen-series is truncated at.
NUM	N (Eqs. 4.2.2, 4.2.3, 4.2.5, 4.2.6)	The value at which the infinite eigen-series is truncated. Sufficient accuracy is generally obtained when N is greater than or equal to five.
NX	Not used	The maximum number of x-directed structural members between any two adjacent vertical members. NX always corresponds to the first array bounds number of XD(#) array in the dimension statement.
NXT	Not used	The total number of x-directed structural members within the structural volume defined by $-b \leq x \leq b$, $-h_2 \leq z \leq 0$, $0 \leq y \leq Y$.
NY	Not used	The maximum number of y-directed structural members between any two adjacent vertical members. NY always corresponds to the first array bounds number of the YD array in the dimension statement.
NYT	Not used	The total number of y-directed structural members within the structural volume defined by $-b \leq x \leq b$, $-h_2 \leq z \leq 0$, $0 \leq y \leq Y$.
NZ	Not used	The total number of vertical structural members in the structural volume defined by $-b \leq x \leq b$, $h_2 \leq z \leq 0$, $0 \leq y \leq Y$. NZ always corresponds to the array bounds number of DX array and the second array bounds number of YD in the dimension statement.
N2	2N	Twice the truncation value, N.
N3	3N	Three times the truncation value, N.
N4	4N	Four times the truncation value, N.
PI	π	3.1416

Program Var.	Narrative Var. (Eq. No.; Sec. No.)	Definition
RO	ρ (Eq. 2.1.1; Sec. 2.1)	Fluid density.
RR	Not used	Computational constant used in calculating the denominators of f_{xz}, f_{xy}, f_{zx}, f_{zy}.
SIG	σ (Sec. 2.1)	Incident wave frequency $2\pi/T$.
SM	Not used	Dummy summation variable used for the calculation of SMX.
SMM	Not used	Dummy summation variable used for the calculation of SMZ.
SMX	Not used	The value of the denominators of Eqs. (5.1.7 and 5.1.12) as calculated by Eq. (5.1.11).
SMZ	Not used	The value of the denominators of Eqs. (5.1.13 and 5.1.15) as calculated by Eq. (5.1.14).
SS	Not used	The complex value of free surface displacement in Region III.
SSMAX	Not used	The maximum absolute value of the free surface displacement in Region III. Indicates what the maximum crest or trough displacement is in Region III.
SSR	Not used	The absolute value of the real part of SS.
SSRR(#)	Not used	Array containing the real parts of the complex free surface displacements at several points within the domain of Region III $b \leq x \leq b+c$. The free surface profile can be obtained at any specified time in Region III by plotting the array values versus the x-coordinate.
SX	S_x (Eq. 2.4.3; Sec. 2.4)	Inertial coefficient for the x-direction.
SZ	S_z (Eq. 2.4.4; Sec. 2.4)	Inertial coefficient for the z-direction.
T	T	Wave period.
TT	Not used	Dummy summation variable used in calculating SS.

Program Var.	Narrative Var. (Eq. No.; Sec. No.)	Definition
USM	u_n	Dummy summation variable used in calculating USUM. Also, a particular mode horizontal velocity component.
USUM	$\Sigma_{n=1}^{N} u_n$	The complex horizontal water particle velocity in Region II due to all wave components.
UUU	$U_R^2 + U_I^2$ (Eqs. 5.1.7, 5.1.12)	The product of the spatial function U and its complex conjugate U^* as used in Eqs. (5.1.7 and 5.1.12).
VF	V_f (Sec. 2.3)	The volume of fluid within the structural volume defined by $-b \leq x \leq b$, $-h_2 \leq z \leq 0$, $0 \leq y \leq Y$.
VIS	ν	Fluid kinematic viscosity.
VT	V_T (Sec. 2.3)	Total volume of the structure defined by $-b \leq x \leq b$, $-h_2 \leq z \leq 0$, $0 \leq y \leq Y$.
VX	V_{Sx} (Sec. 2.3)	The total volume of all x-directed structural members within the structural volume defined by $-b \leq x \leq b$, $-h_2 \leq z \leq 0$, $0 \leq y \leq Y$.
VXX	Not used	Dummy summation variable used in calculating VX.
VY	V_{Sy} (Sec. 2.3)	The total volume of all y-directed structural members within the structural volume defined by $-b \leq x \leq b$, $-h_2 \leq z \leq 0$, $0 \leq y \leq Y$.
VZ	V_{Sz} (Sec. 2.3)	The total volume of all vertical structural members within the structural volume defined by $-b \leq x \leq b$, $-h_2 \leq z \leq 0$, $0 \leq y \leq Y$.
WA(#)	Not used	Work area array required by LEQT1C. Must be dimensioned as four times the value NUM.
WL	L	Wavelength.
WSM	w_n	Dummy summation variable used in calculating WSUM. Also a particular mode vertical velocity component.

Program Var.	Narrative Var. (Eq. No.; Sec. No.)	Definition
WSUM	$\Sigma_{n=1}^{N} w_n$	The complex vertical water particle velocity component in Region II due to all wave components.
WWW	$W_R^2 + W_I^2$ (Eqs. 5.1.13, 5.1.15)	The product of the spatial function W and its complex conjugate W^* as used in Eqs. (5.1.13 and 5.1.15).
X	x	The value of the x-coordinate.
XD(#)	Not used	Array containing the values of the z-coordinates, or depths, of each x-directed structural member.
XDST	Not used	The x-distance between any two adjacent vertical structural members.
XMAX	Not used	The value of the x-coordinate at which the maximum (absolute) value of the water surface displacement in Region III occurs.
Y	Y (Eqs. 5.1.7, 5.1.12, 5.1.13; Fig. 6.2)	The lateral, or y-distance over which the structural configuration regularly repeats itself (see Fig. 6.2).
YD(#)	Not used	Array containing the value of the z-coordinates, or depths, of each y-directed structural member.
Z	z	The value of the z-coordinate.
ZT	ζ (Eq. 3.3.8; Sec. 3.3.1)	$\zeta = \dfrac{-i\sigma\epsilon\sqrt{A_x/A_z}}{A_x}$.
999.9	Not used	This value is read into the XD(#) or YD(#) arrays to inform the program of the portions of these arrays which are not filled by members of the structural configuration. For example, there are four vertical piles in Fig. 1.1 and the maximum number of x-directed members between any two adjacent vertical members is also four. Hence the XD(#) array would be dimensioned as XD(4, 3). This indicates that there can be as many as four x-directed members in the three spaces between the vertical members. In the first space

Program Var.	Narrative Var. (Eq. No.; Sec. No.)	Definition
		there four members and four XD( ) depths are read in. In the next space only two equivalent x-members exist and thus only two XD(#) depths are read in and two 999.9 values are read in. Similarly, one 999.9 value is used for the last space since only three x-members exist (see also Fig. 6.2 and Sec. 6.1.1).

Function Subprogram; CH(A,R)

CH(A,R)	ch.(AR) (Eq. 2.8.9)	Hyperbolic cosine of the complex argument A × R.
A	k_{mn}	The complex wave number referred from the main program (R.M.P.).
R	h_m	The water depth R.M.P.

Function Subprogram; SH(N,A,R)

SH(N,A,R)	sh.(NAR) (Sec. 2.10)	Hyperbolic sine of the complex argument N × A × R.
A	k_{mn}	The complex wave number R.M.P.
N	1 or 2	Integer value, either unity or two, R.M.P.
R	h_m	The water depth R.M.P.

Function Subprogram; TH(N,A,R)

TH(N,A,R)	th.(NAR) (Sec. 2.10)	Hyperbolic of tangent of the complex argument N × A × R.
A	k_{mn}	The complex wave number R.M.P.
N	1	The integer value of unity R.M.P.
R	h_m	The water depth R.M.P.

Program Var.	Narrative Var. (Eq. No.; Sec. No.)	Definition
Function Subprogram; EQ(A, B, C, D)		
EQ(A, B, C, D)	$EQ = \left[\frac{A\ ch.(BC)sh.(AD) - B\ ch.(AD)sh.(BC) - A\ sh.A(D-C)}{(ch.(BC))(A^2-B^2)} \right]$ (Eqs. 4.2.2, 4.2.3).	
A	k_{1m} or k_{3m}	The complex wave number for Region I (Eq. 4.2.2) or Region III (Eq. 4.2.3) R.M.P.
B	k_{2n}	The complex wave number for Region II R.M.P.
C	h_2	The water depth in Region II R.M.P.
D	h_1 or h_3	The water depth in Region I (Eq. 4.2.2) or Region III (Eq. 4.2.3) R.M.P.
Function Subprogram; EQQ(A, B, C, D)		
EQQ(A, B, C, D)	$EQQ = \left[\frac{A\ ch.(BC)sh.(AD) - B\ ch.(AD)sh.(BC) + B\ sh.B(C-D)}{(ch.(BC))(A^2-B^2)} \right]$ (Eqs. 4.2.5, 4.2.6)	
A	k_{2m}	The complex wave number for Region II R.M.P.
B	k_{1n} or k_{3n}	The complex wave number for Region I (Eq. 4.2.5) or Region III (Eq. 4.2.6) R.M.P.
C	h_1 or h_3	The water depth in Region I (Eq. 4.2.5) or Region III (Eq. 4.2.6) R.M.P.
D	h_2	The water depth in Region III.
Function Subprogram; QQ(A, B)		
QQ(A, B)	$QQ = [sh.(2AB) + (2AB)]$ (Eqs. 4.2.2, 4.2.3, 4.2.5, 4.2.6).	
A	k_{mn}	The complex wave number R.M.P.
B	h_m	The water depth R.M.P.

Program Var.	Narrative Var. (Eq. No.; Sec. No.)	Definition

Function Subprogram; EE(K)

EE(K)	$EE = \exp[i2bk\sqrt{A_x/A_z}]$ (Eqs. 4.2.2, 4.2.3, 4.2.5, 4.2.6).	
K	k_{2n} or k_{2m}	The complex wave number for Region II R. M. P.
AXAZ,P,Q,R,S	Not used	Used in determining the sign of the complex square root of A_x/A_z so that wave decay occurs (see Appendix A).

Function Subprogram; CC(A)

CC(A)	A^*	Complex conjugate of the argument 'A' R. M. P.

Function Subprogram; U(CP,CM,X,Z,TM,K,H)

U(CP,CM,X,Z, K,H)	U(x,z) (Sec. 5.1.1)	A single mode of the horizontal spatial velocity function U(x, z) defined in Sec. 5.1.1 for the analytical temporal integrations required in evaluating f_{xz}, f_{xy}.
CP	C_{+n}	The dimensionless amplitude coefficient of the n^{th} modal waveform in Region II referenced to x = -b and oriented in the positive x-direction R. M. P.
CM	C_{-n}	The dimensionless amplitude coefficient on the n^{th} modal waveform in Region II referenced to x = b and oriented in the negative x-direction R. M. P.
X	x	The value of the x-coordinate R. M. P.
Z	z	The value of the z-coordinate R. M. P.
K	k_{2n}	The complex wave number for Region II R. M. P.
H	h_2	The water depth for Region II R. M. P.

Program Var.	Narrative Var. (Eq. No.; Sec. No.)	Definition
Function Subprogram; W(CP, CM, X, Z, TM, K, H)		
W(CP, CM, X, Z, K, H)	W(x, z) (Sec. 5.1.3)	A single mode of the vertical spatial velocity function W(x, z) defined in Sec. 5.1.3 for the analytical temporal integrations required in evaluating f_{zy}, f_{zx}.
CP, CM, X, Z, K, H	See definitions for U(CP, CM, X, Z, K, H).	
Subroutine Subprogram; RAPNEW(D, NUM, H, SIG, G, PI)		
RAPNEW(D, NUM, H, SIG, G, PI)	Not used	Newton-Raphson technique algorithm calculating the one real (first mode, n = 1) wave number and the N-1 pure imaginary wave number ($2 \leq n \leq N-1$) solutions of Eq. (3.1.2) in Region I and III.
D(#)	Not used	Array in which the calculated wave numbers for all N wave modes are stored before being returned to the main program. All the values D(#) are strictly real and thus D ($2 \leq n \leq N-1$) must be multiplied by i after being returned to the main program.
H	h_1 or h_3	Water depth in Region I or Region III.
NUM, SIG, G, PI	See Main Program definitions.	
Subroutine Subprogram; CMPLK2(K2, NUM, H, SIG, SZ, FZ, G, PI, I)		
CMPLK2(K2, NUM, H, SIG, SZ, FZ, G, PI, I)	Not used	Newton-Raphson technique algorithm calculating the first 15 complex wave number solutions of Eq. (2.10.2) in Region II.
AA	Not used	Initial estimate of the imaginary portion of $(k_{2n} \times h_2)$ for the Newton Raphson iterative solution technique when n > 5. For example, $\mathrm{Imag}(k_{26}h_2) \simeq \mathrm{Imag}(k_{25}h_2) + 3.2$.
CS(E)	ch. (E)	Complex hyperbolic cosine function.
KA	Not used	Dummy variable used to retain the previous iteration value of $(k_{2n}h_2)$.

Program Var.	Narrative Var. (Eq. No.; Sec No.)	Definition
DIMSIG(#)	TAPE1 values of $S_z a^2 h_2/g$	One dimensional array values of the dimensionless angular wave frequency stored on TAPE1.
F	Not used	Dummy variable used to check the convergence of the iterative values of $\{k_{2n}h_2\}$. 'F' corresponds to the real portion of the previous iteration value of $\{k_{2n}h_2\}$. Used in conjunction with 'FF'.
FF	Not used	Used in conjunction with 'F'. 'FF' corresponds to the real portion of the current iteration value of $\{k_{2n}h_2\}$. The ratio of F/FF must be close to unity for convergence.
FZ	f_z	Total dimensionless damping coefficient for the z-direction R.M.P.
FZSZ(#)	TAPE1 values of f_z/S_z	One dimensional array values of the vertical direction damping coefficient divided by the vertical direction inertial coefficient. FZSZ values are stored on TAPE1.
G	g	Gravitational acceleration R.M.P.
GA	Not used	Dummy variable used to check the convergence of the iterative values of $\{k_{2n}h_2\}$. 'GA' corresponds to the imaginary portion of the previous iteration value of $\{k_{2n}h_2\}$. Used in conjunction with 'GG'.
GG	Not used	Used in conjunction with 'GA'. 'GG' corresponds to the imaginary portion of the current iteration value of $\{k_{2n}h_2\}$. The ratio GA/GG must be close to unity for convergence.
GM	Not used	Initial estimate of the real portion of $\{k_{2n}h_2\}$ for the Newton-Raphson iterative solution technique when n > 5.
H	h_2	The water depth in Region II R.M.P.
I	i	The imaginary number, $\sqrt{-1}$, R.M.P.
J	Not used	Do loop integer variable.

Program Var.	Narrative Var. (Eq. No.; Sec. No.)	Definition
KH(#)	$k_{2n}h_2$	Complex array containing the 15 solution values $(k_{2n}h_2)$.
KHH	Not used	The value of $(k_{2n}h_2)$ corresponding to the TAPE1 value of DIMSIG that is just above the design value of $S_z\sigma^2h_2/g$ and interpolated between the TAPE1 values of FZSZ just above and just below the design value of f_z/S_z. Used in conjunction with KHL to yield an initial estimate of $(k_{2n}h_2)$ for $n \leq 5$.
KHL	Not used	The value of $(k_{2n}h_2)$ corresponding to the TAPE1 value of DIMSIG that is just below the design value of $S_z\sigma^2h_2/g$ and interpolated between the TAPE1 values of FZSZ just above and just below the design value of f_z/S_z.
KK(#)	Not used	The array in which the values of $(k_{2n}h_2)$ read from TAPE1 are stored.
K2(#)	k_{2n}	The solution values, k_{2n}, of Eq. (2.10.2) returned to the main program.
L	Not used	Do loop integer variable.
M	Not used	Do loop integer variable.
N	Not used	Do loop integer variable.
NUM	N	The value at which the infinite eigen-series are truncated R. M. P. Sufficient accuracy is generally obtained for values N between five and ten although CMPLK2 will calculate the first 15 values of k_{2n} should increased accuracy be desired.
PI	π	3.1416 R. M. P.
REDMSG	$S_z\sigma^2h_2/g$	The design value of $S_z\sigma^2h_2/g$.
REFZSZ	f_2/S_z	The design value of f_z/S_z.
SIG	σ	Incident wave frequency R. M. P.
SZ	S_z	Inertial coefficient for the z-direction R. M. P.
TA(B)	th. (B)	Complex hyperbolic tangent function.

Program Var.	Narrative Var. (Eq. No.; Sec. No.)	Definition
K	Not used	Do loop integer variable.
TAPE1	Not used	Binary file storing the first five solutions $\{k_{2n}h_2\}$ satisfying Eq. (2.10.2) for 35 different values of $S_z\sigma^2 h_2/g$ and 25 different values of f_z/S_z. The value of $S_z\sigma^2 h_2/g$ is stored first and is followed by the value of f_z/S_z and thence by the five values $\{k_{2n}h_2\}$ corresponding to these values of $s_z\sigma^2 h_2/g$ and f_z/S_z. Following that, a new value of f_z/S_z is stored and then the corresponding five values of $\{k_{2n}h_2\}$. This is repeated until all 25 values of f_z/S_z and the values of $\{k_{2n}h_2\}$ corresponding to them and the initial value of $S_z\sigma^2 h_2/g$ are stored. The process is then repeated for new values of $S_z\sigma^2 h_2/g$ until all 35 values of $S_z\sigma^2 h_2/g$ are used. The values of $\{k_{2n}h_2\}$ stored on TAPE1 are used to generate the initial estimates for the first five modal wave number solutions, k_{2n}, from CMPLK2. Examples of listing from TAPE1 are shown in Appendix E.

APPENDIX D

This appendix provides a program listing for the analysis of simple harmonic waves normally incident upon a pile matrix structure.

PROGRAM PILE1

```
      PROGRAM PILE 1 (INPUT,OUTPUT,TAPE1,TAPE5=INPUT,TAPE6=OUTPUT)
      COMPLEX    K1(05),K2(05),K3(05),GG(20,20),BM(20),
     $QQ,EE,SH,TH,CH,GG,EQQ,EQ,BT,ZT,AZ,AX,I,CR,CT,CP,CM,SS,TT,
     $SMX,SM,SMZ,SMM,U,W,USUM,USM,WSUM,WSN,K1ONE,CHK1,CHK2,
     $RR,A1,A2,A3,A4,A5,A6,A7,B1,B2,B3,B4,B5,B6,C1,C2,C3,C4
      DIMENSION D(05),WA(20),DX(09),YD(10,09),XD(10,08),SSRR(41)
      COMMON I,B,AX,AZ,K1ONE,H1,AMP,SIG,G
C
C     INPUT,THE LONG. HALF-WIDTH=B,WATER DEPTHS IN REGIONS 1,2,3=H1,H2,
C     H3,PILE DIAMETER=DI,REF.COEF. OF REFLECTOR-ABSORBER=CRA,DIST FROM
C     REF.-ABSRB. TO STRUCT.=C,LATERAL REPEATING DIST.=Y.
C
      READ(5,20) B,H1,H2,H3,DI,CRA,C,Y
   20 FORMAT(8F10.4)
C
C     INPUT,GRAV. ACCEL=G,DRAG COEF. CONSTANTS=AL,BET,
C     KINEMATIC VISCOSITY=VIS,HORIZ.,VERT. ADDED MASS COEFF.=CMX,CMZ,
C     FLUID DENSITY=RO.
C
      READ(5,30) G,AL,BET,VIS,CMX,CMZ,RO
   30 FORMAT(F6.3,2F4.2,E9.3,2F4.2,F8.3)
C
C     INPUT, MAX. NO.OF X,Y-MEMBERS  BTWN. TWO ADJACECT Z-MBR=NX,NY,
C     TOTAL NO. OF Z-MBR=NZ,EIGENSERIES TRUNCATION NO.=NUM,
C     TOTAL NO. OF X,Y-MBR=NXT,NYT
C
      READ(5,40) NX,NY,NZ,NUM,NXT,NYT
   40 FORMAT(4I2,2I4)
C
C     INITIALIZE X,Z-DIMENSIONLESS DAMPING COEFFS.=FX,FZ.
C
      FX=1.0
      FZ=.5
      NMZ=NZ-1
C
C     CALCULATE MATRIX LOADING SECTION NO. =NP1,NP2,NP3,N2,N3,N4
C
      NP1=NUM+1
      NP2=2*NUM+1
      NP3=3*NUM+1
      N2=2*NUM
      N3=3*NUM
      N4=4*NUM
C
C     INPUT DEPTHS OF ALL Y-MBR STARTING AT TOP SEAWARD EDGE AND GOING
C     ACROSS=YD(L,J).
C
      DO 42 L=1,NY
      READ(5,46) (YD(L,J),J=1,NZ)
   46 FORMAT(8F10.6)
   42 CONTINUE
C
C     INPUT DEPTHS OF ALL X-MBR STARTING AT TOP SEAWARD EDGE AND GOING
C     ACROSS=XD(L,J)
C
      DO 52 L=1,NX
      READ(5,46) (XD(L,J),J=1,NMZ)
   52 CONTINUE
C
C     INPUT X-COORD OF ALL Z-MBR=DX(L)
C
      READ(5,46) (DX(L),L=1,NZ)
      WRITE(6,53) (YD(1,J),J=1,NZ,6)
      WRITE(6,53) (XD(1,J),J=1,NZ,6)
      WRITE(6,53) (DX(J)   ,J=1,NZ,6)
   53 FORMAT(6F10.6//)
C
C     CALCULATE STRUCTURAL VOLUME=VT
C
      VT=2*B*H2*Y
      PI=3.1416
C
C     CALCULATE VOLUME OF ALL X-MBR=VX
C
      VXX=0.
      VX=0.
      DO 561 L=1,NX
```

PROGRAM PILE1

```
          DO 662 J=1,NMZ
          IF(XO(L,J).EQ.999.9) GO TO 662
          VXA=((DI/2.)**2)*PI*ABS(DX(J)-DX(J+1))
          VA=VX+VXA
      662 CONTINUE
      661 CONTINUE
C
C         CALCULATE VOLUME OF ALL Z-MBR=VZ
C
          VZ=((DI/2)**2)*PI*H2*NZ
C
C         CALCULATE VOLUME OF ALL Y-MBR=VY
C
          VY=((DI/2)**2)*PI*NYT*Y
C
C         CALCULATE VOLUME OF FLUID IN STRUCTURE=VF
C
          VF=VT-(VX+VY+VZ)
C
C         CALCULATE STRUCTURAL POROSITY=E
C
          E=VF/VT
C
C         CALCULATE RATIO OF X,Y,Z-MBR VOL. TO STRUCTURAL VOL. =EX,EY,EZ
C
          EX=VX/VT
          EY=VY/VT
          EZ=VZ/VT
C
C         DEFINE I=SQUARE ROOT OF (-1)
C
          I=CMPLX(0.0,1.0)
          NOIV=16
C
C         DEFINE DELTA-Z INCREMENT FOR NUMER. INTEGRATION=DLZ
C
          DLZ=H2/NDIV
C
C         CALCULATE X,Z INERTIAL COEFF.=SX,SZ
          SX=1+(CMX*(EY+EZ)/E)
          SZ=1+(CMZ*(EY+EX)/E)
C
C         INPUT, WAVE PERIOD=T, WAVE AMPLITUDE=AMP.
C
       12 READ(5,10) T, AMP
       10 FORMAT(2F10.7)
C
C         CALCULATE WAVE FREQUENCY=SIG
C
          SIG=2*PI/T
C
C         CALL RAPNEW TO CALCULATE WAVE.NO. IN REGION 1=K1(J)
C
          CALL RAPNEW(D,NUM,H1,SIG,G,PI)
          K1(1)=CMPLX(D(1),0.0)
          K1ONE=K1(1)
          IF(NUM.LT.2) GO TO 627
          DO 51 J=2,NUM
          K1(J)=CMPLX(0.0,D(J))
       51 CONTINUE
      627 CONTINUE
C
C         CALL RAPNEW TO CALCULATE WAVE NO. IN REGION 3=K3(J)
C
          CALL RAPNEW(D,NUM,H3,SIG,G,PI)
          K3(1)=CMPLX(D(1),0.0)
          IF(NUM.LT.2) GO TO 628
          DO 81 J=2,NUM
          K3(J)=CMPLX(0.0,D(J))
       81 CONTINUE
      628 CONTINUE
C
C         DEFINE CHK11=HYPERB. COSINE OF (K1(1)*H1)
C
          CHK11=CH(K1(1),H1)
          WRITE(6,611)AMP,T,D,H1,H2,H3,DI,CRA,C,Y
      611 FORMAT(10F10.5)
```

PROGRAM PILE1

```
      WRITE(6,612)G,AL,BET,CMX,CMZ,RO,VIS,NX,NY,NZ,NUM,NXT,NYT
  612 FORMAT(6F8.4,E11.3,6I6)
      WRITE(6,613)VT,VX,VY,VZ,VF,PI,E,EX,EY,EZ
  613 FORMAT(10F12.3)
      WRITE(6,614)SIG,SX,SZ,I,DLZ,NOIV
  614 FORMAT(6F10.5,I4)
      WRITE(6,24)  (K1(K),K=1,NUM)
      WRITE(6,24)  (K3(K),K=1,NUM)
   24 FORMAT(2F10.5)
   82 CONTINUE
      WRITE(6,664) FX,FZ
  664 FORMAT(1H-, *THE NEW FRICTION FACTORS ARE , FX=*,F11.8,5X,*FZ=*,
     $F11.8////)
C
C     CALL CMPLK2 TO CALCULATE WAVE NO. IN REGION 2=K2(J)
C
      CALL CMPLK2(K2,NUM,N2,SIG,SZ,FZ,G,PI,I)
      WRITE(6,24)  (K2(K),K=1,NUM)
      AX=FX*SIG-(I*SIG*SX)
      AZ=FZ*SIG-(I*SIG*SZ)
      CHK1=CSQRT(AX/AZ)
      CHK2=CHK1/AX
C
C     SET LOCALIZED INTERFACIAL POROSITY=ELOCAL. MAY BE SET DIFFERENT
C     FROM STRUCTURAL POROSITY FOR NON-HOMOGENEOUS STRUCTURES
C
      ELOCAL=E
C
C     CALCULATE BETA AND ZETA CONSTANTS=BT,ZT
C
      BT=-I*SIG*(CSQRT((AX/AZ)))+(ELOCAL          )/AX
      ZT=-I*SIG*(CSQRT((AX/AZ)))+(ELOCAL          )/AX
      WRITE(6,653) AX,AZ,CHK1,CHK2,BT,ZT
  653 FORMAT(12F10.6)
   84 CONTINUE
C
C     BEGIN*B*MATRIX,BM(J),LOADING SEQUENCE STARTING WITH EQ.4.2.2,THEN
C     EQ.4.2.5, EQ.4.2.3 AND EQ.4.2.6
C
      BM(1)=CMPLX(1.,0.)
      M=1
      IF(NUM.LT.2) GO TO 629
      DO 50 J=2,NUM
      M=M+1
      BM(M)=CMPLX(0.,0.)
   50 CONTINUE
  629 CONTINUE
      DO 60 J=1,NUM
      M=M+1
      BM(M)=CMPLX(1.,0.)
   60 CONTINUE
      DO 70 J=1,NUM
      M=M+1
      BM(M)=CMPLX(0.,0.)
   70 CONTINUE
      DO 80 J=1,NUM
      M=M+1
      BM(M)= CMPLX(0.,0.)
   80 CONTINUE
C
C     END *B* MATRIX LOADING SEQUENCE
C
C     BEGIN COEFFICIENT MATRIX,CO(L,J),LOADING SEQUENCE
C     LOAD ZERO COEF. OF CT FROM EQ.4.2.2 AND EQ.4.2.5
C
      DO 90 J=NP1,N2
      DO 100 L=1,N2
      CO(L,J)=CMPLX(0.,0.)
  100 CONTINUE
   90 CONTINUE
C
C     LOAD ZERO COEF. OF CR FROM EQ.4.2.3 AND EQ.4.2.6
C
      DO 110 J=1,NUM
      DO 120 L=NP2,N4
      CO(L,J)=CMPLX(0.,0.)
  120 CONTINUE
```

PROGRAM PILE1

```
  110 CONTINUE
C     LOAD COEF. OF CR FROM EQ. 4.2.2
      DO 130 J=1,NUM
      DO 140 L=1,NUM
      IF (L.EQ.J) GO TO 135
      CO(L,J)=CMPLX(0.,0.)
      GO TO 140
  135 CO(L,J)=CHK11*QQ(K1(J),M1)/(CH(K1(J),M1)*QQ(K1(1),M1))
  140 CONTINUE
  130 CONTINUE
C
C     LOAD COEF. OF CR FROM EQ. 4.2.5
C
      M=0
      DO 150 L=NP1,N2
      M=M+1
      DO 160 J=1,NUM
      CO(L,J)=-1.                    *EQQ(K2(M),K1(J),M1,M2)/
     $EQQ(K2(M),K1(1),M1,M2)
  160 CONTINUE
  150 CONTINUE
C
C     LOAD COEF. OF CT FROM EQ. 4.2.3
C
      K=0
      M=0
      DO 170 J=NP1,N2
      M=M+1
      K=0
      DO 180 L=NP2,N3
      K=K+1
      IF(K.EQ.M) GO TO 175
      CO(L,J)=CMPLX(0.,0.)
      GO TO 180
  175 CO(L,J)=(1.- CRA*CEXP(I*K3(K)*2.*C))*CHK11*QQ(K3(K),M3)/(CH(K3(K),
     $M3)*QQ(K1(1),M1))
  180 CONTINUE
  170 CONTINUE
C
C     LOAD COEF. OF CT FROM EQ. 4.2.6
C
      K=0
      M=0
      DO 190 L=NP3,N4
      M=M+1
      K=0
      DO 200 J=NP1,N2
      K=K+1
      CO(L,J)=4.*CHK11*EQQ(K2(M),K3(K),M3,M2)*(1+CRA*CEXP(I*K3(K)*2.*C))
     $/QQ(K1(1),M1)
  200 CONTINUE
  190 CONTINUE
C
C     LOAD COEF. OF C+ FROM EQ. 4.2.2
C
      K=0
      M=0
      DO 210 L=1,NUM
      M=M+1
      K=0
      DO 220 J=NP2,N3
      K=K+1
      CO(L,J)=4.*ST*CHK11*K2(K)*EQ(K1(M),K2(K),M2,M1)/QQ(K1(1),M1)
  220 CONTINUE
  210 CONTINUE
C
C     LOAD COEF. OF C+ FROM EQ. 4.2.5
C
      K=0
      M=0
      DO 230 L=NP1,N2
      M=M+1
      K=0
      DO 240 J=NP2,N3
      K=K+1
      IF(K.EQ.M) GO TO 235
      CO(L,J) =CMPLX(0.,0.)
```

PROGRAM PILE1

```
      GO TO 240
  235 CO(L,J)=                   QQ(K2(M),M2)/(K2(M)*CH(K2(M),M2)*
     $4.*EQQ(K2(M),K1(1),M1,M2))
  240 CONTINUE
  230 CONTINUE
C
C     LOAD COEF. OF C+ FROM EQ. 4.2.3
C
      K=0
      M=0
      DO 250 L=NP2,N3
      M=M+1
      K=0
      DO 260 J=NP2,N3
      K=K+1
      CO(L,J)=-4.*ZT*CHK11*K2(K)*EE(K2(K))*EQ(K3(M),K2(K),M2,M3)/
     $QQ(K1(1),M1)
  260 CONTINUE
  250 CONTINUE
C
C     LOAD COEF. OF C+ FROM EQ. 4.2.6
C
      K=0
      M=0
      DO 270 L=NP3,N4
      M=M+1
      K=0
      DO 280 J=NP2,N3
      K=K+1
      IF(K.EQ.M) GO TO 275
      CO(L,J) =CMPLX(0.,0.)
      GO TO 280
  275 CO(L,J)=-CHK11*QQ(K2(M),M2)*EE(K2(M))/(QQ(K1(1),M1)
     $*K2(M)*CH(K2(M),M2))
  280 CONTINUE
  270 CONTINUE
C
C     LOAD COEF. OF C- FROM EQ. 4.2.2
C
      K=0
      M=0
      DO 290 L=1,NUM
      M=M+1
      K=0
      DO 300 J=NP3,N4
      K=K+1
      CO(L,J)=-4.*BT*CHK11*K2(K)*EE(K2(K))*EQ(K1(M),K2(K),M2,M1)/
     $(QQ(K1(1),M1))
  300 CONTINUE
  290 CONTINUE
C
C     LOAD COEF. OF C- FROM EQ. 4.2.5
C
      K=0
      M=0
      DO 310 L=NP1,N2
      M=M+1
      K=0
      DO 320 J=NP3, N4
      K=K+1
      IF(K.EQ.M) GO TO 315
      CO(L,J) =CMPLX(0.,0.)
      GO TO 320
  315 CO(L,J)=                   EE(K2(M))*QQ(K2(M),M2)/(K2(M)*CH(K2(M),M2)
     $*4.*EQQ(K2(M),K1(1),M1,M2))
  320 CONTINUE
  310 CONTINUE
C
C     LOAD COEF. OF C- FROM EQ. 4.2.3
C
      K=0
      M=0
      DO 330 L=NP2,N3
      M=M+1
      K=0
      DO 340 J=NP3,N4
      K=K+1
```

PROGRAM PILE1

```
      CO(L,J)=4*ZT*CHK11*K2(K)*EQ(K3(M),K2(K),H2,H3)/QQ(K1(1),H1)
  340 CONTINUE
  330 CONTINUE
C
C     LOAD COEF. OF C- FROM EQ. 4.2.6
C
      K=0
      M=0
      DO 350 L=NP3,N4
      M=M+1
      K=0
      DO 360 J=NP3,N4
      K=K+1
      IF(K.EQ.M) GO TO 355
      CO(L,J) =CMPLX(0.,0.)
      GO TO 360
  355 CO(L,J)=-CHK11*QQ(K2(M),H2)/(K2(M)*CH(K2(M),H2)*QQ(K1(1),H1))
  360 CONTINUE
  350 CONTINUE
C
C     END LOADING SEQUENCE FOR COEF. MATRIX. TRANSFER CO(L,J) AND BM(L)
C     TO MATRIX SOLUTION SUBROUTINE LEQT1C.
C
      CALL LEQT1C(CO,N4,N4,BM,1,N4,0,WA,IER)
C
C     LEQT1C RETURNS SOLUTIONS CR,CT,C+,C-,IN 1ST,2ND,3RD,AND 4TH NUM
C     INCREMENTS OF BM(L). ORIGINAL BM(L) ARRAY IS LOST.
C
      WRITE(6,650) (BM(J),J=1,N4)
  650 FORMAT(2E14.5)
C
C     CALCULATE COMPLEX REF.  COEF. FOR ALL WAVE MODES
C
      CR=CMPLX(0.,0.)
      DO 370 J=1,NUM
      CR=CR+BM(J)
  370 CONTINUE
C
C     CALCULATE COMPLEX TRANS.COEF. FOR ALL WAVE MODES
C
      CT=CMPLX(0.,0.)
      DO 380 J=NP1,N2
      CT=CT+BM(J)
  380 CONTINUE
C
C     CALCULATE COMPLEX C+    COEF. FOR ALL WAVE MODES
C
      CP=CMPLX(0.,0.)
      DO 390 J=NP2,N3
      CP=CP+BM(J)
  390 CONTINUE
C
C     CALCULATE COMPLEX C- COEF. FOR ALL WAVE MODES
C
      CM=CMPLX(0.,0.)
      DO 400 J=NP3,N4
      CM=CM+BM(J)
  400 CONTINUE
C
C     CALCULATE CONSTANTS RR, A1-A7,B1-B6,C1-C3, USED FOR COMPUTATION OF
C     EQ.5.1.11=SMX AS THE DENOMINATORS OF THE DIMENSIONLESS HORIZ.
C     DAMPING FACTORS GIVEN BY EQS.5.1.7 AND 5.1.12, AND USED TO COMPUTE
C     EQ.5.1.14=SMZ AS THE DENOMINATORS OF THE DIMENSIONLESS  VERT.
C     DAMPING FACTORS GIVEN BY EQS.5.1.13 AND 5.1.15   .
C
      RR=-I*2.*E*Y *(G**2)*PI
      SMZ=CMPLX(0.,0.)
      SMX=CMPLX(0.,0.)
      DO 410 M=1,NUM
      DO 409 N=1,NUM
      IF(AIMAG(CHK1).LT.0. .AND.REAL(CHK1)*AIMAG(K2(N)).LT.
     $ABS(AIMAG(CHK1))*REAL(K2(N))) CHK1=-CHK1
      A4=CC(K2(M))
      A1=CH(K2(N),H2)
      A2=CH(A4,H2)
      A3=K2(N)*A4 /(A1*A2)
      A5=SH(1,A4,H2)
```

PROGRAM PILE1

```
      A6=SH(1,K2(N),H2)
      A7=(A4**2)-(K2(N)**2)
      B1=K2(N)*CHK1
      B2=A4*CC(CHK1)
      B4=B1-B2
      B3=(CEXP(I*2.*B*B4)-1.)/B4
      B5=B1+B2
      B6=(CEXP(-I*2.*B*B2)-CEXP(I*2.*B*B1))/B5
      C5=AMP**2
      C1=C5*BM(N2+M)*CC(BM(N2+M))*B3
      C2=C5*BM(N2+M)*CC(BM(N3+M))*B6
      C3=C5*BM(N3+M)*CC(BM(N2+M))*B6
      C4=C5*BM(N3+M)*CC(BM(N3+M))*B3
      SM=RR*CHK1*(CC(CHK1)/(AX*CC(AX)))*A3*((A4*A1*A5-K2(N)*A2*A6)
     $/A7)*(C1+C2+C3+C4)
      SMX=SMX+SM
      SMM=(RR/(AZ*CC(AZ)))*A3*((A4*A6*A2-K2(N)*A5*A1)/A7)*(C1-C2-C3+C4)
      SMZ=SMZ+SMM
      IF(AIMAG(CHK1).LT.0. .AND.REAL(CHK1)*AIMAG(K2(N)).LT.
     $ABS(AIMAG(CHK1))*REAL(K2(N))) CHK1=-CHK1
  409 CONTINUE
  410 CONTINUE
C
C     END COMPUTATION OF SMX, SMZ.
C
C     BEGIN NUMERICAL INTEGRATION SEQUENCE FOR NUMERATOR OF
C     EQ.3.1.12=FXY
C
      FXY=0.
      DO 430 L=1, NY
      DO 440 J=1,NZ
      IF(YD(L,J).EQ.999.9) GO TO 440
C
C     CALCULATE HORIZ. VELOC. SPATIAL FUNC. FOR ALL WAVE MODES=USUM
C
      USUM=CMPLX(0.,0.)
      DO 460 M=1,NUM
      USM=U(BM(N2+M),BM(N3+M),DX(J),YD(L,J),K2(M),H2)
      USUM=USUM+USM
  460 CONTINUE
C
C     CALCULATE HORIZ. VELOC. SPATIAL FUNC. TIMES ITS COMPLEX CONJUGATE
C
      UUU= ((REAL(USUM))**2)+((AIMAG(USUM))**2)
      FXYY= Y   *(AL*VIS*(T/2.)*UUU+DI*BET*(4./3.)*(T/PI)*(UUU**1.5))
      FXY=FXYY+FXY
  440 CONTINUE
  430 CONTINUE
C
C     END CALCULATION OF FXY
C
C     BEGIN NUMERICAL INTEGRATION SEQUENCE FOR NUMERATOR OF
C     EQ.3.1.7 =FXZ
C
      FXZ=0.
      DO 470 J=1,NZ
      IF (DX(J).EQ.999.9) GOTO 470
      Z=DLZ/2
      DO 480 L=1,NDIV
      Z=Z-DLZ
C
C     CALCULATE HORIZ. VELOC. SPATIAL FUNC. FOR ALL WAVE MODES=USUM
C
      USUM= CMPLX(0.,0.)
      DO 500 M=1,NUM
      USM=U(BM(N2+M),BM(N3+M),CX(J),Z,K2(M),H2)
      USUM=USUM+USM
  500 CONTINUE
C
C     CALCULATE HORIZ. VELOC. SPATIAL FUNC. TIMES ITS COMPLEX CONJUGATE
C
      UUU= ((REAL(USUM))**2)+((AIMAG(USUM))**2)
      FXZZ=    DLZ*(AL*VIS*(T/2.)*UUU+DI*BET*(4./3.)*(T/PI)*(UUU**1.5))
      FXZ=FXZ+FXZZ
  480 CONTINUE
  470 CONTINUE
```

PROGRAM PILE1

```
C         END CALCULATION OF FXZ
C
C         CALCULATE NEW TOTAL HORIZ. DIMENSIONLESS DAMPING COEF.=FXNEW
C
          FXNEW=(FXZ+FXY)/SMX
C
C         BEGIN NUMERICAL INTEGRATION SEQUENCE FOR NUMERATOR OF
C         EQ.5.1.13=FZY
C
          FZY=0.
          DO 510 L=1,NY
          DO 520 J=1,NZ
          IF(YO(L,J).EQ.999.9) GO TO 520
C
C         CALCULATE VERT.  VELOC. SPATIAL FUNC. FOR ALL WAVE MODES=WSUM
C
          WSUM=CMPLX(0.,0.)
          DO 540 M=1,NUM
          WSM=W(BM(N2+M),BM(N3+M),DX(J),YO(L,J),K2(M),H2)
          WSUM=WSUM+WSM
      540 CONTINUE
C
C         CALCULATE VERT.  VELOC. SPATIAL FUNC. TIMES ITS COMPLEX CONJUGATE
C
          WWW= ((REAL(WSUM))**2)+((AIMAG(WSUM))**2)
          FZYY= Y*   (AL*VIS*(T/2.)*WWW+DI*BET*(4./3.)*(T/PI)*(WWW**1.5))
          FZY=FZY+FZYY
      520 CONTINUE
      510 CONTINUE
C
C         END CALCULATION OF FZY
C
C         BEGIN NUMERICAL INTEGRATION SEQUENCE FOR NUMERATOR OF
C         EQ.5.1.15=FZX
C
          FZX=0.
          DO 550 L=1,NX
          DO 560 J=1,NMZ
          IF(XO(L,J).EQ.999.9) GO TO 560
C
C         CALCULATE THE DIST. BTWN. PILES=XDST. THE WV. LENG.=WL. 1/25TH OF
C         THE WV. LENG. =DXX. THE NO. OF INCREMENTS OF X-MBR=KDIV. AND THE
C         LENG  OF THE INCREMENT=DLX
C
          XDST=ABS(DX(J)-DX(J+1))
          WL=2.*PI/REAL(K1(1))
          DXX=WL*.04
          KDIV=XDST/DXX
          IF(KDIV .LT. 2) KDIV=2
          DLX=XDST/KDIV
          X=DX(J)-DLX/2.
          DO 570 M=1,KDIV
          X=X+DLX
C
C         CALCULATE VERT.  VELOC. SPATIAL FUNC. FOR ALL WAVE MODES=WSUM
C
          WSUM=CMPLX(0.,0.)
          DO 590 NN=1,NUM
          WSM=W(BM(N2+NN),BM(N3+NN),X,XO(L,J),K2(NN),H2)
          WSUM=WSUM+WSM
      590 CONTINUE
C
C         CALCULATE VERT.  VELOC. SPATIAL FUNC. TIMES ITS COMPLEX CONJUGATE
C
          WWW= ((REAL(WSUM))**2)+((AIMAG(WSUM))**2)
          FZXX= DLX*T*( AL*VIS*.5*WWW + 4.*BET*DI* (WWW**1.5)/ (3.*PI) )
          FZX=FZX+FZXX
      570 CONTINUE
      560 CONTINUE
      550 CONTINUE
C
C         END CALCULATION OF FZX
C
C         CALCULATE NEW TOTAL VERT. DIMENSIONLESS DAMPING COEF.=FZNEW
C
          FZNEW=(FZX+FZY)/SMZ
          WRITE(6,652)FX,FXNEW,FZ,FZNEW
```

PROGRAM PILE1

```
  652 FORMAT(+F14.7)
      WRITE(6,653)
  653 FORMAT(1H0,30X, * NEW ITERATION STARTS HERE *////)
C
C     CHECK FX VS. FXNEW AND FZ VS. FZNEW FOR CONVERGENCE.
C
      IF(FZNEW.EQ.0.) GO TO 672
      IF(FXNEW.EQ.0.) GO TO 671
      IF(ABS(FX/FXNEW-1.).LE.0.05.AND.ABS(FZ/FZNEW-1.).LE.0.05)GO TO 600
  671 IF(ABS(FZ/FZNEW-1.).LE. .05 .AND.FXNEW.EQ. 0.) GO TO 600
      GO TO 673
  672 IF(ABS(FX/FXNEW-1.).LE. .05 .AND. FZNEW.EQ. 0.) GO TO 600
  673 CONTINUE
C
C     IF NOT CONVERGED REDEFINE FX,FZ
C
      FX=    FXNEW
      FZ=    FZNEW
C
C     START ITERATION AGAIN WITH UPDATED FX, FZ VALUES
C
      GO TO 82
C
C     CONVERGENCE
C
  600 CONTINUE
C
C     BEGIN CALCULATION SEQUENCE FOR WATER SURFACE PROFILE IN REGION 3
      XMAX=0.0
      SSMAX=0.0
      DIV=.05
      IF(C.GE.30.) DIV=.025
      NC=(1./DIV)+1.5
      X=B-DIV*C
      DO 720 M=1,NC
      X=X+DIV*C
      SS=0.0
      DO 715 J=1,NUM
      TT=BM(NUM+J)*(CEXP(I*K3(J)*(X-B))+CRA*CEXP((-I)*K3(J)*(X-B-2.*C)))
      SS=SS+TT
  715 CONTINUE
      SSRR(M)=REAL(SS)
      SSR=ABS(REAL(SS))
      IF(SSR.GT.SSMAX) XMAX=X
      IF(SSR.GT.SSMAX)  SSMAX=SSR
  720 CONTINUE
      WRITE(6,725)  (SSRR(M),M=1,10)
      WRITE(6,725)  (SSRR(M),M=11,21)
      IF(C.LT.40.)  GO TO 726
      WRITE(6,725)  (SSRR(M),M=22,31)
      WRITE(6,725)  (SSRR(M),M=32,41)
  726 CONTINUE
  725 FORMAT(1H0,11F10.5)
      WRITE(6,610) CRA,H2,C,SSMAX,XMAX
  610 FORMAT(1H0,*CRA..H2..B..DIMENSIONLESS MAX ETA..XMAX*,5(F10.5,6X))
C
C     END WATER SURFACE PROFILE CALCULATION
C
C     CALCULATE WAVE STEEPNESS=HL
C
      HL=2.*AMP /WL
C
C     WRITE WV. AMP,PERIOD,STEEPNESS, PROP. MODE REF. AND TRAN. COEFS.
C
      WRITE(6,670) AMP,T,HL,CABS(BM(1)),CABS(BM(MP1))
  670 FORMAT(1H-,*AMP=*,F11.4,5X,*PERIOD=*,F11.4,5X,*H/L=*,F6.4,5X,
     $*CR=*,F11.4,5X,*CT=*,F11.4////)
  675 CONTINUE
      STOP
      END
```

FUNCTION CH

```
      COMPLEX FUNCTION CH(A,R)
C
C     THIS FUNCTION SUBPROG. COMPUTES THE HYPERBOLIC COSINE OF THE
C     COMPLEX ARGUMENT REFERRED FROM THE MAIN PROGRAM
C
      COMPLEX A
      CH=(CEXP(A*R)+CEXP(-A*R))/2.
      RETURN
      END
```

FUNCTION SH

```
      COMPLEX FUNCTION SH(N,A,R)
C
C     THIS FUNCTION SUBPROG. COMPUTES THE HYPERBOLIC  SINE  OF THE
C     COMPLEX ARGUMENT REFERRED FROM THE MAIN PROGRAM
C
      COMPLEX A
      SH=(CEXP(N*A*R)-CEXP(-N*A*R))/2.
      RETURN
      END
```

FUNCTION TH

```
      COMPLEX FUNCTION TH(N,A,R)
C
C     THIS FUNCTION SUBPROG. COMPUTES THE HYPERBOLIC TANGENT OF THE
C     COMPLEX ARGUMENT REFERRED FROM THE MAIN PROGRAM
C
      COMPLEX A,SH,CH
      TH=SH(N,A,R)/CH(A,R)
      RETURN
      END
```

FUNCTION EQ

```
      COMPLEX FUNCTION EQ(A,B,C,D)
C
C     THIS FUNCTION SUBPROG. COMPUTES A COMPLEX FUNCTION USED IN
C     EQ.4.2.2 AND EQ.4.2.3
C
      COMPLEX A,B,CH,SH
      E=D-C
      EQ=((A*CH(B,C)*SH(1,A,D))-(B*CH(A,D)*SH(1,B,C))-(A*SH(1,A,E)))/
     $(CH(B,C)*((A**2)-(B**2)))
      RETURN
      END
```

FUNCTION EQQ

```
      COMPLEX FUNCTION EQQ(A,B,C,D)
C
C     THIS FUNCTION SUBPROG. COMPUTES A COMPLEX FUNCTION USED IN
C     EQ.4.2.5 AND EQ.4.2.6
C
      COMPLEX A,B,CH,SH
      E=C-D
      EQQ=((A*CH(B,C)*SH(1,A,D))-(B*CH(A,D)*SH(1,B,C))+(B*SH(1,B,E)))/
     $(CH(B,C)*((A**2)-(B**2)))
      RETURN
      END
```

FUNCTION QQ

```
      COMPLEX FUNCTION QQ(A,B)
C
C     THIS FUNCTION SUBPROG. COMPUTES A COMPLEX FUNCTION USED IN
C     EQS. 4.2.2, 4.2.3, 4.2.5, AND 4.2.6
C
      COMPLEX A,SH
      QQ=SH(2,A,B)+(2*A*B)
      RETURN
      END
```

FUNCTION EE

```
      COMPLEX FUNCTION EE(K)
C
C     THIS FUNCTION SUBPROG. COMPUTES A COMPLEX FUNCTION USED IN
C     EQS. 4.2.2, 4.2.3, 4.2.5, AND 4.2.6
C
      COMPLEX I,K,AX,AZ,K1ONE,AXAZ
      COMMON I,B,AX,AZ,K1ONE,H1,AMP,SIG,G
C
C     THE NEXT 6 LINES CHECK THE SIGN OF THE SQRT OF (AX/AZ) IN ORDER
C     TO ASSURE WAVE DECAY IN THE STRUCTURE
C
      AXAZ=CSQRT((AX/AZ))
      P=REAL(AXAZ)
      Q=AIMAG(AXAZ)
      R=REAL(K)
      S=AIMAG(K)
      IF(Q.LT.0..AND.P*S.LT.ABS(Q)*R)AXAZ=-AXAZ
      EE=CEXP(I*2*B*K*AXAZ)
      RETURN
      END
```

FUNCTION CC

```
      COMPLEX FUNCTION CC(A)
C
C     THIS FUNCTION SUBPROG. COMPUTES THE COMPLEX CONJUGATE OF THE ARG.
C
      COMPLEX A
      CC=CONJG(A)
      RETURN
      END
```

FUNCTION U

```
      COMPLEX FUNCTION U(CP,CM,X,Z,K,H)
C
C     THIS FUNCTION SUBPROG. COMPUTES A SINGLE MODE OF THE HORIZ.
C     SPATIAL VELOC. FUNC. U(X,Z)
C
      COMPLEX CP,CM,K,I,AX,AZ,K1ONE,CH ,AXAZ
      COMMON I,B,AX,AZ,K1ONE,H1,AMP,SIG,G
C
C     THE NEXT 6 LINES CHECK THE SIGN OF THE SQRT OF (AX/AZ) IN ORDER
C     TO ASSURE WAVE DECAY IN THE STRUCTURE
C
      AXAZ=CSQRT((AX/AZ))
      P=REAL(AXAZ)
      Q=AIMAG(AXAZ)
      R=REAL(K)
      S=AIMAG(K)
      IF(Q.LT.0..AND.P*S.LT.ABS(Q)*R)AXAZ=-AXAZ
      U=   (1/AX)*I*G*K*AXAZ          *   ((CP*AMP)*CEXP(I*K*AXAZ
     $   *(X+B))   - (CM*AMP)*   CEXP(-I*K*AXAZ           *(X-B)))*(CH(K,
     $(H+Z))/CH(K,H))
      RETURN
      END
```

FUNCTION W

```
      COMPLEX FUNCTION W(CP,CM,X,Z,K,H)
C
C     THIS FUNCTION SUBPROG. COMPUTES A SINGLE MODE OF THE VERT.
C     SPATIAL VELOC. FUNC.,W(X,Z)
C
      COMPLEX CP,CM,K,I,AX,AZ,K1ONE,CH,SH ,AXAZ
      COMMON I,B,AX,AZ,K1ONE,H1,AMP,SIG,G
C
C     THE NEXT 6 LINES CHECK THE SIGN OF THE SQRT OF (AX/AZ) IN ORDER
C     TO ASSURE WAVE DECAY IN THE STRUCTURE
C
      AXAZ=CSQRT((AX/AZ))
      P=REAL(AXAZ)
      Q=AIMAG(AXAZ)
      R=REAL(K)
      S=AIMAG(K)
      IF(Q.LT.0..AND.P*S.LT.ABS(Q)*R)AXAZ=-AXAZ
      W= (1/AZ) *G*K *(SH(1,K,(H+Z))/CH(K,H)) * ((CP*AMP)*CEXP(I*K*
     $ AXAZ          *(X+B))+  (CM*AMP)* CEXP(-I*K*AXAZ              *
     $ (X-B)))
      RETURN
      END
```

SUBROUTINE RAPNEW

```
      SUBROUTINE RAPNEW(O,NUM,H,SIG,G,PI)
C
C     THIS SUBRTN. COMPUTES THE REGIONS 1 AND 3 EIGENVALUES,I.E. K1(L)
C     AND K3(L), IN THE ARRAY O(L) USING THE NEWTON-RAPHSON TECHNIQUE
C
      DIMENSION O(005)
C
C     COMPUTE THE FIRST, OR PROPAGATING, MODE EIGENVALUE=O(1)
C
      O(1)=.25
    3 OA=O(1)
      O(1)=O(1)-((O(1)*TANH(O(1)*H)-((SIG**2)/G   ))/((TANH(O(1)*H))+
     $(O(1)*H/(COSH(O(1)*H))**2)))
      IF(ABS(OA-O(1)).GT.0.0005) GO TO 3
C
C     COMPUTE THE NUM-1 EVANESCENT MODE EIGENVALUES=O(2) TO O(NUM)
C
      DO 13 J=2,NUM
      O(J)=(J-1)*PI/H
   23 OB=O(J)
      O(J)=O(J)-(((O(J)*TAN(O(J)*H))+((SIG**2)/G   ))/((TAN(O(J)*H))+
     $(O(J)*H*(1/COS(O(J)*H)**2))))
      IF(ABS(OB-O(J)).GT.0.0005) GO TO 23
   13 CONTINUE
C
C     RETURN O(L) TO MAIN PROG.FOR LOADING IN COMPLEX ARRAYS K1(L),K3(L)
C
      RETURN
      END
```

SUBROUTINE CMPLK2

```
      SUBROUTINE CMPLK2(K2,NUM,H,SIG,SZ,FZ,G,PI,I)
C
C     THIS SUBRTN. COMPUTES THE FIRST 15 COMPLEX EIGENVALUES IN REGION 2
C     USING A NEWTON-RAPHSON SOLUTION TECHNIQUE
C
      COMPLEX KH(15), KK(35,25,5),I,TA,CS,KA,KHL,KHH,K2(005)
      DIMENSION DIMSIG(35),FZSZ(25)
C
C     CS=HYPERBOLIC COS. STMT.FUNC..AND TA=HYPERB. TAN. STMT. FUNC.
C
      CS(E)=(CEXP(E)+CEXP(-E))/2.
      TA(B)=(CEXP(B)-CEXP(-B))/(CEXP(B)+CEXP(-B))
C
C     COMPUTE THE DESIGN VALUE OF THE DIMENSIONLESS WAVE FREQ. BEING
C     USED FOR THE PRESENT ANALYSIS=REDMSG
C
      REDMSG=SZ*(SIG**2)*H/G
C
C     COMPUTE THE DESIGN VALUE OF FZ/SZ=REFZSZ
C
      REFZSZ=FZ/SZ
C
C     BEGIN SEARCH THRU DISK FILE=*TAPE1*(ON WHICH INITIAL EST. OF FIRST
C     FIVE MODAL KH VALUES=KK IN REGION 2 ARE STORED FOR 35 VALUES OF
C     DIMENSIONLESS WAVE FREQ.=DIMSIG,AND 25 VALUES OF FZ/SZ=FZSZ).
C
      N=1
      DO 10 M=N,35
C
C     READ STORED VALUES OF DIMSIG,FZSZ, AND KK FROM TAPE1
C
      READ(1)DIMSIG(M)
      DO 15 J=1,25
      READ(1)FZSZ(J),(KK(M,J,K),K=1,5)
   15 CONTINUE
      DO 20 J=2,25
      IF(M.EQ.1)GO TO 20
C
C     SEARCH TAPE1 UNTIL VALUES OF STORED TAPE1 PARAMETERS DIMSIG AND
C     FZSZ JUST ABOVE AND JUST BELOW THE DESIGN VALUES REDMSG AND REFZSZ
C     ARE FOUND
C
      IF(DIMSIG(M-1).LE.REDMSG   .AND.   DIMSIG(M).GE.REDMSG   .AND.
     $FZSZ(J-1).LE.REFZSZ   .AND.   FZSZ(J).GE.REFZSZ)GO TO 30
      GO TO 20
   30 WRITE(6,50)DIMSIG(M-1),REDMSG,DIMSIG(M),FZSZ(J-1),REFZSZ,FZSZ(J)
   50 FORMAT(1H0,/////3F12.4,25X,3F12.4)
      WRITE(6,60)(KK(M-1,J-1,L),L=1,5),(KK(M-1,J,L),L=1,5)
      WRITE(6,60)(KK(M,J-1,L), L=1,5),(KK(M,J,L),L=1,5)
   60 FORMAT(1H0,10F12.4,/10F12.4)
      DO 70 L=1,5
C
C     INTERPOLATE BETWEEN THE KK VALUES FOR THE HIGHER AND LOWER VALUES
C     OF FZSZ CORRESPONDING TO THE HIGHER VALUE OF DIMSIG=KHH
C
      KHH=(KK(M,J,L)-KK(M,J-1,L))* (REFZSZ-FZSZ(J-1))/
     $(FZSZ(J)-FZSZ(J-1))+KK(M,J-1,L)
C
C     INTERPOLATE BETWEEN THE KK VALUES FOR THE HIGHER AND LOWER VALUES
C     OF FZSZ CORRESPONDING TO THE LOWER  VALUE OF DIMSIG=KHL
C
      KHL=(KK(M-1,J,L)-KK(M-1,J-1,L))* (REFZSZ-FZSZ(J-1))/
     $(FZSZ(J)-FZSZ(J-1))+KK(M-1,J-1,L)
C
C     INTERPOLATE BETWEEN KHH AND KHL TO OBTAIN NEWTON-RAPHSON INITIAL
C     ESTIMATES FOR THE FIRST FIVE MODES OF KH(L)
C
      KH(L)=(KHH-KHL)*(REDMSG-DIMSIG(M-1))/(DIMSIG(M)-DIMSIG(M-1))+KHL
   70 CONTINUE
      GO TO 90
   20 CONTINUE
   10 CONTINUE
   90 CONTINUE
      DO 100 J=1,15
      IF(J.GT.5)GO TO 110
  120 KA=KH(J)
```

SUBROUTINE CMPLK2

```
C        COMPUTE KH(L) VALUES USING NEWTON-RAPHSON TECHNIQUE
         KH(J)=KH(J)-(KH(J)*TA(KH(J))-(REDMSG+REDMSG*I*REFZSZ))/
        $(TA(KH(J))+(KH(J)/CS(KH(J))**2))
         GO TO 130
C
C        ESTABLISH INITIAL EST. OF REAL PART OF KH(L) FOR MODES 6-15 AS
C        REAL PART OF PREVIOUS KH.I.E. KH(L-1)
C
     110 GM = REAL(KM(J-1))
C
C        ESTABLISH INITIAL EST. OF IMAG PART OF KH(L) FOR MODES 6-15 AS
C        IMAG PART OF PREVIOUS KH,I.E. KH(L-1),PLUS 3.2
C
         AA=AIMAG(KH(J-1))+3.2
         KH(J)=CMPLX(GM,AA)
         GO TO 120
C
C        BEGIN CHECK FOR CONVERGENCE
C
     130 F=REAL(KA)
         FF=REAL(KH(J))
         GA=AIMAG(KA)
         GG=AIMAG(KH(J))
         IF(FF.EQ. 0.) GO TO 190
         IF(GG.EQ.0.) GO TO 170
         IF(ABS(1-F/FF).GT. .001 .OR. ABS(1-GA/GG).GT. .001) GO TO 120
         GO TO 180
     170 IF(ABS(1-F/FF).GT. .001) GO TO 120
         GO TO 180
     190 IF(ABS(1-GA/GG).GT. .001) GO TO 120
     180 CONTINUE
C
C        END   CHECK FOR CONVERGENCE
C
     100 CONTINUE
         WRITE(6,150)REDMSG,REFZSZ
         WRITE(6,140)(KH(J),J=1,5)
         WRITE(6,140)(KH(J),J=6,10)
         WRITE(6,140)(KH(J),J=11,15)
     140 FORMAT(1H0,5(F7.4,2X,F8.4,5X))
     150 FORMAT(//1H0,20X,*SZ*(SIG**2)*H/G=*,F7.4,15X,*FZSZ=*,F6.4///)
C
C        CALCULATE K2(L) ARRAY FROM KH(L)
C
         DO 160 J=1,NUM
         K2(J)=KH(J)/H
         WRITE(6,140)K2(J)
     160 CONTINUE
         REWIND 1
C
C        RETURN K2(L) ARRAY TO MAIN PROGRAM
C
         RETURN
         END
```

APPENDIX E

An example of the initial estimates of the first five modal k_2h_2 values stored on Tape 1 for use by the iterative Newton-Raphson technique subroutine CMPLK2.

THE VALUE OF SZ*(SIG**2)*H/G ON THIS PAGE IS .0500

FZ/SZ	KH(1)		KH(2)		KH(3)		KH(4)		KH(5)	
0.000	.225	0.000	0.000	3.126	0.000	6.275	0.000	9.419	0.000	12.562
.040	.226	.005	.001	3.126	.000	6.275	.000	9.419	.000	12.562
.080	.226	.009	.001	3.126	.001	6.275	.000	9.419	.000	12.562
.200	.227	.023	.003	3.126	.002	6.275	.001	9.419	.001	12.562
.400	.230	.045	.006	3.126	.003	6.275	.002	9.419	.002	12.562
.600	.234	.066	.010	3.126	.005	6.275	.003	9.419	.002	12.562
.800	.240	.086	.013	3.126	.006	6.275	.004	9.419	.003	12.562
1.000	.247	.105	.016	3.126	.008	6.275	.005	9.419	.004	12.562
1.200	.254	.122	.019	3.126	.010	6.275	.006	9.419	.005	12.562
1.400	.261	.138	.023	3.126	.011	6.275	.007	9.419	.006	12.562
1.600	.269	.154	.026	3.126	.013	6.275	.008	9.419	.006	12.562
1.800	.276	.168	.029	3.126	.014	6.275	.010	9.419	.007	12.562
2.000	.284	.182	.032	3.126	.016	6.275	.011	9.419	.008	12.562

THE VALUE OF SZ*(SIG**2)*H/G ON THIS PAGE IS .1600

FZ/SZ	KH(1)		KH(2)		KH(3)		KH(4)		KH(5)	
0.000	.411	0.000	0.000	3.090	0.000	6.258	0.000	9.408	0.000	12.554
.040	.411	.009	.002	3.090	.001	6.258	.001	9.408	.001	12.554
.080	.411	.017	.004	3.090	.002	6.258	.001	9.408	.001	12.554
.200	.413	.043	.011	3.090	.005	6.258	.003	9.408	.003	12.554
.400	.418	.085	.021	3.090	.010	6.258	.007	9.408	.005	12.554
.600	.426	.125	.032	3.090	.015	6.258	.010	9.408	.008	12.554
.800	.435	.164	.042	3.090	.021	6.258	.014	9.408	.010	12.554
1.000	.446	.199	.053	3.091	.026	6.258	.017	9.408	.013	12.554
1.200	.457	.233	.063	3.091	.031	6.258	.020	9.408	.015	12.554
1.400	.469	.265	.074	3.091	.036	6.258	.024	9.408	.018	12.554
1.600	.481	.295	.084	3.092	.041	6.258	.027	9.408	.020	12.554
1.800	.492	.323	.095	3.092	.046	6.258	.031	9.408	.023	12.554
2.000	.503	.351	.105	3.093	.051	6.258	.034	9.408	.026	12.554

THE VALUE OF SZ*(SIG**2)*H/G ON THIS PAGE IS .3000

FZ/SZ	KH(1)		KH(2)		KH(3)		KH(4)		KH(5)	
0.000	.577	0.000	0.000	3.043	0.000	6.235	0.000	9.393	0.000	12.542
.040	.577	.013	.004	3.043	.002	6.235	.001	9.393	.001	12.542
.080	.577	.025	.008	3.043	.004	6.235	.003	9.393	.002	12.542
.200	.579	.064	.020	3.043	.010	6.235	.006	9.393	.005	12.542
.400	.585	.126	.040	3.044	.019	6.235	.013	9.393	.010	12.542
.600	.594	.185	.061	3.044	.029	6.235	.019	9.393	.014	12.542
.800	.606	.242	.081	3.045	.039	6.235	.026	9.393	.019	12.542
1.000	.618	.295	.101	3.046	.048	6.235	.032	9.393	.024	12.542
1.200	.631	.346	.121	3.047	.058	6.235	.038	9.393	.029	12.543
1.400	.643	.394	.142	3.048	.068	6.236	.045	9.393	.034	12.543
1.600	.655	.440	.162	3.050	.078	6.236	.051	9.393	.038	12.543
1.800	.667	.483	.183	3.051	.087	6.236	.058	9.393	.043	12.543
2.000	.677	.525	.203	3.053	.097	6.236	.064	9.393	.048	12.543

THE VALUE OF SZ*(SIG**2)*H/G ON THIS PAGE IS .6000

FZ/SZ	KH(1)		KH(2)		KH(3)		KH(4)		KH(5)	
0.000	.861	0.000	0.000	2.940	0.000	6.187	0.000	9.361	0.000	12.518
.040	.861	.021	.008	2.940	.004	6.187	.003	9.361	.002	12.518
.080	.861	.042	.017	2.940	.008	6.187	.005	9.361	.004	12.518
.200	.863	.105	.042	2.941	.020	6.187	.013	9.361	.010	12.518
.400	.868	.208	.084	2.941	.039	6.187	.026	9.361	.019	12.518
.600	.876	.307	.127	2.943	.059	6.187	.039	9.361	.029	12.519
.800	.884	.402	.169	2.945	.078	6.187	.051	9.361	.038	12.519
1.000	.892	.493	.213	2.947	.098	6.187	.064	9.361	.048	12.519
1.200	.898	.579	.256	2.951	.118	6.187	.077	9.361	.058	12.519
1.400	.901	.661	.301	2.955	.137	6.188	.090	9.361	.067	12.519
1.600	.902	.739	.347	2.960	.157	6.188	.103	9.361	.077	12.519
1.800	.899	.814	.393	2.967	.177	6.189	.116	9.361	.087	12.519
2.000	.893	.885	.441	2.975	.198	6.189	.129	9.362	.096	12.519

THE VALUE OF SZ*(SIG**2)*H/G ON THIS PAGE IS 1.0000

FZ/SZ	KH(1)		KH(2)		KH(3)		KH(4)		KH(5)	
0.000	1.200	0.000	0.000	2.798	0.000	6.121	0.000	9.318	0.000	12.486
.040	1.200	.033	.014	2.798	.007	6.121	.004	9.318	.003	12.486
.080	1.200	.067	.029	2.798	.013	6.121	.009	9.318	.006	12.486
.200	1.200	.166	.072	2.798	.033	6.121	.021	9.318	.016	12.486
.400	1.199	.330	.144	2.798	.065	6.121	.043	9.318	.032	12.486
.600	1.195	.489	.218	2.799	.098	6.121	.064	9.318	.048	12.486
.800	1.186	.642	.295	2.799	.131	6.121	.086	9.318	.064	12.486
1.000	1.170	.790	.376	2.801	.165	6.121	.108	9.318	.080	12.486
1.200	1.145	.930	.462	2.805	.199	6.121	.130	9.318	.096	12.486
1.400	1.107	1.063	.555	2.812	.233	6.121	.151	9.318	.113	12.486
1.600	1.056	1.185	.656	2.826	.268	6.122	.173	9.318	.129	12.486
1.800	.991	1.293	.765	2.850	.303	6.122	.196	9.318	.145	12.486
2.000	.915	1.382	.881	2.892	.339	6.122	.218	9.318	.162	12.486

THE VALUE OF SZ*(SIG**2)*H/G ON THIS PAGE IS 1.9000

FZ/SZ	KH(1)		KH(2)		KH(3)		KH(4)		KH(5)	
0.000	1.975	0.000	0.000	2.490	0.000	5.975	0.000	9.222	0.000	12.415
.040	1.974	.069	.024	2.489	.012	5.975	.008	9.222	.006	12.414
.080	1.974	.137	.048	2.489	.024	5.975	.016	9.222	.012	12.414
.200	1.967	.343	.120	2.483	.061	5.975	.040	9.221	.030	12.414
.400	1.944	.688	.244	2.462	.122	5.973	.081	9.221	.061	12.414
.600	1.901	1.042	.376	2.421	.184	5.970	.122	9.220	.091	12.414
.800	1.831	1.419	.522	2.346	.248	5.966	.163	9.219	.122	12.413
1.000	1.743	1.866	.671	2.193	.314	5.960	.205	9.217	.153	12.413
1.200	1.774	2.396	.685	1.949	.383	5.952	.247	9.215	.184	12.412
1.400	1.892	2.811	.596	1.814	.456	5.942	.291	9.213	.215	12.411
1.600	1.978	3.156	.521	1.745	.534	5.930	.336	9.210	.247	12.410
1.800	2.027	3.472	.462	1.703	.619	5.914	.381	9.207	.280	12.409
2.000	2.042	3.775	.415	1.676	.714	5.894	.429	9.203	.313	12.407

THE VALUE OF SZ*(SIG**2)*H/G ON THIS PAGE IS 5.0000

FZ/SZ	KH(1)		KH(2)		KH(3)		KH(4)		KH(5)	
0.000	5.000	0.000	0.000	1.941	0.000	5.550	0.000	8.914	0.000	12.177
.040	5.000	.200	.016	1.940	.022	5.549	.018	8.913	.014	12.177
.080	5.000	.400	.032	1.938	.044	5.548	.036	8.913	.029	12.176
.200	5.000	1.000	.079	1.925	.109	5.540	.090	8.910	.072	12.175
.400	5.000	2.000	.141	1.882	.216	5.511	.180	8.898	.145	12.170
.600	5.000	3.000	.177	1.827	.318	5.459	.272	8.877	.220	12.160
.800	5.000	3.999	.191	1.773	.407	5.383	.365	8.845	.296	12.146
1.000	4.999	5.000	.189	1.729	.471	5.285	.459	8.799	.374	12.126
1.200	5.000	6.001	.181	1.695	.501	5.179	.552	8.735	.455	12.100
1.400	5.001	7.000	.169	1.670	.499	5.083	.636	8.647	.540	12.064
1.600	4.999	7.999	.158	1.651	.478	5.006	.697	8.535	.627	12.015
1.800	5.000	9.001	.146	1.637	.450	4.948	.723	8.412	.714	11.949
2.000	5.001	10.000	.136	1.626	.420	4.904	.712	8.299	.797	11.860

THE VALUE OF SZ*(SIG**2)*H/G ON THIS PAGE IS 9.0000

FZ/SZ	KH(1)		KH(2)		KH(3)		KH(4)		KH(5)	
0.000	9.000	0.000	0.000	1.764	0.000	5.240	0.000	8.618	0.000	11.920
.040	9.000	.360	.008	1.764	.019	5.239	.021	8.617	.020	11.919
.080	9.000	.720	.017	1.763	.038	5.237	.042	8.616	.040	11.919
.200	9.000	1.800	.040	1.756	.093	5.225	.105	8.607	.100	11.913
.400	9.000	3.600	.071	1.734	.174	5.183	.206	8.573	.199	11.891
.600	9.000	5.400	.090	1.706	.234	5.122	.297	8.517	.296	11.853
.800	9.000	7.200	.097	1.680	.268	5.053	.369	8.441	.387	11.797
1.000	9.000	9.000	.097	1.658	.280	4.989	.415	8.353	.467	11.721
1.200	9.000	10.800	.094	1.641	.276	4.936	.434	8.266	.526	11.629
1.400	9.000	12.600	.089	1.628	.265	4.893	.431	8.189	.558	11.529
1.600	9.000	14.400	.083	1.617	.251	4.860	.416	8.126	.563	11.435
1.800	9.000	16.200	.078	1.610	.235	4.834	.394	8.076	.548	11.354
2.000	9.000	18.000	.073	1.603	.220	4.814	.371	8.038	.523	11.289

THE VALUE OF SZ*(SIG**2)*H/G ON THIS PAGE IS14.0000

FZ/SZ	KH(1)		KH(2)		KH(3)		KH(4)		KH(5)	
0.000	14.000	0.000	0.000	1.691	0.000	5.059	0.000	8.394	0.000	11.691
.040	14.000	.560	.005	1.691	.014	5.059	.019	8.394	.021	11.691
.080	14.000	1.120	.010	1.690	.027	5.057	.037	8.392	.041	11.689
.200	14.000	2.800	.025	1.686	.066	5.047	.091	8.380	.102	11.679
.400	14.000	5.600	.043	1.673	.120	5.014	.172	8.340	.197	11.643
.600	14.000	8.400	.055	1.656	.156	4.969	.233	8.282	.278	11.585
.800	14.000	11.200	.060	1.640	.173	4.924	.270	8.215	.338	11.511
1.000	14.000	14.000	.060	1.627	.177	4.884	.285	8.151	.372	11.431
1.200	14.000	16.800	.058	1.616	.174	4.852	.285	8.096	.384	11.355
1.400	14.000	19.600	.056	1.608	.166	4.826	.275	8.051	.379	11.289
1.600	14.000	22.400	.052	1.601	.157	4.806	.262	8.016	.365	11.236
1.800	14.000	25.200	.049	1.596	.148	4.790	.247	7.988	.347	11.194
2.000	14.000	28.000	.046	1.592	.139	4.778	.232	7.967	.327	11.161